Precise modeling of prompt photons in associated top-quark pair production

Von der Fakultät für Mathematik, Informatik und Naturwissenschaften der RWTH Aachen University zur Erlangung des akademischen Grades eines Doktors der Naturwissenschaften genehmigte Dissertation

vorgelegt von

Daniel Stremmer, M.Sc.

aus

Trier

Berichter: Prof. Dr. rer. nat. Malgorzata Worek
Prof. Dr. rer. nat. Robert Harlander

Tag der mündlichen Prüfung: 19.07.2024

Abstract

This thesis addresses several aspects of the precise modeling of prompt photons in associated $t\bar{t}$ production using the HELAC-NLO framework, which was extended in various ways to deal with these problems. The first point is the calculation of NLO QCD corrections to the $pp \to t\bar{t}\gamma\gamma$ process in the *di-lepton* and *lepton + jet* decay channels at the LHC, where in the first case both W bosons decay into lepton-neutrino pairs and in the second case one W boson decays into a quark pair. In contrast to previous calculations, we include for the first time photon radiation and NLO QCD corrections in the production and decays of the two top quarks. The narrow-width approximation (NWA) is used to model the decays of the unstable top quarks and W bosons while preserving spin correlations. This calculation is used to quantify the effects of prompt photon radiation in the decays, which were already found to be important in the $pp \to t\bar{t}\gamma$ process. Additionally, we discuss the complications in the *lepton + jet* decay channel that arise at higher orders from additional QCD radiation and can lead to substantial enhancements of the NLO QCD corrections.

Next, we focus on the size of subleading LO and NLO contributions in top-quark pair production with one and two isolated photons. Previous calculations only partially addressed this issue by performing the calculation only with stable top quarks and additionally considering only a subset of the subleading contributions in the case of $pp \to t\bar{t}\gamma\gamma$. In contrast, we calculate the complete NLO corrections to both processes, consisting of the NLO QCD calculation with all subleading LO and NLO contributions, and consistently include higher-order QCD and EW corrections as well as photon bremsstrahlung in all decay stages in the decay chain of the *di-lepton* decay channel. In addition, we introduce an approximation for the full calculation, in which photon radiation in the decays is included only in all LO contributions and in the dominant QCD corrections, while photon radiation in the decays is neglected in the subleading NLO contributions, which are therefore only calculated in the case where all photons are emitted in the production process. This approximation leads to precise results with negligible differences compared to the complete calculation and it significantly simplifies the overall calculation and a possible matching to parton showers.

Finally, we concentrate on the dependence of the theoretical predictions on the different photon isolation criteria. In particular, the experimental measurements rely almost exclusively on the fixed-cone isolation, where a certain amount of hadronic energy is allowed inside a cone around the isolated photon. This photon isolation criterion leads to technical complications in theoretical predictions due to the non-vanishing parton-to-photon fragmentation contribution. Therefore, the smooth-cone photon isolation criterion is often used in such calculations, where the fragmentation contribution completely vanishes, but this photon isolation criterion cannot be directly used in experimental measurements. As a first step towards a better understanding of the different isolation criteria in prompt photon production with a top-quark pair, we perform the calculation of NLO QCD corrections using the fixed-cone isolation for the $pp \to e^+\nu_e\,\mu^-\bar{\nu}_\mu\,b\bar{b}\,\gamma$ process and perform a comparison with predictions using other isolation criteria and different input values.

Zusammenfassung

In dieser Arbeit werden verschiedene Aspekte zur präzisen Modellierung der Photonenstrahlung in assoziierten Top-Quark-Paarprozessen mit Hilfe des HELAC-NLO-Programms behandelt, das zur Bewältigung dieser Probleme erweitert wurde. Der erste Punkt ist die Berechnung der ersten Korrekturen in der Quantenchromodynamik (NLO QCD) im $pp \to t\bar{t}\gamma\gamma$ Prozess am LHC für die beiden Zerfallskanälen, in denen entweder beide W-Bosonen in jeweils ein Lepton und ein Neutrino zerfallen (*di-lepton*) oder ein W-Boson in ein Quarkpaar zerfällt (*lepton + jet*). Im Gegensatz zu früheren Berechnungen berücksichtigen wir erstmals Photonenstrahlung und NLO-QCD-Korrekturen im Produktionsprozess und in den Zerfallsprozessen des Top-Quark-Paares. Die Zerfälle der instabilen Top-Quarks und W-Bosonen werden mit der narrow-width approximation (NWA) unter der Berücksichtigung von Spin-Korrelationen modelliert. Diese Berechnungen werden verwendet, um die Effekte der Photonenstrahlung in den Zerfällen zu quantifizieren, die sich bereits im $pp \to t\bar{t}\gamma$ Prozess als wichtig erwiesen haben. Außerdem gehen wir auf die Komplikationen im *lepton + jet* Zerfallskanal ein, die durch zusätzliche Strahlung von Quarks oder Gluonen in höheren Ordnungen der Störungstheorie verursacht werden und zu einer deutlichen Vergrößerung der NLO-QCD-Korrekturen führen können.

Als nächstes fokussieren wir uns auf die Berechnung von zweitrangigen Korrekturen der führenden Ordnung (LO) und der nächsthöheren Ordnung (NLO) in der Störungstheorie im Fall von Top-Quark-Paarproduktion mit einem und zwei isolierten Photonen. Bisherige Berechnungen behandelten dies nur teilweise, indem sie diese Rechnungen nur für stabile Top-Quarks durchführten und nur einen Teil der zweitrangigen Korrekturen im $pp \to t\bar{t}\gamma\gamma$ Prozess berücksichtigten. Im Gegensatz dazu berechnen wir die kompletten LO- und NLO-Beiträge für beide Prozesse im *di-lepton* Zerfallskanal unter der Berücksichtigung von Korrekturen der Quantenchromodynamik und der elektroschwachen Wechselwirkung sowie der Photonenstrahlung im Produktionsprozess und in den Zerfallsprozessen. Zusätzlich führen wir eine Näherung ein, in der Photonenstrahlung in allen LO Beiträgen und den führenden NLO-QCD-Korrekturen enthalten ist, während Photonenstrahlung in Zerfallsprozessen in den zweitrangigen NLO Korrekturen vernachlässigt wird. Diese Näherung liefert eine präzise Alternative mit vernachlässigbaren Abweichungen gegenüber der kompletten Rechnung, führt jedoch zu signifikanten Vereinfachungen in der Berechnung und in der möglichen Kombinierung mit Partonschauern.

Abschließend konzentrieren wir uns auf die Benutzung von verschiedenen Photonenisolationskriterien in theoretischen Vorhersagen. Insbesondere werden in experiemnentellen Messungen fast ausschließ das fixed-cone Isoliationskriterium benutzt, wobei eine bestimmte Menge an hadronischer Energie innerhalb eines Kegels um das isolierte Photon erlaubt ist. Dieses Isolationskriterium führt zu weiteren Komplikationen in theoretischen Berechnungen aufgrund von Fragmentierungsprozessen von Partonen zu Photonen. Daher wird in theoretischen Berechnungen oftmals das smooth-cone Isolationskriterium genutzt, bei dem keine Fragmentierungsprozesse erlaubt sind, das aber in experimentellen Messungen nicht direkt angewendet werden kann. Als ersten Schritt zum besseren Verständnis dieses Problems führen wir die Berechnung von NLO QCD Korrekturen in Top-Quark-Paarproduktion mit einem isolierten Photon mit dem fixed-cone Isolationskriterium durch und vergleichen diese Ergebnisse mit Berechnungen basierend auf alternativen Photonenisolationskriterien mit unterschiedlichen Parametern.

Eidesstattliche Erklärung

Daniel Stremmer
erklärt hiermit, dass diese Dissertation und die darin dargelegten Inhalte die eigenen sind und selbstständig, als Ergebnis der eigenen originären Forschung, generiert wurden.
Hiermit erkläre ich an Eides statt

1. Diese Arbeit wurde vollständig oder größtenteils in der Phase als Doktorand dieser Fakultät und Universität angefertigt;
2. Sofern irgendein Bestandteil dieser Dissertation zuvor für einen akademischen Abschluss oder eine andere Qualifikation an dieser oder einer anderen Institution verwendet wurde, wurde dies klar angezeigt;
3. Wenn immer andere eigene- oder Veröffentlichungen Dritter herangezogen wurden, wurden diese klar benannt;
4. Wenn aus anderen eigenen- oder Veröffentlichungen Dritter zitiert wurde, wurde stets die Quelle hierfür angegeben. Diese Dissertation ist vollständig meine eigene Arbeit, mit der Ausnahme solcher Zitate;
5. Alle wesentlichen Quellen von Unterstützung wurden benannt;
6. Wenn immer ein Teil dieser Dissertation auf der Zusammenarbeit mit anderen basiert, wurde von mir klar gekennzeichnet, was von anderen und was von mir selbst erarbeitet wurde;
7. Teile dieser Arbeit wurden zuvor veröffentlicht, siehe “List of Publications”.

Datum

Unterschrift

List of publications

Parts of this thesis have already been published or presented during conferences.

Peer-reviewed publications

[1] *Production and decay of the Higgs boson in association with top quarks*
D. Stremmer and M. Worek, JHEP 02 (2022) 196

[2] *$\mathcal{CP}$ structure of the top-quark Yukawa interaction: NLO QCD corrections and off-shell effects*
J. Hermann, D. Stremmer and M. Worek, JHEP 09 (2022) 138

[3] *Study of additional jet activity in top quark pair production and decay at the LHC*
G. Bevilacqua, M. Lupattelli, D. Stremmer and M. Worek, Phys.Rev.D 107 (2023) 11, 114027

[4] *Associated production of a top-quark pair with two isolated photons at the LHC through NLO in QCD*
D. Stremmer and M. Worek, JHEP 08 (2023) 179

[5] *Complete NLO corrections to top-quark pair production with isolated photons*
D. Stremmer and M. Worek, JHEP 07 (2024) 091

Conference proceedings

[1] *$t\bar{t}jj$– NLO QCD corrections to top quark pair production and decays at the LHC*
D. Stremmer, PoS RADCOR2023 (2023) 036

Contents

1. Introduction

The top quark was observed by the CDF [1] and the DØ [2] experiments at the Fermilab Tevatron in 1995 in $p\bar{p}$ collisions with a center-of-mass energy of $\sqrt{s} = 1.8$ TeV. Even before the direct measurement through top-quark pair production, it was expected that the top quark has to exist. In 1964, CP violation was observed in kaon decays [3] which then led to the extension of the previous four-quark model to a six-quark model in which CP violation arises from flavor mixing as part of the Cabibbo-Kobayashi-Maskawa (CKM) mixing matrix. The observation of the Υ meson [4] in 1977 resulted in the discovery of the bottom quark and therefore of the fifth quark. This further strengthened the possible existence of the top quark, which is the corresponding weak isospin partner in the Standard Model (SM). Even before the direct observation of the top quark, it was possible to constrain its mass indirectly in fits to electroweak precision data at LEP [5, 6], where the top quark contributes in higher-order corrections to physical observables such as the Z width. These indirect measurements were affected by uncertainties at the level of 20 GeV [7], which were competitive with the first direct measurements. Shortly after the discovery of the top quark, the uncertainties in direct mass measurements were reduced to $5-6$ GeV [8]. Due to its large mass, the top quark has a special position in the SM. On the one hand, it is the heaviest fermion and thus has the largest Yukawa coupling to the Higgs boson, directly affecting the vacuum stability in the SM [9]. On the other hand, it is the only quark that decays before the hadronization starts, so it can be approximated to a certain extent as a free quark and can therefore be used for important precision tests of perturbation theory in quantum chromodynamics (QCD).

The production of $t\bar{t}$ can be accompanied by additional particles. Indeed, about 50% of the $t\bar{t}$ events at the LHC are produced with an additional hard jet. The production with additional electroweak (EW) particles is usually suppressed relative to the latter due to the different sizes of the strong and electromagnetic coupling constants. The first observation of top-quark pair production with an additional vector boson $t\bar{t} + V$ ($V = \gamma, W^{\pm}, Z$) was the associated production with a photon in pp collisions at the LHC at $\sqrt{s} = 7$ GeV by the ATLAS collaboration [10]. Despite its early observation, this process presents many difficulties in the precise modeling which are rather unique with respect to the other $t\bar{t}V$ processes. First of all, due to the vanishing photon mass the calculation of cross sections always requires the presence of technical cuts, so it is not possible define a total integrated cross section that is fully inclusive. In addition, top quarks are unstable particles and we can only observe their decay products. This implies that photons can be emitted not only during the production of a top-quark pair but also in the decays. The latter contribution was found to be significant and can be as large as 50% of the full process [11, 12]. Therefore, the radiation of photons in the production and decay is equally important and should be

consistently included in theoretical predictions. The large fraction of photons originating from top-quark decays also has a direct impact on the validity of the standard approach to generate Monte Carlo events in associated $t\bar{t}$ production, where the $t\bar{t}\gamma$ process is first generated with on-shell top quarks at next-to-leading order (NLO) QCD and then matched to parton showers. In this case, top-quark decays are included at leading order (LO) with additional corrections from the resummation of soft-collinear effects, possibly preserving spin correlations. However, such an approach does not include photon radiation from the on-shell top quark or its decay products, leading to a significant underestimation of the true result. In general, photon radiation from top-quark decays cannot be produced by a parton shower, since the generation in it is performed using the soft-collinear approximation and cannot correctly reproduce the spectrum of hard photons. In recent measurements, different methods have been used to include the contribution of photon radiation from top-quark decays. On the one hand, the ATLAS collaboration [13] has generated a second sample dedicated to the photon radiation in top-quark decays by first generating the $pp \to t\bar{t}$ process with on-shell top quarks and then including photon radiation in the top-quark decays. This sample is generated only at LO and an overall $\mathcal{K}$-factor is multiplied to estimate the NLO QCD corrections. On the other hand, the CMS collaboration [14] used a different approach, where the full $2 \to 7$ process, i.e. $pp \to t\bar{t}\gamma$ including top-quark decays, is considered at the matrix element level which naturally includes photon radiation in the production and decay stages. But also in this case the calculation is done only at LO and an overall approximate $\mathcal{K}$-factor is applied.

Further complications arise in the calculation of higher-order corrections due to the requirement of photon isolation. In particular, such isolation criteria are used in experimental measurements to enhance the contribution of photon radiation from the hard scattering process with respect to secondary photon radiation from e.g. fragmentation processes or hadron decays, where usually additional hadronic activity around the photon is present. The fixed-cone isolation is used in current measurements, where the hadronic transverse energy inside a cone around the isolated photon candidate must be less than a maximal value that can depend on the transverse momentum of the photon. While such an isolation condition is straightforward to apply in experimental measurements, it leads to infrared (IR) unsafe collinear quark-photon configurations in theoretical higher-order calculations, which are not taken into account in the standard perturbative approach. Instead, it requires the introduction of the non-perturbative parton-to-photon fragmentation functions, which describe the collinear emission of photons from partons, and leads to further technical complications. Therefore, calculations of higher-order corrections in $pp \to t\bar{t}\gamma$ have not yet been performed in combination with the fixed-cone isolation but only with the smooth-cone isolation introduced in Ref. [15], where exactly collinear quark-photon configurations are vetoed and thus the fragmentation contribution vanishes. However, the use of this method is barely possible in experimental measurements and is therefore only used in theoretical higher-order calculations. Furthermore, this isolation condition includes several free parameters, which in principal have to be tuned to mimic the fixed-cone isolation applied in experiments, where in general the relation between the two isolation conditions is process dependent and eventually depends on the actual fiducial phase space. Therefore, the choice of the parameters represents an additional unknown uncertainty in theoretical predictions in comparisons with experimental measurements, which we address in this thesis.

The problems described above for the production of $t\bar{t}\gamma$ may even be more pronounced

in the $pp \to t\bar{t}\gamma\gamma$ process due to the presence of two photons in the final state, and have not yet been studied in the literature. This process is of high relevance as it is the irreducible background to $pp \to t\bar{t}H$ where the Higgs decays into two photons. While the Higgs production process in the $\gamma\gamma$ channel was observed as the first single-channel observation of $pp \to t\bar{t}H$ [16, 17], the prompt production of two photons in association with a top-quark pair has not yet been observed and its background contribution to the $pp \to t\bar{t}H$ measurements is often obtained in a data-driven approach. This is partially related to the fact that in $t\bar{t}\gamma\gamma$ the background from secondary photons is larger than in the case of $pp \to t\bar{t}H(H \to \gamma\gamma)$ since the invariant mass restriction due to the resonance already reduces secondary photon production. Thus, one motivation of this thesis is the improvement of the $t\bar{t}\gamma\gamma$ modeling by consistently including photon radiation and higher-order corrections in both the production and decays of the top-quark pair.

While uncertainties related to the missing higher-order corrections of QCD nature are usually approximated by scale variation of the final result, the uncertainties due to missing subleading EW and/or QCD corrections are often neglected and are assumed to be negligible. However, from simple power counting one obtains $\mathcal{O}(\alpha_s^2) \approx \mathcal{O}(\alpha)$, where α_s and α are the strong and electromagnetic coupling constants, which in principle means that the size of NLO EW corrections can be as large as the NNLO QCD corrections. While the calculation of the latter corrections is not yet possible for the $pp \to t\bar{t}\gamma(\gamma)$ process, the calculation of NLO EW corrections and subleading corrections at the one-loop level was already performed for both processes in Ref. [18], but again only in the case of stable top quarks. Thus, one goal of this thesis is the consistent inclusion of subleading EW/QCD corrections and photon radiation in the production and decay stages of the $t\bar{t}$ pair at the same time to quantify these effects with realistic final states.

This thesis is organized as follows. In the rest of Chapter 1 the properties of the top quark and the theoretical and experimental status of $pp \to t\bar{t} + X$ production processes are summarized. The theoretical background of event generation at hadron colliders, the treatment of unstable particles in perturbation theory, and the structure of isolated photon cross sections are presented in Chapter 2. In Chapter 3 we describe the software and the modifications in the HELAC-NLO framework to perform our numerical calculations. In particular, the calculation of NLO QCD corrections to the $pp \to t\bar{t}\gamma\gamma$ process in the *di-lepton* and *lepton + jet* decay channels, with a special emphasis on the origin of photon radiation and the scale choice, is presented in Chapter 4. Numerical results for the complete NLO results, consisting of the NLO QCD calculation including all subleading LO contributions and NLO QCD and/or EW corrections, are presented in Chapter 5 for the $pp \to t\bar{t}\gamma$ and $pp \to t\bar{t}\gamma\gamma$ processes in the *di-lepton* decay channel, focusing on the individual subleading contributions and their interplay. In Chapter 6 the calculation of $pp \to t\bar{t}\gamma$ in the *di-lepton* decay channel including off-shell effects with the fixed-cone isolation is presented, where a dedicated comparison with other photon isolation criteria is performed. Finally, the main results of this thesis are summarized in Chapter 7.

1.1 Top-quark properties

In the following, we briefly summarize the properties of the top quark and conclude this chapter with a theoretical and experimental overview of the $pp \to t\bar{t} + X$ processes. A

more detailed discussion of theses topic can be found in Refs. [19–21] on which the rest of this chapter is based.

Mass

The top-quark mass is one of the most important parameters in the SM that cannot be predicted by the theory and can therefore only be measured in experiments. Like every quark in the SM, the top quark participates in the strong interactions and is therefore not a direct physical observable that can be observed in experiments. On the other hand, the top quark is special in the sense that it decays via EW interactions before the hadronization begins, and thus the top quark can be seen approximately as a free particle. Therefore, the top quark mass in the pole (on-shell) scheme (m_t^{pole}) can be considered to some extent as the physical mass. This top-quark mass renormalization scheme is the most common one for higher-order corrections and is defined by requiring that all self-energy corrections vanish for on-shell top quarks. By construction, it does not depend on the renormalization scale, is infrared finite and gauge invariant. However, the mass definition in this scheme suffers from the so-called *renormalon ambiguity* [22–24]. This non-perturbative effect comes from infrared sensitive terms in the perturbation series of physical observables, resulting into a asymptotic (divergent) series. This asymptotic behavior is a common feature of QCD, but becomes especially strong when the pole scheme is used. This leads to an intrinsic uncertainty of the pole mass, estimated to be about $110 - 250$ MeV [25, 26]. These renormalon contributions in physical observables can be avoided by using a short-distance mass scheme such as the $\overline{\text{MS}}$ ($\overline{m}_t(\mu)$) or the MSR scheme ($m_t^{\text{MSR}}(R)$). These mass schemes can be related to the pole scheme and are given by

$$m_t^{\text{pole}} - \overline{m}_t(\mu) = \frac{4}{3}\frac{\alpha_s(\mu)}{\pi}\overline{m}_t(\mu) \tag{1.1}$$

for the $\overline{\text{MS}}$ and by

$$m_t^{\text{pole}} - m_t^{\text{MSR}}(R) = \frac{4}{3}\frac{\alpha_s(\mu)}{\pi}R \tag{1.2}$$

for the MSR scheme at the one-loop level. In addition, the mass in both schemes depends on the energy scale denoted by μ/R and thus follows a renormalization group equation, which can be used for the evolution from one scale to another scale.

The most precise determinations of the top-quark mass are performed in so-called direct measurements, which are based on the kinematic reconstruction of the top-quark decay products and the comparison with predictions from Monte Carlo event generators. However, this determination relies heavily on the parton shower and the hadronization, and therefore it is not completely clear how the top quark mass from direct measurements (m_t^{MC}) is related to the top quark mass from different renormalization schemes. However, the differences between m_t^{MC} compared to the pole mass and $m_t^{\text{MSR}}(1\text{ GeV})$ are expected to be about 500 MeV [19]. Figure 1.1 displays a summary plot of the LHC Top Working Group showing the results of direct top-quark mass measurements. This demonstrates that for direct measurements, the uncertainties on m_t^{MC} in single measurements are now below 1 GeV. Recently, the ATLAS and CMS collaborations combined their results on direct top-quark mass measurements at 7 TeV and 8 TeV, and obtained the most precise direct top-quark mass determination of $m_t^{\text{MC}} = 172.52 \pm 0.14\,(\text{stat.}) \pm 0.30\,(\text{sys.})$ [28] with a total uncertainty of only 0.2%.

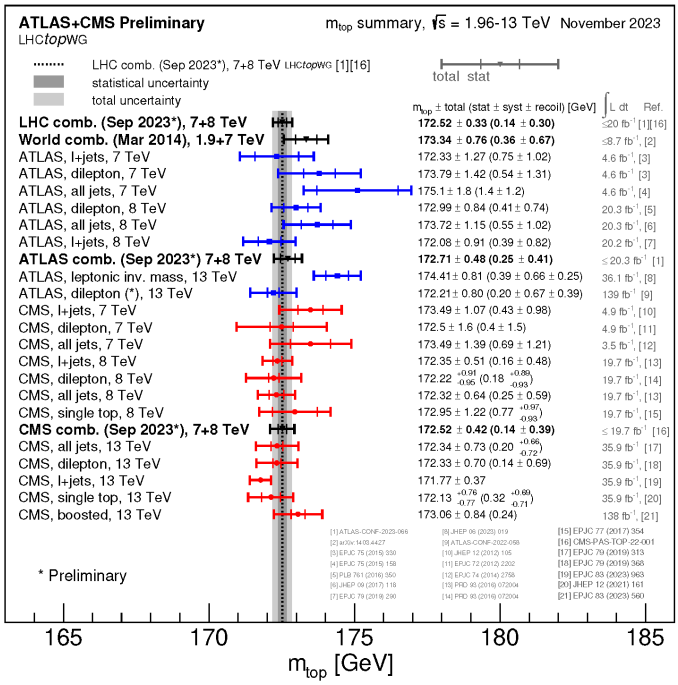

Figure 1.1: *Summary plot of the LHC Top Working Group on direct top-quark mass measurements. Figure taken from Ref. [27].*

Alternatively, indirect top-quark mass measurements in a well defined mass scheme are performed to extract usually the pole mass but also the $\overline{\text{MS}}$ mass. These determinations depend on differential and total cross section-measurements that are unfolded to the parton level and compared with theoretical predictions. Such measurements generally lead to larger uncertainties compared to direct mass measurements and are in the range of $1-2$ GeV. The production of $t\bar{t}j$ is also used to extract top-quark mass using the dimensionless $\mathcal{R}$ observable [29] defined as

$$\mathcal{R}(m_t^R, \rho_s) = \frac{1}{\sigma_{t\bar{t}j}} \frac{d\sigma_{t\bar{t}j}}{d\rho_s}(m_t^R, \rho_s) \qquad \text{with } \rho_s = \frac{2m_0}{\sqrt{s_{t\bar{t}j}}}, \tag{1.3}$$

where $\sqrt{s_{t\bar{t}j}}$ is the invariant mass of the $t\bar{t}j$ system, m_0 is a mass constant and is often set to $m_0 = 170$ GeV. The $\mathcal{R}$ observable can be used with any top-quark mass scheme as indicated by m_t^R. This observable shows an increased sensitivity compared to the analogous observable in $t\bar{t}$ production ($t\bar{t}j \to t\bar{t}$ in Eq. (1.3)). However, the uncertainties obtained with this method are larger than those with $t\bar{t}$ measurements using double and triple differential cross-section distributions due to large parton distribution function (PDF) uncertainties.

Decay

The top quark can only be observed indirectly in experimental measurements through its decay products. Due to the short top-quark lifetime of about $0.5 \cdot 10^{-24}$ s [20], it is expected that the top quark decays before hadronization starts or $t\bar{t}$ quarkonium bound states can be produced [30]. Therefore, the polarization of the top quark is highly correlated with the ones of the decay products. The top-quark spin of $1/2$ in the SM can be probed indirectly

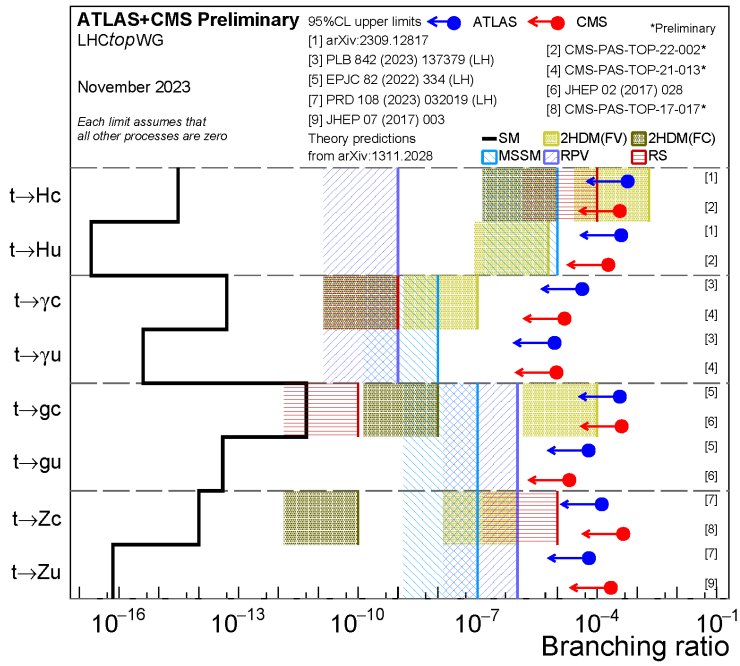

Figure 1.2: *Summary plot of the LHC Top Working Group on the branching ratios of FCNCs in the SM and in various BSM models compared to upper limits derived in experimental measurements. Figure taken from Ref. [27].*

in angular distributions such as the azimuthal angle difference of the two charged leptons in $t\bar{t}$ production in the *di-lepton* decay channel ($\Delta\phi_{\ell^+\ell^-}$). The latest measurements of the top-quark spin correlations by the CMS collaboration show good agreement between experimental measurements and theoretical predictions [31], while the ATLAS collaboration found larger spin correlations with respect to the SM predictions with up to 2.2σ [32]. Recently, the ATLAS collaboration observed spin entanglement in $t\bar{t}$ production [33], which is also the highest energy at which entanglement has been found so far.

The top quark decays almost exclusively into a W boson and a bottom quark ($t \to W^+b$), where the W boson decays further into either two quarks ($W^+ \to q\bar{q}'$) or a lepton-neutrino pair ($W^+ \to \ell^+\nu_\ell$). Due to the mixing of quarks as described by the Cabibbo-Kobayashi-Maskawa (CKM) matrix, the top quark can also decay into a W boson and another down type quark $q = d, s$. However, such decays are suppressed due to the hierarchy in the CKM matrix $|V_{tb}| \gg |V_{td}|, |V_{ts}|$ with $|V_{tb}|$ almost equal to one. At the tree level, no other decays are possible in the SM, while at the one-loop level, the top quark can also decay via flavor-changing neutral currents (FCNCs) in decays of the form $t \to H/\gamma/g/Z + q$, where q is an up-type quark ($q = u, c$). These decays are heavily suppressed because they first appear at the one-level and are further suppressed by the GIM mechanism [34]. Therefore, the corresponding branching ratios in the SM are of the order of $10^{-17} - 10^{-12}$ [35]. As shown in Figure 1.2, FCNCs can be enhanced by different beyond the SM (BSM) models. However, the current experimental precision is not yet at a level to fully probe the branching ratios as predicted by these BSM models.

In Ref. [36] the CMS collaboration studied the ratio of branching ratios $\mathcal{R}_b = \mathcal{B}(t \to Wb)/\sum_q \mathcal{B}(t \to Wq) = 1.014 \pm 0.003\,(\text{stat.}) \pm 0.032\,(\text{sys.})$ in $t\bar{t}$ events. Assuming unitarity

of the CKM matrix, this ratio simply reduces to $\mathcal{R}_b = |V_{tb}|^2$ and can be translated into a measurement of the CKM matrix entry of $|V_{tb}| = 1.007 \pm 0.016\,(\text{stat.} + \text{sys.})$. Using the same unitarity assumption, the CMS collaboration has combined this measurement with the measurement of the t-channel single top-quark cross section [37] to indirectly measure the top-quark width according to the formula

$$\Gamma_t = \frac{\sigma_{t-ch}}{\mathcal{B}(t \to Wb)} \frac{\Gamma(t \to Wb)}{\sigma_{t-ch}^{\text{theo.}}}, \tag{1.4}$$

where σ_{t-ch} ($\sigma_{t-ch}^{\text{theo.}}$) is the measured (theoretical) t-channel single top-quark cross section and $\Gamma(t \to Wb)$ is the partial top-quark width to a bottom quark and a W boson. In this approach they obtained a top-quark width of $\Gamma_t = 1.36 \pm 0.02\,(\text{stat.})^{+0.14}_{-0.11}\,(\text{sys.})$ GeV, which due to the large systematic uncertainties is clearly in good agreement with current theoretical predictions with at least NLO QCD accuracy, where recently the N^{3}LO QCD corrections were calculated in Ref. [38]. In contrast, the most precise direct measurement of the top-quark width was performed by the ATLAS collaboration, where a top-quark width of $\Gamma_t = 1.9 \pm 0.5\,(\text{stat.} + \text{sys.})$ GeV [39] was measured, where the uncertainties are significantly larger than in the indirect measurement.

Charge
In the SM, the top quark is predicted to have a charge of $Q_t = 2/3$ and cannot be detected directly, but only indirectly through its decay products or by comparing experimental measurements with theoretical predictions. The hypothesis that the top quark is an exotic quark with $Q_t = -4/3$ [40, 41], where the top quark would decay into a W^- boson and a bottom quark, was excluded by the CDF collaboration at the 99% confidence level [42] and by the DØ collaboration with more than 5σ [43]. The charge of the top quark was determined by measuring the charges of the decay products, where the charge of b-jets are obtained with jet-charge algorithms. The CMS collaboration also ruled out the hypothesis of an exotic top quark by measuring the asymmetry between two categories. In this case they obtained $A_{\text{meas}} = 0.97 \pm 0.12\,(\text{stat.}) \pm 0.31\,(\text{sys.})$ [44], where $A = -1$ would correspond to the charge of $Q_t = -4/3$ and $A = 1$ to a charge of $Q_t = 2/3$. Finally, the ATLAS collaboration obtained a top-quark charge of $Q_t = 0.64 \pm 0.02\,(\text{stat.}) \pm 0.08\,(\text{sys.})$ by measuring the charges of the top-quark decay products [45]. In this measurement, the alternative hypothesis of $Q_t = -4/3$ is excluded with more than eight standard deviations.

1.2 Top-quark pair production processes

1.2.1 $pp \to t\bar{t}$

The production of a top-quark pair is the main source of top quarks at the LHC and is therefore essential for the precise determination of the top-quark properties. In addition, it also serves as an important test of perturbation theory in QCD and EW theory. The $pp \to t\bar{t}$ process is also an important background for many SM studies or new physics searches, since the different decay channels of the W bosons lead to various different final-state signatures. Considering that the W bosons in the top-quark decays can decay either into a quark pair $W^+ \to q\bar{q}'$ or into a lepton-neutrino pair $W^+ \to \ell^+\nu_\ell$, we encounter three

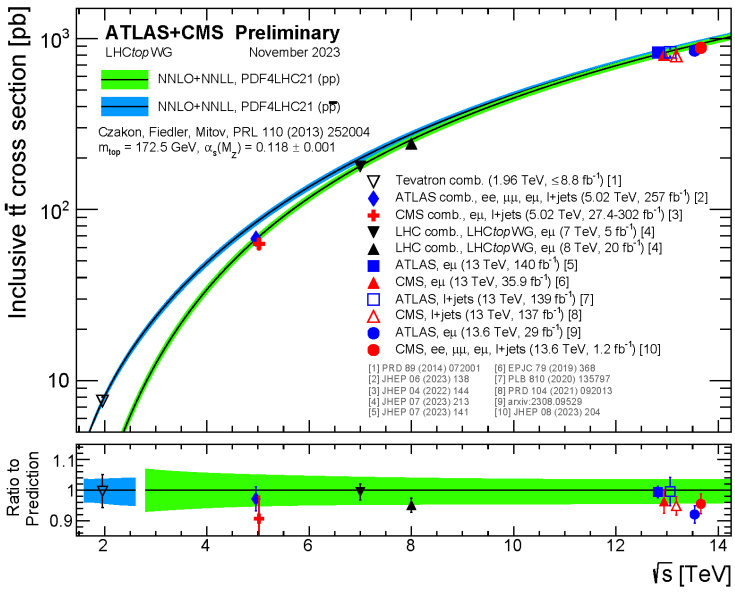

Figure 1.3: *Comparison of inclusive top-pair production cross section between theoretical predictions at NNLO QCD with NNLL resummation [49] with several experimental measurements by the CDF and D0 collaborations in $p\bar{p}$ collisions at $\sqrt{s} = 1.96$ TeV [50], and by the ATLAS and CMS collaborations in pp collisions at $\sqrt{s} = 5.02, 7, 8, 13, 13.6$ TeV [51–59]. Figure taken from Ref. [27].*

different final states. In the *di-lepton* decay channel both W bosons decay leptonically, while in *lepton + jet* decay channel we have one W boson decaying into quarks and the other into leptons, and in the *all-hadronic* decay channel both W bosons decay hadronically. The branching ratios of the different top-quark pair decay channels are given by 10.5%, 43.8% and 45.7% [20]. Often only electrons and muons are included in the event selection in measurement, excluding tau leptons, reducing the branching ratios of the *di-lepton* and *lepton + jet* decay channels. This is because the tau lepton decays predominantly into hadrons, so that the other leptons are easier to detect. In addition, the $pp \to t\bar{t}$ process is also important in the search for new resonances that may decay in two top quarks. Furthermore, this process can be used to constrain the top-quark Yukawa coupling (Y_t) which enters the $t\bar{t}$ cross section due to virtual EW corrections [46]. In this way, the CMS collaboration was able to derive upper limits on Y_t [47, 48].

In Figure 1.3 a summary of the inclusive $t\bar{t}$ cross-section measurements at the different center-of-mass energies is presented, which are compared with current theoretical predictions at next-to-next-to-leading order (NNLO) QCD with soft gluon resummation at next-to-next-to-leading logarithmic (NNLL) accuracy [49]. These results show a remarkably good agreement between experimental measurements and theory, from measurements in $p\bar{p}$ collisions at $\sqrt{s} = 1.96$ TeV by the CDF and D0 collaborations to pp collisions by the CMS and ATLAS collaborations at $\sqrt{s} = 5.02, 7, 8, 13$ TeV [51–57] and most recently at $\sqrt{s} = 13.6$ TeV [58, 59]. The theoretical and experimental uncertainties are in the range of a few percent, while in the latter case they are dominated by systematic uncertainties.

The NLO QCD corrections to the inclusive $t\bar{t}$ cross section in hadron collisions have

been known for more than thirty years [60–63], which were then followed by the calculation of NLO EW corrections first in Ref. [64] and later revisited in Refs. [65–68]. NNLO QCD corrections to the inclusive $t\bar{t}$ production are known for more than 10 years now [49, 69–71] and were later extended to predictions at the differential level [72–74]. These predictions were then combined with subleading LO and NLO contributions in Ref. [75]. While the first calculations of NNLO QCD corrections to $t\bar{t}$ used the on-shell scheme for the top-quark mass renormalization, alternative predictions are available which were obtained with the $\overline{\text{MS}}$ scheme [76]. Fixed-order predictions were further improved by including soft gluon resummation at next-to-leading logarithmic (NNL) accuracy [77, 78] and later at NNLL accuracy [79–85]. The resummation of soft gluon effects and Coulomb enhancements were combined at NNLL accuracy in Ref. [86]. In addition, approximate aN^{3}LO QCD corrections, which are the third-order soft gluon corrections obtained from the soft gluon resummation at NNLL, were calculated in Refs. [87–90]. The inclusion of top-quark decays was performed in several ways. In particular, predictions for on-shell top quarks at NLO QCD have been matched to parton showers using the MC@NLO [91, 92] and the POWHEG method [93, 94]. In Ref. [95] the matching to the predictions at NLO QCD in the narrow-width-approximation (NWA) was performed with approximate off-shell effects. Finally, the first matching of NNLO QCD corrections to parton showers was performed in Refs. [96, 97] based on the MiNNLO$_{\text{PS}}$ approach [98, 99]. At fixed order, top-quark decays were first included using the NWA in Ref. [100] and later in Refs. [101, 102] with massless bottom quarks and in Ref. [103] with massive bottom quarks. In addition, NLO EW corrections were added to the $t\bar{t}$ production in the NWA in Ref. [104]. These calculations were then improved by also including the NNLO QCD corrections to the $t\bar{t}$ production and its decays. This was first done in Ref. [105], while an approximation for the NNLO QCD corrections to the $t\bar{t}$ production was used, and finally in Refs. [106, 107] the complete set of NNLO QCD corrections were calculated. Calculations in the full off-shell approach at NLO QCD were first performed in the *di-lepton* decay channel in Refs. [108–110] with massless bottom quarks and in Refs. [111, 112] in the four-flavor scheme with massive bottom quarks. NLO EW corrections were calculated in [113], and finally full off-shell predictions at NLO QCD in the *lepton + jet* decay channel were presented in Ref. [114]. Full off-shell predictions at NLO QCD were first matched to parton showers in the *di-lepton* decay channel [115] and later in the *lepton + jet* decay channel [116], where in the latter calculation the hadronically decaying W boson is obtained in an approximate way based on the calculation in the *di-lepton* decay channel.

1.2.2 $pp \to t\bar{t}$ + jets

Half of the $t\bar{t}$ events at the LHC are produced with additional hard jets. Such events are not only important for precise predictions of $t\bar{t}$ production and thus for the determination of top-quark properties, but the production of $t\bar{t}$ with additional jets is also an important background in several BSM searches [122–127] and SM measurements that include a W boson pair W^+W^- with additional jets in the final state. In particular, the $pp \to t\bar{t}j$ process is a large background to the Higgs production in vector boson fusion [128, 129]. Furthermore, the $pp \to t\bar{t}b\bar{b}$ production process is the dominant irreducible background of $pp \to t\bar{t}H$ with $H \to b\bar{b}$ decays and also an important background for $t\bar{t}t\bar{t}$ searches [130, 131]. In addition, the production of a top-quark pair with light jets can be used in the search for anoma-

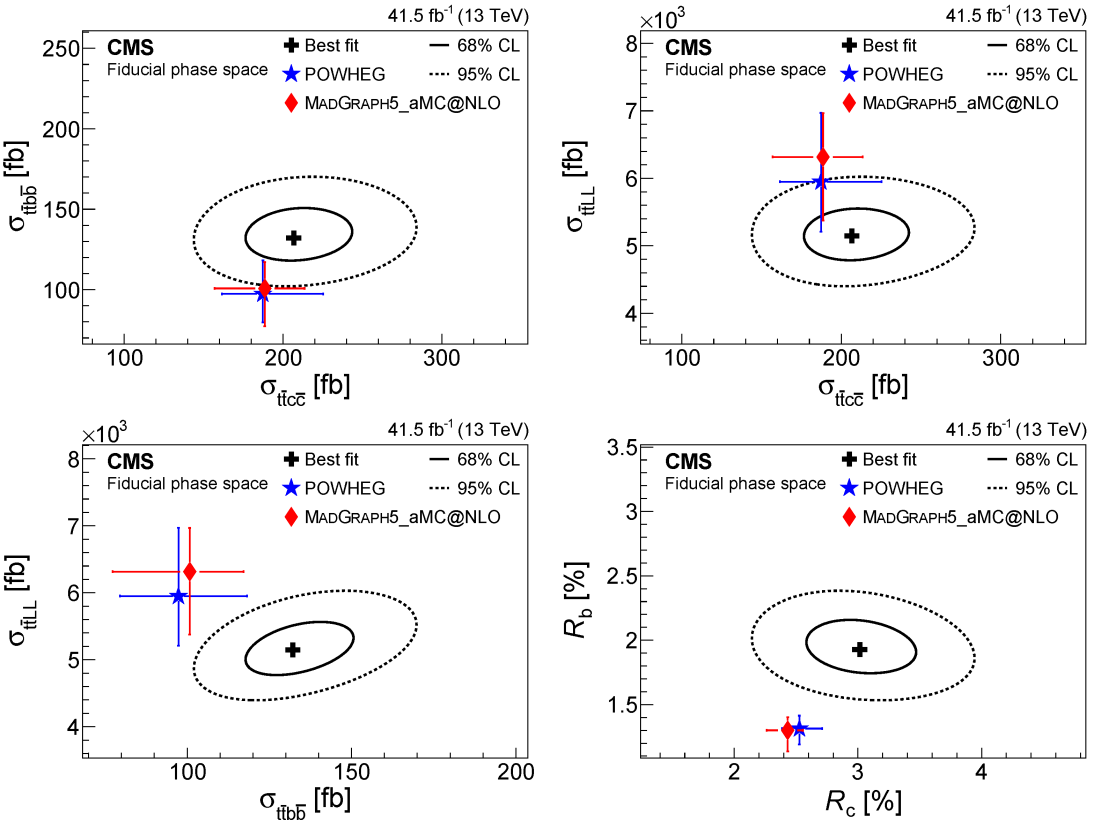

Figure 1.4: *Two-dimensional likelihood scans for combinations of the integrated fiducial cross sections $\sigma_{t\bar{t}LL}$, $\sigma_{t\bar{t}b\bar{b}}$ and $\sigma_{t\bar{t}c\bar{c}}$, and the two cross-section ratios $R_b = \sigma_{t\bar{t}b\bar{b}}/\sigma_{t\bar{t}LL}$ and $R_c = \sigma_{t\bar{t}c\bar{c}}/\sigma_{t\bar{t}LL}$. Experimental measurements are compared with theoretical predictions obtained with* POWHEG *[93–95, 117, 118] and* MadGraph5_aMc@Nlo *[119] with* FxFx *jet matching [120]. Figures taken from Ref. [121].*

lous top-quark dipole moments, i.e. chromo-electric dipole and chromo-magnetic dipole moments, in the t-g vertex [132–134]. This would lead to modifications of the top-quark spin correlations which would be observable in angular distributions of the decay products and could be measured in experiments [135, 136]. Moreover, the $pp \to t\bar{t}j$ process can be used to study the top-quark charge asymmetry, which is enhanced in several BSM models [137–142]. Furthermore, cross-section ratios of $t\bar{t}$ production with heavy and light flavors, such as $R_b = \sigma_{t\bar{t}b\bar{b}}/\sigma_{t\bar{t}jj}$ and $R_c = \sigma_{t\bar{t}c\bar{c}}/\sigma_{t\bar{t}jj}$, can be used as a playground for c- and b-jet tagging in environments with many jets of different production mechanisms. In particular, the study of these processes can be used to better understand the separation of the different processes which would eventually lead to a reduction of systematic uncertainties in experimental measurements such as $pp \to t\bar{t}H$ $(H \to b\bar{b})$, where these processes are important backgrounds. In Figure 1.4, the cross sections $\sigma_{t\bar{t}LL}$ [1], $\sigma_{t\bar{t}b\bar{b}}$ and $\sigma_{t\bar{t}c\bar{c}}$, and the cross section ratios R_b and R_c were studied using two-dimensional likelihood scans by

[1] In this case LL stands for two light jets which are not b or c flavored.

the CMS collaboration [121]. In this case, differences of up to 2.5σ between theoretical predictions obtained with POWHEG [93–95, 117, 118] and MadGraph5_aMc@Nlo [119] with FxFx jet matching [120] and experimental measurements were found in the R_b ratio, where the two theoretical predictions are in good agreement within their uncertainties. These findings are consistent with the recent measurement of the $pp \to t\bar{t}b\bar{b}$ process by the CMS collaboration [143], which showed that none of the event generators used in their analysis was able to describe all measured distributions simultaneously.

The jet activity in $t\bar{t}$ production was already extensively studied at $\sqrt{s} = 7$ TeV and $\sqrt{s} = 8$ TeV by the ATLAS [144–147] and CMS [148–150] collaborations. In addition, in Ref. [149] the $t\bar{t}$ cross section with additional b jets in the final state and in Ref. [146] the R_b ratio were measured. Furthermore, predictions at $\sqrt{s} = 7$ TeV and $\sqrt{s} = 8$ TeV of $pp \to t\bar{t}j$ were used by the ATLAS and CMS collaborations to measure the top-quark pole mass [151, 152] with the $\mathcal{R}(m_t, \rho_s)$ observable as explained in the last section. In Ref. [153] the ATLAS collaboration performed the measurement of the top-quark pole and the $\overline{\text{MS}}$ mass, where the two results are in good agreement when converted to the other scheme. However, the uncertainties of the $\overline{\text{MS}}$ mass are larger because the scale dependence in the sensitive region is larger in this scheme. Also at $\sqrt{s} = 13$ TeV several measurements of the jet activity in $t\bar{t}$ events were performed by the ATLAS [154–156] and CMS [121, 157] collaborations. In Ref. [121] the CMS collaboration measured the $pp \to t\bar{t}c\bar{c}$ for the first time. In addition, the CMS collaboration has measured the top-quark pole mass in $pp \to t\bar{t}j$ events using the $\mathcal{R}(m_t, \rho_s)$ observable [158]. Finally, $pp \to t\bar{t}b\bar{b}$ was studied by the ATLAS [159] and CMS collaborations [160, 161], where in the latter case the $pp \to t\bar{t}jj$ cross section was simultaneously measured and the R_b ratio derived.

The NLO QCD corrections to top-quark pair production with one additional jet, $pp \to t\bar{t}j$, were first computed in Refs. [162, 163]. In Ref. [164] this calculation was further extended by including top-quark decays at LO accuracy using the NWA, and finally, in Ref. [165] the complete set of NLO QCD corrections in the NWA were calculated, including NLO QCD corrections and jet radiation in the production and decay stages of the $t\bar{t}$ pair. Furthermore, this process was matched to parton showers at NLO QCD with stable top quarks in Refs. [166, 167], where in Ref. [168] the matching to parton showers at NLO QCD was improved by including spin correlations between the production and decay stages at LO. Finally, the $pp \to t\bar{t}j$ process was computed, including full off-shell effects in the *di-lepton* decay channel in Refs. [169, 170].

In the case of top-quark pair production with two jets, $pp \to t\bar{t}jj$, the variety of different theoretical predictions is less involved. In particular, the NLO QCD correction with on-shell top quarks were calculated in Refs. [171, 172] and further improved in Ref. [173] by including NLO QCD corrections and jet radiation in the production of $t\bar{t}$ and the decays of the two top quarks using the NWA. For even higher jet multiplicities, NLO QCD corrections are available for the $pp \to t\bar{t}jjj$ process computed in Ref. [174], where NLO QCD corrections were presented for $t\bar{t}$ production with up to three jets at fixed order and with the MiNLO approach [175]. In the latter case, additional Sudakov form factors are multiplied and the scale definition is modified to improve fixed-order predictions of jet cross sections. However, both approaches lead to similar results. Furthermore, NLO EW corrections and subleading LO contributions were calculated for $pp \to t\bar{t}j$ in Ref. [176]. In this case, results were also presented for multi-jet merged top-quark pair production with $t\bar{t} + 0, 1$ jet at NLO QCD and approximate EW corrections and $t\bar{t} + 2, 3, 4$ jets at LO.

On the other hand, $t\bar{t}$ production with jet-merging with up to two jets at NLO QCD was performed in Ref. [177].

Also, the calculation of top-quark pair production with a bottom quark pair ($b\bar{b}$) was also extensively studied in the literature. In particular, the NLO QCD corrections for the $pp \to t\bar{t}b\bar{b}$ process were calculated in [178–183]. Top-quark decays were first included by matching the NLO QCD corrections with parton showers with massless bottom quarks [184, 185] or massive bottom quarks [186–188]. Since this process suffers from large NLO QCD corrections and scale uncertainties, in Ref. [189] the NLO QCD corrections to the $pp \to t\bar{t}b\bar{b}j$ process were studied, which can be used to obtain information about the size of QCD corrections beyond NLO. Finally, full off-shell effects were computed at NLO QCD in the *di-lepton* decay channel in Refs. [190, 191] and a comparison with prediction in the NWA was performed in Ref. [192], where overall good agreement was found between the two calculations at the integrated level and even at the differential level.

1.2.3 $pp \to t\bar{t}$ + photons

All production processes of a top-quark pair and an electroweak vector boson, $pp \to t\bar{t}V$ with $V = \gamma, W^{\pm}, Z$, have been observed at the LHC. Among them, the $pp \to t\bar{t}\gamma$ process has the largest cross section [21, 193]. This process can be used to directly measure the electric charge of the top quark [194] and to probe the structure of the top-quark vertex with photons in the context of Standard Model Effective Field Theory (SMEFT) [195], which allows to constrain the anomalous electric dipole moments that are sensitive to BSM physics [196–203]. However, the modeling of this process is very challenging. In particular, the event generation requires technical cuts due to the vanishing photon mass, and photons can be produced in the production of the $t\bar{t}$ pair, but also in its decays. The contribution of photons originating from top-quark and W-boson decays can become as large as 50% of the full cross section [11, 12], which also reduces the sensitivity to the t-γ vertex. In contrast to top-quark pair production, similar to $t\bar{t}j$, a charge asymmetry is already found at LO for $t\bar{t}\gamma$, which can be used to probe BSM physics [198, 204]. A dedicated study of this asymmetry on the realistic description of the process involving photon radiation from the decay products and spin correlations at NLO QCD in the NWA was presented in Ref. [205]. The impact of subleading LO and NLO contributions on the charge asymmetry was studied in Ref. [18] and was found to be sizeable. Also, the $pp \to t\bar{t}\gamma\gamma$ production process is of large importance because it contributes to the irreducible background to the $pp \to t\bar{t}H$ process in the $H \to \gamma\gamma$ decay channel. Similar to the case of a single photon, the modeling of this process is difficult due to the presence of photons in top-quark decays. The effects of photon radiation in the decays of top quarks and W bosons will be quantified in this thesis.

The first evidence of the $t\bar{t}\gamma$ production process was found in $p\bar{p}$ collisions at the Tevatron with a center-of-mass energy of $\sqrt{s} = 1.96$ TeV by the CDF collaboration [206]. The ATLAS collaboration was able to observe the $pp \to t\bar{t}\gamma$ process at the LHC with $\sqrt{s} = 7$ TeV [10]. Later this process was also measured at $\sqrt{s} = 8$ TeV [207, 208] and $\sqrt{s} = 13$ TeV [13, 14, 209–211] by the ATLAS and CMS collaborations. In particular, both collaborations have used their measurements in the *di-lepton* and *lepton + jet* decay channels [13, 14, 211] to constrain the Wilson coefficients C_{tZ} and $C_{\mathrm{t}\gamma}$ that modify the t-γ and t-Z vertices. The ATLAS collaboration has measured the combined $t\bar{t}\gamma$ and $tW\gamma$ pro-

duction in the $e\mu$ channel [210] and has performed a dedicated comparison of inclusive and differential cross sections with fixed-order predictions including full off-shell effects at NLO QCD [212, 213], finding good agreement. Recently, the charge asymmetry in $pp \to t\bar{t}\gamma$ was measured by the ATLAS collaboration [214], where no deviations from the SM were found. On the other hand, the $pp \to t\bar{t}\gamma\gamma$ process has not yet been observed.

For stable top quarks the NLO QCD corrections of the $pp \to t\bar{t}\gamma$ process are well known [193, 215, 216] and also the NLO EW corrections have been calculated [217]. The complete NLO corrections, including all subleading LO and NLO contributions, were calculated in Ref. [18]. Finally, the aNNLO QCD corrections were calculated and combined with the complete NLO results in Ref. [218]. Top-quark decays have been included on the one hand by matching NLO QCD predictions with stable top quarks with parton showers [219], and on the other hand by using the NWA [11], where NLO QCD corrections are included in the production of the $t\bar{t}$ pair and its decays while preserving spin correlations. The limit of small widths was overcome by the calculation of $t\bar{t}\gamma$ in the full off-shell approach in the *di-lepton* decay channel [212, 213]. A dedicated analysis between the NWA and the full off-shell calculation was performed in Ref. [12]. For the $pp \to t\bar{t}\gamma\gamma$ process the variety of different predictions is considerably smaller, where photon radiation in top-quark decays was consistently neglected. For on-shell top quarks, NLO QCD corrections were calculated and matched to parton showers [119, 193, 220, 221] and also the NLO EW corrections were computed in Ref. [18].

1.2.4 $pp \to t\bar{t} + H$

The Higgs boson was discovered in 2012 by the ATLAS and CMS collaborations [222, 223]. Since then, one of the main goals of the LHC is the precise determination of its properties and its couplings to SM particles. The top quark plays a special role in this program because it is the heaviest particle and therefore has the largest Yukawa coupling (Y_t), which is close to unity. The Higgs production at the LHC is clearly dominated by gluon fusion, even though it is loop-induced. In this case, the Higgs boson couples to massive fermions running inside the loops, and therefore predominantly to the top quark. Thus, gluon fusion can be used to indirectly measure the top-quark Yukawa coupling, where such a measurement can be affected by new massive particles in BSM models. On the other hand, the Higgs production in association with a top-quark pair gives a direct probe of the top-quark Yukawa coupling already at the tree level and therefore becomes essential for a precise measurement of Y_t. However, only 1% of the total Higgs cross section stems from this production channel [224]. Nevertheless, the ATLAS and CMS collaborations were able to observe it in 2018 [225, 226]. In experiments, the Higgs boson can only be measured indirectly via its decay products. In particular, the decay channel into a bottom-quark pair $H \to b\bar{b}$ has the largest branching ratio with about 58% [224]. However, this decay channel suffers from a large QCD background and has not yet been observed in $t\bar{t}H$ using a single decay channel of the Higgs boson. This can be attributed to the enormous reducible background from $t\bar{t}jj$ and the large irreducible background from $t\bar{t}b\bar{b}$ and $t\bar{t}Z(Z \to b\bar{b})$. In this case, the presence of multiple b-jets of different origins complicates the reconstruction of the top quarks and the Higgs boson involved in this process. In contrast, the loop-induced Higgs decay channel into two photons $H \to \gamma\gamma$ with a branching ratio of only about 0.2% [224] has led to the first single-channel observation in $t\bar{t}H$ by the ATLAS and

CMS collaborations [16, 17] due to its clean signature in experiments.

Already before the observation at the center-of-mass energy of 13 TeV at the LHC, several searches were performed for the $t\bar{t}H$ process at 7 TeV and 8 TeV in different Higgs decay channels such as $H \to \gamma\gamma$, $H \to b\bar{b}$, $H \to \tau^+\tau^-$, $H \to WW^*$ and $H \to ZZ^*$ [227–233]. These results were strongly limited by large statistical uncertainties and only with measurements at 13 TeV it was possible to observe this production process. The measurements in the $H \to \gamma\gamma$ [16, 17, 234] and the multilepton channel [235–237], targeting the Higgs decays into WW^*, ZZ^*, $\tau^+\tau^-$, are used to constrain the CP properties of the top-quark Yukawa coupling. The CP-odd scenario is now excluded with 3.9σ by the ATLAS and 3.7σ by the CMS collaborations. The $H \to \gamma\gamma$ and the multilepton channels are still dominated by statistical uncertainties, while the largest systematic uncertainties originate from the modeling of the signal process and background processes such as $t\bar{t}W^\pm$ and $t\bar{t}Z$. Also for $H \to b\bar{b}$ several searches were performed at 13 TeV [238–240], but in contrast to the other decay channels this process is currently not limited by statistical uncertainties, but rather by large systematic uncertainties coming from the background modeling. Finally, this production process is also used to measure the Higgs boson branching ratio into invisible particles [241].

The NLO QCD corrections of $t\bar{t}H$ with stable top quarks and a stable Higgs boson are known for more than twenty years [242–246] and also the NLO EW corrections were calculated [247–249]. These predictions are further improved by including soft gluon resummation effects with (N)NLL accuracy [250–255]. Top-quark decays were first included by matching NLO QCD calculations with stable top quarks to parton showers [193, 256–258], which were recently further improved by including EW Sudakov logarithms [259], that can become sizeable in the high-energy region. On the other hand, top-quark decays were included at the matrix element level in full off-shell calculations at NLO QCD [260] and with NLO EW corrections [261]. Several decay channels of the Higgs boson were included in the NWA, while full off-shell effects are taken into account for all other unstable particles at NLO QCD [262]. Moreover, first steps towards a complete prediction of $t\bar{t}H$ at NNLO QCD were undertaken. In particular, the flavor off-diagonal contributions were calculated [263]. An extensive work was done to calculate the one-loop amplitudes up to $\mathcal{O}(\epsilon^2)$ [264, 265] and to obtain partial results for the two-loop amplitudes [266, 267] in the $q\bar{q}$ channel. Finally, the NNLO QCD corrections were calculated in Ref. [268], where the finite part of the two-loop amplitudes was obtained in a soft Higgs boson approximation.

1.2.5 $pp \to t\bar{t} + W^\pm$

In contrast to most other associated top-quark pair production processes, the $pp \to t\bar{t}W^\pm$ process is not initiated by the gg channel, which is usually the dominant production mode. Due to the charge of the W boson, it can only be produced at LO by the $q\bar{q}'$ channel. This production mechanism has many implications for the properties of this process. In particular, this process is expected to receive substantial NLO and NNLO QCD corrections due to the appearance of the new gq and gg channels at the respective order and the dominance of the gluon PDF at the LHC. These enhancements of higher-order corrections for increasing $\sqrt{s}$ were studied in Ref. [269]. The quark initiated LO production also has the effect that the top-quark charge asymmetry and the asymmetries of the decay products in $pp \to t\bar{t}W^\pm$ [270, 271] are considerably larger than those in $pp \to t\bar{t}$, where differences

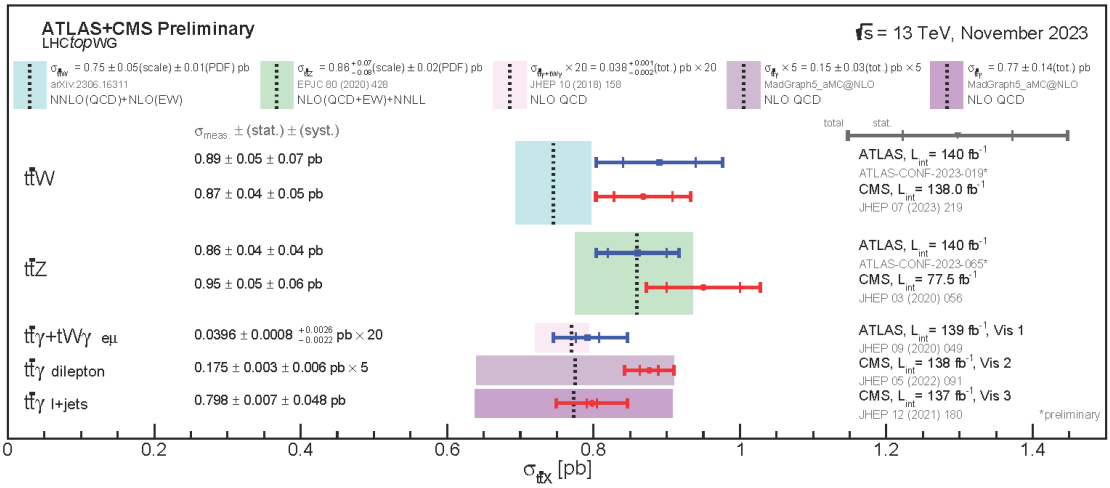

Figure 1.5: *Comparison of experimental measurements of $pp \to t\bar{t}V$ with $V = \gamma, W^{\pm}, Z$ at $\sqrt{s} = 13$ TeV by the ATLAS and CMS collaborations [14, 210, 211, 297–300] with corresponding theoretical predictions [119, 212, 301, 302]. Figure taken from Ref. [27].*

with respect to SM predictions can be interpreted in the context of BSM models. On the other hand, this process features the decays of three W bosons, where each of them can decay either into a lepton-neutrino pair or into two quarks, leading to many different final-state signatures. Therefore, it is an important background process for many measurements such as $pp \to t\bar{t}H$ [193, 225, 226, 237] or $pp \to t\bar{t}t\bar{t}$ [272–275]. This process also contributes to the rare final-state signature of two same-sign leptons, whose production is enhanced in various BSM models such as supersymmetry [276–279], extra dimensions [280] or an extended Higgs sector [281–284]. This final-state signature can also be used in the search for vector-like quarks [285–288], heavy top-quark partners [289, 290], heavy Majorana neutrinos [291] or same-sign top-pair resonances [292, 293]. Lastly, it is also an important process to derive constraints on Wilson coefficients in SMEFT fits [294–296].

The $pp \to t\bar{t}W^{\pm}$ cross section was measured by the ATLAS and CMS collaborations at 8 TeV [303, 304] and at 13 TeV [298, 305–308], where in most cases the cross-section measurements were performed simultaneously with the $pp \to t\bar{t} + Z$ process. Current measurements show a consistent mismatch of the inclusive $pp \to t\bar{t}W^{\pm}$ cross section between measurements and theoretical predictions. In particular, the measured inclusive cross section is larger than the SM predictions, as shown in the in the summary plot of the LHC Top Working Group in Figure 1.5. In this case, recent measurements by the ATLAS and CMS collaborations [297, 298] are compared with the current most advanced theoretical predictions with NNLO QCD corrections to the complete NLO calculation [301], where the two-loop virtual corrections are calculated in an estimated way. In addition, this summary plot also shows the good agreement between theoretical predictions [119, 212, 302] and experimental measurements [14, 210, 211, 299, 300] for the other two $pp \to t\bar{t}V$ processes, $pp \to t\bar{t}\gamma$ and $pp \to t\bar{t}Z$.

The NLO QCD corrections for the $pp \to t\bar{t}W^{\pm}$ process are also well known for many years [309] in the case of stable top quarks and W bosons. These predictions have been further extended by including the decays of top quarks and W bosons preserving spin correlations at LO accuracy [193, 270], where the NLO QCD corrections in the decays

were omitted. The calculation of NLO EW corrections was performed in Refs. [249, 310] and the complete NLO results, including all subleading LO and NLO contributions, are extensively discussed in Ref. [269]. In this case, large enhancements were found for the NLO QCD corrections to the suppressed EW production of $pp \to t\bar{t}W^{\pm}$ at $\mathcal{O}(\alpha^3)$. Recently, the NNLO QCD corrections were combined with the complete NLO results [301], where the NNLO QCD corrections are exact except for the finite part of the two-loop virtual corrections which were obtained in two different approximations. On the one hand, the two-loop amplitudes were obtained by using a soft W boson approximation, where the $t\bar{t}W^{\pm}$ amplitudes are obtained from those of $t\bar{t}$ production [311, 312] and on the other hand the two-loop corrections were calculated by using a massification procedure [313–315] of the leading-color two-loop amplitudes for a W boson and four massless quarks [316, 317]. Furthermore, in Ref. [318] the soft gluon corrections at aNNLO and aN^{3}LO were combined with the complete NLO results. The resummation of soft-gluon effects was performed up to NNLL [319–322]. However, the resummation leads to only minor improvements compared to other $t\bar{t}$ production processes, which is also due to the fact that $t\bar{t}W^{\pm}$ is produced through two quarks at LO. In addition, this process was matched in various ways to parton showers at NLO QCD [193, 270, 323]. In Ref. [324], the subleading NLO QCD corrections to the EW Born production were also included in predictions matched to parton showers. Moreover, decays of the top quarks and W bosons have been included at the matrix element level, preserving spin correlations up to NLO QCD, by the calculation of NLO QCD corrections to the full off-shell calculation in the 3ℓ channel [325, 326]. In addition, the modeling of unstable particles was discussed by comparing the calculations in the full off-shell approach with results in the NWA and the DPA. The impact of the top-quark modeling on charge asymmetries and cross-section ratios was studied in Ref. [271]. Furthermore, the NLO QCD and EW corrections were combined in the full off-shell approach in Ref. [327]. Parton shower predictions and fixed-order results in the full off-shell approach and in the NWA were compared in Ref. [328], where a combination of both calculations is discussed to approximate full off-shell effects in parton shower predictions. Finally, the merging of calculations with different numbers of jets in the final state is an alternative way to estimate higher-order QCD corrections. This multi-jet merging was performed with up to two additional jets in Ref. [329] and further improved in Ref. [330] by including subleading NLO EW corrections to $pp \to t\bar{t}W^{\pm}$. In the latter case, so-called electroweak jets are excluded from the matching to parton showers because their radiation pattern cannot be reproduced by such a parton shower. Finally, the calculation of NLO QCD correction to $pp \to t\bar{t}W^{\pm}j$ in the full off-shell approach was presented in Ref. [331], paving the way for jet merging of $pp \to t\bar{t}W^{\pm}$ including decays at the matrix-element level.

1.2.6 $pp \to t\bar{t} + Z$

While both the $pp \to t\bar{t}W^{\pm}$ and $pp \to t\bar{t}Z$ processes describe the production of a top-quark pair with a heavy gauge boson, these two processes are very different. While in $pp \to t\bar{t}W^{\pm}$ the W boson is usually only coupled to the initial-state quark line and therefore gives no information about the t-W vertex, in $pp \to t\bar{t}Z$ the Z boson is directly connected to either the initial-state quarks or the top quarks. This provides direct insight into the t-Z vertex, which can be affected by new physics such as Z' resonances or vector-like leptons [332–338]. Combined with the $pp \to t\bar{t}\gamma$ process it gives complementary information to the top-quark

couplings to neutral gauge bosons, which can then be used to constrain Wilson coefficients in effective field theories [195, 199, 201, 295, 339–347]. Furthermore, the $pp \to t\bar{t}Z$ process is an important (irreducible) background to $pp \to t\bar{t}H$ in several Higgs decay channels and an important background process in dark-matter searches at the LHC [348–350] when the Z boson decays into a neutrino pair.

The $pp \to t\bar{t}Z$ process has been measured by the ATLAS and CMS collaborations at $\sqrt{s} = 8$ TeV [303, 304] and $\sqrt{s} = 13$ TeV [300, 305, 306, 308, 351, 352]. The statistical and systematic uncertainties of the inclusive cross section are of equal size, while in the 4ℓ channel, where the top quarks and the Z bosons decay into leptons, the statistical uncertainties dominate. As shown in Figure 1.5, the experimental measurements are in good agreement with the complete NLO prediction including soft gluon resummation at NNLL [302]. In addition, recent measurements of the $pp \to t\bar{t}Z$ process by the ATLAS collaboration are used to constrain Wilson coefficients in SMEFT and to measure the top-quark spin correlations [352]. The CMS collaboration has used the top-quark pair final state with additional leptons, including the $pp \to t\bar{t}Z$ process, to set constraints on Wilson coefficients in SMEFT [353].

The NLO QCD corrections are known for more than ten years, first calculated in Ref. [354] and later in Refs. [193, 355]. The NLO EW corrections to the dominant LO contribution were calculated in Ref. [249]. In addition, soft gluon effects were resummed at NNLL accuracy [302, 321, 322, 356]. The decays of unstable particles were first included by matching the NLO QCD corrections with parton showers [323, 357]. These predictions were improved in Ref. [358] by including spin correlations between the production and decay of the top-quark pair and by including the Z boson decay into a lepton pair already at the matrix element level. In this case, the $pp \to t\bar{t}\ell^+\ell^-$ process is considered, including intermediate off-shell Z bosons and photons. Full off-shell predictions at NLO QCD were first calculated in the $Z \to \nu\bar{\nu}$ decay channel [349]. This calculation was used to study the impact of the top-quark modeling on the exclusion limits in dark matter searches between the full off-shell calculation and the NWA [350]. The decays of top quarks and the Z boson in the $Z \to \ell^+\ell^-$ decay channel at the matrix element level were first considered at NLO QCD in Ref. [341] in the NWA and later in Ref. [359] in the full off-shell approach. Recently, these predictions where further improved by including the complete NLO corrections in the full off-shell approach in Ref. [360].

1.2.7 $pp \to t\bar{t} + t\bar{t}$

Lastly, we focus on the $pp \to t\bar{t}t\bar{t}$ process which was recently observed by the ATLAS and CMS collaborations [274, 275]. Besides being the heaviest final state observed at the LHC, this process has many other features which makes it an interesting process to study. First, this process has a high sensitivity to the top-quark Yukawa coupling (Y_t) due to intermediate Higgs bosons already at the tree level. Although the top-quark coupling to the Higgs boson is only present in subleading contributions, this process can still be used to measure Y_t indirectly. In particular, the cross section contains contributions that are proportional to Y_t^2 and Y_t^4, thus showing a large sensitivity to any modifications. In addition, the four top cross section can be enhanced by various BSM models, such as composite top quarks [361–363], heavy Kaluza-Klein gluons and quarks from extra dimensions [364, 365], scalar gluons in supersymmetric extensions of the SM [366–369],

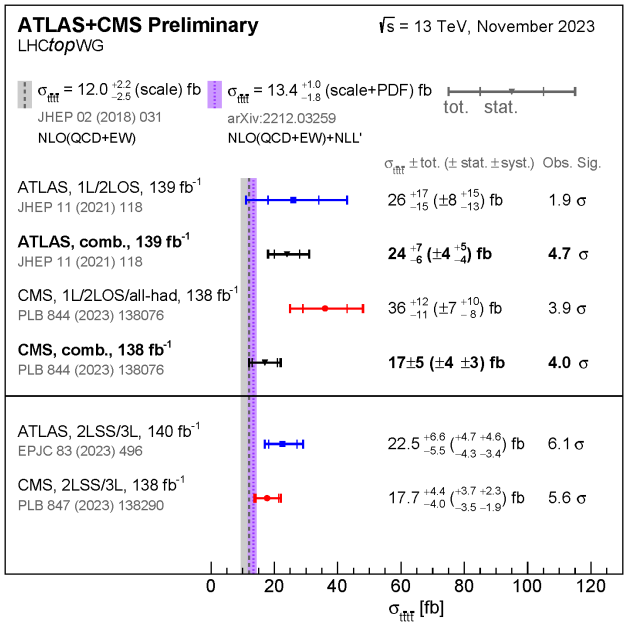

Figure 1.6: *Summary plot of inclusive four-top cross section in various final states by the ATLAS and CMS collaborations at the LHC with* $\sqrt{s} = 13$ TeV *[274, 275, 379, 380] compared with theoretical predictions [269, 381]. Figure taken from Ref. [27].*

top-philic resonances [335, 370–372] or two-Higgs-doublet models [373–375]. In addition, this process can be used to constrain four-fermion operators in SMEFT [376–378].

Several searches for the production of four top quarks were carried out in the past [130, 131, 272, 273, 379, 380, 382–385] and finally observed in 2023 by the ATLAS and CMS collaborations at $\sqrt{s} = 13$ TeV [274, 275] by combining the measurements of the 2ℓ same-sign and 3ℓ decay channels. A summary of the recent measurements compared to the latest theoretical predictions with complete NLO corrections [269] and soft gluon resummation at NNL´ [381] is shown in Figure 1.6. The measurement of $pp \to t\bar{t}t\bar{t}$ is strongly limited by large statistical uncertainties but also suffers from significant systematic uncertainties from the signal and background modeling of processes such as $pp \to t\bar{t}W^{\pm}$ or $pp \to t\bar{t}Z$.

The calculation of NLO QCD corrections for stable top quarks was first performed in Ref. [386] and revisited in Ref. [119, 193]. In addition, all subleading LO and NLO contributions were calculated in Ref. [269], where the individual subleading contributions at different orders in α_s and α can become sizeable. Especially the subleading LO contributions can be as large as 30% of the dominant LO QCD production of four top quarks. However, these different subleading contributions cancel to a large extent and lead in total only to an increase of about 10%. At the differential level the situation might differ, since certain contributions can be enhanced. Furthermore, resummation of soft gluon effects at NNL' was performed in Ref. [381]. The matching of NLO QCD predictions to parton showers was first carried out in Ref. [193] and later in Ref. [387], where in the latter case also subleading LO contributions were included. Recently, the calculation of $pp \to t\bar{t}t\bar{t}$ in the 4ℓ decay channel in the NWA was performed at NLO QCD [388].

2. Theoretical framework

The overall goal of this chapter is to summarize the theoretical background for event generation and the structure of NLO calculations at hadron colliders such as the LHC. In particular, we discuss the complications that arise in the calculation of subleading NLO corrections at fixed order and introduce the corresponding notation for the remainder of this thesis. Furthermore, the treatment of unstable particles in perturbation theory is studied in detail, focusing on the two most common approach at fixed order, the full off-shell calculation and the NWA. Finally, we discuss the structure of isolated photon cross sections and the complications which are introduced by requiring a realistic photon isolation condition as applied in experimental measurements.

2.1 Theoretical predictions at hadron colliders

In hadron-hadron collisions, the starting point is given by the factorization formula, which allows to write the hadronic cross section as the convolution of partonic cross sections with PDFs. This is followed by the hard scattering process, where the partonic cross sections are calculated in perturbation theory up to a specific order in α_s and α by specifying the initial- and final-state particles, where additional radiation can occur. The fixed-order partonic process at the hard scale is then followed by secondary radiation at small scales generated by the parton shower, where logarithmically enhanced contributions are numerically resummed. The effects of secondary radiation are naturally enhanced in QCD compared to QED, because α_s is much larger than α, especially at small scales. The parton shower can be seen as the connection between the hard scattering process and the non-perturbative hadronization at small momentum, where the latter describes the transition from partons to color-singlet hadrons. While in general parton showers and hadronization models are required for a complete description and a direct comparison with experimental measurements, the unfolding of these measurements to the parton level allows also a comparison with theoretical predictions of the hard scattering process at fixed order. The following section is intended to give a compact overview of the dynamics of a scattering process in hadron collisions. More details on the individual topics can be found in Refs. [389–391], which were also used as a basis for this section.

2.1.1 Factorization and PDFs

While the factorization formula has only been proven for deep-inelastic scattering and Drell-Yan production [392–394], it is now used in many applications at the LHC. The factorization theorem at hadron colliders, where we consider proton-proton collisions in

the following, is given by

$$\sigma(p_a, p_b, \mu_R, \mu_F) = \sum_{a,b} \int_0^1 \mathrm{d}x_a \int_0^1 \mathrm{d}x_b \, f_a(x_a, \mu_F) \, f_b(x_b, \mu_F) \, \hat{\sigma}_{ab}(x_a p_a, x_b p_b, \mu_R, \mu_F) \quad (2.1)$$

where $p_{a/b}$ are the four-momenta of the two incoming protons, for which the squared center-of-mass energy is fixed as $s = (p_a + p_b)^2$. The hadronic cross section is obtained by the convolution of the PDFs $f_{a/b}(x_{a/b}, \mu_F)$ with the partonic cross sections $\hat{\sigma}_{ab}$. The summation runs over all partons appearing in the proton. The PDFs $f_a(x, \mu_F)$ can be interpreted at LO as a probability distribution to find the parton a with the momentum fraction x in the proton. At higher orders this interpretation no longer holds, since PDFs are no longer strictly non-negative due to a redefinition to absorb collinear initial-state singularities. This redefinition introduces a dependence on the factorization scale at fixed order, which is described by the Dokshitser-Gribov-Lipatov-Altarelli-Parisi (DGLAP) equations [392, 395–397]. In QCD they are given by

$$\mu_F^2 \frac{\mathrm{d}f_a(x, \mu_F^2)}{\mathrm{d}\mu_F^2} = \frac{\alpha_s}{2\pi} \sum_b \int_x^1 \frac{\mathrm{d}z}{z} P_{ba}(z) f_b\left(\frac{x}{z}, \mu_F^2\right), \quad (2.2)$$

where $P_{ba}(x)$ are the regularized Altarelli-Parisi splitting functions. They describe the collinear splitting of the parton a from the parton b with the momentum fraction x. At LO, the non-vanishing splitting functions are given by

$$\begin{aligned}
P_{qq}(x) &= C_F \left[\frac{1+x^2}{(1-x)_+} + \frac{3}{2}\delta(1-x) \right] \\
P_{gq}(x) &= T_R \left[x^2 + (1-x)^2 \right] \\
P_{qg}(x) &= C_F \left[\frac{1+(1-x)^2}{x} \right] \\
P_{gg}(x) &= 2C_A \left[\frac{x}{(1-x)_+} + \frac{1-x}{x} + x(1-x) \right] + \delta(1-x) \left[\frac{11}{6} C_A - \frac{2}{3} n_f T_R \right],
\end{aligned} \quad (2.3)$$

where the color factors are given in QCD by

$$C_F = \frac{N_c^2 - 1}{2N_c}, \qquad T_R = \frac{1}{2}, \qquad C_A = N_C, \quad (2.4)$$

with $N_c = 3$ and n_f is the number light quark flavors. While in perturbation theory only the scale dependence of PDFs can be determined, these functions are non-perturbative objects and therefore can currently only be precisely determined in fits to experimental data. The calculation of subleading contributions including EW corrections requires the inclusion of photons in the proton and the consistent extension of the DGLAP equations with the corresponding QED splittings. In principle, the inclusion of leptons in the proton would also be necessary, but in practice this is usually neglected due to their small size compared to the overwhelming contribution of the other proton constituents. Nevertheless, leptons were consistently included in the proton PDF in Ref. [398] by applying the methods described in Refs. [399, 400], which are nowadays the standard approach to precisely

determine the photon PDF in the proton. The corresponding splitting functions can be obtained from the QCD ones in Eq. (2.3) by simple substitutions which then lead to

$$\begin{aligned} P_{ff}(x) &= Q_f^2 \left[\frac{1+x^2}{(1-x)_+} + \frac{3}{2}\delta(1-x) \right] \\ P_{\gamma f}(x) &= N_{c,f} Q_f^2 \left[x^2 + (1-x)^2 \right] \\ P_{f\gamma}(x) &= Q_f^2 \left[\frac{1+(1-x)^2}{x} \right] \\ P_{\gamma\gamma}(x) &= -\frac{2}{3}\delta(1-x) \sum_f N_{c,f} Q_f^2, \end{aligned} \tag{2.5}$$

where Q_f is the charge of the fermion, $N_{c,f}$ is a color factor, which is 3 for quarks and 1 for leptons, and the sum runs over all massless fermions. Notably, $P_{\gamma\gamma}$ is the only splitting function that has only a virtual contribution indicated by the delta distribution and no real contributions, in contrast to its QCD counterpart P_{gg}, which also has real corrections due to the self-interaction of gluons.

2.1.2 Hard scattering process

Returning to the factorization formula in Eq. (2.1), the PDFs are convoluted with the partonic cross section $\hat{\sigma}_{ab}$, which describes the hard scattering process $ab \to F + X$ of the two initial state partons (a, b) to a final state F with possible extra radiation (X). The partonic cross section is subject to perturbation theory and is expanded up to the required order in the strong coupling constant α_s and the electromagnetic coupling constant α. Therefore, the partonic cross section can be written as the following expansion

$$\hat{\sigma}_{ab} = \sum_{n \geq n_0} \left(\sum_{i=0}^{n} \alpha_s^{n-i} \alpha^i \, \hat{\sigma}_{ab}^{n-i,i} \right), \tag{2.6}$$

where the dependence on α_s and α is made explicit and the summation for n starts at n_0, which is the smallest possible order in α_s/α and corresponds to the LO partonic cross section. The next possible order is then given at $n = n_0+1$, describing the NLO corrections. The partonic cross section can alternatively be written as

$$\hat{\sigma}_{ab} = \hat{\sigma}_{ab}^0 + \hat{\sigma}_{ab}^1 + ..., \tag{2.7}$$

where $\hat{\sigma}_{ab}^0$ corresponds to the LO contribution and $\hat{\sigma}_{ab}^1$ to the NLO corrections. Thus, the LO and NLO partonic cross sections are then simply given by

$$\begin{aligned} \hat{\sigma}_{ab}^{\mathrm{LO}} &= \hat{\sigma}_{ab}^0, \\ \hat{\sigma}_{ab}^{\mathrm{NLO}} &= \hat{\sigma}_{ab}^0 + \hat{\sigma}_{ab}^1. \end{aligned} \tag{2.8}$$

Since the LO and NLO contributions can depend on different combinations of $\alpha_s^{n-i}\alpha^i$, following the notation of [269, 310] we further divide $\hat{\sigma}_{ab}^0$ and $\hat{\sigma}_{ab}^1$ as

$$\begin{aligned} \hat{\sigma}_{ab}^0 &= \hat{\sigma}_{ab}^{\mathrm{LO}_1} + \hat{\sigma}_{ab}^{\mathrm{LO}_2} + \hat{\sigma}_{ab}^{\mathrm{LO}_3} + ..., \\ \hat{\sigma}_{ab}^1 &= \hat{\sigma}_{ab}^{\mathrm{NLO}_1} + \hat{\sigma}_{ab}^{\mathrm{NLO}_2} + \hat{\sigma}_{ab}^{\mathrm{NLO}_3} + \hat{\sigma}_{ab}^{\mathrm{NLO}_4} ..., \end{aligned} \tag{2.9}$$

where LO_1 is the non-vanishing LO contribution with the highest possible exponent of α_s in $\alpha_s^{n_0-i}\alpha^i$. Typically, LO_1 is the dominant LO contribution due to the power couplings, and the subleading contributions, such as LO_2, are obtained by decreasing the exponent of α_s and increasing the exponent of α by one at each subsequent LO contribution. The same applies to the NLO corrections. Therefore, NLO_1 can be uniquely defined as the NLO QCD corrections to LO_1 and the last NLO contribution as the NLO EW corrections to the last LO contribution, while any other NLO contribution generally consists of both NLO QCD and EW corrections to different LO contributions. For example, if we consider a process with three LO contributions (LO_1, LO_2, LO_3), then we have four NLO contributions (NLO_1, NLO_2, NLO_3, NLO_4) and NLO_4 is purely given by the NLO EW corrections to LO_3, while e.g. NLO_2 usually includes NLO EW corrections to LO_1 and NLO QCD corrections to LO_2. A detailed discussion of the individual contributions is given in Chapter 5 for the processes $pp \to t\bar{t}\gamma$ and $pp \to t\bar{t}\gamma\gamma$ for which we perform the calculation of the complete NLO corrections including all subleading LO and NLO contributions.

Furthermore, we write the LO partonic cross section as

$$\hat{\sigma}_{ab}^{\mathrm{LO}}(p_1, p_2, \mu_R) = \int_n \mathrm{d}\hat{\sigma}_{ab}^{\mathrm{LO}}(p_1, p_2, \mu_R) = \int_n \frac{1}{2\hat{s}} \mathcal{A}_{ab}^{B} \mathrm{d}\Phi_n, \tag{2.10}$$

where $\hat{s} = x_a x_b s$ is the partonic center-of-mass energy, which is part of the flux factor $2\hat{s}$. $\mathcal{A}^B$ is the squared Born (LO) matrix element and $\mathrm{d}\Phi_n$ is the Lorentz invariant phase-space factor for n final state particles given by

$$\mathrm{d}\Phi_n = (2\pi)^4 \, \delta^4 \left(p_1 + p_2 - \sum_{i=3}^{n+2} p_i \right) \prod_{i=3}^{n+2} \frac{\mathrm{d}^3 \vec{p}_i}{(2\pi)^3 \, 2E_i}, \tag{2.11}$$

where we have used $p_1 = x_a p_a$ and $p_2 = x_b p_b$ to distinguish the momenta of the protons and the partons. The phase-space integration can then be performed with nowadays standard techniques based on recursive relations and multi-channel methods, see e.g. [401–403], to properly describe the resonant structure of matrix elements indicated by the propagators. At NLO, the partonic cross section has to be extended to

$$\begin{aligned} \hat{\sigma}_{ab}^{\mathrm{NLO}}(p_1, p_2, \mu_R, \mu_F) = &\int_{n+1} \mathrm{d}\hat{\sigma}_{ab}^{\mathrm{R}}(p_1, p_2, \mu_R) + \int_n \mathrm{d}\hat{\sigma}_{ab}^{\mathrm{LO+V}}(p_1, p_2, \mu_R) \\ &+ \int_n \mathrm{d}\hat{\sigma}_{ab}^{\mathrm{C}}(p_1, p_2, \mu_R, \mu_F), \end{aligned} \tag{2.12}$$

which consists of the LO cross section and corrections of different origins. On the one hand, we have the real emission of additional partons (photons) leading to subprocesses of the form $2 \to n{+}1$ given by the first term, and on the other hand we have the virtual corrections coming from the interference of tree-level and one-loop diagrams given in $\mathrm{d}\hat{\sigma}_{ab}^{\mathrm{V}}$. The sum of the virtual and real corrections is in general not IR finite, and the remaining initial-state collinear singularities are absorbed into a redefinition of the PDFs, leading to additional counterterms given by $\hat{\sigma}_{ab}^{\mathrm{C}}(p_1, p_2, \mu_R, \mu_F)$ which introduce an explicit dependence on μ_F and makes the NLO partonic cross section finite. These counterterms take the following form

at NLO QCD in the $\overline{\text{MS}}$ scheme in dimensional regularization with $d = 4 - 2\epsilon$ dimensions

$$\begin{aligned} \mathrm{d}\hat{\sigma}^{\mathrm{C}}_{ab}(p_1, p_2, \mu_R, \mu_F) = \frac{\alpha_s}{2\pi}\frac{1}{\Gamma(1-\epsilon)}\sum_k \int_0^1 \mathrm{d}z \frac{1}{\epsilon}\left(\frac{4\pi\mu_R^2}{\mu_F^2}\right)^{\epsilon} P_{ak}(z)\,\mathrm{d}\hat{\sigma}^{\mathrm{LO}}_{kb}(zp_1, p_2, \mu_R) \\ + \frac{\alpha_s}{2\pi}\frac{1}{\Gamma(1-\epsilon)}\sum_k \int_0^1 \mathrm{d}z \frac{1}{\epsilon}\left(\frac{4\pi\mu_R^2}{\mu_F^2}\right)^{\epsilon} P_{bk}(z)\,\mathrm{d}\hat{\sigma}^{\mathrm{LO}}_{ak}(p_1, zp_2, \mu_R). \end{aligned} \tag{2.13}$$

In the case of NLO EW corrections, the corresponding collinear QED counterterms has to be included as well, which are again obtained by simple substitutions. After renormalization of the one-loop amplitudes, all UV singularities in $d\hat{\sigma}^{\mathrm{V}}_{ab}$ are removed. However, all three terms in Eq. (2.12) still contain IR divergences. These singularities can be explicitly extracted in dimensional regularization in the last two terms, so that the phase-space integration can be performed numerically in $d = 4$ dimensions. In contrast, in the first term, $\mathrm{d}\hat{\sigma}^{\mathrm{R}}_{ab}$, a numerical integration in $d = 4$ dimensions is not directly applicable, since the IR singularities arise from the phase-space integration in $d = 4 - 2\epsilon$ dimensions over the phase space of the unresolved particles. To overcome this obstacle, we use the dipole subtraction method following the Catani-Seymour [404, 405] and Nagy-Soper subtraction schemes [406]. In this case, Eq. (2.12) is rewritten as

$$\hat{\sigma}^{\mathrm{NLO}}_{ab} = \int_{n+1}\left[\mathrm{d}\hat{\sigma}^{\mathrm{R}}_{ab} - \mathrm{d}\hat{\sigma}^{\mathrm{A}}_{ab}\right] + \int_n \left[\mathrm{d}\hat{\sigma}^{\mathrm{LO+V}}_{ab} + \mathrm{d}\hat{\sigma}^{\mathrm{C}}_{ab} + \int_1 \mathrm{d}\hat{\sigma}^{\mathrm{A}}_{ab}\right] \tag{2.14}$$

where $d\hat{\sigma}^{\mathrm{A}}_{ab}$ is constructed to cancel locally all IR singularities in the first brackets and to allow a numerical phase-space integration in $d = 4$. In addition, the counterterm should be simple enough to perform the integration over the phase space of the unresolved particles and to extract all IR singularities which then cancel with those of the remaining contributions in the second brackets. Only the strict soft and/or collinear limits of the new counterterms are constrained by the singular structure of the gauge theory, and therefore different choices of $\mathrm{d}\hat{\sigma}^{\mathrm{A}}_{ab}$ are possible, which can additionally be used for cross-checks, since the final results should be independent of this counterterm. The subtraction term $\mathrm{d}\hat{\sigma}^{\mathrm{A}}_{ab}$ is then obtained from $\mathrm{d}\hat{\sigma}^{\mathrm{R}}_{ab}$ by replacing the squared real emission matrix element in $\mathcal{A}^R$ by $\mathcal{A}^D$. Using the notation of Ref. [406], this term has the following general form in QCD

$$\mathcal{A}^D\left(\{p\}_{n+1}\right) = \sum_{i,j,k} \mathcal{A}^B(\{\tilde{p}\}_n^{(ijk)}) \otimes \mathcal{D}^{(ijk)}\left(\{\tilde{p}\}_n^{(ijk)}, \{p\}_{n+1}\right)\left(\mathbf{T}_{ij}\cdot\mathbf{T}_k\right), \tag{2.15}$$

where $\{p\}_{n+1}$ represents the momentum set of the $2 \to n+1$ process, $\{\tilde{p}\}_n^{(ijk)}$ is the mapped momentum set to the $2 \to n$ process, and the underlying Born process of $\mathcal{A}^B$ is obtained from the $2 \to n+1$ process by the recombination of the splitting pair $i + j \to \widetilde{ij}$. The momentum mapping $\{p\}_{n+1} \to \{\tilde{p}\}_n^{(ijk)}$ has to preserve the on-shell masses of all particles, and additionally in the strict singular limit, the momentum of the splitting pair has to reduce to $\tilde{p}_i = p_i \pm p_j$ for final/initial-state splittings, while the momenta of all other particles remain unchanged ($\tilde{p}_k = p_k$). The Born matrix element of the underlying process is then combined with the so-called dipoles $\mathcal{D}^{(ijk)}$, where spin correlations are denoted by the symbol $\otimes$ and the last term represents the color correlators, where the color operators T_k are defined in Ref. [404]. In general, the momentum mapping and the dipole terms

depend explicitly on the splitting pair and the spectator parton k. This means that the matrix element $\mathcal{A}^B(\{\tilde{p}\}_n^{(ijk)})$ has to be recalculated for each spectator k. In the Nagy-Soper subtraction scheme, which we use to obtain all numerical results in this thesis, the momentum mapping is defined in such a way that it does not explicitly depend on k. Therefore, Eq. (2.15) can be simplified to

$$\mathcal{A}^D_{\mathrm{NS}}\left(\{p\}_{n+1}\right) = \sum_{i,j} \mathcal{A}^B(\{\tilde{p}\}_n^{(ij)}) \otimes \left(\sum_k \mathcal{D}^{(ijk)}\left(\{\tilde{p}\}_n^{(ij)}, \{p\}_{n+1}\right) (\mathbf{T}_{ij} \cdot \mathbf{T}_k) \right). \tag{2.16}$$

This form makes it apparent that such a momentum mapping leads to a reduced number of matrix element evaluations in the subtraction term, since only the color and dipole summation depend on the spectator k. In fact, in the Nagy-Soper subtraction this number scales as m^2, where m is the number of colored particles in the process, compared to m^3 in the Catani-Seymour subtraction scheme.

A second difference between the two subtraction schemes can be found in the handling of helicity states in the subtraction term. The original formulation of the Catani-Seymour subtraction relies on spin-summed matrix elements and does not allow for various methods to simplify the matrix element calculation and to speed up the phase-space integration such as helicity sampling, where the full spin summation is replaced by a multi-channel Monte Carlo integration over the different non-vanishing helicity configurations. In Ref. [407] the Catani-Seymour subtraction was extended to arbitrary helicity eigenstates, which allows the usage of the helicity sampling method. A different strategy to overcome the bottleneck of full spin summation in the calculation of matrix elements is the random polarization method [406, 408, 409], where the polarization states are replaced by linear combinations of helicity eigenstates and the spin summation is replaced by an integration over a phase parameter. In detail, the polarization state of a gluon/photon is replaced by

$$\varepsilon_\mu(p, \phi) = e^{i\phi}\varepsilon_\mu(p, +) + e^{-i\phi}\varepsilon_\mu(p, -), \tag{2.17}$$

where $\varepsilon_\mu(p, \pm)$ are helicity eigenstates. The spin summation is then replaced according to

$$\sum_s |\mathcal{M}_s|^2 = \frac{1}{2\pi} \int_0^{2\pi} |\mathcal{M}_\phi|^2 \, \mathrm{d}\phi. \tag{2.18}$$

The phase parameter ϕ is generated uniformly and usually different values of ϕ do not lead to large differences in $|\mathcal{M}_\phi|^2$, because both helicity eigenstates are always included. This formalism can be directly extended to the case of massless/massive fermions and also to massive gauge bosons, where in the latter case the third eigenstate is added without any phase parameter to Eq. (2.17). This method has the advantage that the discrete multi-channel Monte Carlo integration in the helicity sampling approach is avoided, where first the non-zero helicity states has to be found. The Catani-Seymour subtraction was extended in Ref. [410] to the random polarization method. On the other hand, in the Nagy-Soper subtraction scheme, the dipole terms explicitly depend on the polarization vectors, such that both methods can directly be used.

2.1.3 Parton shower and hadronization

Finally, further real radiation is generated with parton showers, which can be seen as the connection of the hard scattering process at the hard scale with the non-perturbative

hadronization of partons to color-neutral hadrons at a small scale of the order $\Lambda_{\mathrm{QCD}} < 1$ GeV. In particular, this introduces a cutoff scale in the parton-shower evolution, below which no further radiation is produced by the parton shower. By construction, the parton shower also approximates higher-order real corrections by considering the soft-collinear limits of QCD in $1 \to 2$ splittings of external (initial and finale-state) partons. Therefore, this approach does not correctly recover the spectra of hard emission of extra partons described in regular fixed-order calculations. Due to the requirement of unitarity in the parton shower, virtual corrections are also included, which can be obtained to large extent from this requirement. Thus, the parton shower can be seen a probabilistic way to describe multiple emissions starting from a hard scattering process. This can be understood by considering the Sudakov form factor [389] given by

$$\Delta_{ij;k}(t, t_0) = \exp\left(-\int_{t_0}^{t} \mathrm{d}\Phi_1 \mathcal{K}_{ij;k}(\Phi_1)\right) \tag{2.19}$$

where Φ_1 describes the phase-space variables of the one-particle phase space, t is the evolution variable and $\mathcal{K}_{ij;k}(\Phi_1)$ are the splitting functions with the splitting parton i, the emitted parton j and the spectator parton k. This Sudakov form factor represents the no-branching probability in the evolution between the scales t and t_0. There are several choices of evolution variables t, the momentum mapping in the splitting $1 \to 2$ and the splitting functions $\mathcal{K}_{ij;k}$. These choices can have an impact on the accuracy of the specific parton shower and introduce uncertainties in the parton shower evolution, which can be approximated by the differences between various parton shower models such as Herwig [411], Pythia [412] or Sherpa [413], which are extensively used in current studies at the LHC. The first emission from the parton shower starting from a hard Born process can be written as

$$\mathrm{d}\sigma_n^{\mathrm{Born}} = \mathrm{d}\Phi_n \, \mathcal{B}_n(\Phi_n) \left\{ \Delta_n(\mu_Q^2, t_c) + \int_{t_c}^{\mu_Q^2} \mathrm{d}\Phi_1 \left[K_n(\Phi_1) \Delta_n(\mu_Q^2, t(\Phi_1)) \right] \right\}, \tag{2.20}$$

where $\mathcal{B}_n$ is the Born matrix element including symmetry factors, $K_n(\Phi_1)$ is the sum of the individual contributions $\mathcal{K}_{ij;k}(\Phi_1)$ in all possible combinations, $\Delta_n(\mu_Q^2, t_c)$ is the corresponding Sudakov form factor and t_c is the cutoff scale of the parton shower. The first term represents the probability for no emissions between the hard scale μ_Q^2 and the cutoff scale t_c, while the second term describes a single $1 \to 2$ splitting at the scale $t(\Phi_1)$ with no further emissions above this scale. The case of multiple emissions can be implemented by iterating this equation inside the integral describing the first emission. In particular, one can define a so-called paton shower all-emission operator $\mathcal{E}(\mu_Q^2, t_c)$ [389] as

$$\mathcal{E}_n(t_1, t_c) = \Delta_n(t_1, t_c) + \int_{t_c}^{t_1} \mathrm{d}\Phi_1 \left[K_n(\Phi_1) \Delta_n(t_1, t(\Phi_1)) \otimes \mathcal{E}_{n+1}(t(\Phi_1), t_c) \right]. \tag{2.21}$$

The structure is very similar to the one in Eq. 2.20 with the extension that further radiation is allowed with the recursive use of $\mathcal{E}_{n+1}(t(\Phi_1), t_c)$ inside the integral. The Born process with multiple additional radiation generated by the parton shower is then obtained with

$$\mathrm{d}\sigma_n^{\mathrm{Born}} = \mathrm{d}\Phi_n \, \mathcal{B}_n(\Phi_n) \, \mathcal{E}_n(\mu_Q^2, t_c). \tag{2.22}$$

The combination of parton showers with calculations including higher-order corrections requires a careful matching between both parts in order to avoid double counting of radiation generated in the higher-order calculations at fixed order and the radiation generated in the parton shower. In particular, at NLO QCD the first (hardest) radiation is generated by the hard scattering process, while all further radiation is produced in the parton shower. The two most commonly used approaches for the matching of hard scattering processes at NLO with parton showers, are the MC@NLO [91] and the POWHEG [93, 94] methods. In addition, processes with different jet multiplicities can be combined in the so-called multijet merging. This has the background that the parton showers cannot recover the effects of hard QCD radiation but can be described by the same hard process with an increasing number of jets in the final state. This requires are careful combination of (NLO) calculations with different jet multiplicities to avoid double counting. Usually a merging scale is introduced to combine such calculations. Established methods in the literature to perform the multijet merging of NLO calculations with different jet multiplicities are the FXFX [120], MEPS@NLO [414, 415] and MINLO [175] approaches.

In the last step, the hadronization of partons to color-neutral hadrons has to be included to make the predictions directly comparable to real events in experiments. At first sight, this hadronization can be thought of in analogy to the splittings of partons from hadrons in the initial state described by PDFs. The corresponding counterpart for such transitions from partons to hadrons of final-state particles is described by fragmentation functions. However, the hadronization of a single parton does not necessarily lead to exactly one hadron, but rather to multiple ones. Therefore, more sophisticated approaches has to be used for the proper description of the non-perturbative transition from quarks to hadrons. Usually, the hadronization in modern applications is described by the string (Lund) model [416, 417] and cluster models based on the preconfinement property of QCD [418] that partons are produced in color singlet clusters in the evolution of the parton shower.

2.2 Top-quark modeling in perturbation theory

2.2.1 Full off-shell calculation

The two most common approaches to consistently describing the production and decay of a top-quark pair at the matrix element level in fixed-order calculations are the so-called *full off-shell* calculations and the NWA. In the following, the two approaches and the differences between them will be discussed. In the full off-shell calculation, only the initial- and final-state particles, after the decays of all unstable resonances, are specified and no assumptions are made about the possible internal resonance structures, which automatically takes into account all possible intermediate contributions with different resonance structures. This also means that the final state consists only of stable particles with $\Gamma = 0$. In the case of top-quark pair production, intermediate unstable top quarks and W bosons are found, where the corresponding decay chain in the *di-lepton* decay channel has the following form

$$pp \to t(\to W^+(\to e^+\nu_e)\, b)\, \bar{t}(\to W^-(\to \mu^-\bar{\nu}_\mu)\, \bar{b}). \tag{2.23}$$

In the full off-shell approach we do not consider the exact decay chain but instead only the initial- and final-state particles, resulting to the following process under consideration

$$pp \to e^+\nu_e\, \mu^-\bar{\nu}_\mu\, b\bar{b}. \tag{2.24}$$

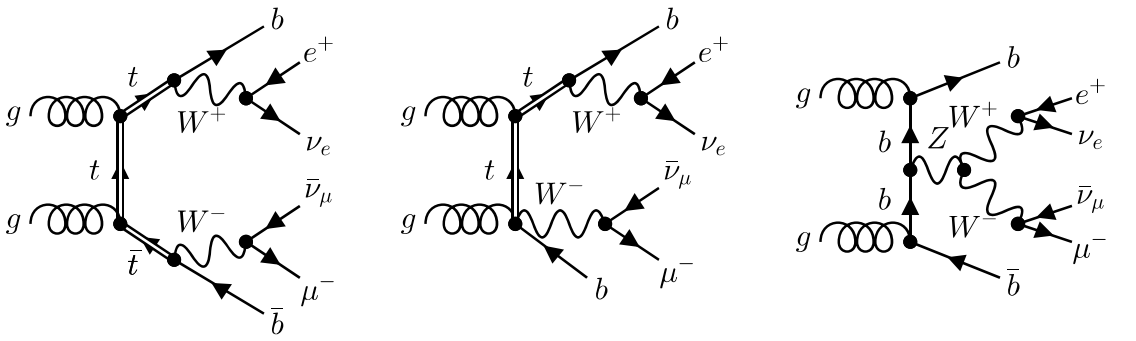

Figure 2.1: *Example Feynman diagrams for double-, single- and non-resonant contributions. All Feynman diagrams in this thesis were produced with the help of the* FeynGame *program [419].*

Thus, this process includes all Feynman diagrams with two resonant top quarks by construction, as well as all Feynman diagram with only one or even none resonant top quark with the same final-state particles. In addition, all interference effects between these contributions are automatically included. Example diagrams for the different resonance structures, which we call in the following *double-*, *single-* and *non-resonant contributions*, are shown in Figure 2.1. Usually in experimental measurements the double-resonant contribution is considered as the signal process for the $t\bar{t}$ measurement and is obtained from the on-shell approximation, while the single- and non-resonant contributions are treated as background processes. Thus, the full off-shell calculation consistently combines the considered signal and background processes and all interference effects already at the matrix element level. In contrast, in the on-shell approximation, the signal and background processes are calculated independently, which requires special care in the case of $t\bar{t}$ and tW to avoid double counting. In particular, the latter process gives rise to the $tW^-\bar{b}$ process at NLO, which has the same resonance structure as $t\bar{t}$. The double counting is then removed by defining the NLO QCD corrections of tW in the diagram removal (DR) [420] or diagram subtraction (DS) [421, 422] approaches, where the double-resonant contribution is removed by either by removing the double-resonant Feynman diagrams at the amplitude or squared amplitude level in a non-gauge invariant way, or by subtracting a counterterm that locally mimics the double resonant contribution in the region close to the on-shell masses of the resonances. The use of such methods introduces additional systematic uncertainties, which cannot be systematically assessed, but are often estimated rather naively by the differences between the various approaches. While these differences are small for most phase-space regions, they can be enhanced in certain regions sensitive to off-shell effects, either in high p_T regions or in observables with kinematic edges related to the on-shell masses of the top quark and the W boson. In particular, substantial differences for the m_{bl}^{minimax} observale, defined as

$$m_{bl}^{\text{minimax}} = \min\left[\max\left(m_{b_1 l_1}, m_{b_2 l_2}\right), \max\left(m_{b_1 l_2}, m_{b_2 l_1}\right)\right], \tag{2.25}$$

above 150 GeV are found in Ref. [423] and shown in Fig. 2.2. In this case, the DR and DS methods are not able to fully describe the experimental data over the complete range of this observable. The definition of m_{bl}^{minimax} is designed to reconstruct the b-jet and the charged lepton coming from the same top quark. This observable is highly sensitive to off-shell effects since in the on-shell approximation an upper limit is given by the masses of the

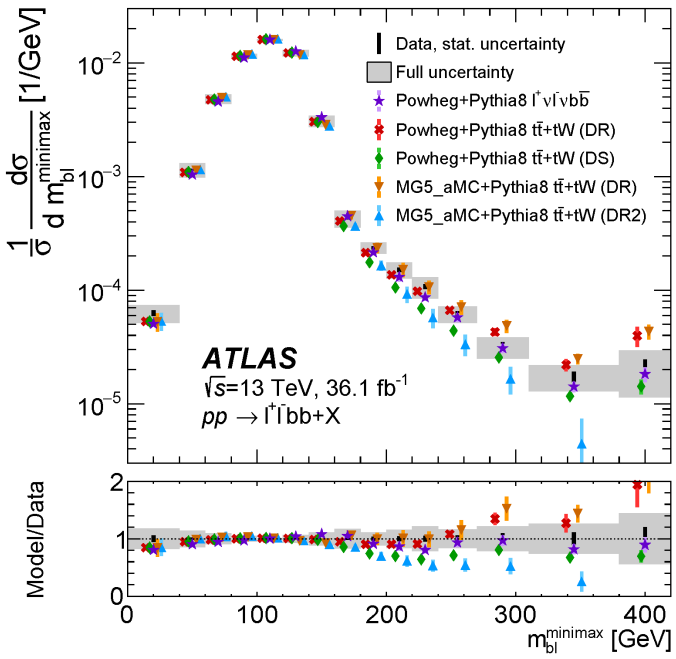

Figure 2.2: *Comparison of different approaches, full off-shell, DS and DR, to generate* $t\bar{t}+tW$ *for the* m_{bl}^{minimax} *observable. Figure taken from Ref. [423].*

top quark and W boson by $m_{bl}^{\text{minimax}} < \sqrt{m_t^2 - m_W^2} \approx 150$ GeV. An improved agreement was found with the full off-shell calculation matched to parton showers as implemented in POWHEG [115, 424], where a good agreement with experimental data was found over the full range.

In the full off-shell approach, the denominator of the propagators of unstable particles are replaced in the following way

$$\frac{1}{p^2 - m^2} \to \frac{1}{p^2 - m^2 + im\Gamma}, \tag{2.26}$$

such that the invariant mass distributions of unstable particles in resonant contributions are described by Breit-Wigner propagators of the form

$$\text{BW}(p^2) = \frac{1}{(p^2 - m^2)^2 + m^2\Gamma^2}. \tag{2.27}$$

This is usually achieved in full off-shell calculations by using the *complex-mass scheme* which was first introduced for tree-level processes in Ref. [403], later generalised to the one-loop order in Refs. [425–427] and provides a gauge invariant inclusion of the widths of unstable particles. At the tree-level, the widths are introduced by replacing the real masses of unstable particles (fermions and bosons) with complex masses everywhere in the Feynman rules, which are defined as

$$\mu_X^2 = m_X^2 - im_X\Gamma_X. \tag{2.28}$$

This also means that the weak mixing angle becomes complex according to

$$c_w^2 = 1 - s_w^2 = \frac{\mu_W^2}{\mu_Z^2}. \tag{2.29}$$

At the one-loop order, the bare masses are split into complex masses and complex counterterms as

$$m_{X,0}^2 = \mu_X^2 + \delta\mu_X^2, \tag{2.30}$$

for unstable bosons (H, $W^\pm$, Z) and as

$$m_{f,0} = \mu_f + \delta\mu_f, \tag{2.31}$$

for unstable fermions (top quark). Furthermore, the on-shell renormalization, as described in e.g. Ref. [428], has to be generalized for the case of the complex-mass scheme, which will be briefly summarized for the case of the W boson, where all additional complications are present. The renormalized W-boson fields are introduced by

$$W_0^\pm = \left(1 + \frac{1}{2}\mathcal{Z}_W\right) W^\pm, \tag{2.32}$$

where the renormalization constant $\mathcal{Z}_W$ is complex and is used for W^+ and W^-, such that $W^- \neq (W^+)^\dagger$. This implies that the Lagrangian expressed in terms of the renormalized fields without counterterms is not hermitian, but with counterterms, which is then equal to the bare Lagrangian, is of course still hermitian. The renormalization constants are then derived from the renormalized transverse W-boson self-energy, which is given by

$$\hat{\Sigma}_T^W(k^2) = \Sigma_T^W(k^2) - \delta\mu_W^2 + \left(k^2 - \mu_W^2\right)\delta\mathcal{Z}_W. \tag{2.33}$$

In particular, both renormalization constants are fixed by the two conditions

$$\hat{\Sigma}_T^W(\mu_W^2) = 0 \qquad \text{and} \qquad \hat{\Sigma}_T'^W(\mu_W^2) = 0 \tag{2.34}$$

where $\hat{\Sigma}_T'^W(\mu_W^2)$ is the derivative of $\hat{\Sigma}_T^W(\mu_W^2)$. In the complex renormalization we take into account the real and imaginary parts of the self-energies in the definition of the renormalization constants, while in the on-shell scheme only the real part is taken into account. These conditions then result to the following solutions for the renormalization constants

$$\delta\mu_W^2 = \Sigma_T^W(\mu_W^2) \qquad \text{and} \qquad \delta\mathcal{Z}_W = -\Sigma_T'^W(\mu_W^2). \tag{2.35}$$

The analytic continuation of Σ_T^W to complex squared momenta required for the renormalization constants can be avoided by expanding the (unrenormalized) self-energy about real arguments, where special care is required for photon exchange contributions in in the case of charged particles due to a branching point at $k^2 = \mu_W^2$. This results into an additional constant c_T^W, which has to be added to the expansion resulting to

$$\Sigma_T^W(\mu_W^2) = \Sigma_T^W(m_W^2) + \left(\mu_W^2 - m_W^2\right)\Sigma_T'^W(m_W^2) + c_T^W + \mathcal{O}(\alpha^3), \tag{2.36}$$

where c_T^W is given by

$$c_T^W = \frac{\alpha}{\pi}\left(m_W^2 - \mu_W^2\right). \tag{2.37}$$

A similar counterterm is required in the case of unstable fermions due to photon and gluon exchange diagrams. The renormalization constants can then be expanded up to the required order for NLO EW corrections, which then leads to

$$\begin{aligned} \delta\mu_W^2 &= \Sigma_T^W(m_W^2) + \left(\mu_W^2 - m_W^2\right)\Sigma_T'^W(m_W^2) + c_T^W, \\ \mathcal{Z}_W &= -\Sigma_T'^W(m_W^2) \end{aligned} \tag{2.38}$$

In practical applications, where the complex-mass scheme is required for the W boson due to internal resonances and a non-zero W boson width is used, the W boson should not be considered as a possible external particle, so that the field renormalization constant of the W boson, $\mathcal{Z}_W$, drops out completely.

The complex-mass schemes preserves the bare Lagrangian but its perturbative expansion is rearranged in such way that the imaginary part of the complex mass becomes part of the propagators and is therefore resummed, while the imaginary part of the counterterm is not. All relations which do not involve complex-conjugates, such as Slavnov-Taylor and Ward identities, are preserved, since in these cases the complex-mass scheme is only an analytic continuation. However, the Cutkosky cutting rules do not longer hold, which then cannot be used to prove unitarity order by order. Nevertheless unitarity holds (up to higher-orders) if unstable particles are excluded from external states, as it was explicitly shown for scalar theories in Ref. [429], since the bare Lagrangian is unchanged.

In summary, all contributions with the same initial- and finial-state particles are included in the full off-shell calculation at the matrix element level, while in experiments often different resonance structures are divided into signal and background processes. The mass spectrum of a unstable particle is described by a Breit-Wigner propagator which requires the inclusion of the width of the unstable particle in the propagator with the complex-mass scheme.

2.2.2 Narrow width approximation

Usually, the dominant contribution of the full off-shell calculation is indeed coming from a specific resonance structure involving unstable particles. This contribution can be isolated from the full calculation by using the Narrow-Width Approximation (NWA), i.e. the limit of small widths $\Gamma/m \ll 1$. In this limit, the Breit-Wigner propagator leads to

$$\frac{1}{(p^2-m^2)^2+m^2\Gamma^2} \overset{\Gamma/m\to 0}{\longrightarrow} \frac{\pi}{m\Gamma}\delta(p^2-m^2), \tag{2.39}$$

which implies that all diagrams which are less singular than the specific resonance structure are neglected and the delta distribution forces the unstable particles to be on-shell. Following our example process of $t\bar{t}$ production, the NWA implies in the limit Γ_t/m_t that only the double-resonant contribution is kept and all single- and non-resonant contributions as well as all the interference effects are neglected. In addition, the width is set to zero everywhere in the matrix element except in the resonant propagators. Finally, the NWA allows to factorize the cross section into the production of $t\bar{t}$ followed by the decays of the two top quarks, which can be written as

$$\mathrm{d}\sigma = \mathrm{d}\sigma_{t\bar{t}}\,\frac{\mathrm{d}\Gamma_t}{\Gamma_t}\,\frac{\mathrm{d}\Gamma_{\bar{t}}}{\Gamma_t}, \tag{2.40}$$

where $d\sigma_{t\bar{t}}$ is the production cross section of a top-quark pair, $d\Gamma_t/d\Gamma_{\bar{t}}$ describes the subsequent decays of the two top quarks and Γ_t is the top-quark width. Spin correlations between the production and decay terms are understood, which originate from the numerators of the propagators of the unstable particles. The numerator can be written in the on-shell limit as the sum of polarization vectors, as for example in the case of top quarks as

$$\begin{aligned}(\not{p}_t + m_t) &= \sum_s u_s(p_t)\bar{u}_s(p_t), \\ (\not{p}_{\bar{t}} - m_t) &= \sum_s v_s(p_{\bar{t}})\bar{v}_s(p_{\bar{t}}),\end{aligned} \tag{2.41}$$

where the two top quarks are on-shell with $p_t^2 = p_{\bar{t}}^2 = m_t^2$. This approximation leads to enormous simplifications in the calculation of the matrix elements but also in the phase-space integration. Effectively the complexity of a $2 \to 6$ process is reduced to the computation of several subprocesses with smaller multiplicities in the final state. Moreover, we also use the NWA to model decays of the W boson, so that the top-quark decays are further expanded as

$$\mathrm{d}\Gamma_t = \mathrm{d}\Gamma_{t\to W^+b}\frac{\mathrm{d}\Gamma_{W^+}}{\Gamma_W}. \tag{2.42}$$

In the calculation of higher-order corrections, two different approaches are present to handle the top-quark widths in the denominator. In the unexpanded NWA, only the nominator is expanded and not the top-quark width in the denominator. In this case, the differential cross section at NLO (QCD) can be written schematically as

$$\mathrm{d}\sigma_{\mathrm{NLO}} = \left(\mathrm{d}\sigma^0_{t\bar{t}} + \mathrm{d}\sigma^1_{t\bar{t}}\right)\frac{\mathrm{d}\Gamma^0_t}{\Gamma^{\mathrm{NLO}}_t}\frac{\mathrm{d}\Gamma^0_{\bar{t}}}{\Gamma^{\mathrm{NLO}}_t} + \mathrm{d}\sigma^0_{t\bar{t}}\left(\frac{\mathrm{d}\Gamma^1_t}{\Gamma^{\mathrm{NLO}}_t}\frac{\mathrm{d}\Gamma^0_{\bar{t}}}{\Gamma^{\mathrm{NLO}}_t} + \frac{\mathrm{d}\Gamma^0_t}{\Gamma^{\mathrm{NLO}}_t}\frac{\mathrm{d}\Gamma^1_{\bar{t}}}{\Gamma^{\mathrm{NLO}}_t}\right). \tag{2.43}$$

In the alternative approach, the expanded NWA, the top-quark width in the denominator is expanded and is related to the first approach by

$$\mathrm{d}\sigma^{\mathrm{exp}}_{\mathrm{NLO}} = \left(\frac{\Gamma^{\mathrm{NLO}}_t}{\Gamma^{\mathrm{LO}}_t}\right)^2 \mathrm{d}\sigma_{\mathrm{NLO}} - 2\,\frac{\Gamma^1_t}{\Gamma^0_t}\,\mathrm{d}\sigma_{\mathrm{LO}}, \tag{2.44}$$

where the first terms rescales the unexpanded NLO calculation to the LO top-quark width and the second term is coming from the expansion $\Gamma^{\mathrm{NLO}}_t = \Gamma^0_t + \Gamma^1_t$ in the denominator. Essentially, the differences between the two schemes are of higher orders and the numerical differences between both schemes should decrease with increasing perturbative order. The definition of the unexpanded version is inspired by the full off-shell calculation, where an expansion of the widths is generally not possible. Thus, it is expected that this scheme is closer to the results in the full off-shell calculation than the expanded NWA. On the other hand, the expanded NWA relies on a consistent expansion of all parameters in the calculation, so that also the top-quark width in the denominator must be expanded. This scheme has the property, that after integrating out all the decays, the inclusive $t\bar{t}$ production cross section is recovered with $\sigma^{\mathrm{NLO}}_{t\bar{t}} = \sigma^0_{t\bar{t}} + \sigma^1_{t\bar{t}}$ in this case. Of course, this statement no longer holds, if for example different scales are used in the top-quark width Γ_t and in the hard scattering process, as it is typically done. In addition, in processes like $pp \to t\bar{t}j$ or $pp \to t\bar{t}\gamma$, where no inclusive cross section can be defined, i.e. a cross section without any technical cuts, and where the jets/photons can be emitted from the decays themselves,

this property of recovering the inclusive cross section has no meaning anymore. Therefore, whenever the NWA is used in this thesis for the calculation of $pp \to t\bar{t}\gamma$ and $pp \to t\bar{t}\gamma\gamma$, we always refer to the unexpanded NWA.

2.3 Isolated photon production

In scattering processes at the LHC, photons can be radiated in many places. While dedicated experimental measurements are mostly interested in primary photons originating from the hard scattering process, background contributions from secondary production mechanisms like fragmentation processes or decays of hadrons (e.g. $\pi^0 \to \gamma\gamma$) are present. Photons originating from these secondary production mechanisms are usually accompanied by additional hadronic activity. Therefore, photon isolation criteria, restricting the hadronic activity around the photon candidate, are used in experimental studies to reduce these background contributions. Also in theoretical higher-order calculations photon isolation conditions are often used to avoid collinear quark-photon configurations, so that the parton-to-photon fragmentation contribution vanishes. In particular, such collinear configurations are present in the case where an additional (unresolved) quark is generated in the calculation of the real corrections from which the photon is emitted $q \to q\gamma$. Collinear photon radiation off partons can be consistently described by the introduction of the non-perturbative parton-to-photon fragmentation functions, which leads to further technical complications in the calculation of higher-order corrections. In principle (at least at NLO), it is sufficient to require an angular separation between quarks and photons to remove the collinear IR singularities and the fragmentation contribution. However, quark- and gluon-initiated jets are not distinguished in experimental measurements. Therefore, the same event selection has to be applied to both types of jets in order to closely follow the experimental setup. Thus, this approach would also introduce an angular separation between photons and (unresolved) gluons which would disturb the cancellation of soft gluon IR singularities between the real and virtual corrections.

2.3.1 Photon isolation criteria

Smooth-cone isolation

On the other hand, the fragmentation contribution can be fully avoided in an IR-safe way by the so-called smooth-cone isolation [15]. In this approach, an event is rejected unless the following condition is fulfilled for all isolated photons in the hard scattering process before the jet clustering

$$E_{T,\text{had}}(R) \leq \epsilon_\gamma \, E_{T,\gamma} \left(\frac{1-\cos(R)}{1-\cos(R_{\gamma j})} \right)^n , \tag{2.45}$$

for all $R \leq R_{\gamma j}$ and where the transverse hadronic energy, $E_{T,\text{had}}(R)$, is given by the sum of all transverse energies of partons inside the cone with radius R as defined by

$$E_{T,\text{had}}(R) = \sum_i E_{T,i} \, \Theta(R - R_{\gamma i}), \tag{2.46}$$

where $R_{\gamma i}$ is given by

$$R_{\gamma i} = \sqrt{(y_\gamma - y_i)^2 + (\phi_\gamma - \phi_i)^2} \, . \tag{2.47}$$

The transverse energies of the partons and the photon are denoted by $E_{T,i}$ and $E_{T,\gamma}$, respectively. Since this method is barely usable in experimental analyses, the parameters $R_{\gamma j}$, n and ϵ_γ have to be tuned in general to mimic the isolation criterion that is used in the experimental analysis. However, this tuning is highly dependent on the actual process and also on the exact event selection. In general, the smooth-cone isolation, even after tuning, is not able to fully recover the exact isolation criterion used in experiments, which means that the use of the smooth-cone photon isolation is always affected by additional (unknown) uncertainties. In principle, the complete functional form on the right hand side in Eq. (2.45) can be modified as long as the requirements for this function as given in Ref. [15] are satisfied. The smooth-cone isolation is designed to allow soft radiation within the cone, but to remove exact collinear parton-photon configurations, so that the $q \to q\gamma$ collinear singularity is removed and the fragmentation contribution vanishes.

Fixed-cone isolation
The fixed-cone isolation is the standard method in experimental analyses for processes with isolated photons, where a certain amount of transverse hadronic energy inside a cone of radius $R_{\gamma j}$ around the photon candidate is allowed. We parameterize this condition as

$$E_{T,\mathrm{had}}(R_{\gamma j}) \leq E_{T,\mathrm{max}}(E_{T,\gamma}), \tag{2.48}$$

where $E_{T,\mathrm{max}}(E_{T,\gamma})$ is the maximal transverse hadronic energy allowed inside this cone which can be a constant number, a function depending on $E_{T,\gamma}$ or a combination of both. This isolation criterion allows for arbitrarily soft gluon radiation inside the cone, but also allows for collinear configurations between photons and partons. Therefore, the contribution of the parton-to-photon fragmentation function does not vanish as in the smooth-cone isolation and must be consistently included. Thus, the collinear singularities stemming from photon radiation off quarks are absorbed into a redefinition of the quark-to-photon fragmentation function in analogy to the redefinition of PDFs. At NNLO QCD, even the introduction of a gluon-to-photon fragmentation function is required. While this approach is straightforward to apply in experimental analyses, it leads to further complications in theoretical predictions, because additional subtraction terms has to be included, which have to be differential with respect to the photonic energy fraction inside the splitting parton. Furthermore, it is possible to combine the smooth-cone and fixed-cone isolation criteria in a so-called hybrid photon isolation [430]. In this case, the smooth-cone isolation with $\widetilde{R}_{\gamma j} < R_{\gamma j}$ is applied first to remove all collinear photon singularities and the fragmentation contribution, and then the fixed-cone isolation is applied. This photon isolation criterion is designed to more closely resemble the fixed-cone isolation than the smooth-cone isolation.

Democratic clustering
The democratic clustering approach [431, 432], is an alternative photon isolation criterion, where photons and partons are clustered together with a standard jet clustering algorithm. In this case, a cluster containing a photon is then considered as an isolated photon, if the energy fraction

$$z_\gamma = \frac{E_\gamma}{E_\gamma + E_{\mathrm{jet}}}, \tag{2.49}$$

is larger than a minimal value z_{cut}, where E_γ and E_{jet} are the energies of the photon and the jet, respectively. The original formulation of z_γ was designed for lepton colliders, where the energies can be measured more precisely than in hadron colliders. In the latter case, an alternative definition can be used

$$z_\gamma = \frac{E_{T,\gamma}}{E_{T,\gamma} + E_{T,\text{jet}}}. \tag{2.50}$$

where $E_{T,\text{jet}}$ is the transverse energy of the jet, which is given by the sum of all transverse energies of partons inside this jet. This definition ensures that all properties of the original definition of z_γ are preserved and that in the exact collinear limit both definitions become equal. The democratic clustering approach was used for the first measurement of the quark-to-photon fragmentation function by ALEPH [433]. This photon isolation criterion requires also the introduction of parton-to-photon fragmentation functions since collinear configurations are allowed. Furthermore, it provides a natural photon isolation criterion for the calculation including EW corrections where the clustering of partons with photons is necessary for IR-safe observables.

2.3.2 Isolated photon cross sections

Next, we discuss the structure of isolated photon cross sections with the inclusion of parton-to-photon fragmentation functions. Following Ref. [434], we write the partonic differential cross section of the production of a isolated photon as

$$\mathrm{d}\hat{\sigma}^{\gamma+X} = \mathrm{d}\hat{\sigma}_\gamma + \sum_p \mathrm{d}\hat{\sigma}_p \otimes D^B_{p\to\gamma}, \tag{2.51}$$

where $\mathrm{d}\hat{\sigma}_\gamma$ is the usual production cross section of a photon, $\mathrm{d}\hat{\sigma}_p$ is the production cross section of a massless parton (quark or gluon) instead of a photon convoluted with the bare parton-to-photon fragmentation function $D^B_{p\to\gamma}$, which describes the fragmentation from a parton p to a jet containing a photon with the energy fraction z_γ. The latter contribution vanishes completely when either the smooth-cone or the hybrid photon isolation is used. By employing the power counting of $D_{p\to\gamma} = \mathcal{O}(\alpha)$, the photon cross section can be expanded at LO and NLO to

$$\begin{aligned} \mathrm{d}\hat{\sigma}^{\gamma+X,\text{LO}} &= \mathrm{d}\hat{\sigma}^{\text{LO}}_\gamma \\ \mathrm{d}\hat{\sigma}^{\gamma+X,\text{NLO}} &= \mathrm{d}\hat{\sigma}^{\text{NLO}}_\gamma + \sum_p \mathrm{d}\hat{\sigma}^{\text{LO}}_p \otimes D_{p\to\gamma} - \frac{\alpha}{2\pi}\sum_p \mathrm{d}\hat{\sigma}^{\text{LO}}_p \otimes \mathbf{\Gamma}^{(0)}_{p\to\gamma}, \end{aligned} \tag{2.52}$$

where $D_{p\to\gamma}$ are the factorized fragmentation functions and $\mathbf{\Gamma}_{i\to j}$ are the factorization kernels. The LO contribution is given purely by the direct contribution at LO, while the NLO cross section is given by the direct photon production at the matrix element level at NLO and the convolutions of the LO cross section with a parton instead of a photon with the factorized fragmentation functions and the factorization kernels. Alternatively, we write the differential cross section at NLO as

$$\mathrm{d}\hat{\sigma}^{\gamma+X,\text{NLO}} = \mathrm{d}\hat{\sigma}^{\gamma+X,\text{NLO}}_{\text{dir}} + \mathrm{d}\hat{\sigma}^{\gamma+X,\text{NLO}}_{\text{frag}}, \tag{2.53}$$

where the full calculation is given by the sum of the direct contribution $\mathrm{d}\hat{\sigma}_{\mathrm{dir}}^{\gamma+X,\mathrm{NLO}}$ and the fragmentation contribution $\mathrm{d}\hat{\sigma}_{\mathrm{frag}}^{\gamma+X,\mathrm{NLO}}$, which are both IR finite and are given by

$$\mathrm{d}\hat{\sigma}_{\mathrm{dir}}^{\gamma+X,\mathrm{NLO}} = \mathrm{d}\hat{\sigma}_{\gamma}^{\mathrm{NLO}} - \frac{\alpha}{2\pi}\sum_{p}\mathrm{d}\hat{\sigma}_{p}^{\mathrm{LO}} \otimes \mathbf{\Gamma}_{p\to\gamma}^{(0)}, \tag{2.54}$$

and

$$\mathrm{d}\hat{\sigma}_{\mathrm{frag}}^{\gamma+X,\mathrm{NLO}} = \sum_{p}\mathrm{d}\hat{\sigma}_{p}^{\mathrm{LO}} \otimes D_{p\to\gamma}. \tag{2.55}$$

All non-perturbative effects of the fragmentation functions are included in the latter contribution, which depends on the particular parametrization of the fragmentation functions. The bare and factorized parton-to-photon fragmentation functions are connected through

$$D_{i\to\gamma}(z,\mu_{Fr}^2) = \sum_{j}\mathbf{\Gamma}_{i\to j}(z,\mu_{Fr}^2) \otimes D_{j\to\gamma}^{B}(z), \tag{2.56}$$

where μ_{Fr} is the fragmentation scale and where we have used

$$D_{\gamma\to\gamma}(z,\mu_{Fr}^2) = D_{\gamma\to\gamma}^{B}(z) = \delta(1-z). \tag{2.57}$$

The inversion of Eq. (2.56) up to NLO leads then to

$$D_{p\to\gamma}^{B}(z) = D_{p\to\gamma}(z,\mu_a^2) - \frac{\alpha}{2\pi}\mathbf{\Gamma}_{p\to\gamma}^{(0)}, \tag{2.58}$$

which was already used in Eq. (2.52). Since the gluon does not couple directly with the photon, we have $\mathbf{\Gamma}_{g\to\gamma}^{(0)} = 0$ and $D_{g\to\gamma} = \mathcal{O}(\alpha\alpha_s)$. Therefore, the gluon-to-photon fragmentation function is not explicitly required in NLO calculations as in our case, but it becomes mandatory at higher orders. The factorization kernel of the quark-to-photon fragmentation function is given by

$$\mathbf{\Gamma}_{q\to\gamma}^{(0)} = -Q_q^2\, P_{q\to\gamma}(z)\frac{(4\pi)^\epsilon}{\Gamma(1-\epsilon)}\left(\frac{\mu_R^2}{\mu_{Fr}^2}\right)^{\epsilon}\frac{1}{\epsilon}, \tag{2.59}$$

where the quark-to-photon splitting function $P_{q\to\gamma}(z)$ is given by

$$P_{q\to\gamma}(z) = \frac{1+(1-z)^2}{z}. \tag{2.60}$$

The splitting functions required for initial state splittings for the PDFs and for final state splittings for fragmentation functions are in general different and correspond to space-like and time-like splitting functions, respectively. At LO, however, the space-like and time-like splitting functions coincide and in our case we have simply factored out the charge of the quark in $P_{q\to\gamma}(z)$ with respect to $P_{f\gamma}(z)$ in Eq. (2.5) for a simpler notation in the following.

Similar to the case of PDFs, evolution equations can be derived for the fragmentation functions by requiring that the bare fragmentation functions are independent of the fragmentation scale

$$\mu_{Fr}^2\frac{\mathrm{d}D_{p\to\gamma}^{B}(z)}{\mathrm{d}\mu_{Fr}^2} = 0. \tag{2.61}$$

This equation can be expended up to $\mathcal{O}(\alpha)$, which then leads to the following evolution equation for the quark-to-photon fragmentation function

$$\mu_{Fr}^2 \frac{\partial D_{q\to\gamma}(z,\mu_{Fr})}{\partial \mu_{Fr}^2} = \left(\frac{\alpha Q_q^2}{2\pi}\right) P_{q\to\gamma}(z), \tag{2.62}$$

which completely determines the μ_{Fr} dependence of the LO fragmentation function. The solution of $D_{q\to\gamma}$ at LO is then given by

$$D_{q\to\gamma}^{(\mathrm{LO})}(z,\mu_{Fr}) = D_{q\to\gamma}^{np}(z,\mu_0) + \left(\frac{\alpha Q_q^2}{2\pi}\right) P_{q\to\gamma}^{(0)}(z)\, \log\left(\frac{\mu_{Fr}^2}{\mu_0^2}\right), \tag{2.63}$$

where $D_{q\to\gamma}^{np}(z,\mu_0^2)$ at the scale μ_0^2 is non-perturbative input, which has to be obtained in comparisons with experimental measurements. A first determination of the LO quark-to-photon fragmentation function was performed by ALEPH [433] which resulted into

$$D_{q\to\gamma}^{np(\mathrm{LO})}(z,\mu_0) = \left(\frac{\alpha Q_q^2}{2\pi}\right) \left(-P_{q\to\gamma}^{(0)}(z)\log(1-z)^2 - 13.26\right), \tag{2.64}$$

with $\mu_0 = 0.14$ GeV. The NLO quark-to-photon fragmentation function was obtained in a similar approach in Refs. [432, 435], where the non-perturbative input is obtained by a fit to the experimental data to the ALEPH photon+jet data [433].

Alternatively, in the so-called conventional approach, see also e.g. Ref. [436] for more details and a comparison between the conventional and the fixed-order approach discussed above, the parton-to-photon fragmentation function is the solution of the inhomogeneous evolution equation

$$\mu_{Fr}^2 \frac{\partial D_{p\to\gamma}(z,\mu_{Fr})}{\partial \mu_{Fr}^2} = \left(\frac{\alpha}{2\pi}\right) K_{p\to\gamma}(z) + P_{p\to i} \otimes D_{i\to\gamma}, \tag{2.65}$$

with the parton-to-photon kernels $K_{p\to\gamma}$ and $P_{p\to i}$ are the usual parton-to-parton splitting functions. The solution is then given by the sum of a pointlike (perturbative) solution of the inhomogenous evolution equation and a hadronic (non-perturbative) solution of the homogenous evolution equation with $P_{p\to i} = 0$. In contrast to the fixed-order approach the solutions are not expanded but resummed at e.g. leading logarithm (LL) or at beyond leading logarithm (BLL) accuracy where also the running of the strong coupling constant $\alpha_s(\mu_{Fr})$ is taking into account by considering it as a function of the fragmentation scale. The non-perturbative input for the fragmentation function is then obtained using a vector meson dominance model, where gluons and quarks are assumed to first fragment into vector mesons, which then turn into photons. Such an approach was used for example in the determination of the BFGI and BFGII sets [437], where the evolution of the fragmention functions is included at NLL accuracy. The two sets differ mainly in the gluon-to-photon fragmentation function, which was partially fixed in the second set to overcome the small constraints from the data that the authors expect probably led to an underestimation of the gluon-to-photon fragmentation function in the first set.

3. Computational framework

After summarizing the general structure of NLO calculations with unstable particles and photon isolation criteria, we describe in the following how the calculation is organized and the different contributions are calculated. In particular, we first discuss the calculation of tree-level and one-loop matrix elements with recursive relations using the program RECOLA [438, 439]. Afterwards, we describe the calculation of real and virtual corrections in our framework with special emphasis on the former contribution. In particular, we discuss the original formulation of the Nagy-Soper subtraction scheme in detail and the extension for calculations involving internal on-shell resonances required in the NWA. Furthermore, we explain the extension of the Catani-Seymour and Nagy-Soper subtraction schemes for calculations with QED-like IR singularities and realistic photon isolation criteria, such as the fixed-cone isolation or the democratic clustering approach.

3.1 Recursive calculation of matrix-elements

The calculation of tree-level and one-loop matrix elements is performed with the matrix-element generator RECOLA [438, 439] using recursive relations based on Dyson-Schwinger equations [440–442], which relate correlation functions of decreasing multiplicity in a recursive way. This recursive approach is directly suitable for a complete numerical construction of amplitudes, because the recalculation of subamplitudes can easily be avoided since recurring structures are directly factored out in this approach. On the other hand, in the traditional approach with Feynman diagrams, a fast evaluation of matrix elements would require numerous analytic simplifications, so that this approach is not suitable for a fully numerical calculation. The general strategy of the generation of tree-level currents in RECOLA, which is based on the approach in HELAC-PHEGAS [443–445], can be described as follows. Considering a process of the form $1+2 \to 3+4+...+n$, a subamplitude involving a set of i external particles combined to the particle P can be displayed graphically as

$$w(P,\{i\}) = \quad P \quad \{i\}\,, \tag{3.1}$$

where the set $\{i\}$ consists of i integer values between 1 and n representing the external particles in this current, where each external particle can occur only once at most. Instead of such an array $\{i\}$ describing the external particles, it is also possible to uniquely assign an integer value m_i to each array. This also corresponds to the binary notation, where the integer value is given by

$$m_i = \sum_{k\in\{i\}} 2^{k-1}, \tag{3.2}$$

which has the property that if two currents involving the external particles $\{j\}$ and $\{k\}$ are combined into one current $\{i\}$ with $\{i\} = \{j\} \cup \{k\}$ and $\{j\} \cap \{k\} = \emptyset$, then the corresponding binary value is simply given by the sum

$$m_i = m_j + m_k. \tag{3.3}$$

In the case where $\{i\}$ consists of only one external particle, the current $w(P, \{i\})$ is then simply given by the corresponding external polarization vector. The recursive relations of subamplitudes can then be schematically written as

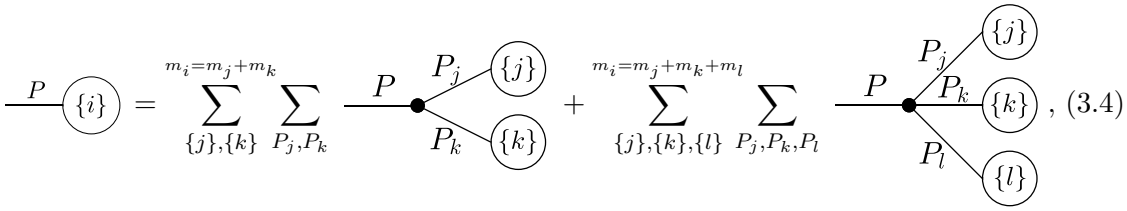

, (3.4)

where the first term represents all contributions obtained from 3-point and the second term from 4-point vertices. Each term in the sums is also called a *branch* and the dots represent the vertex function, which determines how the currents in each branch are combined depending on the resulting particle P as well as all other particles involved in the vertex (P_j, P_k and P_l). Only 3-point and 4-point vertices are present in the SM, where in the latter case no fermions contribute. The final matrix element can then be obtained by performing this recursive construction of currents with $n-1$ particles of the process where one external particle $P_{\bar{i}}$ is excluded. The current of the $n-1$ particles have to result into the same particle $P_{\bar{i}}$ as the missing external particle. This current is then simply multiplied by the inverse propagator to remove the propagator of the vertex function and by the corresponding polarization vector of the external particle $P_{\bar{i}}$.

In general, this calculation has to be performed for each helicity configuration of external particles, which would then require the numeric evaluation of this recursive approach of 2^n times, assuming only fermions and massless vector bosons as external particles. In practice, Recola takes into account the helicity states of external particles inside the construction of the currents $w(P, \{i\})$ to avoid the recomputation of currents with the same helicity configurations. In addition, helicity states of external massless fermions are taken into account to simplify the vertices and to avoid the calculation of vanishing helicity configurations by using the chiral representation for spinors. Although this results in a significant speed-up in the computation of squared matrix elements with full spin summation, we use instead the random polarization method, as described in the last chapter. This leads to a further speed-up in the phase-space integration with respect to the full spin summation, because only the computation of a single helicity amplitude with modified external polarization vectors is required. In practice, this is achieved in Recola by deactivating the helicity optimization for massless fermions, which is used to filter all vanishing helicity configurations and to simplify the vertex functions. Since in the random polarization method the external polarization vector is constructed by a linear combination of two (three) helicity eigenstates, these optimizations cannot be used in this case. Furthermore, we limit the number of helicity configurations to one, which has the effect that the generation of skeletons for the recursive algorithm is speed-up, since less currents and branches are required, and that the memory consumption is reduced.

The calculation of one-loop matrix elements in RECOLA [438, 439] is performed by reducing the one-loop matrix elements to tensor integrals $T_{(t)}^{\mu_1\dots\mu_{r_t}}$ and tensor coefficients $c_{\mu_1\dots\mu_{r_t}}^{(t)}$ as

$$\mathcal{M}_{1-\text{loop}} = \sum_t c_{\mu_1\dots\mu_{r_t}}^{(t)} T_{(t)}^{\mu_1\dots\mu_{r_t}} + \mathcal{A}_{\text{CT}}, \tag{3.5}$$

where the counterterm contribution is denoted by $\mathcal{A}_{\text{CT}}$ and the tensor integrals are defined as

$$T_{(t)}^{\mu_1\dots\mu_{r_t}} = \frac{(2\pi\mu)^{4-D}}{i\pi^2} \int \mathrm{d}^D q \frac{q^{\mu_1}\dots q^{\mu_{r_t}}}{D_0^{(t)}\dots D_{k_t}^{(t)}}, \tag{3.6}$$

where k_t is the number of propagators, r_t the rank of the tensor integral and the propagators are given by

$$D_i^{(t)} = \left(q + p_i^{(t)}\right)^2 - \left(m_i^{(t)}\right)^2, \tag{3.7}$$

with $p_0^{(t)} = 0$. The construction of the tensor coefficients is again based on recursion relations and are constructed from tree-level matrix elements with two additional particles in the final state ($2 \to n+2$), where additional particle-antiparticle pairs are added to the corresponding Born process. The tree-level matrix elements are directly related to the one-loop matrix element by cutting one of the loop lines. Therefore, the one-loop matrix element can be constructed out of these tree-level matrix elements, where additional rules have to be applied to avoid double counting of diagrams. Finally, scalar and tensor integrals are calculated numerically with COLLIER [446].

The color part of QCD particles in RECOLA is handled in a similar way as in HELAC-DIPOLES [445] using the color-flow decomposition [447], where the gluon field with one index in the adjoint representation of SU(3) is replaced by two indices in the fundamental representation by rewriting the Lagrangian as a function of

$$(\mathcal{A}_\mu)_j^i = \frac{1}{\sqrt{2}} A_\mu^a (\lambda^a)_j^i, \tag{3.8}$$

where λ^a are the Gell-Mann matrices and the ranges of the indices are restricted to the $a = 1, ..., 8$ and $i, j = 1, .., 3$. Thus, the new gluon field in the fundamental representation ($3 \cdot 3 = 9$) has one component more than in the adjoint representation (8), but the number of degrees of freedom is unchanged due to the relation

$$\sum_i (\mathcal{A}_\mu)_i^i = 0, \tag{3.9}$$

which is simply following from the properties of the Gell-Mann matrices ($\text{Tr}(\lambda^a) = 0$). This replacement leads to new Feynman rules [438, 447], which have the property that the complete color structure in the Feynman rules are simply given by combinations of Kronecker δs. Therefore, the matrix element in this representation for n_g gluons and n_q quarks and antiquarks can be written as

$$\mathcal{M}_{j_1\dots j_n}^{i_1\dots i_n} = \sum_\sigma \delta_{j_{\sigma_1}}^{i_1} \delta_{j_{\sigma_2}}^{i_2} \dots \delta_{j_{\sigma_n}}^{i_n} \mathcal{M}_\sigma \tag{3.10}$$

with $n = n_g + n_q$ and the summation $\sigma = (\sigma_1, \sigma_2, ..., \sigma_n)$ runs over all permutations of $(1, 2, ..., n)$. Thus, the calculation of the full matrix elements is reduced to the calculation

of the non-vanishing subamplitudes $\mathcal{M}_\sigma$ of the $n!$ permutations. Since in this method the exact values of the indices are not required and $\mathcal{M}_\sigma$ is uniquely defined by the given color structure through the product of Kronecker δs, these subamplitudes are also called *structure-dressed* amplitudes. In addition, Recola takes the color structure into account in the construction of subamplitudes to avoid the recalculation of specific parts.

Since the traces of the gluon fields vanish, additional relations are present between the subamplitudes $\mathcal{M}_\sigma$ in the presence of external gluons. This can be understood in the following way. Assuming that the indices i_1, j_1 correspond to a single gluon, then the following equation must hold

$$0 = \delta^{j_1}_{i_1} \mathcal{M}^{i_1 \dots i_n}_{j_1 \dots j_n}, \tag{3.11}$$

where summation is understood over indices which appear twice. This can then be repeated for all external gluons, which then leads to a system of linear equations. These linear equations can then be solved for all $\mathcal{M}_\sigma$, which are associated with at least one self-connected gluon, which would correspond to a color structure involving the factor $\delta^{i_1}_{j_1}$ in the example above. To illustrate this in more detail, we consider the following simple example of the $gg \to q\bar{q}$ process, where the matrix element can be decomposed in the following form

$$\begin{aligned} \mathcal{M}^{i_1 i_2 i_3}_{j_1 j_2 j_3} = {} & \delta^{i_1}_{j_1}\delta^{i_2}_{j_2}\delta^{i_3}_{j_3}\mathcal{M}_1 + \delta^{i_1}_{j_1}\delta^{i_2}_{j_3}\delta^{i_3}_{j_2}\mathcal{M}_2 + \delta^{i_1}_{j_2}\delta^{i_2}_{j_1}\delta^{i_3}_{j_3}\mathcal{M}_3 \\ & + \delta^{i_1}_{j_2}\delta^{i_2}_{j_3}\delta^{i_3}_{j_1}\mathcal{M}_4 + \delta^{i_1}_{j_3}\delta^{i_2}_{j_1}\delta^{i_3}_{j_2}\mathcal{M}_5 + \delta^{i_1}_{j_3}\delta^{i_2}_{j_2}\delta^{i_3}_{j_1}\mathcal{M}_6, \end{aligned} \tag{3.12}$$

where the indices i_1, j_1 (i_2, j_2) correspond to the first (second) gluon and the indices i_3, j_3 to the quark-antiquark pair. Therefore, we can apply the condition in Eq. (3.11), which then leads to

$$\begin{aligned} 0 &= \delta^{j_1}_{i_1}\mathcal{M}^{i_1 i_2 i_3}_{j_1 j_2 j_3} \\ &= \delta^{i_2}_{j_2}\delta^{i_3}_{j_3}(N_c\mathcal{M}_1 + \mathcal{M}_3 + \mathcal{M}_6) + \delta^{i_2}_{j_3}\delta^{i_3}_{j_2}(N_c\mathcal{M}_2 + \mathcal{M}_4 + \mathcal{M}_5) \end{aligned} \tag{3.13}$$

and

$$\begin{aligned} 0 &= \delta^{j_2}_{i_2}\mathcal{M}^{i_1 i_2 i_3}_{j_1 j_2 j_3} \\ &= \delta^{i_1}_{j_1}\delta^{i_3}_{j_3}(N_c\mathcal{M}_1 + \mathcal{M}_2 + \mathcal{M}_3) + \delta^{i_1}_{j_3}\delta^{i_3}_{j_1}(\mathcal{M}_4 + \mathcal{M}_5 + N_c\mathcal{M}_6), \end{aligned} \tag{3.14}$$

where in the two cases both brackets have to vanish. In this example, the subamplitudes $\mathcal{M}_1$, $\mathcal{M}_2$ and $\mathcal{M}_6$ are associated with self-connected gluons and thus we solve this system of linear equations for them. This leads to the following solutions

$$\mathcal{M}_2 = \mathcal{M}_6 = -\frac{1}{N_c}\left(\mathcal{M}_4 + \mathcal{M}_5\right) \tag{3.15}$$

and

$$\mathcal{M}_1 = -\frac{1}{N_c}\left(\mathcal{M}_3 + \mathcal{M}_6\right) = -\frac{1}{N_C}\mathcal{M}_3 + \frac{1}{N_c^2}\left(\mathcal{M}_4 + \mathcal{M}_5\right). \tag{3.16}$$

Therefore, in this example it is sufficient to calculate only the three subamplitudes $\mathcal{M}_3$, $\mathcal{M}_4$ and $\mathcal{M}_5$ and the other three subamplitudes ($\mathcal{M}_1$, $\mathcal{M}_2$ and $\mathcal{M}_6$) can be obtained with the solutions above. Instead of solving a system of linear equations, in Recola all

subamplitudes corresponding to self-connected gluons are obtained in a more systematical way by the use of projectors, which are defined as

$$P^{ij'}_{ji'} = \delta^i_{i'}\delta^{j'}_j - \frac{1}{N_c}\delta^i_j\delta^{j'}_{i'}, \tag{3.17}$$

which have the property

$$P^{ij'}_{ji'}(\lambda^a)^{i'}_{j'} = (\lambda^a)^i_j. \tag{3.18}$$

Therefore, this projector acts in the same way as the unity matrix on the matrix element if the indices i', j' correspond to a single gluon. Furthermore, we have

$$P^{ij'}_{ji'}\delta^{i'}_{j'} = 0, \tag{3.19}$$

which means that the use of the projector on the matrix element effectively eliminates all contributions proportional to $\delta^{i'}_{j'}$, but in the same step replaces this color structure contribution with subamplitudes from different color structures. Therefore, it is sufficient to calculate only the subamplitudes which are not associated with self-connected gluons and apply this projector for each external gluon. Thus, the complete matrix element in the example above is then simply given by

$$\mathcal{M}^{i_1i_2i_3}_{j_1j_2j_3} = P^{i_2j'_2}_{j_2i'_2}P^{i_1j'_1}_{j_1i'_1}\left(\delta^{i'_1}_{j'_2}\delta^{i'_2}_{j'_1}\delta^{i_3}_{j_3}\mathcal{M}_3 + \delta^{i'_1}_{j'_2}\delta^{i'_2}_{j_3}\delta^{i_3}_{j'_1}\mathcal{M}_4 + \delta^{i'_1}_{j_3}\delta^{i'_2}_{j'_1}\delta^{i'_3}_{j'_2}\mathcal{M}_5\right). \tag{3.20}$$

The correctness of this can be easily verified by expanding this product, which then leads to

$$\begin{aligned}\mathcal{M}^{i_1i_2i_3}_{j_1j_2j_3} &= \delta^{i_1}_{j_2}\delta^{i_2}_{j_1}\delta^{i_3}_{j_3}\mathcal{M}_3 + \delta^{i_1}_{j_2}\delta^{i_2}_{j_3}\delta^{i_3}_{j_1}\mathcal{M}_4 + \delta^{i_1}_{j_3}\delta^{i_2}_{j_1}\delta^{i_3}_{j_2}\mathcal{M}_5 \\ &\quad - \frac{1}{N_c}\left(\delta^{i_1}_{j_1}\delta^{i_2}_{j_3}\delta^{i_3}_{j_2} + \delta^{i_1}_{j_3}\delta^{i_2}_{j_2}\delta^{i_3}_{j_1}\right)(\mathcal{M}_4 + \mathcal{M}_5) \\ &\quad + \delta^{i_1}_{j_1}\delta^{i_2}_{j_2}\delta^{i_3}_{j_3}\left(\frac{1}{N_c^2}(\mathcal{M}_4 + \mathcal{M}_5) - \frac{1}{N_c}\mathcal{M}_3\right),\end{aligned} \tag{3.21}$$

which agrees with the results above. Finally, the color summation of the squared amplitude can be obtained by

$$\mathcal{A}^B = \sum_{\sigma,\bar{\sigma}}\mathcal{C}_{\sigma,\bar{\sigma}}\mathcal{M}_\sigma\mathcal{M}^*_{\bar{\sigma}}, \tag{3.22}$$

where the color matrix $\mathcal{C}_{\sigma,\bar{\sigma}}$ is given by

$$\mathcal{C}_{\sigma,\bar{\sigma}} = \sum_{i_1,\ldots,i_n}\sum_{j_1,\ldots,j_n}\delta^{i_1}_{j_{\sigma_1}}\ldots\delta^{i_n}_{j_{\sigma_n}}\delta^{j_{\bar{\sigma}_1}}_{i_1}\ldots\delta^{j_{\bar{\sigma}_n}}_{i_n} = (N_c)^{m(\sigma,\bar{\sigma})}, \tag{3.23}$$

where $m(\sigma,\bar{\sigma})$ is the number of cycles in the chain of Kronecker δs. The calculation of color-correlated squared matrix elements requires the insertion of products of color operators $\mathbf{T}_i \cdot \mathbf{T}_k$ into the color matrix, for which the color operators have to be first transformed into the correct representation. These products of color operators lead then again to sums and products of only Kronecker δs which determine how the color indices of the Kronecker δ chains are combined in the computation of the color matrix. The transformation of color operators into the fundamental representation is for example presented in Ref. [439].

3.2 Real corrections

As discussed in the last chapter, the general structure of NLO calculation using a subtraction scheme can be written as

$$\hat{\sigma}_{ab}^{\mathrm{NLO}} = \int_{n+1} \left[\mathrm{d}\hat{\sigma}_{ab}^{\mathrm{R}} - \mathrm{d}\hat{\sigma}_{ab}^{\mathrm{A}}\right] + \int_{n} \left[\mathrm{d}\hat{\sigma}_{ab}^{\mathrm{LO+V}} + \mathrm{d}\hat{\sigma}_{ab}^{\mathrm{C}} + \int_{1} \mathrm{d}\hat{\sigma}_{ab}^{\mathrm{A}}\right]. \tag{3.24}$$

The first brackets indicate the real subtracted contribution (**RS**), while the second brackets contain the Born contribution with one-loop correction (LO+V) and the integrated dipoles. The calculation is split as follows, the **RS**, LO+V contributions and the integrated dipoles are calculated separately. The latter term is further divided into the **I** and **KP** operators closely following the structure introduced in the Catani-Seymour subtraction scheme [404], where the sum of the integrated dipoles and the counterterms from the factorization are written as

$$\int_{n} \left[\mathrm{d}\hat{\sigma}_{ab}^{\mathrm{C}} + \int_{1} \mathrm{d}\hat{\sigma}_{ab}^{\mathrm{A}}\right] = \int_{n} \mathbf{I} \otimes \mathrm{d}\hat{\sigma}_{ab}^{\mathrm{LO}} + \int_{n} \int_{0}^{1} \mathrm{d}x\, \mathbf{KP}_{aa',bb'} \otimes \mathrm{d}\hat{\sigma}_{a'b'}^{\mathrm{LO}} \tag{3.25}$$

The **I** operator contains all logarithmic dependencies on the renormalization scale as well as all IR ϵ poles that cancel with those of the virtual corrections. On the other hand, the **KP** operator contains all logarithmic dependencies on the factorization scale and all non-diagonal terms in flavor space with respect to the initial-state particles. However, all terms contain either a $\delta_{aa'}$ or $\delta_{bb'}$ since only single $1 \to 2$ splittings are allowed at NLO. Still, the definitions of both operators are not unique and finite diagonal terms in flavor space can be shifted arbitrarily between both contributions. All terms are calculated within the Helac-Dipoles framework, where the Catani-Seymour and the Nagy-Soper subtraction schemes are implemented. In addition, we have interfaced it with Recola for the calculation of all tree-level and one-loop amplitudes, as described in the last section. The phase-space integration is performed with the help of the programs Kaleu [448] and Parni [449], where the latter program is also used for the numerical integration of the integrated dipoles in the Nagy-Soper subtraction scheme. Within Helac-Dipoles, integrated and differential cross sections can be calculated, which we have extended for the simultaneous calculation of different factorization/renormalization scales in a single run. In addition, it is possible to generate partially unweighted events [170] which are saved in modified Les Houches Event Files (LHEFs) [450, 451]. These event files can then be used for a flexible generation of integrated and differential cross sections for different PDF sets and scale settings for the same event selection as in the generation or for a more exclusive setup without performing the whole calculation again from scratch.

Besides the extensions of Helac-Dipoles, which will be discussed in the following of this chapter, we have performed several structural changes in the program to fully benefit from the construction of the Nagy-Soper subtraction scheme, that the momentum mapping does not depend on the spectator parton k. In particular, we have modified the structure to avoid the recomputation of certain parts in the calculation such as the event selection, renormalization/factorization scales and histogramming for dipoles with the same splitting partons i and j but different spectator partons k. In addition, we have implemented the possibility to sum over the PDFs for subprocesses that have the same matrix elements in the **KP** operator as explained in Appendix A.

3.2.1 Nagy-Soper subtraction scheme

Before we discuss the modifications in the Nagy-Soper subtraction scheme for calculations involving internal on-shell resonances, we summarize first the original formulation of the Nagy-Soper subtraction scheme [406] as implemented in HELAC-DIPOLES, where we focus on final-state splittings, which have to be modified for the extension to the NWA.

Momentum mapping
We consider a partonic process of the form $2 \to n+1$ and define the quantities Q, P_{ij} and K as

$$\begin{aligned} Q = p_1 + p_2 = \sum_{l=3}^{n+3} p_l, \\ P_{ij} = p_i + p_j \qquad \text{and} \qquad K = Q - P_{ij}, \end{aligned} \tag{3.26}$$

where Q is the total partonic momentum, P_{ij} is momentum sum of the emitter pair and K is the so-called collective spectator, which is the total momentum of all final-state particles that are not included in the splitting $\widetilde{ij} \to i + j$. Then, the momentum mapping for the dipole terms is defined as [452]

$$P_{ij} = \beta \tilde{p}_i + \gamma Q, \tag{3.27}$$

so that $\tilde{p}_i$ lies in the Q-P_{ij} plane. The new parameters β and γ are uniquely given from the two conditions, that the total momentum Q and that the virtuality of the collective spectator K are preserved

$$\begin{aligned} \tilde{Q} &= Q, \\ \widetilde{K}^2 &= K^2. \end{aligned} \tag{3.28}$$

This leads to the following solutions

$$\beta = 2\sqrt{\frac{(P_{ij}\cdot Q)^2 - P_{ij}^2 Q^2}{(m_i^2 + 2P_{ij}\cdot Q - P_{ij}^2)^2 - 4m_i^2 Q^2}}, \tag{3.29}$$

and

$$\gamma = \frac{2P_{ij}\cdot Q + \beta(P_{ij}^2 - 2P_{ij}\cdot Q - m_i^2)}{2Q^2}. \tag{3.30}$$

From the second condition in Eq. (3.28), we know that the transformation for K, and in particular for all spectators k_i, is given by a Lorentz transformation $k_i^\mu = \Lambda^\mu{}_\nu \tilde{k}_i^\nu$, where the explicit representation is given by [452]

$$\Lambda(K, \widetilde{K})^\mu{}_\nu = g^\mu{}_\nu - \frac{2(K+\widetilde{K})^\mu (K+\widetilde{K})_\nu}{(K+\widetilde{K})^2} + \frac{2K^\mu \widetilde{K}_\nu}{K^2}, \tag{3.31}$$

with

$$\widetilde{K} = Q - \tilde{p}_i. \tag{3.32}$$

Subtraction terms

The dipole terms $\mathcal{D}^{(ijk)}$ in Eq. (2.16) are further decomposed into a diagonal term $W^{(ii,j)}$ and an interference term $W^{(ik,j)}$ according to

$$\mathcal{D}^{(ijk)}_{\tilde{s}_1\tilde{s}_2} = W^{(ii,j)}_{\tilde{s}_1\tilde{s}_2}\delta_{ik} + W^{(ik,j)}_{\tilde{s}_1\tilde{s}_2}(1-\delta_{ik}), \tag{3.33}$$

where the spin dependence is written explicitly with the spin indices $\tilde{s}_{1/2}$. We use the axial gauge for external gluons with the reference vector Q such that the completeness relation takes the following form

$$\begin{aligned} D(p,Q)^{\mu\nu} &= \sum_s \varepsilon^\mu(p,s,Q)^*\varepsilon^\nu(p,s,Q) \\ &= -g^{\mu\nu} + \frac{p^\mu Q^\nu + Q^\mu p^\nu}{p\cdot Q} - \frac{Q^2 p^\mu p^\nu}{(p\cdot Q)^2}, \end{aligned} \tag{3.34}$$

where in the following we suppress the dependence on Q in $\varepsilon^\mu(p,s) = \varepsilon^\mu(p,s,Q)$. On the other hand, we use a different axial gauge for internal gluons where we choose a light-like vector n_i as our reference vector. For final state dipoles, n_i is defined as

$$n_i = Q - \frac{Q^2}{Q\cdot\tilde{p}_i + \sqrt{(Q\cdot\tilde{p}_i)^2 - Q^2 m_i^2}}, \tag{3.35}$$

and the numerator of the gluonic propagator reduces to

$$D^{\mu\nu}(P,n_i) = -g^{\mu\nu} + \frac{P^\mu n_i^\nu + P^\nu n_i^\mu}{P\cdot n_i}. \tag{3.36}$$

The diagonal and interference terms, $W^{(ii,j)}$ and $W^{(ik,j)}$, are defined as

$$\begin{aligned} W^{(ii,j)}_{\tilde{s}_1\tilde{s}_2} &= \sum_{s_i,s_j} v^{(ij)}_{\tilde{s}_1 s_i s_j}\left(v^{(ij)}_{\tilde{s}_2 s_i s_j}\right)^*, \\ W^{(ik,j)}_{\tilde{s}_1\tilde{s}_2} &= \sum_{s_i,s_j} v^{(ij),eik}_{\tilde{s}_1 s_i s_j}\left(v^{(kj),eik}_{\tilde{s}_2 s_i s_j}\right)^*. \end{aligned} \tag{3.37}$$

where $v^{(ij)}$ are splitting functions, which are obtained by factorizing the divergent matrix element $\mathcal{M}^{div}_{n+1}$ in the singular $p_i\cdot p_j \to 0$ according to

$$\mathcal{M}^{div}_{n+1,s_i s_j} = \sum_{\tilde{s}_i=\pm} \mathcal{H}_{n,\tilde{s}_i}\, v^{(ij)}_{\tilde{s}_i s_i s_j}\mathbf{T}_{ij}, \tag{3.38}$$

where $\mathcal{H}_n$ is the corresponding LO matrix element of the underlying Born process that is obtained from the combination $i+j=\widetilde{ij}$. The spin indices of the $2\to n+1$ and the $2\to n$ processes are distinguished by a tilde, similar to the case of the momenta. The splittings functions in QCD for the three possible splittings $q\to qg$, $g\to q\bar{q}$ and $g\to gg$ are given for final state dipoles by

$$\begin{aligned} v^{(ij)}_{\tilde{s}_i s_i s_j}(q\to qg) &= \frac{\sqrt{4\pi\alpha_s}}{P_{ij}^2 - m_i^2}\frac{\bar{u}(\tilde{p}_i,\tilde{s}_i)\not{n}_i(\not{P}_{ij}+m_i)\not{\varepsilon}(p_j,s_j)u(p_i,s_i)}{2\tilde{p}_i\cdot n_i}, \\ v^{(ij)}_{\tilde{s}_i s_i s_j}(g\to q\bar{q}) &= -\frac{\sqrt{4\pi\alpha_s}}{P_{ij}^2}\varepsilon^\mu(\tilde{p}_i,\tilde{s}_i)D_{\mu\nu}(P_{ij},n_i)\bar{u}(p_j,s_j)\gamma^\nu u(p_i,s_i), \\ v^{(ij)}_{\tilde{s}_i s_i s_j}(g\to gg) &= \frac{\sqrt{4\pi\alpha_s}}{P_{ij}^2}D^{\mu\nu}(P_{ij},n_i)G_{\nu\rho\sigma}\varepsilon_\mu(\tilde{p}_i,\tilde{s}_i)\varepsilon^\rho(p_i,s_i)^*\varepsilon^\sigma(p_j,s_j)^*, \end{aligned} \tag{3.39}$$

where $G_{\nu\rho\sigma}$ is the triple gluon vertex given by

$$G_{\nu\rho\sigma} = g_{\nu\rho}(p_j - p_i)_\sigma + g_{\rho\sigma}(p_i + P_{ij})_\nu + g_{\sigma\nu}(-P_{ij} - p_j)_\rho. \tag{3.40}$$

The second splitting function in Eq. (3.39) contains only collinear singularities, while the other two splitting functions contain collinear and/or soft singularities. For the interference terms $W^{(ik,j)}$, the eikonal approximation is used for simplification, since only soft singularities are allowed in this case, because triple collinear configurations are removed by the jet function in NLO calculations. The eikonal approximation of the splitting functions is given by

$$v^{(ij),eik}_{\tilde{s}_i s_i s_j} = \sqrt{4\pi\alpha_s}\,\delta_{\tilde{s}_i s_i}\frac{\varepsilon(p_j, s_j)^* \cdot p_i}{p_i \cdot p_j}, \tag{3.41}$$

where its form is independent of the actual QCD splitting. Since the interference term $W^{(ik,j)}$ contains only soft singularities, the momentum mapping for this term can be chosen from either the $\widetilde{ij} \to i + j$ or the $\widetilde{kj} \to k + j$ splittings. This ambiguity is fixed by rewriting $W^{(ik,j)}$ as a linear combination of terms that are calculated with the two different momentum mappings as

$$W^{(ik,j)} = A_{ik}W^{(ik,j)}_{[i]} + A_{ki}W^{(ik,j)}_{[k]}, \tag{3.42}$$

where the subscript $[i/k]$ indicates which momentum mapping is used and the coefficients A_{ik} and A_{ki} are normalized to

$$A_{ik} + A_{ki} = 1. \tag{3.43}$$

We use the definition of A_{ik} introduced in Ref. [453], where the coefficients are given by

$$A_{ik} = \frac{p_i \cdot p_j\, p_k \cdot p_j}{2p_i \cdot D(p_j, Q) \cdot p_k}\left(\frac{p_i \cdot D(p_j, Q) \cdot p_i}{(p_i \cdot p_j)^2} - A'_{ik}\frac{\hat{P}_{ik} \cdot D(p_j, Q) \cdot \hat{P}_{ik}}{(p_i \cdot p_j\, p_k \cdot p_j)^2}\right), \tag{3.44}$$

with the vector

$$\hat{P}_{ik} = (p_i \cdot p_j)p_k - (p_k \cdot p_j)p_i, \tag{3.45}$$

and the coefficients A'_{ik} are defined as

$$A'_{ik}(\{p\}_{n+1}) = \frac{p_k \cdot p_j\, p_i \cdot Q}{p_k \cdot p_j\, p_i \cdot Q + p_i \cdot p_j\, p_k \cdot Q}, \tag{3.46}$$

which are normalized to $A'_{ik} + A'_{ki} = 1$.

Subtraction terms in the random polarization method

The use of the random polarization method in the Nagy-Soper subtraction leads only to modifications to the dipoles terms required for the actual subtraction, while the integrated dipoles are untouched. In this case, the polarization vectors of fermions and gluons of the particle p_i and p_j in the splitting functions in Eq. (3.39) are replaced by a linear combination of helicity eigenstates as defined in Eq. (2.17) and the polarization sums are removed in the definition of the diagonal and interference terms in Eq. (3.37). In addition,

the eikonal approximation of the splittings functions in Eq. (3.41) for spin eigenstates has to be generalised to the random polarization method, which leads to

$$v_{\tilde{s}_i}^{(ij),eik}(\phi_i,\phi_j) = \sqrt{4\pi\alpha_s}\left(e^{i\phi_i}\delta_{\tilde{s}_i,+} + e^{-i\phi_i}\delta_{\tilde{s}_i,-}\right)\frac{\varepsilon(p_j,\phi_j)^*\cdot p_i}{p_i\cdot p_j}. \tag{3.47}$$

The interference term $W^{(ik,j)}$ in the random polarization method can then be written as

$$\begin{aligned} W_{\tilde{s}_1\tilde{s}_2}^{(ik,j)}(\phi_i,\phi_j) = 4\pi\alpha_s &\frac{\varepsilon(p_j,\phi_j)^*\cdot p_i}{p_i\cdot p_j}\frac{\varepsilon(p_j,\phi_j)\cdot p_k}{p_k\cdot p_j} \\ &\times\left(\delta_{\tilde{s}_1,+}\delta_{\tilde{s}_2,+} + \delta_{\tilde{s}_1,-}\delta_{\tilde{s}_2,-} + e^{2i\phi_i}\delta_{\tilde{s}_1,+}\delta_{\tilde{s}_2,-} + e^{-2i\phi_i}\delta_{\tilde{s}_1,-}\delta_{\tilde{s}_2,+}\right), \end{aligned} \tag{3.48}$$

where the first two terms in the brackets can be combined to $\delta_{\tilde{s}_1\tilde{s}_2}$, which corresponds to the usual interference term $W^{(ik,j)}$ and the additional two terms are required for the correct subtraction, where similar spurious terms appear in the squared real emission matrix element. However, these terms integrate exactly to zero, because of the phase factor of $e^{\pm 2i\phi}$. The interference terms $W^{(ik,j)}$ are divided again into two contributions that are obtained with different momentum mappings. In this case, the polarized coefficients A_{ik} are required, which are given by [453]

$$A_{ik} = \frac{p_i\cdot p_j\, p_k\cdot p_j}{\varepsilon_j^*\cdot p_i\,\varepsilon_j\cdot p_k + \varepsilon_j^*\cdot p_k\,\varepsilon_j\cdot p_i}\left(\frac{\varepsilon_j^*\cdot p_i\,\varepsilon_j\cdot p_i}{(p_i\cdot p_j)^2} - A'_{ik}\frac{\varepsilon_j^*\cdot \hat{P}_{ik}\,\varepsilon_j\cdot \hat{P}_{ik}}{(p_i\cdot p_j\, p_k\cdot p_j)^2}\right), \tag{3.49}$$

where A'_{ik} are the same coefficients as before and are defined in Eq. (3.46), and ε_j is the polarization vector of the gluon (photon) p_j in the random polarization method.

Integrated dipoles

For the calculation of the integrated dipoles we use the spin-averaged versions of the diagonal term $W^{(ii,j)}$ and the interference term $W^{(ik,j)}$ and follow the approach of Ref. [454] for further simplifications. In $d = 4-2\epsilon$ dimensions, the spin-averaged terms are given by

$$\begin{aligned} \overline{W}^{(ii,j)} &= F_i\sum_{\tilde{s}_i=\pm} W_{\tilde{s}_i\tilde{s}_i}^{(ii,j)}, \\ \overline{W}^{(ik,j)} &= F_i\sum_{\tilde{s}_i=\pm} W_{\tilde{s}_i\tilde{s}_i}^{(ik,j)}, \end{aligned} \tag{3.50}$$

where F_i is given by $1/2$ if the splitting parton $\tilde{p}_i$ is a quark and $1/(2(1-\epsilon))$ if it is a gluon. Furthermore, the diagonal and interference terms in Eq. (3.33) are rewritten by using

$$(\mathbf{T}_i\cdot\mathbf{T}_i) = -\sum_{k\neq i}\frac{1}{2}\left[(\mathbf{T}_i\cdot\mathbf{T}_k) + (\mathbf{T}_k\cdot\mathbf{T}_i)\right], \tag{3.51}$$

so that the diagonal and interference terms for a single momentum mapping can be cast into the following form

$$\frac{1}{2}\left[(\mathbf{T}_i\cdot\mathbf{T}_k) + (\mathbf{T}_k\cdot\mathbf{T}_i)\right]\left[\overline{W}^{(ii,j)} - \overline{W}^{(ik,j)}\right]. \tag{3.52}$$

Following [454], the term in the last brackets is further divided into

$$\overline{W}^{(ii,j)} - \overline{W}^{(ik,j)} = \underbrace{\left(\overline{W}^{(ii,j)} - \overline{W}^{(ii,j),eik}\right)}_{\mathcal{D}_{ii}} + \underbrace{\left(\overline{W}^{(ii,j),eik} - \overline{W}^{(ik,j)}\right)}_{\mathcal{I}_{ik}}, \tag{3.53}$$

where the first term $\mathcal{D}_{ii}$ can only have collinear singularities by construction, while the second term $\mathcal{I}_{ik}$ can contain soft and/or collinear singularities. The introduction of the two new terms $\mathcal{D}_{ii}$ and $\mathcal{I}_{ik}$ has two advantages. First of all, the calculation of the integrated dipoles for the first term is drastically simplified, since only collinear divergences can appear. Second, the term $\mathcal{I}_{ik}$ can be simplified to the following universal form

$$\mathcal{I}_{ik} = 4\pi\alpha_s A'_{ik} \frac{-((p_j \cdot p_k)p_i - (p_i \cdot p_j)p_k)^2}{(p_i \cdot p_j)^2 (p_j \cdot p_k)^2}, \tag{3.54}$$

which does not depend on the actual QCD splitting.

The phase space of the $n+1$ process is factorized into the following form

$$\mathrm{d}\Phi_{n+1}(p_i, p_j, k_1, ...; Q) = \mathrm{d}\Phi_n(\tilde{p}_i, \tilde{k}_1, ...; Q) \times \mathrm{d}\xi_{fin}, \tag{3.55}$$

where $\mathrm{d}\Phi_n(\tilde{p}_i, \tilde{k}_1, ...; Q)$ is the phase space of the mapped momentum set and $\mathrm{d}\xi_{fin}$ is the integral measure for the integrated dipoles that is given by

$$\mathrm{d}\xi_{fin} = \frac{\mathrm{d}P_{ij}^2}{2\pi} \left(\frac{\lambda(Q^2, P_{ij}^2, K^2)}{\lambda(Q^2, m_i^2, K^2)}\right)^{\frac{d-3}{2}} \mathrm{d}\Phi_2(p_i, p_j, P_{ij}) \tag{3.56}$$

where $\mathrm{d}\Phi_2(p_i, p_j, P_{ij})$ is the two-particle phase space involving two angular integration variables and $\lambda(x, y, z)$ is the usual Källen function defined as

$$\lambda(x, y, z) = x^2 + y^2 + z^2 - 2xy - 2xz - 2yz. \tag{3.57}$$

The integration is performed in the center-of-mass system (rest frame of Q). The orientation is chosen such that the directions of $\tilde{p}_i$ and the z-axis coincide. The x-axis is fixed by requiring that the spatial direction of the spectator parton $\tilde{p}_k$ lies on the x-z plane. The azimuthal angle integration is performed with the variable ϕ_j, which is the azimuthal angle between the parton p_j and the x-z plane as shown in Fig. 3.1. The collinear limit is parametrized with the variable $\cos\theta_j$, which is the angle between the z-axis and p_j, and thus coincides with the angle between p_j and $\tilde{p}_i$ in this frame. Additionally, in the collinear limit with $\tilde{p}_i \approx p_i + p_j$, we get $\cos\theta_j \approx \cos\theta_{ij}$, where the latter angle is the angle between p_i and p_j. To isolate soft and collinear limits and thus to simplify the calculation, the integration variable P_{ij}^2 is replaced by the dimensionless variable $e = \bar{E}_j / \bar{E}_j^{max}$ with

$$\bar{E}_j = \frac{\sqrt{Q^2}(P_{ij}^2 - m_i^2)}{P_{ij}^2 - m_i^2 + 2\sqrt{Q^2}(\tilde{p}_i^0 - \cos\theta_j |\vec{\tilde{p}}_i|)}, \tag{3.58}$$

where the maximum of $\bar{E}_j$ is obtained by the replacement $P_{ij}^2 \to P_{ij,max}^2$. Thus, we end up with the following three integration variables

$$\begin{aligned} e &\in [0, 1], \\ c \equiv \cos\theta_j &\in [-1, 1], \\ \phi \equiv \cos\phi_j &\in [0, 2\pi]. \end{aligned} \tag{3.59}$$

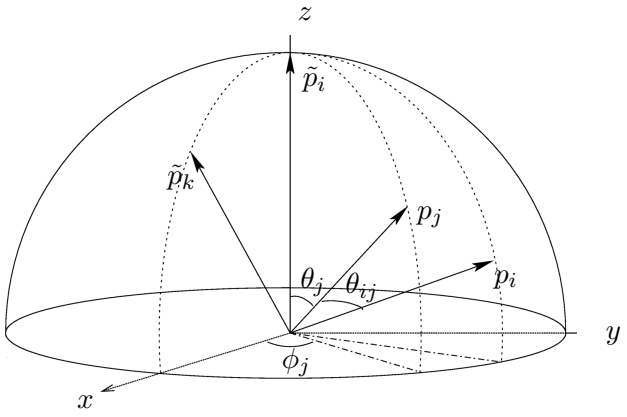

Figure 3.1: *Parameterization of the angular variables for the final-state dipoles. Figure taken from Ref. [406].*

The general strategy of the integration over the unresolved phase space is as follows. For example in the case of $\mathcal{I}_{ik}$ defined in Eq. (3.54), the integration is written as

$$I_{ik} \equiv \int \mathrm{d}\xi_{fin} \mathcal{I}_{ik} = \int \mathrm{d}e\, \mathrm{d}c\, \mathrm{d}\phi\, J(e,c,\phi)\, I_{ik}(e,c,\phi), \tag{3.60}$$

where $J(e,c,\phi)$ is obtained from the Jacobian in Eq. (3.56) and the variable transformation $P_{ij}^2 \to e$. The azimuthal integration is performed analytically and the pole structure is factored out in the following form

$$I_{ik} = \int \mathrm{d}e\, \mathrm{d}c \frac{\mathcal{N}_{ik}^{d=4-2\epsilon}(e,c)}{(1-c)^{1+\epsilon}\, e^{1+2\epsilon}}, \tag{3.61}$$

where the superscript $d = 4 - 2\epsilon$ indicates the number of space-time dimensions. In the next step, the integrand is rewritten by inserting suitable counterterms, so that the whole integral can either be solved by simple analytic integrals of by numerical integration. In particular, I_{ik} is rewritten as

$$\begin{aligned} I_{ik} = & \int \mathrm{d}e\, \mathrm{d}c \frac{1}{(1-c)\, e} \left[\mathcal{N}_{ik}^{d=4}(e,c) - \mathcal{N}_{ik}^{d=4}(0,c) - \mathcal{N}_{ik}^{d=4}(e,1) + \mathcal{N}_{ik}^{d=4}(0,1)\right] \\ & + \int \mathrm{d}e\, \mathrm{d}c \frac{1}{(1-c)^{1+\epsilon}\, e^{1+2\epsilon}} \left[\mathcal{N}_{ik}^{d=4-2\epsilon}(0,c) - \mathcal{N}_{ik}^{d=4-2\epsilon}(0,1)\right] \\ & + \int \mathrm{d}e\, \mathrm{d}c \frac{1}{(1-c)^{1+\epsilon}\, e^{1+2\epsilon}} \left[\mathcal{N}_{ik}^{d=4-2\epsilon}(e,1) - \mathcal{N}_{ik}^{d=4-2\epsilon}(0,1)\right] \\ & + \int \mathrm{d}e\, \mathrm{d}c \frac{1}{(1-c)^{1+\epsilon}\, e^{1+2\epsilon}} \left[\mathcal{N}_{ik}^{d=4-2\epsilon}(0,1)\right], \end{aligned} \tag{3.62}$$

where the first line is finite by construction and is calculated numerically in our approach during the phase-space integration. Since in general collinear singularities are still included in $\mathcal{N}_{ik}^{d=4-2\epsilon}(0,c)$ in the second line, again a suitable counterterm is introduced to regularize these singularities. The calculation is then performed by first solving the simple integral over e, expanding the results up to ϵ^0 and then solving the integration over c. Similar

strategies are also applied for the remaining terms in the third and fourth line, so that the final result can be written as

$$I_{ik} = \frac{1}{\epsilon^2} G_{ik}^{(2)} + \frac{1}{\epsilon} G_{ik}^{(1)} + \int \mathrm{d}e \, \mathrm{d}c \, \mathcal{G}_{ik}^{(0)} \tag{3.63}$$

Phase-space restriction on subtraction terms

To minimize the number of subtraction terms required in the calculation, it is possible to restrict the phase-space of the dipoles in the non-singular regions. While in the Catani-Seymour subtraction scheme this is done by directly restricting the integration limits of the integration variables [180, 455, 456], an alternative method is used in the Nagy-Soper subtraction scheme which is directly applicable in this semi-numerical approach. In particular, we define the variable [167]

$$e^{-t} = \frac{2p_i \cdot p_j}{2Q \cdot P_{ij} - P_{ij}^2 + m_i^2} = \frac{2p_i \cdot p_j}{2Q \cdot \tilde{p}_i}, \tag{3.64}$$

where t is the shower time, which was proposed in Ref. [457] as a new ordering variable for parton showers. This variable has the properties that in singular limits we have $e^{-t} \to 0$, and that e^{-t} is smaller than one for final-state dipoles, but can be larger than one for initial-state dipoles. The phase-space restriction is then implemented through the condition

$$e^{-t} < \alpha, \tag{3.65}$$

where we usually choose values for α in the range $[0.01, 1.00]$ and all results in the next chapters are generated with $\alpha = 0.01$. In addition, this phase-space restriction can also be used to cross-check the calculation of the real corrections, sine the final result (**RS**+**I**+**KP**) should not depend on α. Usually this is realized by a second calculation where we set $\alpha = 1.00$. The implementation of this phase-space restriction is straightforward and can directly be applied for all dipole terms in the real subtracted contributions (**RS**). Also in the calculation of the integrated dipoles this can be easily included by inserting the Heaviside function $\theta(\alpha - e^{-t})$ in the first term in the first line ($\mathcal{N}_{ik}^{d=4}(e,c)$) in Eq. (3.62). Since the integration in this case is done numerically anyway, the inclusion of this phase-space restriction does not lead to any further complications.

Subtraction terms in the NWA

Next, we discuss the new modifications in the Nagy-Soper subtraction for calculations involving internal on-shell resonances as required in the NWA. Such an calculation can be divided into a production stage of unstable particles and its decays, which again can include subsequent decays of other unstable particles. In top-quark processes, we usually encounter the following decay chain

$$pp \to t(\to W^+(\to \ell^+ \nu_\ell)\, b)\, \bar{t}(\to W^-(\to \ell^- \bar{\nu}_\ell)\, \bar{b}), \tag{3.66}$$

where we start with the production of a top-quark pair, where each top quark further decays into a bottom quark and an unstable W gauge boson. In this example, the two W bosons decay into lepton-neutrino pairs. Thus, we have in total five sub-processes, namely the production process and four decay processes. The production does not require any

fundamental modifications with respect to the original formulation. In particular, when an unstable particle, in this case $t/\bar{t}$ or $W^{\pm}$ in subsequent decays in the calculation of EW corrections, the polarized diagonal ($W^{(ii,j)}$) and interference terms ($W^{(ik,j)}$) are replaced by the corresponding spin-averaged versions $\overline{W}^{(ii,j)}$ and $\overline{W}^{(ik,j)}$ given in Eq. (3.50) in $d = 4$ dimensions. We perform this replacement because the spin over the unstable particles is already summed up in the matrix elements, and due to the mass of the unstable particles, only soft singularities are present for which the spin correlations are not required. For simplicity, we replace $\overline{W}^{(ii,j)}$ by $\overline{W}^{(ii,j),eik}$ when the unstable particle is a massive gauge boson ($W^{\pm}$). This contribution is only necessary for the calculation of EW corrections, where photons can be radiated off the W boson in the top-quark decays. The momentum of unstable particles is generally affected by the momentum mapping in the subtraction terms which has to be transported to their decay products. Following Ref. [12], this is done by considering that the momentum of an unstable particle before and after the momentum mapping is the same in its rest frame of e.g. an unstable top quark. Thus, the top-quark momentum after the mapping is connected to the original momentum by

$$\tilde{p}_t = (\tilde{\Lambda}^{-1}\Lambda)p_t \tag{3.67}$$

where $\Lambda/\tilde{\Lambda}$ transforms the top-quark momentum into its rest frame according to

$$\Lambda p_t = p_t^{\mathrm{CM}} = \tilde{p}_t^{\mathrm{CM}} = \tilde{\Lambda}\tilde{p}_t. \tag{3.68}$$

Thus, the same Lorentz transformation that connects $\tilde{p}_t$ and p_t is also applied to all its decay products.

Next, we turn to decay processes, where the mother particle of the decay process has to be generally included in the subtraction like in radiative of top-quark decays ($t \to W^+bg$), where gluons can be radiated off top quarks. In analogy to the original formulation, we define the total momentum of the decay process as Q_{dec} given by

$$Q_{\mathrm{dec}} = \sum_{l=1}^{n_{\mathrm{dec}}} p_l \tag{3.69}$$

where the summation runs over all particles participating in the decay process. In order to reuse as much as possible from the original formulation, we replace everywhere, in the momentum mapping and in the subtraction terms, Q by Q_{dec}. On the one hand, this guarantees that the momentum of the mother particle is not changed under momentum mapping and on other hand, the gauge dependence of the subtraction terms is properly taken into account by changing the gauge of the polarization vectors of gluons/photons by choosing Q_{dec} as the reference vector instead of Q. In practice, we perform a gauge transformation to the polarization vectors entering the subtraction terms, which is given by

$$\epsilon^{\mu}(p,s,Q) \to \epsilon^{\mu}(p,s,Q_{\mathrm{dec}}) = \epsilon^{\mu}(p,s,Q) - \frac{Q_{\mathrm{dec}}\cdot\epsilon(p,s,Q)}{Q_{\mathrm{dec}}\cdot p}p^{\mu}. \tag{3.70}$$

In this way, all integrated dipoles of the original formulation can be directly reused and do not need to be recalculated. In order to take into account IR singularities related to the massive mother particle in the initial state, we do exclude the mother particle from the list of possible emitters and only take it into account as a possible spectator particle.

We use the same subtraction terms, leading to the same integrated dipoles, as in the original formulation when the spectator particle k is not the mother particle. In the other case, where the spectator particle k is the mother particle, the interference term $W^{(ik,j)}$ is replaced by $W^{(ik,j)}_{\text{dec}}$ which we define as

$$W^{(ik,j)}_{\text{dec}} = W^{(ik,j)} + W^{(ki,j)} - W^{(kk,j),eik}. \tag{3.71}$$

This substitution takes properly into account all soft singularities related to radiation off the mother particle. However, it turns out that due to the gauge choice of the polarization vectors of gluons/photons, the dipole term $W^{(ik,j)}_{\text{dec}}$ vanishes because of $Q_{\text{dec}} \cdot \epsilon(p_j, s, Q_{\text{dec}}) = 0$. Nevertheless, it can be easily shown that all soft singularities are properly taken into account by performing a similar calculation as in Eq. (3.53), but in this case for the polarized subtraction terms, which then leads to

$$W^{(ii,j)}_{\tilde{s}_1\tilde{s}_2} - W^{(ik,j)}_{\text{dec},\tilde{s}_1\tilde{s}_2} = \underbrace{(W^{(ii,j)}_{\tilde{s}_1\tilde{s}_2} - W^{(ii,j),eik}_{\tilde{s}_1\tilde{s}_2})}_{\widetilde{\mathcal{D}}_{ii,\tilde{s}_1\tilde{s}_2}} + \underbrace{(W^{(ii,j),eik}_{\tilde{s}_1\tilde{s}_2} - W^{(ik,j)}_{\text{dec},\tilde{s}_1\tilde{s}_2})}_{\delta_{\tilde{s}_1\tilde{s}_2}\mathcal{I}_{ik,\text{dec}}}, \tag{3.72}$$

where again the first term $\widetilde{\mathcal{D}}_{ii}$ can only have collinear singularities by construction while the latter term $\mathcal{I}_{ik,\text{dec}}$ contain in general collinear and/or soft singularities. The latter term can be simplified to

$$\mathcal{I}_{ik,\text{dec}} = \frac{4\pi\alpha_s}{(p_i \cdot p_j)^2 (p_j \cdot p_k)^2} \left[\hat{P}_{ik} \cdot D(p_j, ...) \cdot \hat{P}_{ik}\right], \tag{3.73}$$

with $\hat{P}_{ik}$ defined in Eq. (3.45) and $D(p_j, ...)$ is the spin summation over the polarization vectors of gluons/photons, so that it can be written as

$$D(p_j, ...)^{\mu\nu} = -g^{\mu\nu} + \text{gauge terms}, \tag{3.74}$$

where the gauge terms are proportional to either p_j^μ or p_j^ν. As already indicated in Eq. (3.73), it turns out that $\mathcal{I}_{ik,\text{dec}}$ is independent of the gauge, because p_j is orthogonal to $\hat{P}_{ik}$ ($p_j \cdot \hat{P}_{ik} = 0$) and thus all gauge terms vanish. This shows that all soft singularities are properly taken into account, even though in this gauge choice $W^{(ik,j)}_{\text{dec}}$ is exactly zero. The calculation of the integrated dipoles is then conceptually identical as the in the original formulation. The spin average of the first term in Eq. (3.72) ($\widetilde{\mathcal{D}}_{ii}$) leads directly to the already known collinear terms $\mathcal{D}_{ii}$ from Eq. (3.53). For the latter term, $\mathcal{I}_{ik,\text{dec}}$, the calculation has to be performed from scratch following the semi-numerical approach. In particular, after performing the spin average, this term then leads to

$$\mathcal{I}_{ik,dec} = 4\pi\alpha_s \frac{-((p_j \cdot p_k)p_i - (p_i \cdot p_j)p_k)^2}{(p_i \cdot p_j)^2 (p_j \cdot p_k)^2}, \tag{3.75}$$

which is identical to $\mathcal{I}_{ik}$ in Eq. (3.54) with the replacement $A'_{ik} \to 1$. The new integrated dipole is implemented for massive and massless emitters, where the massive version can used for e.g. gluon radiation off massive bottom quarks or photon radiation off $W^\pm$ gauge bosons in top-quark decays.

Finally, all dipoles in the production stage or in the decay processes are taken into account in the phase-space generation through additional channels for each different splitting pair (i, j). The general strategy is explained in Ref. [109] for the Catani-Seymour subtraction scheme, which was later extended for the Nagy-Soper subtraction [406] in HELAC-DIPOLES. For calculations in the NWA, the phase-space integration is performed independently for each subprocess (production process and decay processes) with a separate instance of KALEU. Therefore, the additional channels for the dipole contributions are constructed individually for each instance. For example, considering the process

$$gg \to t(\to W^+(\to \ell^+\nu_\ell)\, bg)\, \bar{t}(\to W^-(\to \ell^-\bar{\nu}_\ell)\, \bar{b})\, g, \tag{3.76}$$

where the gluons are radiated from different subprocesses, then additional channels for the dipoles are constructed for the production process $gg \to t\bar{t}g$ and the decay process $t \to W^+bg$, separately. In general, the additional dipole channels in decay processes lead to only small improvements, while they are essential for an efficient phase-space integration in the production process.

3.2.2 QED-like subtraction

In the following we describe the extension of the Catani-Seymour and Nagy-Soper subtraction schemes for calculations involving QED-like singularities involving a photon. Starting from the definition of the dipole contribution in QCD of $\mathcal{A}^D$ in Eq. (2.15), the QED-like version for additional photon radiation is obtained by the substitution of

$$(\mathbf{T}_{ij} \cdot \mathbf{T}_k) \to (\mathbf{Q}_{ij} \cdot \mathbf{Q}_k)\,, \tag{3.77}$$

where $\mathbf{Q}_k$ are charge operators with a relative minus sign for initial- and final-state particles, so that the charge conservation is fulfilled and can be written as

$$\sum_k \mathbf{Q}_k = 0. \tag{3.78}$$

Additionally, we obtain

$$\sum_{k \neq ij} \mathbf{Q}_{ij}\mathbf{Q}_k = -\mathbf{Q}_{ij}^2, \tag{3.79}$$

which guarantees the correct collinear limit. The same replacement is also used in the case of initial-state splittings, where a photon splits into a fermion-antifermion pair ($\gamma \to q\bar{q}$) as shown in the lower fermion line on the left in Figure 3.2. On the other hand, for the $q \to \gamma q$ splitting, as shown in the upper fermion line on the left in the same figure, we have the case where the splitting particle ($\tilde{p}_i$) is a photon with $Q_{ij} = 0$. Therefore, we perform the following replacement of the color operators instead

$$(\mathbf{T}_{ij} \cdot \mathbf{T}_k) \to -w_k\, \mathbf{Q}_i^2, \tag{3.80}$$

where the weights w_k are normalized to $\sum_k w_k = 1$. The weights can be chosen arbitrarily, e.g. each spectator particle can be chosen with the same weight. Instead, we simply set the weights to $w_k = \delta_{kk_0}$, which means that we choose exactly one spectator particle. Since the calculation of the real subtracted part and the integrated dipoles are done independently, one has to make sure that the same spectator is used in both cases, because in

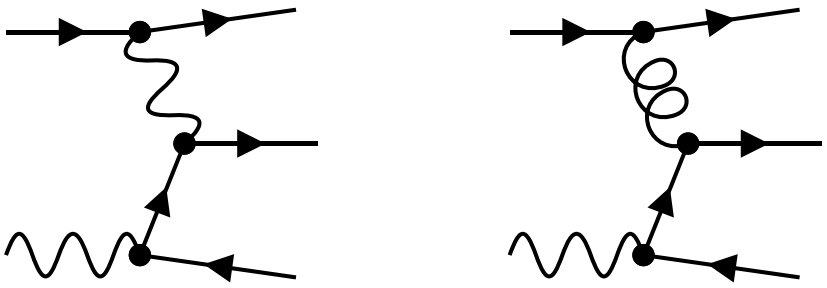

Figure 3.2: *Example Feynman diagrams for the $q\gamma \to t\bar{t}q$ process at order $\mathcal{O}(g^3)$ (left) and $\mathcal{O}(gg_s^2)$ (right).*

general the momentum mapping as well as the dipole terms $\mathcal{D}^{(ijk)}$ depend on the spectator particle and thus could lead to mismatches if different spectators are chosen in both parts. In the Nagy-Soper subtraction scheme, this ambiguity is not present, because the momentum mapping and the dipole term $\mathcal{D}^{(ijk)}$ for (initial-state) collinear singularities are independent of the spectator particle k. The QED dipole terms are obtained directly from the QCD ones in HELAC-DIPOLES by simple substitutions of the color factors, which are set to appropriate values whether the QCD or QED version is required. The program is able to handle QCD and QED-like singularities simultaneously. This is required in the calculation of subleading NLO corrections, where subprocesses such as the $q\gamma \to t\bar{t}q$ process at $\mathcal{O}(\alpha_s^2\alpha)$, shown on the right in Figure 3.2, are present. In this case, initial-state QCD and QED singularities are present due to the $q \to gq$ and the $\gamma \to q\bar{q}$ splittings. This is also required, when using a realistic photon isolation criterion, where the collinear quark-photon singularities have to be subtracted from the real matrix element. In addition, the singular structure of a subprocess can differ at different orders of α_s and α. The two Feynman diagrams in Figure 3.2 correspond to the $q\gamma \to t\bar{t}q$ process, but for different orders in α_s and α. In particular, the square of the left Feynman diagram contributes to $\mathcal{O}(\alpha^3)$ and of the right Feynman diagram to $\mathcal{O}(\alpha_s^2\alpha)$. Furthermore, the two Feynman diagrams differ only by a gluon/photon connecting the two fermion lines. Therefore, the left diagram contains only QED singularities, while the right diagrams contains QED and QCD singularities, where the $q \to \gamma q$ splitting is replaced by $q \to gq$. Furthermore, it turns out that $q\gamma \to t\bar{t}q$ at $\mathcal{O}(\alpha_s\alpha^2)$, which corresponds to the interference of contributions from the left and right Feynman diagrams, is IR finite for $q \neq b$ for a diagonal CKM matrix, which simply follows from the fact that $q\bar{q} \to t\bar{t}$ vanishes at $\mathcal{O}(\alpha_s\alpha)$ due to color algebra, and that all collinear singularities are proportional to the underlying Born matrix element. Therefore, no subtraction scheme is required for this specific contribution, and the naive use of it can reduce the efficiency of the phase-space integration. This is related to the fact, that in general, like in the Catani-Seymour subtraction scheme, the dipole terms and the phase-space mapping depend on the spectator particle k, so that the whole subtraction term is only proportional to the underlying Born matrix element in the exact collinear limit, which would vanish in this case. Away from the collinear limit, the complete subtraction term is not proportional to the Born matrix element, which means that a finite contribution is subtracted in the real subtracted calculation and is added back again in

the integrated dipoles. As mentioned before, in the Nagy-Soper subtraction scheme the initial-state collinear subtraction terms and the momentum mapping do not depend on the spectator particle, and thus the correspinding counterterm is always proportional to the underlying Born matrix element. Therefore, we do not encounter the possible efficiency reduction in the phase-space integration since the counterterm vanishes also away from the collinear limit in this case. In the Catani-Seymour subtraction scheme, it is possible to redefine the dipole terms for such initial-state singularities by choosing exactly one spectator particle and replacing the color/charge correlator by a color/charge factor. In this case, the corresponding counterterm is then proportional to the underlying Born matrix element and the corresponding counterterm for such initial-state collinear singularities vanishes if the underlying Born matrix element is exactly zero.

In order to avoid the construction of unnecessary dipoles, we have implemented a *dipole cleaner*, which filters certain dipoles that do not pass the event selection (e.g. number of tagged b-jets) or that a dipole is not possible at a certain order in α_s and α. The calculation is organized in such a way that either only one contribution is calculated at a specific order in α_s and α, or alternatively all possible orders in α_s and α for a process are calculated at once in a single run. The latter method is convenient for the calculation of the complete NLO corrections, where various orders in α_s and α are present, while the first method can be used if e.g. only the NLO QCD corrections are calculated. The calculation of the QCD and QED-like integrated dipoles in the **I** and **KP** operator can be done simultaneously. In general, we can again choose which orders are calculated in α_s and α and whether either QCD or QED-like or both types of dipoles are calculated at the same time. Furthermore, the internal reweighting to additional scale configurations as well as the information stored in the LHEFs are extended to take into account the multiple orders in α_s and α and the different QCD and QED-like dipoles, which requires a lot of additional bookkeeping during the calculation. Finally, these modifications in HELAC-DIPOLES allow the calculation of QCD and/or EW real corrections at NLO for regular calculations (without internal on-shell resonances) in both subtraction schemes and in nested decay chains (NWA) with the Nagy-Soper subtraction scheme. The implementation of the Catani-Seymour subtraction scheme in the NWA is currently limited to massless emitter in decay processes, but can be extended to massive emitters with the results in Ref. [103].

3.2.3 Photon fragmentation

The use of the fixed-cone isolation or the democratic clustering approach introduces an additional dependence on the photonic energy fraction z_γ in the splitting $q \to q\gamma$, which has to be included in the subtraction terms. In the latter approach, the condition for identifying whether a cluster consists of an isolated photon is also applied to the subtraction terms with the kinematics of the splitting pair before the recombination. Therefore, we need a proxy variable $\tilde{z}_\gamma$ in the subtraction terms, which has the conditions that it reduces to $\tilde{z}_\gamma \to z_\gamma$ in the collinear limit, to $\tilde{z}_\gamma \to 0$ in the soft limit of the photon and is in the range of zero and one. Since $\tilde{z}_\gamma$ describes the photonic energy fraction of the splitting, this variable necessarily depends on the momentum of the real process before the recombination of the two splitting particles, and thus also on the integration variables of the unresolved phase-space integration of the integrated dipoles. The photon isolation is implemented in the dipole subtraction by including the $\tilde{z}_\gamma$ dependence in the jet function. In that case,

the jet function describes the entire event selection starting from the photon isolation condition to the clustering of particles and the final cuts. Therefore, the usual jet function $J_n(\{\tilde{p}\}_n^{(ijk)})$ in the subtraction term is replaced by $J_n(\{\tilde{p}\}_n^{(ijk)}, \tilde{z}_\gamma)$, where we explicitly show the dependence on $\tilde{z}_\gamma$ which is in general a function of the integration variables. In particular, in the democratic clustering approach, we can write the jet function as

$$J_n(\{\tilde{p}\}_n^{(ijk)}, \tilde{z}_\gamma) = J_n(\{\tilde{p}\}_n^{(ijk)}, \tilde{p}_\gamma = \tilde{p}_i)\, \Theta(\tilde{z}_\gamma - z_{\text{cut}}), \tag{3.81}$$

where the Heaviside function comes directly from the isolation condition and ensures that all soft singularities are excluded and that the event is only accepted if the photonic energy fraction is above the minimal value z_{cut}, where the cluster is considered as a photon. In addition, we explicitly indicate that the photon momentum in this case is simply given by the momentum of the combined splitting pair $\tilde{p}_i$. In this photon isolation approach, the jet function is factorized into another jet function that no longer depends on $\tilde{z}_\gamma$, and on a Heaviside function that contains the full $\tilde{z}_\gamma$ dependence. Therefore, in this case, it would be possible to obtain the integrated dipoles by simply restricting the phase space of the integration variables by the Heaviside function.

In the fixed-cone isolation, the momenta of the collinear photon and parton are not recombined. Therefore, the corresponding momenta of the photon $\tilde{p}_\gamma$ and of the parton $\tilde{p}_q$ are given by

$$\begin{aligned} \tilde{p}_\gamma &= \tilde{z}_\gamma \tilde{p}_i, \\ \tilde{p}_q &= (1 - \tilde{z}_\gamma)\tilde{p}_i. \end{aligned} \tag{3.82}$$

Thus, in this case the, jet function can be written as

$$J_n(\{\tilde{p}\}_n^{(ijk)}, \tilde{z}_\gamma) = J_n(\{\tilde{p}\}_n^{(ijk)}, \tilde{p}_\gamma = \tilde{z}_\gamma \tilde{p}_i)\, \Theta(\tilde{z}_\gamma - z_{\text{cut}}(\tilde{p}_i)), \tag{3.83}$$

where the dependence on $\tilde{z}_\gamma$ in the jet function on the right hand side is explicitly shown. The lower limit z_{cut} is obtained by inserting the relations from Eq. (3.82) into the isolation condition in Eq. (2.48), where z_{cut} is general a function of the momentum of the splitting particle $\tilde{p}_i$. Thus, the jet function of the dipoles in the fixed-cone isolation cannot be factorized in a similar way as in the democratic clustering approach.

In the next step we describe the modifications in the Catani-Seymour and the Nagy-Soper subtraction schemes for calculations involving parton-to-photon fragmentation functions and in particular the treatment of the additional dependence on $\tilde{z}_\gamma$. While the calculation of the real subtracted contribution is straightforward, we focus on the complications arising in the integrated dipoles.

Catani-Seymour subtraction scheme

In the Catani-Seymour subtraction scheme, the use of parton-to-photon fragmentation functions was described in detail in Ref. [458] for massless spectators and we closely follow this approach. In particular, we use the standard dipole for final-state emitters with final-state spectators for the $q \to qg$ splitting, which can be easily transferred to the $q \to q\gamma$ splitting as discussed in the last section. We do not include the corresponding dipoles with initial-state spectators to avoid the complications arising from the additional +-distributions of the momentum fraction x of the initial-state partons in the integrated dipoles. Therefore, in analogy to the collinear initial-state QED singularities, we choose

exactly one spectator parton. The photonic energy fraction in this scheme can be identified as

$$\tilde{z}_\gamma = \tilde{z}_j = \frac{p_j \cdot p_k}{p_i \cdot p_k + p_j \cdot p_k} \tag{3.84}$$

which is connected with the usual integration variable by $\tilde{z}_i = 1 - \tilde{z}_\gamma$ [404]. Therefore, the integrated dipole can be written as

$$\begin{aligned}
\mathcal{V}_{q\gamma}^{\text{coll}}(\alpha, \epsilon, z_{\text{cut}}) &= Q_q^2 \int_0^{1-z_{\text{cut}}} \mathrm{d}\tilde{z}_i \, (\tilde{z}_i(1-\tilde{z}_i))^{-\epsilon} \int_0^{\alpha} \mathrm{d}y \, y^{-1-\epsilon}(1-y)^{1-2\epsilon} \\
&\quad \times \left[\frac{2}{1-\tilde{z}_i + y\tilde{z}_i} - (1+\tilde{z}_i) - \epsilon(1-\tilde{z}_i) \right] \\
&= Q_q^2 \int_0^{1-z_{\text{cut}}} \mathrm{d}\tilde{z}_i \left[\frac{1+\tilde{z}_i^2}{1-\tilde{z}_i} \left(-\frac{1}{\epsilon} + \log(\tilde{z}_i(1-\tilde{z}_i)) + \log(\alpha) \right) + \alpha(1+\tilde{z}_i) \right. \\
&\qquad \left. + 1 - \tilde{z}_i - \frac{2}{\tilde{z}_i(1-\tilde{z}_i)} \log\left(\frac{1-\tilde{z}_i + \alpha\tilde{z}_i}{1-\tilde{z}_i} \right) \right],
\end{aligned} \tag{3.85}$$

where the non-singular phase-space region of the y integration is further restricted by α as for the usual Catani-Seymour dipoles introduced in Ref. [455]. The ϵ poles between the integrated dipole and the factorization kernel $\mathbf{\Gamma}^{(0)}_{q\to\gamma}$ in Eq. (2.59) cancel exactly because of

$$P_{q\to\gamma}(\tilde{z}_\gamma) = P_{q\to\gamma}(1-\tilde{z}_i) = \frac{1+\tilde{z}_i^2}{1-\tilde{z}_i}. \tag{3.86}$$

Nagy-Soper subtraction scheme

In the Nagy-Soper subtraction scheme, we write the dipole terms $\mathcal{D}^{(ijk)}$ as

$$\mathcal{D}^{(ijk)}_{\tilde{s}_1\tilde{s}_2} = W^{(ii,j)}_{\tilde{s}_1\tilde{s}_2}\delta_{ik}, \tag{3.87}$$

where we have neglected the interference term $W^{(ik,j)}$ in Eq. (3.33), since all soft singularities are removed by the photon isolation criterion. Therefore, in the calculation of the integrated dipoles, the interference term $\mathcal{I}_{ik}$ in Eq. (3.53) vanishes and the diagonal term $\mathcal{D}_{ii}$ simplifies to

$$\mathcal{D}_{ii} = \overline{W}^{(ii,j)}. \tag{3.88}$$

We use the same integration variables as in the original formulation for the calculation of the integrated dipole, and only factor out the collinear singularity, so that the integration can be written as

$$D_{ii} = \int \mathrm{d}e \, \mathrm{d}c \, \Theta(\tilde{z}_\gamma(e,c) - z_{\text{cut}}) \, \frac{\mathcal{N}_{ii}^{d=4-2\epsilon}(e,c)}{(1-c)^{1+\epsilon}}, \tag{3.89}$$

where we have introduced the Heaviside function limiting $\tilde{z}_\gamma$, which is a function of the integration variables e and c. The functional form of $\tilde{z}_\gamma$ is not important at this stage, and different choices can be easily incorporated in our framework. Following the semi-numerical approach, we again insert a counterterm to regulate the collinear singularity and we write

D_{ii} as

$$\begin{aligned} D_{ii} = &\int \mathrm{d}e\,\mathrm{d}c \frac{1}{(1-c)} \left[\mathcal{N}_{ii}^{d=4}(e,c)\Theta(\tilde{z}_\gamma(e,c)-z_{\mathrm{cut}}) - \mathcal{N}_{ii}^{d=4}(e,1)\Theta(\tilde{z}_\gamma(e,1)-z_{\mathrm{cut}})\right], \\ &+ \int \mathrm{d}e\,\mathrm{d}c \frac{1}{(1-c)^{1+\epsilon}} \left[\mathcal{N}_{ii}^{d=4-2\epsilon}(e,1)\Theta(\tilde{z}_\gamma(e,1)-z_{\mathrm{cut}})\right], \end{aligned} \tag{3.90}$$

where the first line can be integrated numerically, where $\tilde{z}_\gamma(e,c)$ has to be evaluated in the counterterm at $c = 1$. The numerator of the second line no longer depends on c, which makes the integration over c trivial. In addition, we expand the numerator as $\mathcal{N}_{ii}^{d=4-2\epsilon}(e,1) = \mathcal{N}_{ii}^{0}(e,1) + \epsilon\mathcal{N}_{ii}^{1}(e,1)$ and we obtain the following for D_{ii}

$$\begin{aligned} D_{ii} = &\int \mathrm{d}e\,\mathrm{d}c \frac{1}{(1-c)} \left[\mathcal{N}_{ii}^{d=4}(e,c)\Theta(\tilde{z}_\gamma(e,c)-z_{\mathrm{cut}}) - \mathcal{N}_{ii}^{d=4}(e,1)\Theta(\tilde{z}_\gamma(e,1)-z_{\mathrm{cut}})\right], \\ &- \int \mathrm{d}e\,\Theta(\tilde{z}_\gamma(e,1)-z_{\mathrm{cut}}) \left[\mathcal{N}_{ii}^{1}(e,1) - \log(2)\,\mathcal{N}_{ii}^{0}(e,1)\right] \\ &- \int \mathrm{d}e\,\Theta(\tilde{z}_\gamma(e,1)-z_{\mathrm{cut}}) \frac{1}{\epsilon}\mathcal{N}_{ii}^{0}(e,1), \end{aligned} \tag{3.91}$$

where all ϵ poles are present in the last line. The discussion so far was independent of the form of $\tilde{z}_\gamma(e,c)$ and different choices can be used. In our case, we define $\tilde{z}_\gamma(e,c)$ as

$$\tilde{z}_\gamma(e,c) = \frac{p_j \cdot Q}{p_i \cdot Q + p_j \cdot Q} \tag{3.92}$$

which basically coincides with the choice in the Catani-Seymour subtraction scheme with $p_k \to Q$ and is therefore independent of the spectator particle k. Since the integration of the unresolved phase space is performed in the rest frame of Q, the relation of $\tilde{z}_\gamma(e,c)$ can be written in this frame as

$$\tilde{z}_\gamma(e,c) = \frac{E_j}{E_i + E_j}, \tag{3.93}$$

where the energies E_i and E_j are functions of e and c. In the collinear limit ($c = 1$), the photonic energy fraction can expressed as a function of the integration variable e as

$$\tilde{z}_\gamma(e,1) = \frac{1}{1 + \frac{\tilde{p}_i^0}{\sqrt{Q^2}}\frac{1-e}{e}} = \frac{e\sqrt{Q^2}}{e\sqrt{Q^2} + (1-e)\tilde{p}_i^0}. \tag{3.94}$$

This equation can be used to solve it for e, so that e can be written as a function of $\tilde{z}_\gamma$, which then can be used for a variable transformation of the last two lines in Eq. (3.91). In particular, $e(\tilde{z}_\gamma)$ can be written as

$$e(\tilde{z}_\gamma) = \frac{\tilde{z}_\gamma \tilde{p}_i^0}{(1-\tilde{z}_\gamma)\sqrt{Q^2} + \tilde{z}_\gamma \tilde{p}_i^0}, \tag{3.95}$$

and performing the variable transformation $e \to \tilde{z}_\gamma$ to the singular part in Eq. (3.91) leads then to

$$D_{ii}^{\mathrm{sing.}} = -\int \mathrm{d}e\,\Theta(\tilde{z}_\gamma(e,1)-z_{\mathrm{cut}}) \frac{1}{\epsilon}\mathcal{N}_{ii}^{0}(e,1) = -\int_{z_{\mathrm{cut}}}^{1} \mathrm{d}\tilde{z}_\gamma \frac{1}{\epsilon} P_{q\to\gamma}(\tilde{z}_\gamma), \tag{3.96}$$

where also in this case the ϵ poles of the integrated dipoles cancel exactly with those from the factorization kernel $\mathbf{\Gamma}^{(0)}_{q\to\gamma}$ in Eq. (2.59) rendering the whole calculation finite. In our current implementation we instead perform the transformation $\tilde{z}_\gamma \to e$ for the fragmentation function and the mass factorization kernel, which simplifies the simultaneous calculation of the integrated dipoles and the convolution with the fragmentation functions.

3.3 Virtual corrections

The calculation of the virtual corrections is performed using reweighting techniques [180], where in the first step unweighted events of the Born cross section of a subprocess are generated, which are used to compute the virtual corrections. This approach minimizes the number of the evaluations of one-loop matrix elements. The sum of the partonic Born cross section with the corresponding virtual corrections can be written schematically as

$$\sigma_{ab}^{\mathrm{LO+V}} = \int_0^1 \mathrm{d}x_a \int_0^1 \mathrm{d}x_b \int_n \mathrm{d}\Phi_n \, f_a(x_a,\mu_F)\, f_b(x_b,\mu_F)\, \frac{1}{2\hat{s}} \left(\mathcal{A}_{ab}^B + \mathcal{A}_{ab}^V\right), \tag{3.97}$$

where $\mathcal{A}_{ab}^V$ denotes the interference contribution of the Born matrix element with the one-loop matrix element. This can be rewritten in the following way by factoring out the Born contribution as

$$\sigma_{ab}^{\mathrm{LO+V}} = \int_0^1 \mathrm{d}x_a \int_0^1 \mathrm{d}x_b \int_n \mathrm{d}\Phi_n \, f_a(x_a,\mu_F)\, f_b(x_b,\mu_F)\, \frac{1}{2\hat{s}} \mathcal{A}_{ab}^B \left(1 + \frac{\mathcal{A}_{ab}^V}{\mathcal{A}_{ab}^B}\right), \tag{3.98}$$

which makes the actual reweighting approach apparent. In particular, the generation of unweighted events following the Born phase space amounts to the generation of the integration variables x_i and Φ_n according to the following probability distribution

$$g(\vec{X}) \equiv g(x_1, x_2, \Phi_n) = \frac{\mathrm{d}\sigma_{ab}^{\mathrm{LO}}}{\sigma_{ab}^{\mathrm{LO}} \mathrm{d}x_1 \mathrm{d}x_2 \mathrm{d}\Phi_n}, \tag{3.99}$$

which fulfils the following normalization condition by construction

$$\int \mathrm{d}\vec{X} g(\vec{X}) = 1. \tag{3.100}$$

Thus, the integration of a function $f(\vec{X})$ multiplied with the probability distribution $g(\vec{X})$ can then be written in terms of N unweighted events following the probability distribution $g(\vec{X})$ as

$$\int \mathrm{d}\vec{X} g(\vec{X}) f(\vec{X}) = \frac{1}{N} \sum_{i=1}^{N} f(\vec{X}_i), \tag{3.101}$$

where the equality holds only in the large N limit, and for finite N we have to take into account the Monte Carlo integration error. In our case, the function $f(\vec{X})$ can easily be identified with the brackets in Eq. (3.98) and is thus given by

$$f(\vec{X}) = \left(1 + \frac{\mathcal{A}_{ab}^V}{\mathcal{A}_{ab}^B}\right), \tag{3.102}$$

and the original integral can be obtained by the following sum

$$\sigma_{ab}^{\mathrm{LO+V}} = \sigma_{ab}^{\mathrm{LO}} \frac{1}{N} \sum_{i=1}^{N} \left(1 + \frac{\mathcal{A}_{ab}^{V}(\vec{X}_i)}{\mathcal{A}_{ab}^{B}(\vec{X}_i)} \right). \tag{3.103}$$

In practice, we generate partially unweighted events, where a weight factor $w(\vec{X}_i)$ has to be included in the sum above which is simply one for fully unweighted events. The new reweighting factor obtained by the function $f(\vec{X})$ is then also stored in the same LHEF.

In addition to the overall weight of an event, it is also necessary to parametrize the dependence on the renormalization scale (μ_R) of the virtual corrections to allow the reweighting to different renormalization scales. At the one-loop level, the weight of the virtual corrections can be written as

$$w^{\mathrm{V}}(\mu_R) = w_0^{\mathrm{V}}(\mu_R) + \frac{1}{\epsilon} w_1^{\mathrm{V}}(\mu_R) + \frac{1}{\epsilon^2} w_2^{\mathrm{V}}(\mu_R). \tag{3.104}$$

The logarithmic dependence on the finite part ($w_0^{\mathrm{V}}(\mu_R)$) is given by

$$w_0^{\mathrm{V}}(\mu_R) = w_{0,0}^{\mathrm{V}} + w_{0,1}^{\mathrm{V}} \log \mu_R^2 + w_{0,2}^{\mathrm{V}} \log^2 \mu_R^2, \tag{3.105}$$

where the coefficients $w_{0,i}^{\mathrm{V}}$ do not explicitly depend on the renormalization scale, but still indirectly through $\alpha_s(\mu_R)$. The logarithmic dependencies on the renormalization scale occur from the renormalization counterterms in dimensional regularization and the IR ϵ poles. In principle, it is also possible to distinguish the logarithmic dependence of both origins and to use μ_{IR} instead of μ_R for all logarithms of IR origin, where the dependence on μ_{IR} is canceled in the sum of real and virtual corrections. For simplicity, we set $\mu_{\mathrm{IR}} = \mu_R$. The coefficient in front of $\log^2 \mu_R^2$ is purely originating from the $1/\epsilon^2$ pole. The only explicit $\log \mu_R^2$ dependence of the counterterms arises from the α_s renormalization in the $\overline{\mathrm{MS}}$ scheme, which can alternatively be obtained by requiring that the NLO cross section is independent of the renormalization scale (up to higher orders) and the renormalization group equation of α_s. The simplest and most time-consuming way to obtain these coefficients is the calculation of the virtual corrections $w^{\mathrm{V}}(\mu_R)$ for three different values of μ_R and the subsequent solution of a system of linear equations for the coefficients w_i^{V}. This method is used in HELAC-1LOOP [459], and it slows down the calculation significantly, because the one-loop matrix element is always calculated three times. Since the origin of the logarithmic dependence is well known, they can be obtained in an alternative way from the α_s renormalization counterterm and the IR ϵ poles. For this we discuss first the logarithmic dependence on μ_R of the integrated dipoles encoded in the (**I**) operator, where the logarithmic dependence is completely encoded in the ϵ poles, which cancel with those of the virtual corrections. In that case, the finite reminder can be parametrized in the same way as for the virtual corrections by

$$w_0^{\mathrm{I}}(\mu_R) = w_{0,0}^{\mathrm{I}} + w_{0,1}^{\mathrm{I}} \log \mu_R^2 + w_{0,2}^{\mathrm{I}} \log^2 \mu_R^2. \tag{3.106}$$

For the **I** operator, the explicit μ_R dependence comes only from the ϵ poles, which allows to factor out the μ_R dependence of the entire **I** operator, including the ϵ poles, in the following way

$$\begin{aligned} w^{\mathrm{I}}(\mu_R) &= w_0^{\mathrm{I}}(\mu_R) + \frac{1}{\epsilon} w_1^{\mathrm{I}}(\mu_R) + \frac{1}{\epsilon^2} w_2^{\mathrm{I}}(\mu_R) \\ &= \mu_R^{2\epsilon} \left(\tilde{w}_0^{\mathrm{I}} + \frac{1}{\epsilon} \tilde{w}_1^{\mathrm{I}} + \frac{1}{\epsilon^2} \tilde{w}_2^{\mathrm{I}} \right) + \mathcal{O}(\epsilon), \end{aligned} \tag{3.107}$$

where the coefficients $\tilde{w}_i^{\mathrm{I}}$ are independent of μ_R. This equation can be expanded up to the order $\mathcal{O}(\epsilon^0)$, which then results to

$$w^{\mathrm{I}}(\mu_R) = \left(\tilde{w}_0^{\mathrm{I}} + \tilde{w}_1^{\mathrm{I}} \log \mu_R^2 + \frac{1}{2}\tilde{w}_2^{\mathrm{I}} \log^2 \mu_R^2\right) + \left(\tilde{w}_1^{\mathrm{I}} + \tilde{w}_2^{\mathrm{I}} \log \mu_R^2\right)\frac{1}{\epsilon} + \tilde{w}_2^{\mathrm{I}}\frac{1}{\epsilon^2}, \tag{3.108}$$

where the logarithmic dependence on the rernormalization scale of the finite part can be easily read off. Furthermore, this equation can be used to express the coefficients $\tilde{w}_i^{\mathrm{I}}$ with the coefficients w_i^{I}, which are calculated in the program. Therefore, the logarithmic dependence of the finite part of the $\mathbf{I}$ operator is then given by

$$\begin{aligned} w_0^{\mathrm{I}}(\mu_R) =& \left(w_0^{\mathrm{I}}(\mu_{R,0}) - w_1^{\mathrm{I}}(\mu_{R,0}) \log \mu_{R,0}^2 + \frac{1}{2} w_2^{\mathrm{I}}(\mu_{R,0}) \log^2 \mu_{R,0}^2\right) \\ &+ \left(w_1^{\mathrm{I}}(\mu_{R,0}) - w_2^{\mathrm{I}}(\mu_{R,0}) \log \mu_{R,0}^2\right) \log \mu_R^2 \\ &+ \left(\frac{1}{2} w_2^{\mathrm{I}}(\mu_{R,0})\right) \log^2 \mu_R^2, \end{aligned} \tag{3.109}$$

where $\mu_{R,0}$ is an arbitrary scale, and in particular the sum in each bracket is independent of $\mu_{R,0}$. Setting $\mu_R = \mu_{R,0}$ would reduce this equation to a simple identity. Furthermore, the implicit dependence on μ_R through $\alpha_s(\mu_R)$ would require further reweighting with some factor $(\alpha_s(\mu_R)/\alpha_s(\mu_{R,0})^n$ where n is the power of α_s. In the case of the virtual corrections, we have to take into account the α_s renormalization constant, which then leads to the following parameterization of the logarithmic dependence of the virtual corrections

$$\begin{aligned} w_0^{\mathrm{V}}(\mu_R) =& \left[w_0^{\mathrm{V}}(\mu_{R,0}) - \left(w_1^{\mathrm{V}}(\mu_{R,0}) + n_0\, w^{\mathrm{B}} \frac{\alpha_s}{\pi}\beta_0\right) \log \mu_{R,0}^2 + \frac{1}{2} w_2^{\mathrm{V}}(\mu_{R,0}) \log^2 \mu_{R,0}^2\right] \\ &+ \left[w_1^{\mathrm{V}}(\mu_{R,0}) + n_0\, w^{\mathrm{B}} \frac{\alpha_s}{\pi}\beta_0 - w_2^{\mathrm{V}}(\mu_{R,0}) \log \mu_{R,0}^2\right] \log \mu_R^2 \\ &+ \left[\frac{1}{2} w_2^{\mathrm{V}}(\mu_{R,0})\right] \log^2 \mu_R^2, \end{aligned} \tag{3.110}$$

where w^B is the corresponding Born weight with $\alpha_s = \alpha_s(\mu_{R,0})$, n_0 is the power of α_s of the Born process where $n = n_0 + 1$ has to hold. If there exists no Born contribution which satisfies this condition, then the virtual corrections consist of only EW corrections where the α_s renormalization does not enter and we simply set $n_0 = 0$. Finally, β_0 is the one-loop contribution to the renormalization group equation of α_s and is given by

$$\beta_0 = \frac{11}{4} - \frac{1}{6} N_f, \tag{3.111}$$

where N_f is the number of light flavors. Therefore, the logarithmic dependence can be completely reconstructed by the calculation of the finite part and the ϵ poles for a single value of the renormalization scale ($\mu_{R,0}$). Although HELAC-1LOOP was used in the present work only for cross-checks for single phase-space points for the NLO QCD corrections to $pp \to t\bar{t}\gamma\gamma$ in the NWA, we have implemented this alternative method, which leads to a drastic speed-up of the calculation. In our case, we use RECOLA for the computation of the one-loop correction, where by default only the finite part is calculated and the computation of the ϵ poles with RECOLA would require two additional computations of the

one-loop amplitude. Therefore, the ϵ poles of the one-loop amplitudes are obtained during the phase-space integration from the integrated dipoles using the relation $w^{\mathrm{V}}_{1(2)} = -w^{\mathrm{I}}_{1(2)}$.

In Recola, the one-loop integrals are reduced to tensor integrals $T^{\mu_1\dots\mu_{r_t}}_{(t)}$ and tensor coefficients $c^{(t)}_{\mu_1\dots\mu_{r_t}}$ according to Eq. (3.5). We have implemented an alternative reduction method of one-loop matrix elements to scalar integrals based on the OPP reduction technique [460] at the integrand level by interfacing Recola with CutTools [461], where the scalar integrals are calculated with OneLOop [462]. The reduction and calculation of the one-loop integrals can be performed in this case with quadruple precision. The OPP method requires numerous evaluations of the numerator of one-loop integrals with different values of the integration variable q for the reduction. In our case, the numerator is obtained with the q-independent tensor coefficients (in double precision) already calculated in Recola, which means that only the tensor $q^{\mu_1}...q^{\mu_{r_t}}$ in Eq. (3.6) has to be reevaluated for each value of q to construct the full numerator. A similar approach was already employed in Ref. [463]. This second reduction method can be used for additional cross-checks, and we employ it for phase-space points that are marked as possibly unstable by Collier to reevaluate the one-loop corrections by performing the reduction and the computation of scalar integrals with quadruple precision. The disadvantage of this method compared to the original reduction scheme in Recola is clearly that the partial results for a specific color structure and helicity state cannot be reused in general, and therefore the reduction at the integrand level has to be performed for all non-vanishing helicity configurations and color structures. This can lead to a significant increase in the computation of one-loop matrix elements, which is in our case not important because we always use the random polarization, where we have only one helicity configuration. Furthermore, the color optimization in Recola reduces the number of color structures to a minimal set, which is rather limited in our current calculation of $pp \to t\bar{t}\gamma(\gamma)$ with 2 non-self-connected color structures in the $q\bar{q}$ channel and 3 in the gg channel.

In Recola it is possible to generate matrix elements with a specific resonance structure. Such matrix elements can be used directly for calculations in the pole approximation or by performing the usual $\Gamma/m \to 0$ limit in the resonant Breit-Wigner propagators for calculations in the NWA. Since the symmetry factor in Recola is always calculated from the perspective of an off-shell calculation, we have to correct it, when identical particles appear in different subprocesses in the decay chain. We have also implemented a second fully automatic approach for the construction of tree-level and one-loop matrix elements based on the on-shell amplitudes of the individual subprocesses in the decay chain, which we obtain from Recola and where we set the widths of all unstable particles to zero. These amplitudes are then combined accordingly in helicity and color space to obtain the corresponding matrix elements in the NWA. Again, this can be used for cross-checks, but within this implementation it is straightforward to discard one-loop corrections in specific parts of the decay chain, which allows to calculate one-loop corrections to the production process while omitting all one-loop corrections in the decay processes.

Since in our process we encounter unstable particles such as top quarks and W bosons, it is necessary to use the complex-mass scheme and to perform the renormalization accordingly, which we have briefly discussed in the last chapter using the example of the W boson. Additionally, we are interested in the calculation of EW corrections to processes with photons in the final state. This requires a mixed renormalization scheme, where the

total power of α^n is split to $\alpha_{G_\mu}^{n-n_\gamma}\alpha(0)^{n_\gamma}$, where n_γ is the number of photons appearing in the final state at the Born level. This means that all powers of α associated with the emission of final photons are renormalized in the on-shell scheme, while all remaining powers are renormalized in the G_μ scheme. This ensures a proper cancellation of all IR singularities between real and virtual corrections [18, 427]. Photons appearing in the initial state are not affected by this since initial-state photon splittings into quarks are included in the calculation. Therefore, $\alpha = \alpha_{G_\mu}$ is used for the electromagnetic coupling constant and the corresponding QED collinear counterterms from the redefinition of the PDFs. The change of the renormalization scheme can be understood as follows. In QCD, gluon- and quark-initiated jets are not distinguished, therefore in the calculation of jet cross sections all kind of possible splittings, such as $g \to q\bar{q}$, are included in the calculation to ensure the proper cancellation of all IR singularities between the real and virtual corrections. On the other hand, charged leptons, jets and photons give rise to different signatures in the final state and are therefore usually separated. Thus, $\gamma \to f\bar{f}$ splittings are not included for final-state photons in the calculation of photon cross sections, since they would lead to different final state signatures. By omitting this contribution, one has to switch from a $\overline{\text{MS}}$ like renormalization scheme (α_{G_μ}) to an on-shell one ($\alpha(0)$). In practice, we first perform the complete renormalization in the G_μ scheme and add a suitable counterterm to change the renormalization scheme for n_γ powers of α to the on-shell scheme. This counterterm is given by

$$2\, n_\gamma \,\text{Re}\left(\delta Z_e\big|_{\alpha(0)} - \delta Z_e\big|_{G_\mu}\right) \mathrm{d}\sigma^{\text{LO}} = n_\gamma \,\text{Re}\left(\Delta r^{(1)}\right) \mathrm{d}\sigma^{\text{LO}}, \tag{3.112}$$

where $\Delta r^{(1)}$ corresponds to the NLO EW corrections to the muon decay [428, 464–466], $\delta Z_e\big|_{\alpha(0)}$ and $\delta Z_e\big|_{G_\mu}$ are the renormalization constants of the electric charge e in the on-shell and G_μ scheme, respectively. During the whole calculation, and also in Eq. (3.112), we always use $\alpha = \alpha_{G_\mu}$ and at the end the final result is rescaled by $(\alpha(0)/\alpha_{G_\mu})^{n_\gamma}$. This also implies that the relative EW corrections are always calculated with $\alpha = \alpha_{G_\mu}$.

3.4 Numerical checks

Various checks were performed to ensure the correctness of the new functionalities in Helac-Dipoles, which we list in the following. First of all, the new extension of the Nagy-Soper subtraction for calculations in the NWA was used in the calculation of NLO QCD corrections to $pp \to t\bar{t}jj$ in *di-lepton* decay channel [173], where jet radiation and NLO QCD corrections were consistently included in the $t\bar{t}$ production process and the decays of the top quarks. In this case, the real corrections were cross-checked with an alternative calculation based on the Catani-Seymour subtraction scheme, were the missing polarized dipoles for the $g \to gg$ and $g \to q\bar{q}$ splittings in top-quark decays were implemented as explained in Ref. [467]. The unpolarized dipole terms for the $q \to qg$ and $g \to gg$ splittings can be found in Refs. [165, 468], while the polarized $q \to qg$ splitting and the general implementation of the Catani-Seymour subtraction in the NWA in Helac-Dipoles are discussed in Ref. [12]. In the same calculation we also cross-checked the new interface with Recola, which was used for all tree-level matrix elements in the case of the Nagy-Soper subtraction scheme, while in the case of the Catani-Seymour subtraction scheme the Helac matrix-element generator is used [443, 445]. Additionally, the virtual

	HELAC-DIPOLES	analytic
$\Gamma_t^{\text{NLO QCD,real}}/\Gamma_t^{\text{LO}}$	$-0.6360(4)$	$-0.63546...$
$\Gamma_t^{\text{NLO QCD,LO+V}}/\Gamma_t^{\text{LO}}$	$1.551(1)$	$1.5507...$
$\Gamma_t^{\text{NLO QCD}}/\Gamma_t^{\text{LO}}$	$0.9148(9)$	$0.91526...$

Table 3.1: *Comparison of numerical results with analytical results for the relative NLO QCD corrections to the top-quark width with massive bottom quarks and the W boson decaying into a lepton-neutrino pair in the NWA.*

corrections were computed with RECOLA and cross-checked with HELAC-1LOOP [459]. A comparison of the two setups, the Nagy-Soper subtraction scheme with RECOLA and the Catani-Seymour subtraction scheme with HELAC-NLO at the integrated level can be found in Ref. [467], where a good agreement between both calculations is found with numerical uncertainties of about $0.1\% - 0.2\%$.

This comparison with the Catani-Seymour subtraction scheme essentially tested almost all parts of the new implementation of the Nagy-Soper subtraction in the NWA, except for the dipole contribution with massive emitters in decay processes, which in our case is required for the calculation of NLO EW corrections in top-quark decays were photons can be radiated from the resonant W boson. Since in our implementation the new dipole term is independent of the actual splitting, the photon emission from W bosons and the gluon emission from massive bottom quarks require the same new integrated dipole. Therefore, we have numerically recalculated the top-quark width with massive bottom quarks and the W boson decaying into a lepton-neutrino pair in the NWA. Instead of calculating the $t \to W^+(\to \ell^+\nu_\ell)b$ process to obtain the top-quark width, we have used a different strategy that can be used directly to test our whole setup. In particular, we consider the $gg \to t\bar{t}$ subprocess in the NWA in the following decay chain

$$gg \to t(\to W^+(\to \ell^+\nu_\ell)b)\,\bar{t}(\to W^-(\to \ell^-\bar{\nu}_\ell)\bar{b}), \tag{3.113}$$

and compute it once at LO and once by including NLO QCD corrections only in the top-quark decay ($t \to W^+(\to \ell^+\nu_\ell)b$). The ratio of the two calculations is equal to the relative size of the NLO QCD corrections to the top-quark width ($\Gamma_t^{\text{NLO QCD}}/\Gamma_t^{\text{LO}}$) if no phase-space cuts are applied. In particular, we cross-check our numerical calculation with the known analytical NLO QCD corrections of the top-quark width with massive bottom quarks [469, 470], and further check the real and virtual corrections separately with the analytical results given in Ref. [103]. The comparison of the numerical results obtained with the Nagy-Soper subtraction scheme and RECOLA compared with the analytical results is presented in Table 3.1, where LO + V corresponds to the sum of the virtual corrections and the LO contribution, and the sum of the real corrections and LO + V corresponds to the top quark width at NLO QCD. A good agreement is found for the partial results with statistical uncertainties of about $0.06\% - 0.07\%$ as well as for the full result with slightly larger statistical uncertainties of about 0.1% due to cancellations between the real and virtual corrections. For this comparison we have used the following numerical values for

the masses

$$m_t = 173.2 \text{ GeV}, \qquad m_W = 80.399 \text{ GeV}, \qquad m_b = 4.95 \text{ GeV}, \tag{3.114}$$

and we have used $\mu_R = m_t$ with $\alpha_s(m_t) = 0.107610535193374$.

We have also recalculated the NLO EW corrections to the top-quark width with massive bottom quarks, where the W boson decays into a lepton-neutrino pair in the NWA. The general setup for the numerical calculation with HELAC-DIPOLES is essential the same as discussed for the NLO QCD corrections above. In this case, the EW corrections are consistently included in the top-quark decay as well as the W boson decay. Using the setup of Ref. [471], we obtain $\delta^{\alpha} = 1.348(3)\%$ for the relative size of NLO EW corrections, which is in agreement with the NLO EW corrections reported within of $\delta^{\alpha} = 1.35\%$.

Finally, we have reproduced the calculation of NLO EW corrections to full off-shell top-quark pair production in the *di-lepton* decay channel $pp \to e^+\nu_e\mu^-\bar{\nu}_\mu b\bar{b}$ presented in Ref. [113], where the whole setup of the calculation can be found. In this case, the NLO EW calculation consists of the dominant LO contribution at the order $\mathcal{O}(\alpha_s^2\alpha^4)$ with the NLO EW corrections including all contributions at the order $\mathcal{O}(\alpha_s^2\alpha^5)$, which generally consists of the EW corrections to the LO process at $\mathcal{O}(\alpha_s^2\alpha^4)$ and the QCD corrections to the LO process at $\mathcal{O}(\alpha_s^1\alpha^5)$. However, all contributions with either bottom quarks or photons in the initial state are neglected. In our case, the calculation is performed again with the Nagy-Soper subtraction scheme with an earlier version of the program, where the tree-level matrix elements for the real corrections are obtained with HELAC instead of RECOLA, but the virtual corrections are still calculated with RECOLA. The numerical results at the integrated level from our calculation and from Ref. [113], where the latter is denoted by DP, are given by

$$\begin{aligned} \sigma_{\text{NLO EW}} &= 3212.1(3) \text{ fb}, \\ \sigma_{\text{NLO EW}_{\text{DP}}} &= 3211.7(3) \text{ fb}, \end{aligned} \tag{3.115}$$

where good agreement is found between the two calculations with statistical uncertainties of about 0.01%. However, the NLO EW corrections in this case are only 0.4%. We have performed a similar comparison at the differential level and present in Figure 3.3 the observables p_{T,b_1}, $p_{T,t}$, M_t, $M(be^+)$, $\Delta\phi_{e^+\mu^-}$ and y_t as an example of our comparison, where the data points of the calculation in Ref. [113] were provided by the authors. Overall, we find a good agreement between the two calculations over the entire phase space for all observables.

In addition to the cross-checks discussed in this section, we have further verified the correctness of our calculations in the next chapters by performing the calculation of the real corrections with two values of the α parameter, restricting the non-singular phase space of the dipoles, to verify the independence of it. Furthermore, we explicitly checked for all subprocesses that the IR ϵ poles between the virtual and real corrections, encoded in the $\mathbf{I}$ operator, cancel.

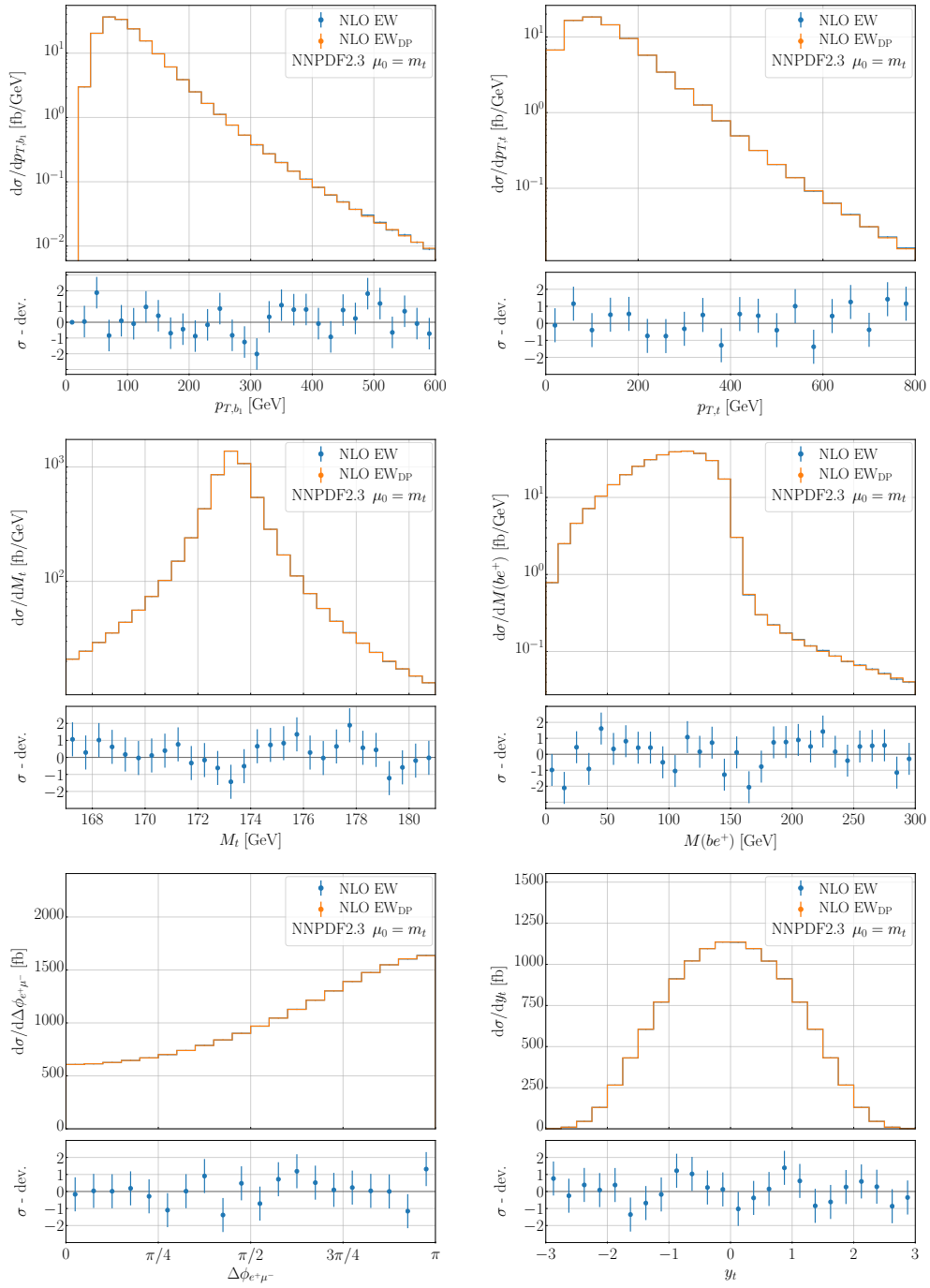

Figure 3.3: *Comparison of the NLO EW corrections to* $pp \to e^+\nu_e\mu^-\bar{\nu}_\mu b\bar{b}$ *obtained with* HELAC-DIPOLES *and* RECOLA *compared to the results of Ref. [113] (indicated by DP). Numerical results are presented for* p_{T,b_1}, $p_{T,t}$, M_t, $M(be^+)$, $\Delta\phi_{e^+\mu^-}$ *and* y_t. *MC integrations errors are also displayed.*

4. Prompt photon distribution in $t\bar{t}\gamma\gamma$ at NLO QCD

The focus of this thesis is the precise modeling of top-quark pair production with isolated photons. We start the discussion with the calculation of NLO QCD corrections to the $pp \to t\bar{t}\gamma\gamma$ process for the LHC Run II center-of-mass energy of $\sqrt{s} = 13$ TeV. In contrast to previous calculations of this process, we consistently include photon radiation as well as NLO QCD corrections in the production of $t\bar{t}$ as well was in the decays of all unstable particles. We consider the *di-lepton* and *lepton + jet* decay channel, and quantify the effects of photon radiation originating from the top-quark and W-boson decays.

This chapter is structured as follows. In Section 4.1 we give a brief definition of the process, which is followed by a summary of the input parameters of our calculation in Section 4.2. Finally, in the Section 4.3 and the Section 4.4 we present numerical results at the integrated and differential fiducial cross-section level for the two decay channels. These results were already published in Ref. [472], from where we have also taken the tables and figures shown in this chapter.

4.1 Process definition

In this calculation we consider the Born-level process at $\mathcal{O}(\alpha_s^2\alpha_6)$ and calculate the corresponding α_s corrections. Specifically, we perform the calculation in the *di-lepton* and *lepton + jet* decay channels using the NWA to model the decays of intermediate top quarks and W bosons, leading to the following decay chains for both processes at LO

$$\begin{aligned} pp \to t\bar{t}\,(\gamma\gamma) \to W^+W^-\,b\bar{b}\,(\gamma\gamma) \to \ell^+\nu_\ell\,\ell^-\bar{\nu}_\ell\,b\bar{b}\,\gamma\gamma, \\ pp \to t\bar{t}\,(\gamma\gamma) \to W^+W^-\,b\bar{b}\,(\gamma\gamma) \to \ell^-\bar{\nu}_\ell\,jj\,b\bar{b}\,\gamma\gamma, \end{aligned} \tag{4.1}$$

with $\ell^\pm = \mu^\pm, e^\pm$ and where the brackets around the photons indicate that photon bremsstrahlung is included in all parts of the entire decay chain. The differential cross section can then be written as

$$\begin{aligned} d\sigma_{\text{Full}} = &\overbrace{d\sigma_{t\bar{t}\gamma\gamma} \times \frac{d\Gamma_t}{\Gamma_t} \times \frac{d\Gamma_{\bar{t}}}{\Gamma_t}}^{\sigma_{\text{Prod.}}} + \overbrace{d\sigma_{t\bar{t}\gamma} \times \left(\frac{d\Gamma_{t\gamma}}{\Gamma_t} \times \frac{d\Gamma_{\bar{t}}}{\Gamma_t} + \frac{d\Gamma_t}{\Gamma_t} \times \frac{d\Gamma_{\bar{t}\gamma}}{\Gamma_t} \right)}^{\sigma_{\text{Mixed}}} \\ &+ \underbrace{d\sigma_{t\bar{t}} \times \left(\frac{d\Gamma_{t\gamma\gamma}}{\Gamma_t} \times \frac{d\Gamma_{\bar{t}}}{\Gamma_t} + \frac{d\Gamma_t}{\Gamma_t} \times \frac{d\Gamma_{\bar{t}\gamma\gamma}}{\Gamma_t} + \frac{d\Gamma_{t\gamma}}{\Gamma_t} \times \frac{d\Gamma_{\bar{t}\gamma}}{\Gamma_t} \right)}_{\sigma_{\text{Decay}}} . \end{aligned} \tag{4.2}$$

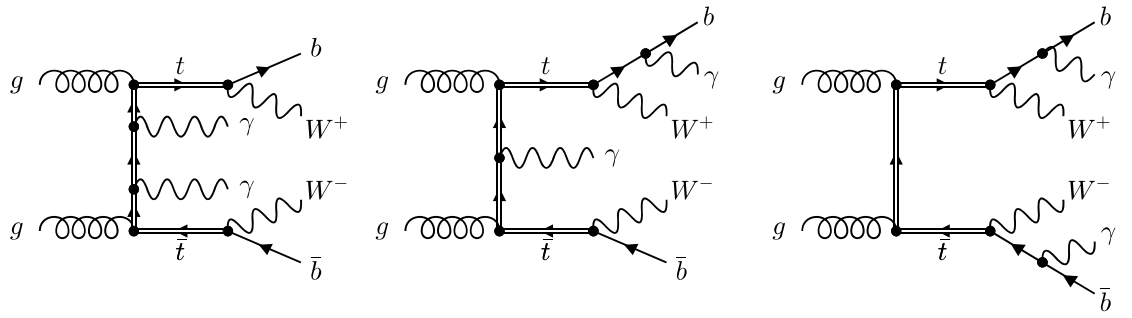

Figure 4.1: *Example Feynman diagrams for the three resonant contributions, Prod., Mixed and Decay at LO, where W-boson decays are supressed.*

where we also defined the *Prod.*, *Mixed* and *Decay* contributions based on the origin of photon bremsstrahlung in the decay chain. In particular, the *Prod.* contribution contains only photon bremsstrahlung in the production process followed by top-quarks decays without any additional photons. This approximation was used in earlier calculations where the effects of photon radiation from any charged particles in the decays of top quarks and W bosons were neglected. The *Decay* contribution includes only photon bremsstrahlung in the decays of unstable particles, and in the *Mixed* contribution photon radiation is present simultaneously in the production process and in the decay processes. The sum of all three terms is denoted as the full calculation. Example diagrams for the different resonant structures are depicted in Figure 4.1. Since W-boson decays are also modeled in the NWA, the top-quark decays in Eq. (4.2) are further expanded as

$$d\Gamma_{t+n\gamma} = \sum_{i=0}^{n} d\Gamma_{t\to bW^++i\gamma} \frac{d\Gamma_{W^++(n-i)\gamma}}{\Gamma_W}\,, \tag{4.3}$$

leading to a total of 15 possibilities or resonant histories from where the photons can be radiated in the decay chain at LO. Due to QCD radiation at NLO, this number increases to 45 in the *di-lepton* and to 60 in the *lepton + jet* decay channel, where in the latter case gluon radiation is also included in the hadronically decaying W boson. At LO we encounter the following partonic subprocesses

$$\begin{aligned} gg &\to \ell^+\nu_\ell\,\ell^-\bar{\nu}_\ell\,b\bar{b}\,\gamma\gamma\,, \\ q\bar{q}/\bar{q}q \;\to\; \ell^+\nu_\ell\,\ell^-\bar{\nu}_\ell\,b\bar{b}\,\gamma\gamma\,, &\qquad b\bar{b}/\bar{b}b \;\to\; \ell^+\nu_\ell\,\ell^-\bar{\nu}_\ell\,b\bar{b}\,\gamma\gamma\,, \end{aligned} \tag{4.4}$$

in the *di-lepton* and

$$\begin{aligned} gg &\to \ell^-\bar{\nu}_\ell\,q\bar{q}'\,b\bar{b}\,\gamma\gamma\,, \\ q\bar{q}/\bar{q}q \;\to\; \ell^-\bar{\nu}_\ell\,q\bar{q}'\,b\bar{b}\,\gamma\gamma\,, &\qquad b\bar{b}/\bar{b}b \;\to\; \ell^-\bar{\nu}_\ell\,q\bar{q}'\,b\bar{b}\,\gamma\gamma\,, \end{aligned} \tag{4.5}$$

in the *lepton + jet* decay channel with $q = u, d, c, s$ and $q\bar{q}' = u\bar{d}, c\bar{s}$. Since there is no cross-talk between the decays and the production process, the calculation is performed for exactly one lepton, one quark-pair configuration and a multiplicity factor of four is used. At NLO QCD we encounter new partonic subprocesses in the calculation of real corrections, which can be constructed from the Born partonic subprocesses by gluon radiation and

crossing of initial- and final-state particles leading to

$$
\begin{aligned}
& gg \to \ell^+\nu_\ell\,\ell^-\bar{\nu}_\ell\,b\bar{b}\,\gamma\gamma\,g\,, \\
q\bar{q}/\bar{q}q \;&\to\; \ell^+\nu_\ell\,\ell^-\bar{\nu}_\ell\,b\bar{b}\,\gamma\gamma\,g\,, & b\bar{b}/\bar{b}b \;&\to\; \ell^+\nu_\ell\,\ell^-\bar{\nu}_\ell\,b\bar{b}\,\gamma\gamma\,g\,, \\
gq/qg \;&\to\; \ell^+\nu_\ell\,\ell^-\bar{\nu}_\ell\,b\bar{b}\,\gamma\gamma\,q\,, & g\bar{q}/\bar{q}g \;&\to\; \ell^+\nu_\ell\,\ell^-\bar{\nu}_\ell\,b\bar{b}\,\gamma\gamma\,\bar{q}\,, \\
gb/bg \;&\to\; \ell^+\nu_\ell\,\ell^-\bar{\nu}_\ell\,b\bar{b}\,\gamma\gamma\,b\,, & g\bar{b}/\bar{b}g \;&\to\; \ell^+\nu_\ell\,\ell^-\bar{\nu}_\ell\,b\bar{b}\,\gamma\gamma\,\bar{b}\,,
\end{aligned}
\tag{4.6}
$$

in the *di-lepton* and

$$
\begin{aligned}
& gg \to \ell^-\bar{\nu}_\ell\,q\bar{q}'\,b\bar{b}\,\gamma\gamma\,g\,, \\
q\bar{q}/\bar{q}q \;&\to\; \ell^-\bar{\nu}_\ell\,q\bar{q}'\,b\bar{b}\,\gamma\gamma\,g\,, & b\bar{b}/\bar{b}b \;&\to\; \ell^-\bar{\nu}_\ell\,q\bar{q}'\,b\bar{b}\,\gamma\gamma\,g\,, \\
gq/qg \;&\to\; \ell^-\bar{\nu}_\ell\,q\bar{q}'\,b\bar{b}\,\gamma\gamma\,q\,, & g\bar{q}/\bar{q}g \;&\to\; \ell^-\bar{\nu}_\ell\,q\bar{q}'\,b\bar{b}\,\gamma\gamma\,\bar{q}\,, \\
gb/bg \;&\to\; \ell^-\bar{\nu}_\ell\,q\bar{q}'\,b\bar{b}\,\gamma\gamma\,b\,, & g\bar{b}/\bar{b}g \;&\to\; \ell^-\bar{\nu}_\ell\,q\bar{q}'\,b\bar{b}\,\gamma\gamma\,\bar{b}\,,
\end{aligned}
\tag{4.7}
$$

in the *lepton + jet* decay channel. Since photon radiation is a pure EW effect, the calculation of NLO QCD corrections can be done independently for each resonant history, which simplifies the calculation and allows to quantify the contributions of different resonant structures.

4.2 Input parameters for LHC Run II

The calculation is performed in the five-flavor scheme and we keep the CKM mixing matrix diagonal. We use the NNPDF3.1 NLO PDF set [473] at LO and NLO QCD, in which the running of the strong coupling constant is performed with two-loop accuracy. Alternatively, we provide theoretical predictions for the MSHT20 NLO [474] and CT18 NLO [475] PDF sets to quantify the differences in the integrated fiducial cross section when using different PDF parametrizations. The PDF sets are accessed via the LHAPDF interface [476]. As already explained in the last chapter, we use a mixed input scheme for the electromagnetic coupling constant. In particular, we use $\alpha(0)$ for electromagnetic couplings associated with final-state photon radiation with $\alpha^{-1}(0) = 137.035999084$ [477], while for all other powers of α we use the G_μ-scheme, where α_{G_μ} is given by

$$
\alpha_{G_\mu} = \frac{\sqrt{2}}{\pi}\,G_\mu\,m_W^2\,\left(1-\frac{m_W^2}{m_Z^2}\right), \qquad\qquad G_\mu = 1.1663787\cdot 10^{-5}\ \text{GeV}^{-2}\,, \tag{4.8}
$$

with $m_W = 80.379$ GeV and $m_Z = 91.1876$ GeV. We first perform the full calculation in the G_μ-scheme and then rescal the final results by $\alpha^2/\alpha^2_{G_\mu} = 0.93044....$ For the remaining SM input parameters we use $m_t = 172.5$ GeV and $\Gamma_W = 2.0972$ GeV, and all other particles are considered to be massless. The calculation of the LO and NLO QCD top-quark width is based on Refs. [110, 469], which then leads to the following numerical values

$$
\Gamma_t^{\text{LO}} = 1.4806842\ \text{GeV}\,, \qquad\qquad \Gamma_t^{\text{NLO QCD}} = 1.3535983\ \text{GeV}\,, \tag{4.9}
$$

where we have used $\alpha_s(\mu_R = m_t)$ to compute the NLO QCD corrections.

Partons with a pseudo-rapidity of $|\eta| < 5$ are clustered into jets with the *anti-k_T* jet algorithm [478] with $R = 0.4$. The final state signature is based on the specific decay

channel. In particular, in the *di-lepton* decay channel we require two opposite-sign charged leptons and exactly two b-jets, and in the *lepton + jet* decay channel we require one negatively charged lepton, exactly two b-jets and at least two light jets. Following Ref. [107], we define a b-jet as a jet with nonzero net bottomness, where the bottomness of a bottom quark is 1, of an anti-bottom quark is -1 and of any other parton is 0. This corresponds to the following recombination rules in the jet algorithm in our case

$$bg \to b, \qquad \bar{b}g \to \bar{b}, \qquad b\bar{b} \to g, \qquad bb \to b, \qquad \bar{b}\bar{b} \to \bar{b}. \tag{4.10}$$

The calculation is based on the smooth-cone isolation as explained in Section 2.3, where the fragmentation contribution vanishes. In particular, we set the input parameters of it to $R_{\gamma j} = 0.4$ and $\epsilon_\gamma = n = 1$. In Section 4.4.1 we briefly assess the dependence on these parameters in the calculation of NLO QCD corrections in the *lepton + jet* decay channel. The two prompt photons has to fulfil the following conditions

$$p_{T,\gamma} > 25 \text{ GeV}\,, \qquad |y_\gamma| < 2.5\,, \qquad \Delta R_{\gamma\gamma} > 0.4\,, \tag{4.11}$$

while the (b-tagged) jets have to pass

$$\begin{aligned} &p_{T,b} > 25 \text{ GeV}\,, \qquad |y_b| < 2.5\,, \qquad \Delta R_{bb} > 0.4\,, \\ &p_{T,j} > 25 \text{ GeV}\,, \qquad |y_j| < 2.5\,, \qquad \Delta R_{jj} > 0.4\,. \end{aligned} \tag{4.12}$$

Charged leptons must satisfy the following cuts

$$p_{T,\ell} > 25 \text{ GeV}\,, \qquad |y_\ell| < 2.5\,, \qquad \Delta R_{\ell\ell} > 0.4\,, \tag{4.13}$$

and there are no further restrictions on the kinematics of the possible extra jet at NLO and on the missing transverse momentum ($p_T^{miss} = |\vec{p}_{T,\nu_\ell} + \vec{p}_{T,\bar{\nu}_\ell}|$). In addition, we require that all charged leptons, jets and photons have to be separated according to

$$\begin{aligned} &\Delta R_{l\gamma} > 0.4\,, \qquad \Delta R_{lb} > 0.4\,, \qquad \Delta R_{lj} > 0.4\,, \\ &\Delta R_{b\gamma} > 0.4\,, \qquad \Delta R_{bj} > 0.4\,, \qquad \Delta R_{\gamma j} > 0.4\,. \end{aligned} \tag{4.14}$$

In the *lepton + jet* decay channel, we apply an additional cut on the invariant mass of a light-jet pair to suppress configurations at NLO QCD where the two jets originating from the hadronic W boson decay are clustered into one jet by the jet algorithm, and where the additional radiation gives rise to a second hard jet [114]. In particular, the event is rejected unless one resolved light-jet pair fulfils the following condition

$$|m_W - M_{jj}| < 15 \text{ GeV}\,. \tag{4.15}$$

The dependence on this cut will be examined in the later discussion. This additional requirement also leads to a reduciton of photon radiation from the hadroincally decaying W boson [11].

We set the renormalization and factorization scales to one common scale $\mu_R = \mu_F = \mu_0$ and present results for two different scale choices. The first one is given by

$$\mu_0 = \frac{E_T}{4}\,, \tag{4.16}$$

where E_T is defined as

$$E_T = \sqrt{m_t^2 + p_{T,\,t}^2} + \sqrt{m_t^2 + p_{T,\,\bar{t}}^2} + \sum_{i=1}^{n_\gamma} p_{T,\,\gamma_i}\,, \tag{4.17}$$

where $p_{T,\,t}$ and $p_{T,\,\bar{t}}$ are the transverse momenta of the on-shell top quarks in the decay chain and we have $n_\gamma = 2$. Alternatively, it is possible to reconstruct the top quarks or to include the photons in the scale definition in a resonance manner, so that only the transverse momenta of the photons produced in the production process are taken into account. Both variations lead to similar results as our choice. As a second scale choice we use a fixed scale, which we define as

$$\mu_0 = m_t\,. \tag{4.18}$$

The results of the two scale settings are compared at the integrated and differential level. Theoretical uncertainties from missing higher-order corrections are estimated by the 7-point scale variation in which the factorization and renormalization scales are varied independently in the range

$$\frac{1}{2}\,\mu_0 \leq \mu_R\,, \mu_F \leq 2\,\mu_0\,, \qquad\qquad \frac{1}{2} \leq \frac{\mu_R}{\mu_F} \leq 2\,, \tag{4.19}$$

which results in the following pairs which have to be evaluated

$$\left(\frac{\mu_R}{\mu_0}\,, \frac{\mu_F}{\mu_0}\right) = \Big\{\,(2,1)\,, (0.5,1)\,, (1,2)\,, (1,1), (1,0.5), (2,2), (0.5,0.5)\Big\}\,. \tag{4.20}$$

The final uncertainties are then given by the maximum and minimum of this envelope.

4.3 Di-lepton channel

4.3.1 Integrated fiducial cross sections

In the discussion of the NLO QCD corrections in the $pp \to t\bar{t}\gamma\gamma$ process, we start with the results at the integrated level in the *di-lepton* decay channel shown in Table 4.1. We present results at LO and NLO QCD for the three resonant contributions *Prod.*, *Mixed* and *Decay* as well as for the full calculation. The NNPDF3.1 NLO PDF set is used and the integrated fiducial cross sections are shown for the two scale choices $\mu_0 = E_T/4$ and $\mu_0 = m_t$. In addition, theoretical uncertainties from missing higher-order corrections estimated by scale variation and MC integration errors are given. Finally, the $\mathcal{K}$-factor, defined as $\mathcal{K} = \sigma_{\text{NLO}}/\sigma_{\text{LO}}$, is calculated for all contributions. By comparing the LO and NLO predictions of the full calculation, we find NLO QCD corrections at the level of 30%, which have the same size as the scale uncertainties at LO. The NLO QCD corrections lead to a reduction of the scale uncertainties by a factor of 5 to about 6%. The central values between the two scale settings differ by about 2% at LO and 1% at NLO QCD, and are therefore negligible with respect to the corresponding scale uncertainties. In addition, the scale uncertainties are basically the same for both scales. The largest contribution does not originate from the *Prod.* contribution used in previous calculation, which amounts to

μ_0			LO	NLO	$\mathcal{K} = \sigma_{\text{NLO}}/\sigma_{\text{LO}}$
$E_T/4$	σ_{Full}	[fb]	$0.13868(3)^{+31.2\%}_{-22.1\%}$	$0.1773(1)^{+1.8\%}_{-6.2\%}$	1.28
	$\sigma_{\text{Prod.}}$	[fb]	$0.05399(2)^{+30.6\%}_{-21.7\%}$	$0.07130(6)^{+2.5\%}_{-7.2\%}$	1.32
	σ_{Mixed}	[fb]	$0.06022(2)^{+31.9\%}_{-22.5\%}$	$0.07733(8)^{+1.5\%}_{-6.2\%}$	1.28
	σ_{Decay}	[fb]	$0.024473(7)^{+30.9\%}_{-22.1\%}$	$0.02863(4)^{+0.9\%}_{-4.9\%}$	1.17
m_t	σ_{Full}	[fb]	$0.13620(3)^{+31.3\%}_{-22.1\%}$	$0.1758(1)^{+1.6\%}_{-6.3\%}$	1.29
	$\sigma_{\text{Prod.}}$	[fb]	$0.05484(2)^{+31.2\%}_{-21.9\%}$	$0.07091(6)^{+2.2\%}_{-6.7\%}$	1.29
	σ_{Mixed}	[fb]	$0.05847(2)^{+31.8\%}_{-22.4\%}$	$0.07651(8)^{+1.4\%}_{-6.5\%}$	1.31
	σ_{Decay}	[fb]	$0.022883(7)^{+30.5\%}_{-21.9\%}$	$0.02840(3)^{+0.8\%}_{-4.7\%}$	1.24

Table 4.1: *Integrated fiducial cross sections at LO and NLO QCD for $pp \to t\bar{t}\gamma\gamma$ in the di-lepton decay channel at the LHC with $\sqrt{s} = 13$ TeV. Results are presented for the full calculation and the three resonant contributions Prod., Mixed and Decay. The $\mu_0 = E_T/4$ and $\mu_0 = m_t$ scale settings and the NNPDF3.1 NLO PDF set are used. Scale uncertainties estimated by scale variation and MC integration errors are also displayed.*

$39\% - 40\%$ of the full calculation. Therefore, in the naive approach by using only the *Prod.* contribution and neglecting photon radiation in the decays of unstable particles, the cross section can be highly underestimated by more than a factor of 2. The *Mixed* contribution amounts to $43\% - 44\%$ of the full calculations, which is slightly larger than the *Prod.* contribution and the largest overall. Finally, the *Decay* contribution is about $16\% - 18\%$ of the full calculation and is thus about three times smaller than the *Prod.* or *Mixed* contributions. Nevertheless, this contribution is about three times larger than the NLO QCD scale uncertainties and therefore not negligible. Overall, we find that the size of the individual resonant configurations is rather constant with respect to the NLO QCD corrections, as can be seen from the size of the NLO QCD corrections of the full calculation and the *Prod.* and *Mixed* contributions, which are all around 30% for both scale choices. Only the NLO QCD corrections in the *Decay* contribution are slightly reduced to 17% for $\mu_0 = E_T/4$ and 24% for $\mu_0 = m_t$, which results in a slight reduction of the *Decay* contribution at NLO QCD.

In order to investigate the large contribution of photon bremsstrahlung originating from the top-quark and W-boson decays, we have split the full calculation as well as the resonant contributions at NLO QCD into the different production channels gg, $q\bar{q}$ and $qg + \bar{q}g$ as shown in Table 4.2, where bottom quarks are understood to be included in the definition of q. The predictions are given for the $\mu_0 = E_T/4$ scale, but the conclusions are the same for $\mu_0 = m_t$. In particular, we find that the full calculation is dominated by the gg channel with about 56%. In contrast, in $t\bar{t}$ production the gg channel dominates completely with almost 90% [113]. This already shows that photon bremsstrahlung disfavors the gluon induced channels. For the *Prod.* contribution, we even find that the gg channel is no

		gg	gg/pp	$q\bar{q}$	$q\bar{q}/pp$	$qg + \bar{q}g$	$(qg + \bar{q}g)/pp$
$\sigma^{\text{NLO}}_{\text{Full}}$	[fb]	0.0999(1)	56.4%	0.04307(4)	24.3%	0.03428(4)	19.3%
$\sigma^{\text{NLO}}_{\text{Prod.}}$	[fb]	0.02587(4)	36.3%	0.02672(4)	37.5%	0.01871(3)	26.2%
$\sigma^{\text{NLO}}_{\text{Mixed}}$	[fb]	0.04928(8)	63.7%	0.01408(2)	18.2%	0.01398(2)	18.1%
$\sigma^{\text{NLO}}_{\text{Decay}}$	[fb]	0.02476(4)	86.5%	0.002268(3)	7.9%	0.00160(2)	5.6%

Table 4.2: *Integrated fiducial cross sections at NLO QCD for $pp \to t\bar{t}\gamma\gamma$ in the di-lepton decay channel at the LHC with $\sqrt{s} = 13$ TeV. Results are presented for the full calculation and the three resonant contributions Prod., Mixed and Decay divided into the different production channels gg, $q\bar{q}$ and $qg/\bar{q}g$. The $\mu_0 = E_T/4$ scale setting and the NNPDF3.1 NLO PDF set are used. MC integration errors are also displayed.*

longer dominant, since it amounts to only 36.3% of all partonic subprocesses. In this case, the $q\bar{q}$ process is about the same size with 37.5% and even the $qg + \bar{q}g$, which first enters at NLO, amounts to 26.2%. This situation changes drastically in the case of the *Mixed* contribution, where the gg channel becomes dominant again with about 64% and even the absolute cross section increases by almost a factor of 2. On the other hand, the $q\bar{q}$ channel is only 18% and about half the size of the $q\bar{q}$ channel in the *Prod.* contribution in absolute values. From simple phase-space arguments, it is expected that the cross section in the *Mixed* contribution should decrease with respect to the *Prod.* contribution, because photon radiation in the decays of the unstable particles drastically limits the available phase space. This behavior coincides with the one of the $q\bar{q}$ and $qg+\bar{q}g$ channels, but differs significantly in the gg channel. A similar behavior can be found in the *Decay* channel, where the gg channel dominates with 87%, as expected from top-quark pair production, but also the absolute value of the integrated cross section is only reduced by a factor of 2 compared to *Mixed*, and is therefore similar in size as the *Prod.* one. Contrary, the absolute value of the $q\bar{q}$ channel is reduced by about a factor of 6. We conclude that the presence of photons in the production process heavily suppresses the gg channel, where the photons can only be radiated (at LO) from the top-quark line. This suppression is lifted off in the *Mixed* and *Decay* contributions where the suppression due to the limited phase space in the decay processes becomes relevant. However, it turns out that these two effects almost fully cancel each other out in the *Decay* contribution, so that the *Prod.* and *Decay* contributions are of the same size, and the *Mixed* contribution is almost as large as the other two combined.

Finally, in Table 4.3 we present the integrated fiducial cross section at NLO QCD using $\mu_0 = E_T/4$ for our default PDF set (NNPDF3.1 NLO), and the CT18NLO and MSHT20 NLO PDF sets. In addition, we display the corresponding internal PDF uncertainties as well as the scale uncertainties for comparison. The PDF uncertainties are in the range of 1% (NNPDF3.1) to 2% (CT18). Thus, these uncertainties are smaller by a factor of $3 - 6$ than the respective scale uncertainties at NLO and of minor importance at the current precision. The differences between the predictions using the three different PDF sets are well within the corresponding PDF uncertainties. The largest differences are found between

PDF set	$\sigma^{\text{NLO}}_{\text{Full}}$ [fb]	δ_{scale}	δ_{PDF}
NNPDF3.1	0.1773(1)	$^{+1.8\%}_{-6.2\%}$	$^{+1.0\%}_{-1.0\%}$
CT18	0.1730(2)	$^{+1.8\%}_{-6.2\%}$	$^{+1.9\%}_{-2.0\%}$
MSHT20	0.1742(2)	$^{+1.8\%}_{-6.2\%}$	$^{+1.4\%}_{-1.3\%}$

Table 4.3: *Integrated fiducial cross sections at NLO QCD for $pp \to t\bar{t}\gamma\gamma$ in the di-lepton decay channel at the LHC with $\sqrt{s} = 13$ TeV. Results are presented for the NNPDF3.1, CT18 and MSHT20 PDF sets using the $\mu_0 = E_T/4$ scale choice. Scale uncertainties from missing higher-orders are shown in δ_{scale} and internal PDF uncertainties in δ_{PDF}.*

the NNPDF3.1 and CT18 PDF sets of 2.4%.

4.3.2 Differential fiducial cross-section distributions

Already at the integrated level, we have seen that the NLO QCD corrections lead to sizeable effects, which are of the same size as the corresponding LO scale uncertainties. It is therefore important to extend this discussion at the differential level, where further shape distortions are possible. In addition, we are interested in the scale choice, whether the fixed scale is sufficient or should be even preferred in some cases. In Figure 4.2 we present the differential fiducial cross-section distributions for the transverse momentum and the invariant mass of the two-photon system, $p_{T,\gamma_1\gamma_2}$ and $M_{\gamma_1\gamma_2}$, and the observables H_T^{phot} and H_T^{vis}. Results are presented for the $pp \to t\bar{t}\gamma\gamma$ process in the *di-lepton* decay channel at the LHC with $\sqrt{s} = 13$ TeV. In particular, we show the LO (dashed) and the NLO QCD (solid) calculations for the $\mu_0 = E_T/4$ (blue) and $\mu_0 = m_t$ (orange) scale choices using the NNPDF3.1 PDF set. The lower two panels display the differential $\mathcal{K}$-factors of the two scale settings. The first two observables, $p_{T,\gamma_1\gamma_2}$ and $M_{\gamma_1\gamma_2}$, are interesting to study because they are the irreducible background to $p_{T,H}$ and M_H in the $pp \to t\bar{t}H$ process with $H \to \gamma\gamma$. For $\mu_0 = E_T/4$ we find large NLO QCD corrections up to 65% for $p_{T,\gamma_1\gamma_2}$ and 70% for $M_{\gamma_1\gamma_2}$, which exceed the LO uncertainties of about 35%. Employing the fixed scale of $\mu_0 = m_t$, the NLO QCD corrections are reduced to $22\% - 32\%$ for $p_{T,\gamma_1\gamma_2}$ and $26\% - 42\%$ for $M_{\gamma_1\gamma_2}$, providing better agreement with the LO predictions, especially in the tails. The NLO scale uncertainties increase towards the tails from 5% to 13%, while the scale uncertainties in the tails amount to 10% for the fixed scale. Also the differences in the central value between the two scale choices increase towards the tails from 2% to 5%, which are well within the corresponding uncertainty bands. The situation is very similar for the purely photonic observable H_T^{phot}, defined as

$$H_T^{phot} = p_{T,\,\gamma_1} + p_{T,\,\gamma_2}\,. \tag{4.21}$$

More precisely, the use of the fixed scale reduces the NLO QCD corrections from more than 55% to maximal 30%. Additionally, the NLO scale uncertainties are slightly reduced for $\mu_0 = m_t$ with 10% compared to 12% for $\mu_0 = E_T/4$. As for the last observables, differences up to 5% are found between the two scale settings. Lastly, for the H_T^{vis} observable, which

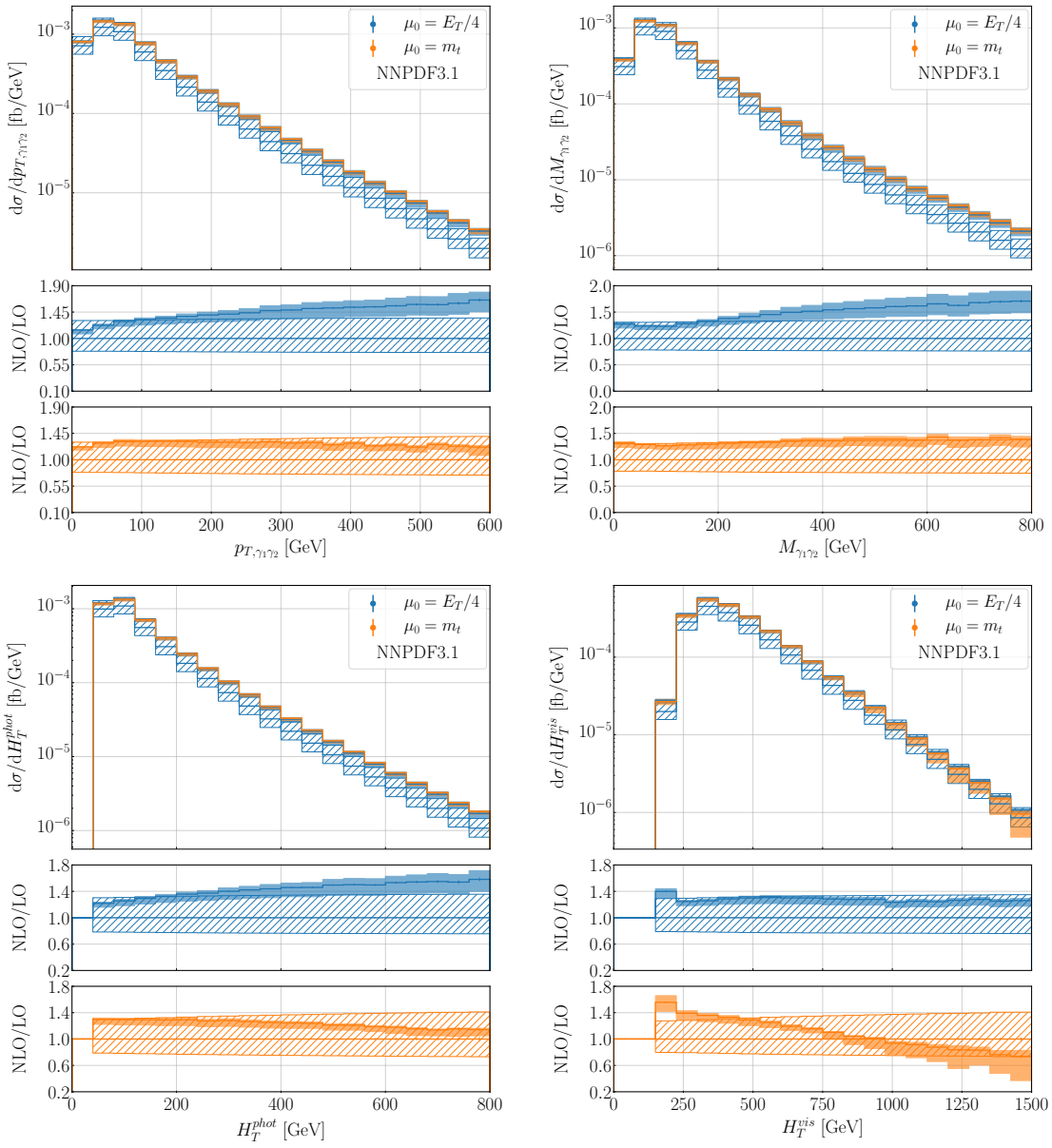

Figure 4.2: *Differential fiducial cross-section distributions for the observables* $p_{T,\gamma_1\gamma_2}$, $M_{\gamma_1\gamma_2}$, H_T^{phot} *and* H_T^{vis} *for* $pp \to t\bar{t}\gamma\gamma$ *in the di-lepton decay channel at the LHC with* $\sqrt{s} = 13$ TeV. *LO (dashed) and NLO QCD (solid) results are presented for the two scale choices* $\mu_0 = E_T/4$ *(blue) and* $\mu_0 = m_t$ *(orange) employing the NNPDF3.1 PDF set. The corresponding differential* $\mathcal{K}$*-factors are shown in the lower two panels. Scale uncertainties and MC integration errors are also displayed.*

is given by

$$H_T^{vis} = p_{T,\ell^+} + p_{T,\ell^-} + p_{T,b_1} + p_{T,b_2} + p_{T,\gamma_1} + p_{T,\gamma_2}, \tag{4.22}$$

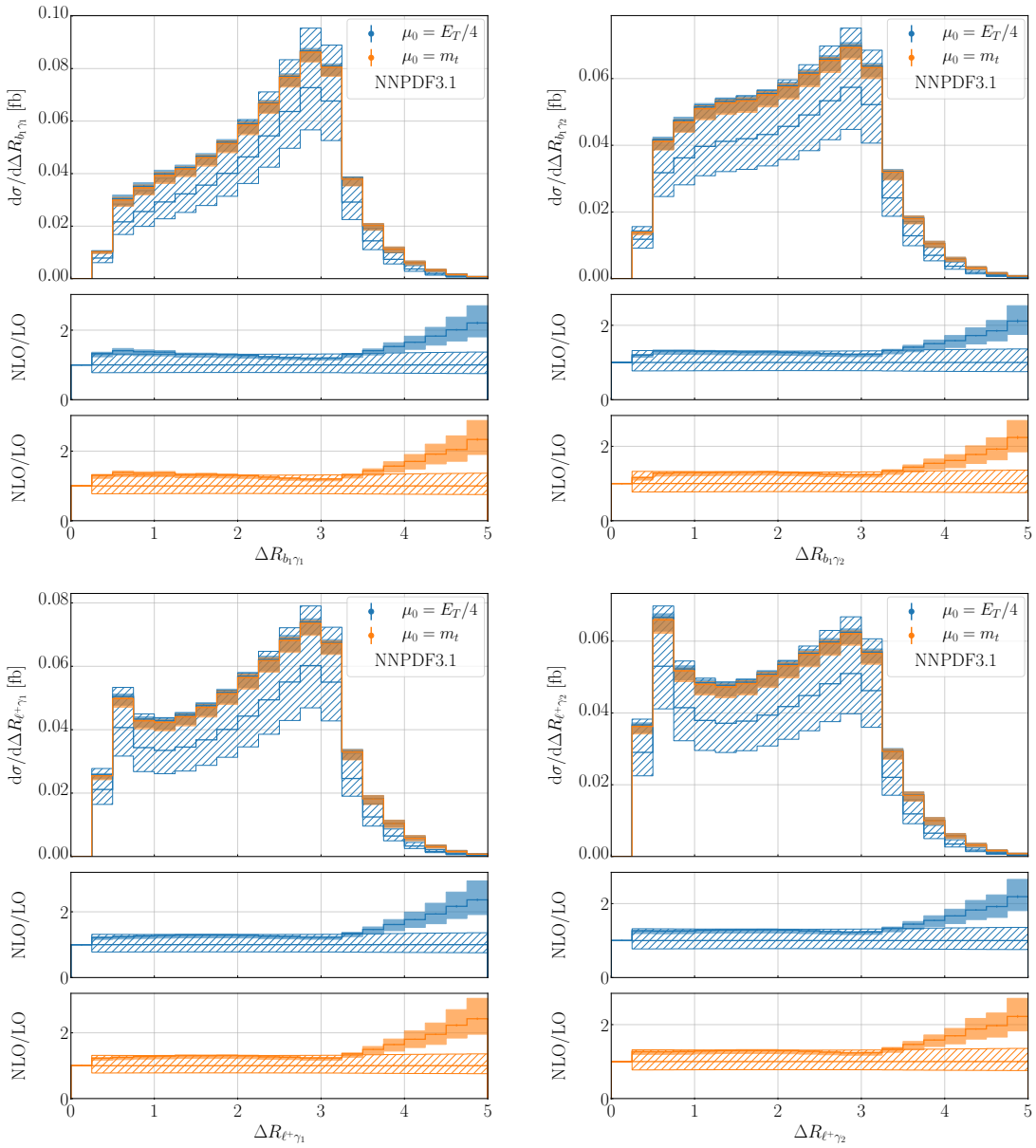

Figure 4.3: *Same as Figure 4.2 but for the observables* $\Delta R_{b_1\gamma_1}$, $\Delta R_{b_1\gamma_2}$, $\Delta R_{\ell^+\gamma_1}$ *and* $\Delta R_{\ell^+\gamma_2}$.

the overall picture is quite different. The $\mu_0 = E_T/4$ scale leads to rather constant NLO QCD corrections in the range of $25\% - 30\%$, which lie within the LO uncertainty bands. In contrast to the previous observables, H_T^{vis} is not purely given by the kinematics of the two photons and we find that the scale $\mu_0 = m_t$ leads to unstable results in the tail of this distribution. In particular, the NLO QCD corrections constantly decrease towards the tail and reach up to -30%, where NLO scale uncertainties of about 50% are found, exceeding the LO ones.

At next we present in Figure 4.3 the ΔR_{ij} separations between the hardest b-jet and the hardest/second hardest photon, $\Delta R_{b_1\gamma_1}$ and $\Delta R_{b_1\gamma_2}$, and the ΔR separations between ℓ^+ and the hardest/second hardest photon, $\Delta R_{\ell^+\gamma_1}$ and $\Delta R_{\ell^+\gamma_2}$. These observables can be used to study the prompt photon distribution. All four angular distributions have a peak at about $\Delta R_{ij} \approx 3$, indicating that the top-quark decay products and the two isolated photons are preferably produced in back-to-back configurations. On the other hand, a second peak is found for $\Delta R_{\ell^+\gamma_1}$ and $\Delta R_{\ell^+\gamma_2}$ at small angular separations, which is completely absent for $\Delta R_{b_1\gamma_1}$ and only a small enhancement is found for $\Delta R_{b_1\gamma_2}$. This clearly shows that photons are radiated more collinearly with respect to the charged leptons, either due to photon emission in W-boson decays ($W^+ \to \ell^+\nu_\ell\gamma$) or collinear emission of photons from W bosons in top-quark decays ($t \to W^+b\gamma$). The size of the NLO QCD corrections for both scale settings is very similar for all four observables and is usually within the LO uncertainty bands below $\Delta R_{ij} \approx 3$. In this region, the largest NLO QCD corrections of about 40% are found for the $\Delta R_{b_1\gamma_1}$ observable at the beginning of the spectrum. In addition, the scale uncertainties are reduced from $30\% - 35\%$ at LO to $5\% - 8\%$ at NLO QCD. The NLO QCD corrections are significantly enhanced for ΔR_{ij} separations above 3 and reach more than 100%. On the other hand, the absolute size of the differential cross-section distribution also decreases rapidly in this region. The central predictions between the two scale settings only differ by at most $2\% - 3\%$, showing that in angular distributions both scale choices can be safely used as at the integrated fiducial level.

Finally, we concentrate on the kinematics of the usual $t\bar{t}$ decay products and show the $M_{b_1b_2}$, p_{T,b_1b_2}, $\Delta R_{b_1b_2}$ and $\Delta\Phi_{\ell^+\ell^-}$ observables in Figure 4.4. The $M_{b_1b_2}$ observable generally resembles the behavior of H_T^{vis}. Again, the $\mu_0 = E_T/4$ scale leads to rather flat NLO QCD corrections in the range of $25\% - 30\%$, which are within the LO scale uncertainties. The fixed scale leads to a continuous decrease of the distribution towards the tails, while simultaneously the NLO scale uncertainties increase up to 20%. Probing even higher values of $M_{b_1b_2}$ would lead to the same conclusion as for H_T^{vis}, that the NLO uncertainty bands would exceed the LO ones. When using the dynamical scale $\mu_0 = E_T/4$, the scale uncertainties are reduced to 8% at NLO. The p_{T,b_1b_2} distribution is part of a special class of observables, which are well known to be affected by large NLO QCD corrections [107, 110, 260, 262, 349]. In particular, large values of the p_{T,b_1b_2} observable are suppressed at LO, because the two top quarks are produced back-to-back. This means that the transverse momentum of the b_1b_2 system cancels to a large extent, even though the transverse momenta of the b-jets can be large. Such effects, but suppressed, can be seen for similar observables like p_T^{miss} or $p_{T,\,\ell^+\ell^-}$, which are also built from the decay products of the two top quarks. This kinematic suppression of p_{T,b_1b_2} in the tail is lifted at NLO QCD due to the presence of additional hard jets which recoil against the $t\bar{t}$ system. In this case, the two top-quarks and their decay products are not produced back-to-back, and larger values of p_{T,b_1b_2} are possible. Even though two additional photons are present in this process, which partially removes this kinematic suppression, we still encounter huge NLO QCD corrections of more than 300% for $\mu_0 = E_T/4$ and 200% for $\mu_0 = m_t$ in the tail. In particular, we have checked that the NLO QCD corrections for the *Prod.* contribution are similar to those for the full process, while the NLO QCD corrections for the *Mixed* and *Decay* contributions are further enhanced to 400% and 900%, respectively. Thus, we find that the suppression of the LO prediction is reduced with an increasing number of photons in the production process, but the NLO QCD corrections remain enormous. The central

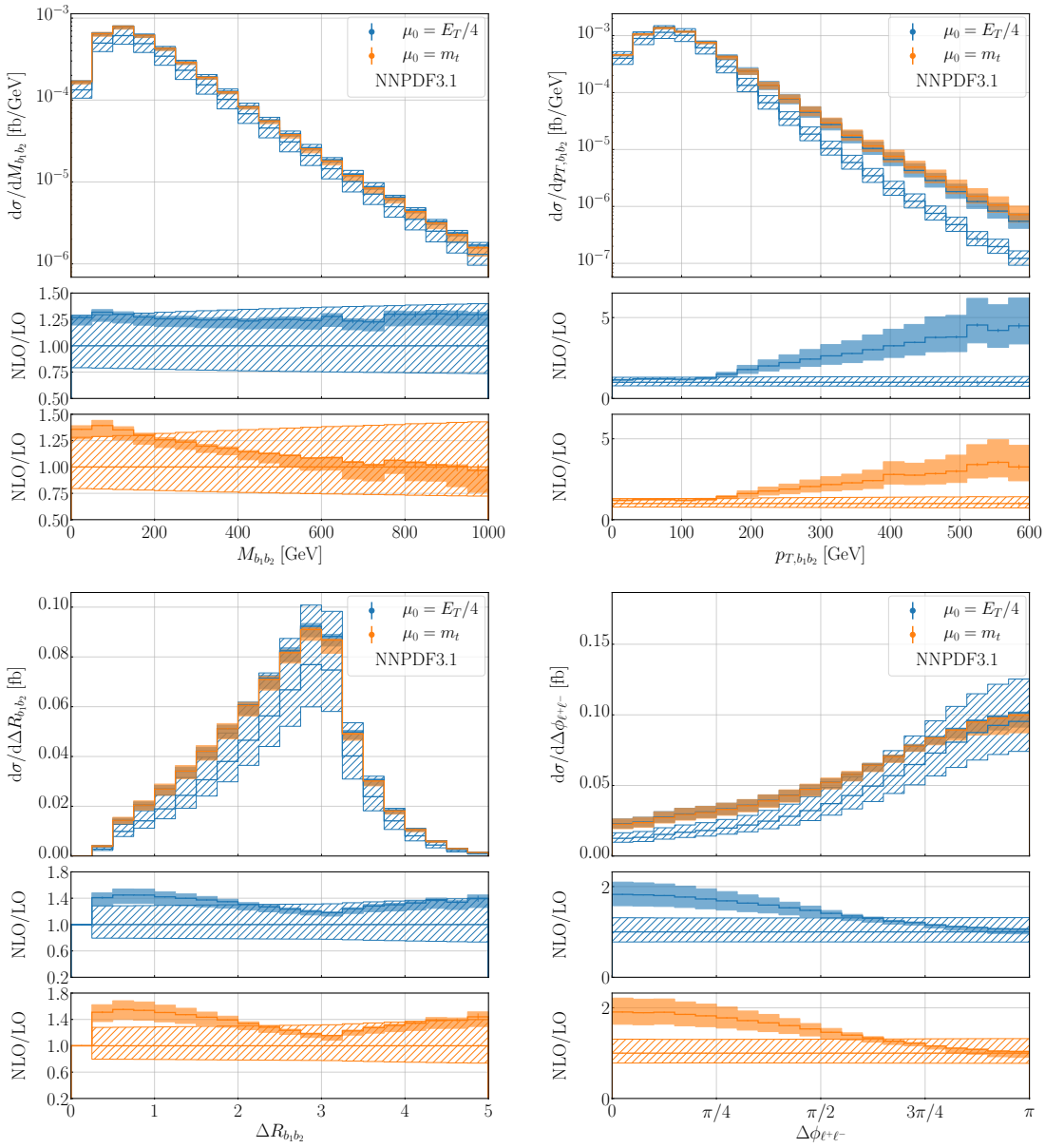

Figure 4.4: *Same as Figure 4.2 but for the observables* $M_{b_1b_2}$, p_{T,b_1b_2}, $\Delta R_{b_1b_2}$ *and* $\Delta\Phi_{\ell^+\ell^-}$.

predictions between the two scale settings differ by about 30% in the tail. These large differences originate from the huge NLO QCD corrections, so that this region is populated by the real corrections with additional hard jet radiation and is thus only described with LO precision. Therefore, large scale uncertainties of about 40% at NLO can be found in this phase-space region, which are of the same size as the LO scale uncertainties. Large NLO QCD corrections are not only restricted to the tails of dimensionful observables, but are also present in the case of angular distributions, as in the case of $\Delta R_{b_1b_2}$ and $\Delta\Phi_{\ell^+\ell^-}$. For $\Delta R_{b_1b_2}$ we find large QCD corrections of up to 45% for $\mu_0 = E_T/4$ and 55% for $\mu_0 = m_t$

for small angular separations, while the corrections are reduced to $15\% - 20\%$ in the bulk of the distribution in the back-to-back region at $\Delta R_{ij} \approx 3$. Thus, shape distortions of up to 30% are found and therefore the higher-order corrections cannot be approximated by an overall $\mathcal{K}$-factor applied to all bins. The scale uncertainties are reduced in the bulk from 30% at LO to 5% at NLO, which further increase up to 10% towards smaller and larger angular separations. Finally, we find QCD corrections up to 80% for $\mu_0 = E_T/4$ and 90% for $\mu_0 = m_t$ for $\Delta\Phi_{\ell^+\ell^-}$. These corrections decrease to a few percent towards larger angles. Similarly, the NLO scale uncertainties of about 15% at the beginning of the spectrum reduce to $5\% - 10\%$ towards larger separations in the azimuthal plane. The central values between the two scale choices differ at most by 2% for both angular distributions.

4.3.3 Prompt photon distribution at the differential level

In the last part of the discussion in the *di-lepton* decay channel, we focus on the prompt photon distribution in differential distributions. In Figure 4.5 we present the differential fiducial cross-section distributions of $p_{T,\gamma_1\gamma_2}$, H_T^{vis}, $M_{b_1b_2}$ and p_{T,b_1b_2} at NLO QCD for the full calculation as well as the three resonant contributions *Prod.*, *Mixed* and *Decay*. Results are shown for $\mu_0 = E_T/4$ and the NNPDF3.1 PDF set. The lower panels display the relative size of the different resonant contributions with respect to the full calculation. Similar to the integrated level, the beginning of the spectrum of $p_{T,\gamma_1\gamma_2}$, which represents the bulk of the distribution, is dominated by *Mixed* with up to 47% of the full calculation. The *Decay* contribution also has sizeable effects with up to 32% in this region, but it drops off rapidly towards higher energies. Above $p_{T,\gamma_1\gamma_2} > 300$ GeV, this contribution is less than 1% and therefore negligible with respect to the theoretical uncertainties. The *Prod.* contribution behaves oppositely to the other two. At the beginning of the spectrum, the *Decay* and *Prod.* contributions are equal in size, while the latter increases continuously towards the tail to more than 80% of the full calculation. Therefore, the *Prod.* contribution is clearly dominating at high energies, but still the *Mixed* contribution can be as large as 20% and cannot be neglected with respect to the scale uncertainties of about 12%. Furthermore, these high-energy regions are not yet accessible by current measurements, while the bulk of the distribution at the beginning of the spectrum can be already probed, where all three resonant contributions have to be consistently included for accurate predictions. The overall behaviour of H_T^{vis} is very similar. In this case, the first bin is even dominated by the *Decay* contribution with 60%, but it again falls rapidly to less than 1% above $H_T^{vis} > 750$ GeV. At the beginning of the spectrum, the *Prod.* contribution only amounts to 7% of the full calculation, but in the tail it dominates again with more than 90%. The *Mixed* contribution is again the most important one at small energies with up to 50% and decreases towards the tails to less than 10%, thus becoming comparable in size to the scale uncertainties. Also in the case of hadronic observables like $M_{b_1b_2}$ and p_{T,b_1b_2} this behaviour is not altered. In particular, the *Mixed* contribution is as large as 45% in the bulk of the distributions and decreases to $20\% - 25\%$ in the tails, thus remaining non-negligible. The tails are again dominated by *Prod.* with $70\% - 80\%$ and still remains important at the start of the spectra with about 30%. Finally, the *Decay* contribution is about $20\% - 25\%$ of the full calculation at small energies, but in contrast to the two photonic observables described before, it remains above 1% over the whole spectra. Therefore, the decrease of the *Decay* contribution is still significant, but less pronounced compared to photonic

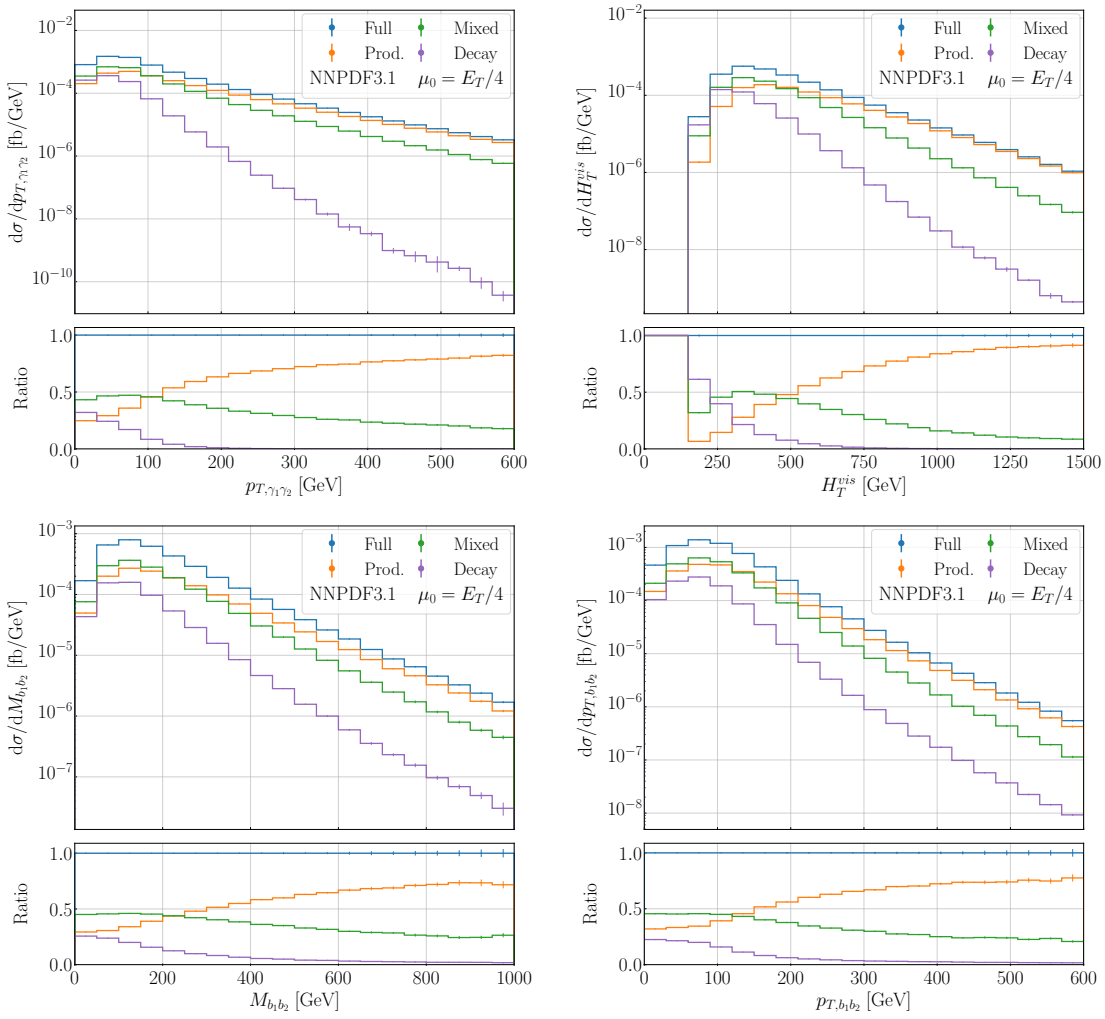

Figure 4.5: *Differential fiducial cross-section distributions at NLO QCD for the observables $p_{T,\gamma_1\gamma_2}$, H_T^{vis}, $M_{b_1b_2}$ and p_{T,b_1b_2} for $pp \to t\bar{t}\gamma\gamma$ in the di-lepton decay channel at the LHC with $\sqrt{s} = 13$ TeV. Results are shown for the full calculation as well as the resonant contributions Prod., Mixed and Decay with $\mu_0 = E_T/4$ and NNPDF3.1 PDF. Ratios to the full calculation are shown in the lower panels and MC integration errors are also given.*

observables. For $M_{b_1b_2}$ this contribution still remains comparable in size with respect to the scale uncertainties at around $M_{b_1b_2} \approx 500$ GeV.

Next, we discuss the prompt photon distribution in angular observables and focus on the same distributions as in the discussion of NLO QCD corrections. In particular, in Figure 4.6 we show the observables $\Delta R_{b_1\gamma_1}$, $\Delta R_{b_1\gamma_2}$, $\Delta R_{\ell^+\gamma_1}$ and $\Delta R_{\ell^+\gamma_2}$. The relative size of the *Mixed* contribution is quite constant for all four observables with about $40\% - 54\%$. The *Prod.* and *Decay* contributions behave again rather oppositely. The latter one is the largest one for small angular separations ranging between $23\% - 41\%$ and decreases for larger values of ΔR_{ij} to about 5%. Finally, the *Prod.* contribution increases from $10\% - 23\%$

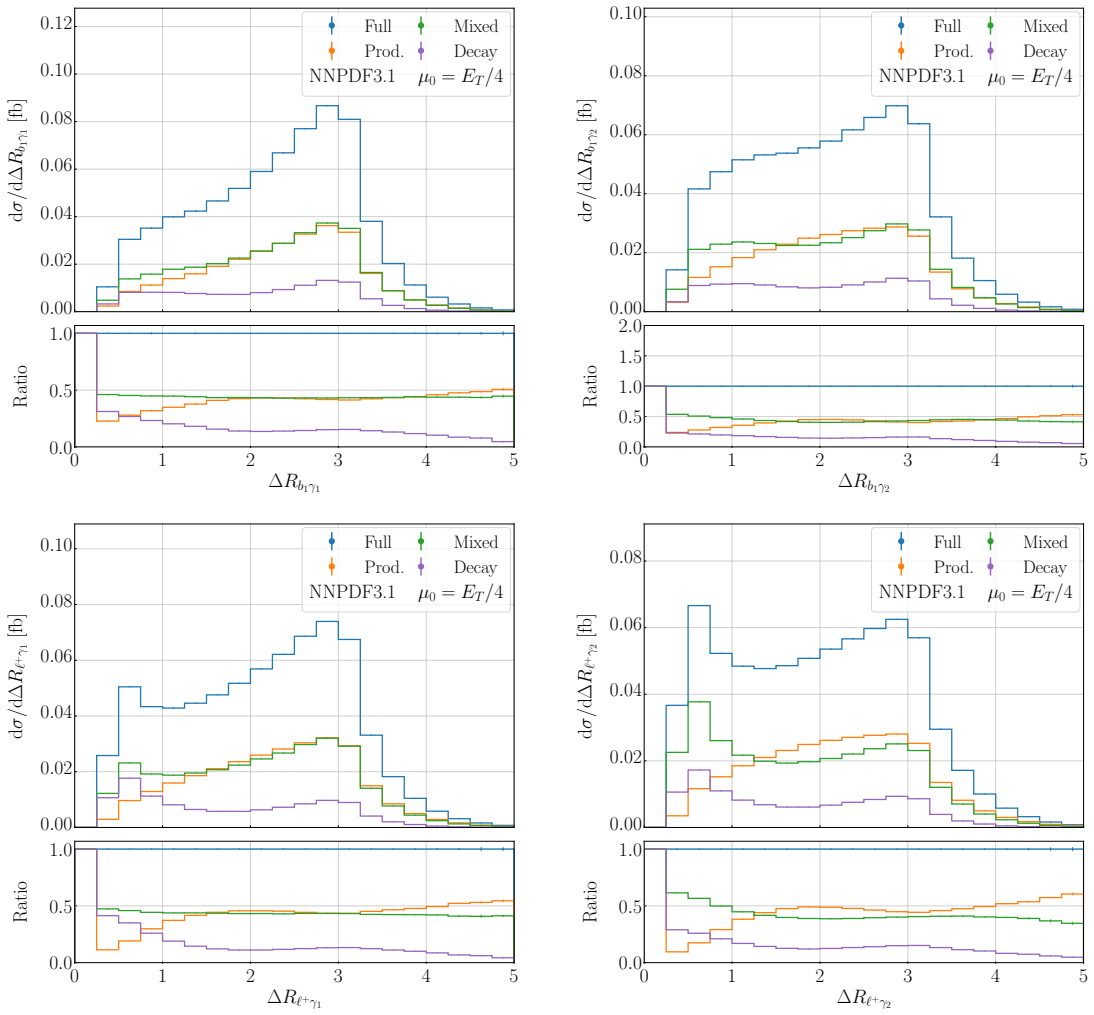

Figure 4.6: *Same as Figure 4.5 but for the observables* $\Delta R_{b_1\gamma_1}$, $\Delta R_{b_1\gamma_2}$, $\Delta R_{\ell^+\gamma_1}$ *and* $\Delta R_{\ell^+\gamma_2}$.

to about $50\% - 60\%$ towards larger angular separations. The different behaviours can be understood as follows. The suppression of the *Prod.* contribution at small ΔR_{ij} is due to the enhancements in *Mixed* and *Decay*, where photons are radiated in the top-quark and W-boson decays. Especially in the case of $\Delta R_{\ell^+\gamma_1}$ and $\Delta R_{\ell^+\gamma_2}$, these two contributions are enhanced due to photon radiation off W bosons in top-quark decays and photon radiation in W-boson decays, resulting in a second peak at small angular separations. This peak is completely absent in $\Delta R_{b_1\gamma_1}$ and only a slight enhancement can be found in $\Delta R_{\ell^+\gamma_2}$. On the one hand, this shows that such collinear photon radiation to the decay products is purely originating from the *Mixed* and *Decay* contribution, which would be completely missing if photon radiation is not properly taken into account in the whole decay chain. On the other hand, the differences between the leptonic and hadronic angular separations show that prompt photon radiation off charged lepton is preferred compared to the case

of b-jets. At $\Delta R_{ij} \approx 3$, a peak is found for all three resonant contributions, where the photons and charged leptons/b-jets are produced back-to-back. In this region, the *Prod.* and *Mixed* contributions become similar in size with about $40\% - 45\%$ of the full calculation. However, the *Decay* contribution remains significant with about $10\% - 15\%$. In conclusion, it is generally important to properly include prompt photon radiation from all decay stages to obtain accurate results. The effects from photon radiation in top-quark and W-boson decays cannot be obtained by simple reweighting, since their size depends highly on the specific phase-space region.

4.4 Lepton + jet channel

4.4.1 Integrated fiducial cross sections

In next step, we turn to the $pp \to t\bar{t}\gamma\gamma$ process in the *lepton + jet* decay channel and start with the discussion of the integrated fiducial cross section. Generally, we are interested in possible similarities and differences compared to the *di-lepton* decay channel. The first difference, which is directly apparent from the different final states, is that in the *lepton + jet* decay channel the decays of the two top quarks are no longer symmetric. In this case, one W boson decays into a lepton-neutrino pair and the other one decays into two quarks (jets). Therefore, the prompt photon distribution might differ due to the different number of charged particles and their different charges. In addition, the applied phase-space cuts are not the same for the decay products of the two W bosons, which can further enhance this asymmetry between the two top quarks. As already mentioned before, in the *lepton + jet* decay channel we apply an additional cut where we require that the invariant mass of at least one pair of resolved light jets lies within a window around the W-boson mass. This cut is used to suppress kinematic configurations in the real corrections where one of the two jets from the W-boson decays is unresolved or the two jets from the W-boson decay are recombined into a single jet, and additional jet radiation in the production of $t\bar{t}$ gives rise to a second hard jet. Such cases are not included in the Born process due to the requirement of at least two resolved light jets, which means that at LO both jets of the W boson decay have to be resolved and are not allowed to be recombined or unresolved. Therefore, the inclusion of such events in the real corrections can significantly enhance the size of NLO QCD corrections, since such configurations are not included at LO and additional jets produced in the production of $t\bar{t}$ are not affected by the (finite) masses of the top quark and the W boson, which limit the available phase space of the two jets originating from the W-boson decay. Thus, the additional cut is used to suppress kinematic configurations in which the two jets of the W boson are not resolved. Since such a cut was not required in the *di-lepton* decay channel, we investigate in the following the dependence of the NLO QCD corrections on this cut by varying Q_{cut} in the condition

$$|m_W - M_{jj}| < Q_{\text{cut}}. \tag{4.23}$$

In particular, we vary Q_{cut} between 5 GeV and 50 GeV in 5 GeV steps. The LO and NLO QCD cross sections as a function of Q_{cut} with the corresponding scale uncertainties are shown in Figure 4.7 for the full calculation as well as the three resonant contribution *Prod.*, *Mixed* and *Decay*. The results are presented for $\mu_0 = E_T/4$ and the NNPDF3.1

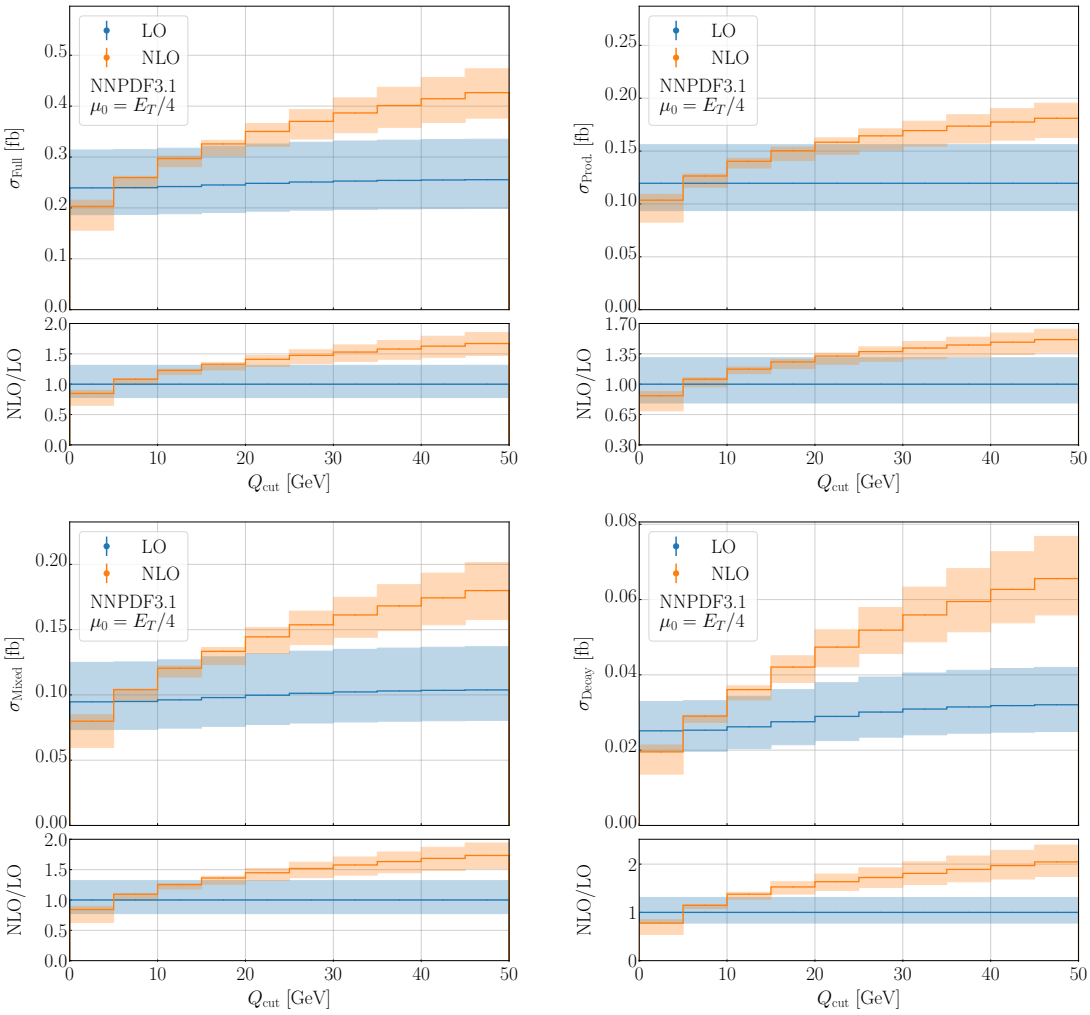

Figure 4.7: *Integrated fiducial cross sections at LO and NLO QCD for* $pp \to t\bar{t}\gamma\gamma$ *in the lepton + jet decay channel at the LHC with* $\sqrt{s} = 13$ TeV *as a function of* Q_{cut} *with the condition* $|m_W - M_{jj}| < Q_{\text{cut}}$*. Results are presented for the full calculation and three resonant contributions Prod., Mixed and Decay with* $\mu_0 = E_T/4$ *and NNPDF3.1 PDF. Lower panels display the* $\mathcal{K}$*-factor and the corresponding scale uncertainties are shown.*

PDF set. The lower panels display the corresponding $\mathcal{K}$-factors. At LO, we find only a small dependence on Q_{cut}, since in the two extreme cases of $Q_{\text{cut}} = 5$ GeV and no cut ($Q_{\text{cut}} \to \infty$) the full calculations differ by only 7%. The Q_{cut} dependence at LO originates solely from the resonant histories where one or two photons are emitted from the hadronically decaying W boson. Therefore, the *Prod.* contribution is independent of Q_{cut} and only a weak dependence can be found for the full calculation. In contrast, at NLO QCD the dependence is significantly enhanced due to the configurations described above, where the two light quarks from the W-boson decay lead to only a single resolved jet and the second hard jet is produced in the production of $t\bar{t}$. In particular, we find

μ_0			LO	NLO	$\mathcal{K} = \sigma_{\text{NLO}}/\sigma_{\text{LO}}$
$E_T/4$	σ_{Full}	[fb]	$0.24214(4)^{+31.1\%}_{-22.0\%}$	$0.2973(3)^{+1.9\%}_{-5.4\%}$	1.23
	$\sigma_{\text{Prod.}}$	[fb]	$0.11960(3)^{+30.5\%}_{-21.6\%}$	$0.1405(2)^{+2.1\%}_{-4.6\%}$	1.17
	σ_{Mixed}	[fb]	$0.09632(3)^{+31.9\%}_{-22.5\%}$	$0.1205(2)^{+1.5\%}_{-5.7\%}$	1.25
	σ_{Decay}	[fb]	$0.026230(9)^{+30.9\%}_{-22.1\%}$	$0.03629(7)^{+3.3\%}_{-7.7\%}$	1.38
m_t	σ_{Full}	[fb]	$0.23898(4)^{+31.2\%}_{-22.1\%}$	$0.2948(3)^{+1.6\%}_{-5.4\%}$	1.23
	$\sigma_{\text{Prod.}}$	[fb]	$0.12107(3)^{+31.0\%}_{-21.8\%}$	$0.1402(2)^{+1.8\%}_{-4.2\%}$	1.16
	σ_{Mixed}	[fb]	$0.09340(3)^{+31.8\%}_{-22.4\%}$	$0.1193(3)^{+1.4\%}_{-6.0\%}$	1.28
	σ_{Decay}	[fb]	$0.024500(9)^{+30.4\%}_{-21.8\%}$	$0.03534(7)^{+4.3\%}_{-8.2\%}$	1.44

Table 4.4: *Same as Table 4.1 but for the lepton + jet decay channel.*

NLO QCD corrections of about 140% when no cut is applied. These large higher-order corrections are reduced to 67% for $Q_{\text{cut}} = 50$ GeV and to 41% for $Q_{\text{cut}} = 25$ GeV, where in the latter case the LO and NLO QCD corrections start to overlap within the uncertainty bands. Our default choice of $Q_{\text{cut}} = 15$ GeV corresponds to the third bin where the NLO QCD prediction lies in the LO uncertainty band. Since these large NLO QCD corrections originate from kinematic configurations with hard additional radiation, these contributions are described only at LO accuracy, so that larger scale uncertainties can be found for the NLO QCD calculation compared to the *di-lepton* decay channel. In particular, scale uncertainties of about 23% at NLO are found when no cut is applied on the invariant mass, which is almost four times as large size as in the *di-lepton* decay channel. For our default choice, the scale uncertainties are reduced to 5.4% and become equal to those in the *di-lepton* decay channel. These large NLO QCD corrections are further enhanced in the *Mixed* and *Decay* contributions, where one or two photons are produced in the decays of top quarks and W bosons, leading to an additional suppression of the phase space of the two light jets originating from the W-boson decay. Therefore, the NLO QCD corrections increase to 150% for *Mixed* and 200% for *Decay* when no cut is applied. These are reduced to 25% and 38% for our standard choice of $Q_{\text{cut}} = 15$ GeV. Finally, the impact on *Prod.* is the smallest, where we still find NLO QCD corrections of more than 100% for no cut, which are reduced to 17% for $Q_{\text{cut}} = 15$ GeV.

In Table 4.4 we present the numerical values of the LO and NLO QCD cross sections of the $pp \to t\bar{t}\gamma\gamma$ process in the *lepton + jet* decay channel. In particular, we again show results for the two scale choices $\mu_0 = E_T/4$ and $\mu_0 = m_t$ for the full calculation as well as for the three resonant contributions *Prod.*, *Mixed* and *Decay*. As mentioned above, for our default choice of $Q_{\text{cut}} = 15$ GeV, we find NLO QCD corrections of about 23% for $\mu_0 = E_T/4$, which are equal in size as those for $\mu_0 = m_t$. Therefore, the NLO QCD corrections of the full calculation are within the LO scale uncertainties for both scale settings. The largest NLO QCD corrections are found for the *Decay* contribution

	$\sigma^{\text{NLO}}_{\text{Full}}$ [fb]
$\epsilon_\gamma = 1.0$	$0.2973(3)^{+1.9\%}_{-5.4\%}$
$\epsilon_\gamma = 0.5$	$0.2832(7)^{+1.5\%}_{-4.2\%}$
$E_{T,\gamma}\,\epsilon_\gamma = 10$ GeV	$0.2666(8)^{+1.0\%}_{-7.2\%}$

Table 4.5: *Integrated fiducial cross sections at NLO QCD for $pp \to t\bar{t}\gamma\gamma$ in the lepton + jet decay channel at the LHC with $\sqrt{s} = 13$ TeV. Results are presented for three different parameter choices of the smooth-cone isolation. The scale $\mu_0 = E_T/4$ and the NNPDF3.1 PDF set are used. Scale uncertainties estimated by scale variation and MC integration errors are also displayed.*

with about 38% for $\mu_0 = E_T/4$ and 44% for $\mu_0 = m_t$, which is also the case where the predictions of the two scale choices differ at most with about 2.5%. These differences are reduced to less than 1% for all other resonant contributions. The scale uncertainties are reduced by almost a factor of 6 from 31% at LO to 5.4% at NLO QCD. The relative size of the individual resonant contributions slightly deviates from those found in the *di-lepton* decay channel. In particular, the *Prod.* contribution amounts to 50% at LO and 48% at NLO QCD of the full calculation and is thus the largest contribution at the integrated level. The *Mixed* contribution is slightly smaller and is about 40% of the full calculation, while *Decay* is only 10% at LO and 12% at NLO QCD. The increase of *Prod.* with respect to the *di-lepton* decay channel is due to the additional cut on the invariant mass of at least one light jet pair. Indeed, by omitting this cut, the *Prod.* contribution decreases to 40% and the *Mixed* contribution increases to 43%, recovering the relative contributions of the *di-lepton* decay channel.

The use of the smooth-cone isolation introduces an additional (unknown) uncertainty in comparisons with experimental measurements, where the fixed-cone isolation is usually used, if no dedicated tuning to an alternative calculation with the fixed-cone isolation is performed. The dependence on these parameters increases with a large number of jets and photons, as for example in the *lepton + jet* decay channel, where at NLO QCD we have 5 jets and 2 photons in the final state. Since different parameters are used in the literature [11, 212, 479–487], we briefly examine the dependence by modifying the prefactor of the smooth-cone isolation defined in Eq. (2.45). In particular, in Table 4.5 we present numerical results using $\mu_0 = E_T/4$ and the NNPDF3.1 PDF set for our default choice of $\epsilon = 1.0$ and the two alternatives $\epsilon = 0.5$ and $E_{T,\gamma}\,\epsilon_\gamma = 10$ GeV, where the latter choice is inspired by other recent calculations of isolated photon cross sections. We find that these modifications lead to a reduction of the cross section by about 5% and 10%, respectively. Thus, these differences are not covered by the scale uncertainties at NLO, and a dedicated tuning of these parameters would be required to avoid any inconsistencies with respect to the experimental setup. These effects are reduced in the *di-lepton* decay channel to about 3% and 6%, respectively. Therefore, the differences in the *di-lepton* decay channel obtained with different input parameters are also as large as the corresponding scale uncertainties and could affect a comparison between experimental measurements and

theoretical predictions. This brief comparison of different input parameters should only be considered as an exemplary study to highlight the strong dependence on these parameters. A more detailed discussion of the different photon isolation conditions is presented for the simpler $pp \to t\bar{t}\gamma$ process in the *di-lepton* decay channel in Chapter 6, where less photons and jets are present in the final state.

4.4.2 Differential fiducial cross-section distributions

We continue the discussion of the $pp \to t\bar{t}\gamma\gamma$ process in the *lepton + jet* decay channel with the study of NLO QCD corrections in differential fiducial cross-section distributions. We present in Figure 4.8 the distributions of the $\Delta R_{b_1\gamma_1}$, $\Delta R_{b_1\gamma_2}$, $\Delta R_{\ell^+\gamma_1}$ and $\Delta R_{\ell^+\gamma_2}$ observables. The structure of the plots is identical to those for the *di-lepton* decay channel and show the results for the two scale choices $\mu_0 = E_T/4$ (blue) and $\mu_0 = m_t$ (orange) at LO (dashed) and at NLO QCD(solid). For the two hadronic observables p_{T,b_1}, p_{T,b_1b_2}, we find huge NLO QCD corrections of more than 350% and 800% for $\mu_0 = E_T/4$. These higher-order corrections are substantially larger than in the *di-lepton* decay channel, and still arise from large real corrections with an additional hard jet in the production of $t\bar{t}$, which recoils against the $t\bar{t}$ system and additionally softens the phase-space constraints of the top-quark decay products in the case where this jet is misidentified as a decay product of the W boson. In contrast to the *di-lepton* decay channel, a simple jet veto on the softest jet in the case of three jets in the final state would not significantly reduce these corrections. Since the tails are dominated by hard jet radiation, these phase-space regions are only described with LO accuracy, as can be directly seen from the NLO scale uncertainties in the range of 30% to 45%, exceeding the LO ones of about 35%. The alternative scale choice, $\mu_0 = m_t$, does not lead to any improvements. In addition, the differences in the central value between the two scale settings are as large as the scale uncertainties. On the other hand, for the two photonic observables p_{T,γ_1} and p_{T,γ_2} the situation is similar as in the case of the photonic observables in the *di-lepton* decay channel. In particular, we find NLO QCD corrections of about $15\% - 20\%$ in the bulk of the distributions at the beginning of the spectra, which increase to $40\% - 50\%$ in the tails. Thus, the NLO QCD corrections in the tails are larger than the corresponding LO uncertainty bands. As in the *di-lepton* decay channel, we find that the use of $\mu_0 = m_t$ leads to a reduction of the NLO QCD corrections in photonic observables. In this case, the higher-order effects are reduced to less than 10% in the tails. For $\mu_0 = E_T/4$ the scale uncertainties increase towards higher energies from 5% to 10%. The fixed scale resembles this behavior for p_{T,γ_1}, while for p_{T,γ_2} larger scale uncertainties of about 15% are found in the tail. The central predictions between the two scale settings do not differ by more than 5%.

In Figure 4.9 we show the differential distributions of the observables $p_{T,\gamma_1\gamma_2}$, $M_{\gamma_1\gamma_2}$, $\Delta R_{\ell^-\gamma_1}$ and $\Delta R_{\ell^-\gamma_2}$. The situation is very similar for the photonic observables $p_{T,\gamma_1\gamma_2}$ and $M_{\gamma_1\gamma_2}$ compared to the last two and to those in the *di-lepton* decay channel. In particular, we find that the NLO QCD corrections increase towards the tails from $10\% - 20\%$ to $50\% - 60\%$ using $\mu_0 = E_T/4$. The fixed scale choice leads to a reduction to $20\% - 30\%$ at high energies, improving the agreement within the LO scale uncertainties. While for $\mu_0 = E_T/4$ we find scale uncertainties of about 12% in the tails, these are slightly reduced to $7\% - 8\%$ for $\mu_0 = m_t$. The central values differ by 6% at most. The two spectra $\Delta R_{\ell^-\gamma_1}$ and $\Delta R_{\ell^-\gamma_2}$ are very similar to the counter parts in the *di-lepton* decay channel. We find

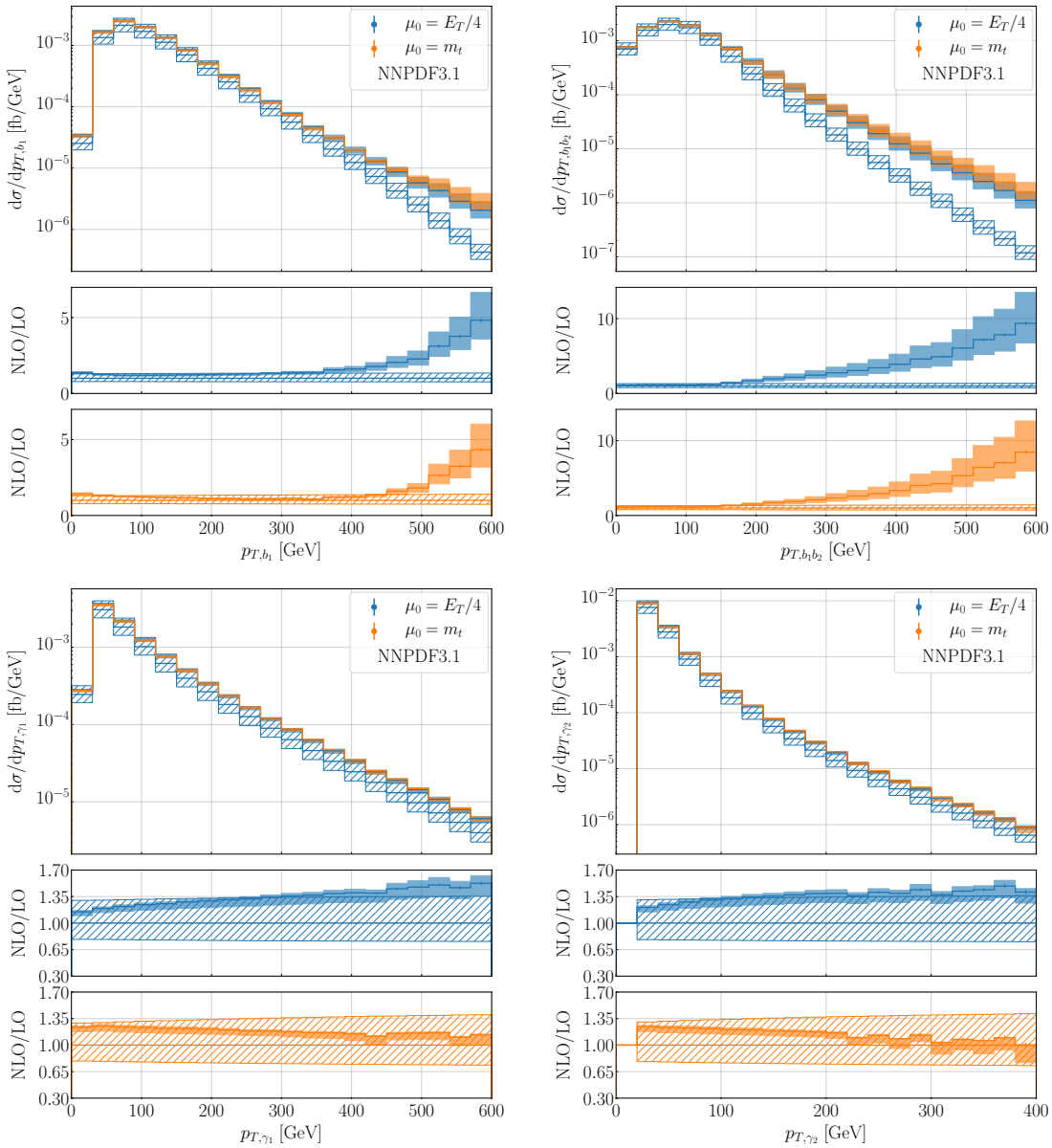

Figure 4.8: *Same as Figure 4.2 but for the lepton + jet decay channel for the observables* p_{T,b_1}, p_{T,b_1b_2}, p_{T,γ_1} *and* p_{T,γ_2}.

again two peaks in both distributions, where the first comes from photon radiation off the W boson in the top-quark decay and photon radiation in the W-boson decay, and the second originates from back-to-back configurations. Again, the latter peak is enhanced for the hardest photon and the first peak for the second hardest photon. The NLO QCD corrections are about $15\% - 20\%$ for both scale settings below the second peak at around $\Delta R_{ij} \approx 3$. Afterwards, the higher-order corrections increase significantly to more than 100% as in the *di-lepton* decay channel. Below $\Delta R_{ij} \approx 3$ the scale uncertainties are

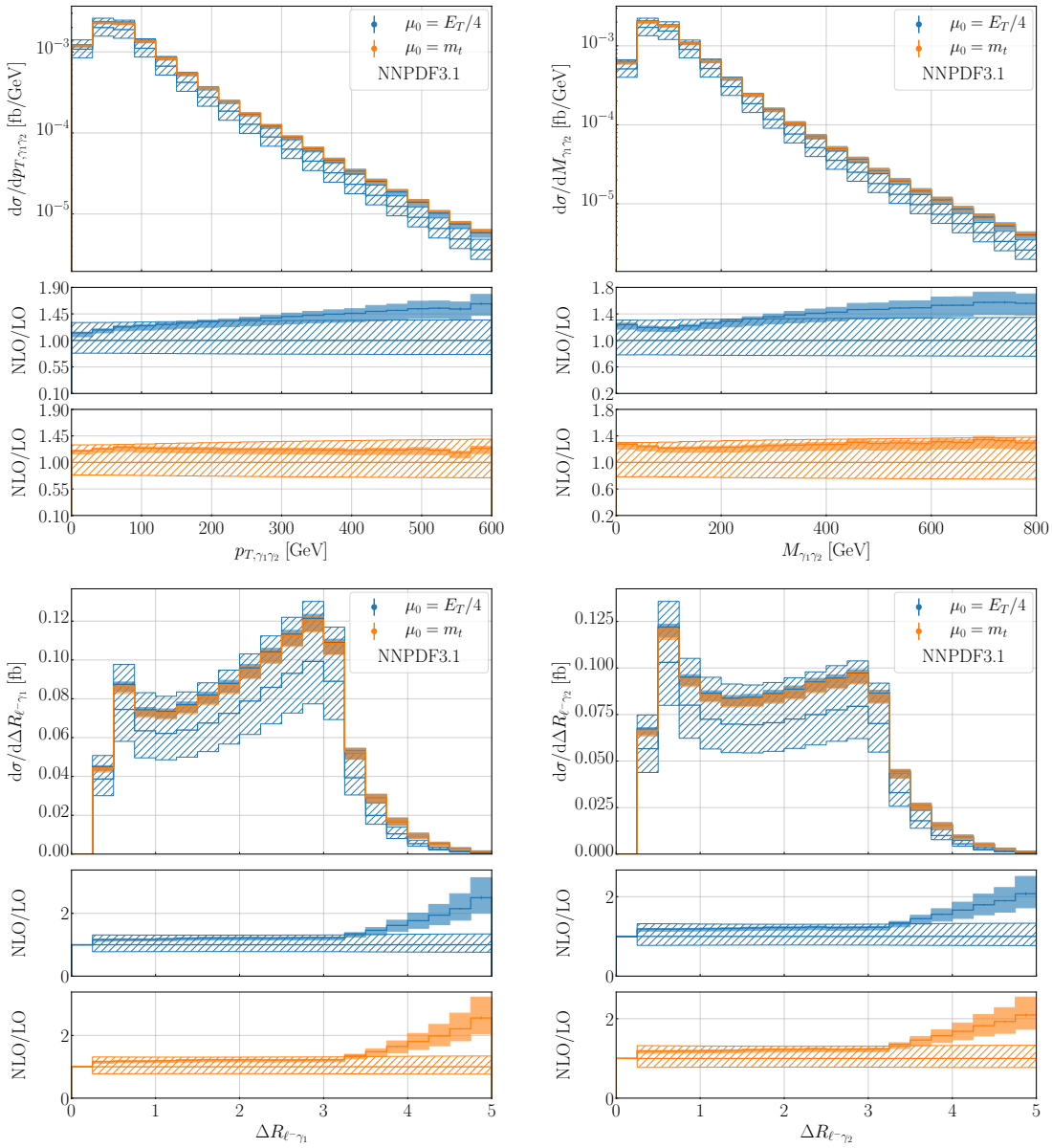

Figure 4.9: *Same as Figure 4.8 but for the observables* $p_{T,\gamma_1\gamma_2}$, $M_{\gamma_1\gamma_2}$, $\Delta R_{\ell^-\gamma_1}$ *and* $\Delta R_{\ell^-\gamma_2}$.

reduced by factor of 6 from 30% to 5%. The predictions between the two scale choices differ by maximal 2%.

Finally, in Figure 4.10 we present the differential distributions of the observables p_{T,j_1}, p_{T,j_2}, $\Delta R_{j_1 j_2}$ and $\Delta\Phi_{j_1 j_2}$, which are constructed purely from the kinematics of the two hardest light jets j_1 and j_2. Already from the previous discussion at the integrated level of the dependence on Q_{cut} and the large NLO QCD corrections in p_{T,b_1} and $p_{T,b_1 b_2}$, it is expected that we encounter at least similar large NLO QCD corrections in certain phase-space regions. Exactly because of these extreme values in the differential $\mathcal{K}$-factors, we do

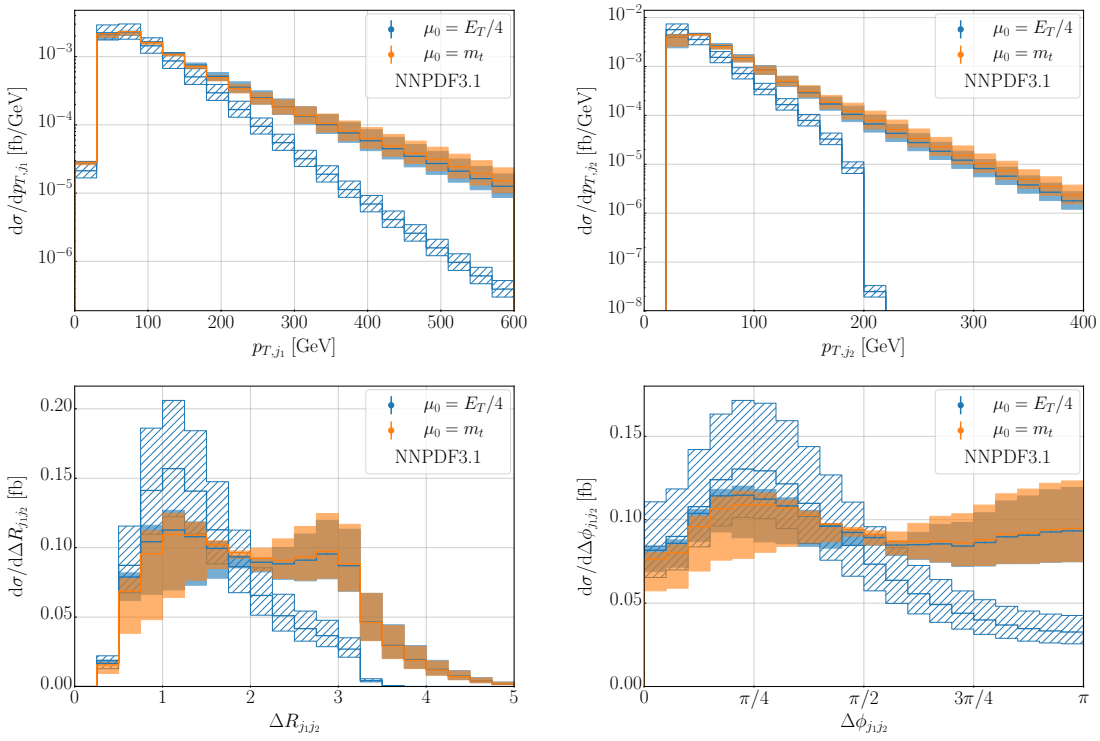

Figure 4.10: *Same as Figure 4.8 but without ratio plots for the observables* p_{T,j_1}, p_{T,j_2}, $\Delta R_{j_1j_2}$ *and* $\Delta\Phi_{j_1j_2}$.

not show the lower panels for these four observables. For the transverse momenta of the hardest and second hardest jets, p_{T,j_1} and p_{T,j_2}, we find huge NLO QCD corrections in the tails with differential $\mathcal{K}$-factors of more than 25 for p_{T,j_1}. The transverse momentum of the second hardest light jet is kinematically limited at LO by the finite mass of the W boson. Even if the W boson mass would follow a Breit-Wigner distribution, the additional cut on the invariant mass of at least one light jet pair would result into a similar kinematic edge [114]. Therefore, at LO above $p_{T,j_2} \approx 220$ GeV this distribution vanishes completely. This kinematic edge is no longer present at NLO due to additional radiation, and therefore we get non-zero contributions even after 220 GeV. NLO scale uncertainties of more than 50%, exceeding the LO uncertainties, are found for both distributions for the two scale choices. Differences in the central value of about 20% for p_{T,j_1} and 30% for p_{T,j_2} are found. Higher-order corrections of more than 50% are already found for moderate values of about $p_{T,j_1} > 180$ GeV and $p_{T,j_2} > 60$ GeV. This clearly shows that higher orders in perturbation theory are required for precise predictions of these observables. These large QCD corrections are not only related to dimensionful observables, but also to angular distributions such as $\Delta R_{j_1j_2}$ and $\Delta\Phi_{j_1j_2}$. At LO we find only one peak in the $\Delta R_{j_1j_2}$ spectrum at around $\Delta R_{j_1j_2} \approx 1$, which is clearly due to the production mechanism that both jets are produced in the decay of the same W boson and are therefore highly boosted in the same direction. At NLO this peak is substantially reduced and a second peak appears at $\Delta R_{j_1j_2} \approx 3$ where the two hardest light jets are produced back-to-back. Such configurations

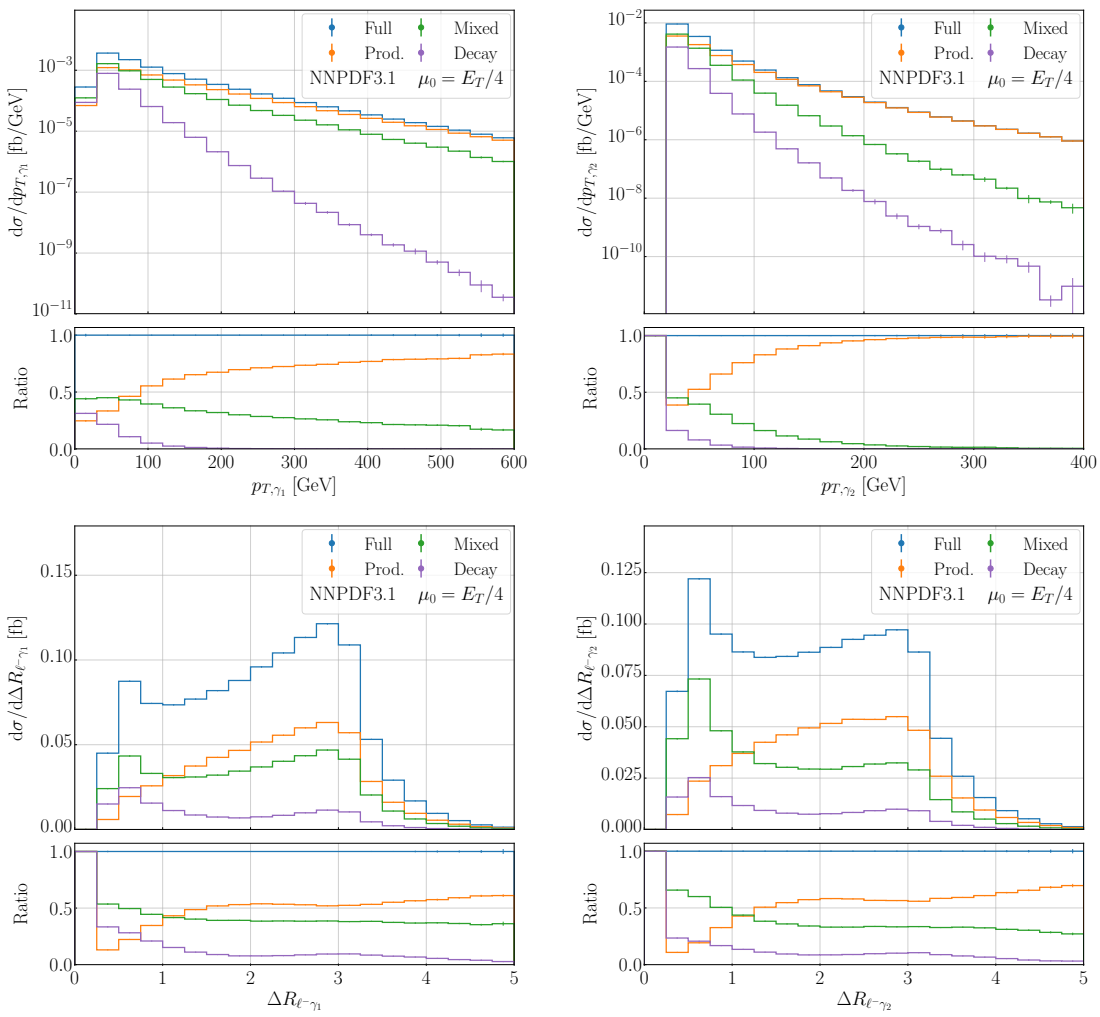

Figure 4.11: *Same as Figure 4.5 but for the lepton + jet decay channel for the observables* p_{T,γ_1}, p_{T,γ_2}, $\Delta R_{\ell^-\gamma_1}$ *and* $\Delta R_{\ell^-\gamma_2}$.

are due to real radiation, mainly from the production of $t\bar{t}$, where the additional hard jet recoils against the $t\bar{t}$ system. Over the most part of the spectrum, large scale uncertainties of about $20\% - 30\%$ are found, which further increase to more than 50% above $\Delta R_{j_1 j_2} \approx 3$. The predictions between the two scales differ by up to 16% below the first peak, while above the peak the differences reduce to less than 5%. Also in the $\Delta\Phi_{j_1 j_2}$ spectrum we find many similarities to $\Delta R_{j_1 j_2}$. In particular, we find again a peak for small angular separations at $\pi/4$ due to the production mechanism, which is suppressed at NLO due to additional hard jets appearing in the production process. In addition, large NLO QCD corrections of more than 150% are found for large separations in the azimuthal plane. The scale uncertainties vary widely between $15\% - 30\%$ in most regions and differences of up to 7% are found between the two scale choices.

4.4.3 Prompt photon distribution at the differential level

At last we discuss the prompt photon distribution in the *lepton + jet* decay channel in differential fiducal cross-section distributions. Therefore, in Figure 4.11 we show the observables p_{T,γ_1}, p_{T,γ_2}, $\Delta R_{\ell^-\gamma_1}$ and $\Delta R_{\ell^-\gamma_2}$. The structure of the plots is the same as in the *di-lepton* decay channel and we use $\mu_0 = E_T/4$ and the NNPDF3.1 PDF set. The overall distribution is very similar as in the *di-lepton* decay channel, but as already seen at the integrated level, the *Prod.* contribution is enhanced due to the event selection. We find that in the bulk of the p_{T,γ_1} and p_{T,γ_2} distributions the *Mixed* contribution is still very important with up to 45% of the full calculation. In the tails, this contribution decreases to 17% for p_{T,γ_1} and to less than 1% for p_{T,γ_2}. While in the latter case the *Mixed* contribution becomes completely negligible in the high energy regime, for p_{T,γ_1} this contribution still remains significant compared to the scale uncertainties of about 10% in this region. The *Decay* contribution is generally non-negligible at the beginning of the two spectra with 31% for p_{T,γ_1} and 16% for p_{T,γ_2} of the full calculation, but drops rapidly for photonic observables to less than 1% above 180 GeV for both. Finally, the *Prod.* contribution increases from 25% to 83% for p_{T,γ_1} and from 39% to 99% for p_{T,γ_2} towards the tails. Thus, for the latter distribution, the *Prod.* contribution completely dominates the full calculation, which would also be the case in the *di-lepton* decay channel. But as in the *di-lepton* decay channel, all three resonant contributions have to the included for accurate theoretical predictions in the phase-space regions that are currently accessible or will be accessible in the near future by experiments at the LHC. Finally, we find for the two angular observables $\Delta R_{\ell^-\gamma_1}$ and $\Delta R_{\ell^-\gamma_2}$ a similar prompt photon distribution as in the *di-lepton* decay channel. The first peak is purely generated by the *Mixed* and *Decay* contributions, where we find effects up to 66% and 33%, respectively. All resonant contributions give non-negligible effects in the second peak around $\Delta R_{ij} \approx 3$, describing back-to-back configurations. It is dominated by the *Prod.* contribution with $50\% - 55\%$ while the *Mixed* and *Decay* contributions lead still to substantial effects with up to 40% and 10%, respectively. This demonstrate once more that only a full calculation is able to properly describe the prompt photon radiation pattern, since otherwise the normalization is underestimated and whole peaks in angular distributions can be missed.

5. Complete NLO corrections to $t\bar{t}\gamma$ and $t\bar{t}\gamma\gamma$

After the discussion of the prompt photon distribution for the $pp \to t\bar{t}\gamma\gamma$ process and the importance of photon radiation in top-quark and W-boson decays, we next assess the size of subleading contributions at LO and NLO by calculating the so-called complete NLO corrections. In this case we include the dominant LO contribution with the corresponding NLO QCD corrections as in the last chapter, but in addition we include all LO and NLO contributions at different orders in α_s and α. These missing contributions are usually not taken into account in the estimation of theoretical uncertainties and are expected to be negligibly small with respect to the other theoretical uncertainties. Therefore, we are interested in whether this statement holds for the $pp \to t\bar{t}\gamma$ and $pp \to t\bar{t}\gamma\gamma$ processes in the *di-lepton* decay channel, where again the NWA is used for the decays of all unstable particles in the decay chain. Previous studies of these subleading corrections were performed only in the limit of stable top quarks, where photon radiation was neglected in all decay processes, which clearly leads to an underestimation of the full process and can potentially affect the relative size of subleading corrections. Therefore, our goal is to quantify the size of subleading corrections with realistic final states and by consistently including subleading corrections and photon radiation in the $t\bar{t}$ production process and all decay processes. Finally, we study the origin of the dominant subleading corrections by performing an alternative calculation in which the subleading NLO corrections are only included in the $t\bar{t}$ production process in the *Prod.* contribution, where all photons are produced in the $t\bar{t}$ production.

The structure of this chapter is similar to the last one. In particular, in Section 5.1 we describe the complete process in detail and define the different subleading contributions at LO and NLO. The input parameters are mostly the same as in the previous chapter for the LHC Run II, but a few modifications in the setup were performed for the consistent inclusion of EW corrections and photon initiated partonic subprocesses, which are listed in Section 5.2. Finally, in Section 5.3 and Section 5.4 we present numerical results for both processes at the integrated and differential fiducial cross-section level and discuss the relative size of the different subleading contributions. These results were already published in Ref. [488] from which also all tables and figures in this chapter are taken from.

5.1 Process definitions

We consider the $pp \to t\bar{t}\gamma$ and $pp \to t\bar{t}\gamma\gamma$ processes in the *di-lepton* decay channel, where the NWA is used for the decays of all unstable particles, leading to the following decay

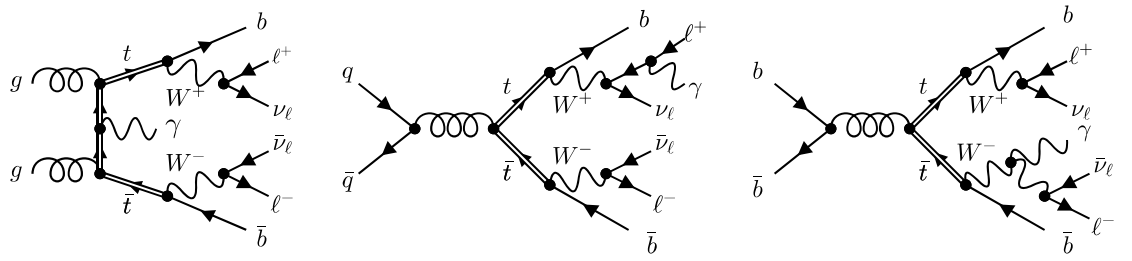

Figure 5.1: *Example Feynman diagrams for $pp \to t\bar{t}\gamma$ contributing to* LO_1.

chains

$$\begin{aligned} pp &\to t\bar{t}(\gamma) \to W^+W^-\, b\bar{b}(\gamma) \to \ell^+\nu_\ell\, \ell^-\bar{\nu}_\ell\, b\bar{b}\,\gamma + X, \\ pp &\to t\bar{t}(\gamma\gamma) \to W^+W^-\, b\bar{b}(\gamma\gamma) \to \ell^+\nu_\ell\, \ell^-\bar{\nu}_\ell\, b\bar{b}\,\gamma\gamma + X, \end{aligned} \tag{5.1}$$

where again the brackets indicate that the photon can be radiated at different stages of the decay chain. We calculate the complete NLO corrections for both processes including all subleading LO and NLO contributions, and consistently including photon radiation and higher-order corrections in the production stage and all decay processes in the decay chain. The photons can be radiated in the $t\bar{t}$ production and in the top-quark and W-boson decays, leading to 5 (15) resonant histories for $pp \to t\bar{t}\gamma(\gamma)$. At NLO, this number increases to 15 (45) due to additional gluon radiation and to 15 (35) due to additional photon radiation. We work in the five-flavor scheme and include photons in the initial state for the consistent calculation of EW corrections. Finally, the CKM mixing matrix is still kept diagonal.

5.1.1 LO contributions

Following the notation which we have introduced for the individual LO and NLO contributions in Section 2.1, the first LO contribution, LO_1, is the QCD induced production of a top-quark pair in association with photons at $\mathcal{O}(\alpha_s^2\alpha^{4+n_\gamma})$ with $n_\gamma = 1\,(2)$ for $pp \to t\bar{t}\gamma(\gamma)$. As expected, this is the dominant contribution at LO, which we have already considered in the previous calculation of $pp \to t\bar{t}\gamma\gamma$ in the last chapter. For completeness, we list all contributing partonic subprocesses, which can be summarized as follows

$$\begin{aligned} & gg \to \ell^+\nu_\ell\, \ell^-\bar{\nu}_\ell\, b\bar{b}\,\gamma(\gamma)\,, \\ q\bar{q}/\bar{q}q \;\to\; & \ell^+\nu_\ell\, \ell^-\bar{\nu}_\ell\, b\bar{b}\,\gamma(\gamma)\,, \qquad\qquad b\bar{b}/\bar{b}b \;\to\; \ell^+\nu_\ell\, \ell^-\bar{\nu}_\ell\, b\bar{b}\,\gamma(\gamma)\,. \end{aligned} \tag{5.2}$$

Example Feynman diagrams contributing at this order are shown in Figure 5.1. This contribution is obtained by the square of matrix elements at the order $\mathcal{O}(g_s^2 g^{4+n_\gamma})$. While the gg channel is only non-zero at this order, the quark-induced ones have additional contributions at the order $\mathcal{O}(g^{6+n_\gamma})$. This contribution interfered with the QCD induced one gives rise to the second LO contribution, LO_2, at the order $\mathcal{O}(\alpha_s^1\alpha^{5+n_\gamma})$. Due to color algebra, this interference contribution is exactly zero in the case of non-bottom quarks in the initial state. On the other hand, bottom quark induced partonic subprocesses lead to additional t-channel Feynman diagrams with an intermediate W boson, as illustrated in Figure 5.2, so that the interference between the different orders does no longer vanish.

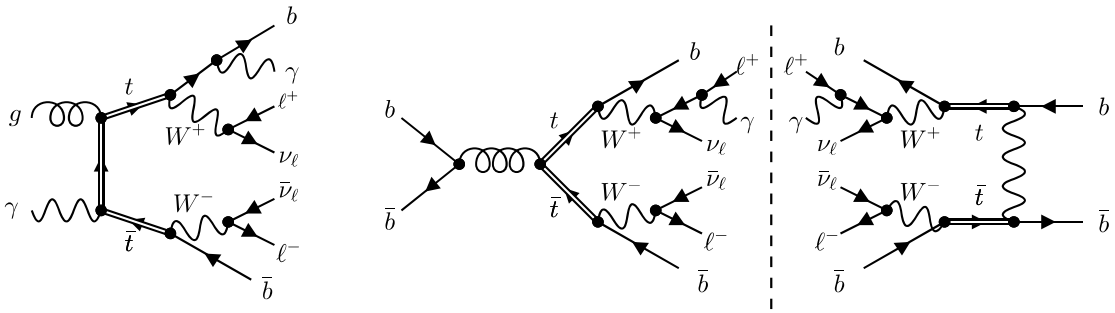

Figure 5.2: *Example Feynman diagrams for* $pp \to t\bar{t}\gamma$ *contributing to* LO_2.

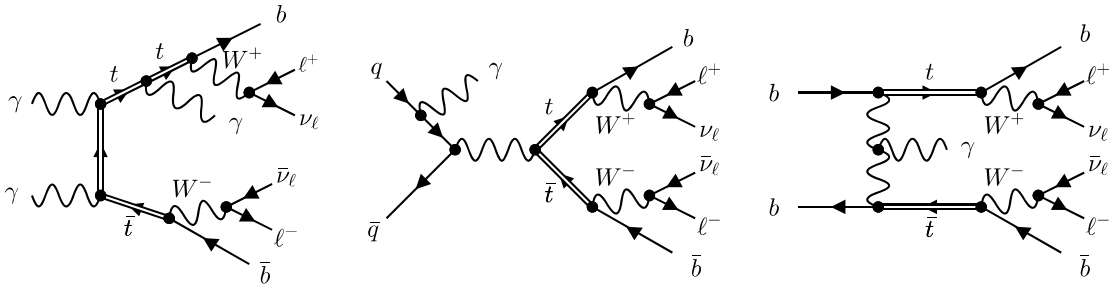

Figure 5.3: *Example Feynman diagrams for* $pp \to t\bar{t}\gamma$ *contributing to* LO_3.

Similar diagrams do not appear in the other quark induced channels because we work with a diagonal CKM matrix. Furthermore, at this order we encounter the photon induced $g\gamma$ channel, as shown in Figure 5.2, which is obtained by the square of the matrix element at the order $\mathcal{O}(g_s^1 g^{5+n_\gamma})$. Thus, the full set of partonic subprocesses in LO_2 is given by

$$g\gamma/\gamma g \;\to\; \ell^+\nu_\ell\,\ell^-\bar{\nu}_\ell\,b\bar{b}\,\gamma(\gamma)\,, \qquad\qquad b\bar{b}/\bar{b}b \;\to\; \ell^+\nu_\ell\,\ell^-\bar{\nu}_\ell\,b\bar{b}\,\gamma(\gamma)\,. \tag{5.3}$$

Finally, the quark induced channels and the $\gamma\gamma$ channel contribute to the final LO contribution at $\mathcal{O}(\alpha^{6+n_\gamma})$, LO_3, which is the pure EW production of top quarks. Therefore, this contribution is suppressed by the different power couplings and by an additional PDF suppression, since no gluon induced subprocesses are present. All partonic subprocesses contributing to LO_3 are given by

$$\begin{aligned} &\gamma\gamma \to \ell^+\nu_\ell\,\ell^-\bar{\nu}_\ell\,b\bar{b}\,\gamma(\gamma)\,, \\ q\bar{q}/\bar{q}q \;\to\; &\ell^+\nu_\ell\,\ell^-\bar{\nu}_\ell\,b\bar{b}\,\gamma(\gamma)\,, \qquad\qquad b\bar{b}/\bar{b}b \;\to\; \ell^+\nu_\ell\,\ell^-\bar{\nu}_\ell\,b\bar{b}\,\gamma(\gamma)\,, \end{aligned} \tag{5.4}$$

and example Feynman diagrams are presented in Figure 5.3. We call the complete LO calculation as LO, which is simply the sum of the three individual contributions.

5.1.2 NLO contributions

In the following, we discuss all NLO contributions. These are obtained by QCD and/or EW corrections to the different LO contributions and amount to four different contributions (NLO_{1-4}), as exemplified in Figure 5.4. In general, a clear distinction is only possible for NLO_1 and NLO_4, which represent the NLO QCD corrections to LO_1 and the NLO EW corrections to LO_3, respectively. For NLO_2 and NLO_3, no clear distinction between QCD

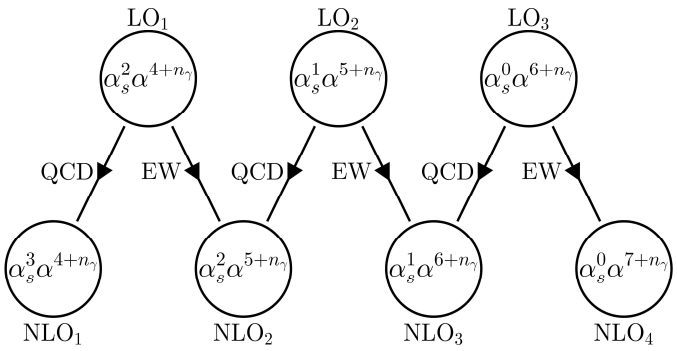

Figure 5.4: *LO and NLO contributions for* $pp \to t\bar{t}\gamma(\gamma)$ *with* $n_\gamma = 1(2)$.

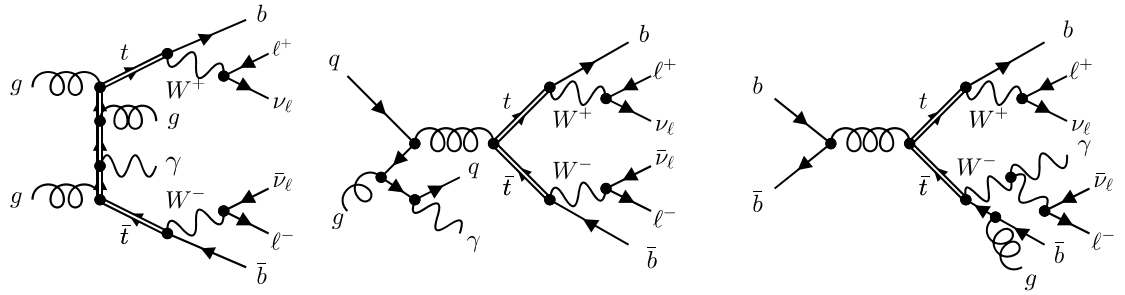

Figure 5.5: *Example Feynman diagrams for* $pp \to t\bar{t}\gamma$ *contributing to* NLO_1.

and EW corrections is possible for the real and virtual corrections, as we will elaborate in this section.

As expected, the dominant the contribution at NLO is NLO_1 at the order $\mathcal{O}(\alpha_s^3\alpha^{4+n_\gamma})$. In this case, the virtual corrections are obtained from the interference of one-loop diagrams at $\mathcal{O}(g_s^4 g^{4+n_\gamma})$ with tree-level ones at $\mathcal{O}(g_s^2 g^{4+n_\gamma})$. In particular, we encounter the same partonic subprocesses in the virtual corrections as in LO_1, while additional ones appear in the calculation of the real corrections, which can be obtained by gluon radiation and the crossing of initial- and final-state particles. These can be summarized as

$$
\begin{aligned}
& gg \to \ell^+\nu_\ell\,\ell^-\bar{\nu}_\ell\,b\bar{b}\,\gamma(\gamma)\,g\,, \\
q\bar{q}/\bar{q}q \;&\to\; \ell^+\nu_\ell\,\ell^-\bar{\nu}_\ell\,b\bar{b}\,\gamma(\gamma)\,g\,, \qquad & b\bar{b}/\bar{b}b \;&\to\; \ell^+\nu_\ell\,\ell^-\bar{\nu}_\ell\,b\bar{b}\,\gamma(\gamma)\,g\,, \\
gq/qg \;&\to\; \ell^+\nu_\ell\,\ell^-\bar{\nu}_\ell\,b\bar{b}\,\gamma(\gamma)\,q\,, \qquad & g\bar{q}/\bar{q}g \;&\to\; \ell^+\nu_\ell\,\ell^-\bar{\nu}_\ell\,b\bar{b}\,\gamma(\gamma)\,\bar{q}\,, \\
gb/bg \;&\to\; \ell^+\nu_\ell\,\ell^-\bar{\nu}_\ell\,b\bar{b}\,\gamma(\gamma)\,b\,, \qquad & g\bar{b}/\bar{b}g \;&\to\; \ell^+\nu_\ell\,\ell^-\bar{\nu}_\ell\,b\bar{b}\,\gamma(\gamma)\,\bar{b}\,,
\end{aligned}
\tag{5.5}
$$

and example Feynman diagrams are shown in Figure 5.5. Although we are mainly interested in the subleading LO and NLO contributions in this chapter, the calculation of NLO_1 is essential to properly quantify the importance of these subleading effects. In particular, we use the NLO QCD calculation, given by

$$
\mathrm{NLO}_{\mathrm{QCD}} = \mathrm{LO}_1 + \mathrm{NLO}_1\,, \tag{5.6}
$$

as our baseline to assess the size of subleading effects. The NLO QCD calculation is simply the sum of LO_1 and the corresponding NLO QCD corrections and coincides with the definition for the $pp \to t\bar{t}\gamma\gamma$ process in the last chapter.

The first subleading NLO contribution, NLO_2, at $\mathcal{O}(\alpha_s^2\alpha^{5+n_\gamma})$ is obtained from the NLO EW corrections to LO_1 and the NLO QCD corrections to LO_2. In particular, the virtual corrections consist of the interference of one-loop diagrams at $\mathcal{O}(g_s^4 g^{4+n_\gamma})$ with tree-level ones at $\mathcal{O}(g^{6+n_\gamma})$, which can be clearly classified as a part of the NLO QCD corrections to LO_2. On the other hand, for the interference of one-loop amplitudes at $\mathcal{O}(g_s^2 g^{6+n_\gamma})$ with tree-level ones at $\mathcal{O}(g_s^2 g^{4+n_\gamma})$ a clear distinction is only possible in the gg channel, where this interference corresponds to the NLO EW corrections to LO_1. For the quark induced channels, the one-loop amplitudes at $\mathcal{O}(g_s^2 g^{6+n_\gamma})$ can be seen as the EW one-loop corrections to the Born amplitudes at $\mathcal{O}(g_s^2 g^{4+n_\gamma})$ or as the QCD one-loop corrections to the Born amplitudes at $\mathcal{O}(g^{6+n_\gamma})$. Therefore, a complete distinction is not possible. Finally, in the $g\gamma$ channel the interference of the one-loop amplitude at $\mathcal{O}(g_s^3 g^{5+n_\gamma})$ with the tree-level amplitude at $\mathcal{O}(g_s^1 g^{5+n_\gamma})$ corresponds to the NLO QCD corrections to LO_2. In the calculation of the corresponding real corrections we encounter a larger number of partonic subprocesses involving QCD or QED-like IR singularities. The first set of subprocesses is very similar to that of NLO_1 in Eq. (5.5), which corresponds to additional QCD radiation to the interference contribution in LO_2. Therefore, the gg channel is absent here, and the first set of partonic subprocesses is given by

$$\begin{aligned}
q\bar{q}/\bar{q}q &\to \ell^+\nu_\ell\,\ell^-\bar{\nu}_\ell\,b\bar{b}\,\gamma(\gamma)\,g\,, & b\bar{b}/\bar{b}b &\to \ell^+\nu_\ell\,\ell^-\bar{\nu}_\ell\,b\bar{b}\,\gamma(\gamma)\,g\,,\\
gq/qg &\to \ell^+\nu_\ell\,\ell^-\bar{\nu}_\ell\,b\bar{b}\,\gamma(\gamma)\,q\,, & g\bar{q}/\bar{q}g &\to \ell^+\nu_\ell\,\ell^-\bar{\nu}_\ell\,b\bar{b}\,\gamma(\gamma)\,\bar{q}\,,\\
gb/bg &\to \ell^+\nu_\ell\,\ell^-\bar{\nu}_\ell\,b\bar{b}\,\gamma(\gamma)\,b\,, & g\bar{b}/\bar{b}g &\to \ell^+\nu_\ell\,\ell^-\bar{\nu}_\ell\,b\bar{b}\,\gamma(\gamma)\,\bar{b}\,.
\end{aligned} \tag{5.7}$$

Although the interference contribution of $q\bar{q}$ vanishes in LO_2 due to color algebra, the corresponding QCD real and virtual corrections are non-zero because the QCD corrections modify the color structure. In particular, the interference of diagrams where the gluon is emitted from initial-state quarks with diagrams where the gluon is radiated from (top) quarks in the final state does not vanish, as explained in Refs. [113, 360]. This also implies that in the $q\bar{q}$ channel in NLO_2 the additional gluon can only be radiated from the $t\bar{t}$ production and cannot be produced in top-quark decays. Since the underlying Born process $q\bar{q}$ vanishes in LO_2, the $q\bar{q}$ channel does not contain collinear but only soft singularities. Therefore, the qg channel, which is obtained by crossing of initial- and final-state particles of the $q\bar{q}$ channel, is finite at this order, because in this channel only collinear initial-state singularities can be present, which vanish since the underlying Born matrix process $q\bar{q}$ is exactly zero. Thus, no dipole subtraction is necessary in this case and its naive application could reduce the efficiency of the phase-space integration, as already explained in Chapter 3. Since the $b\bar{b}$ channel leads to a non-vanishing contribution in LO_2, collinear singularities are present in the bottom quark induced channels and gluon radiation from top-quark decays has to be consistently included. Additional partonic subprocesses appear due to photon radiation of the Born subprocesses in LO_1 leading to

$$\begin{aligned}
gg &\to \ell^+\nu_\ell\,\ell^-\bar{\nu}_\ell\,b\bar{b}\,\gamma\gamma(\gamma)\,,\\
q\bar{q}/\bar{q}q &\to \ell^+\nu_\ell\,\ell^-\bar{\nu}_\ell\,b\bar{b}\,\gamma\gamma(\gamma)\,, \qquad b\bar{b}/\bar{b}b \to \ell^+\nu_\ell\,\ell^-\bar{\nu}_\ell\,b\bar{b}\,\gamma\gamma(\gamma)\,,
\end{aligned} \tag{5.8}$$

where unresolved photons are allowed simultaneously at different stages of the decay chain, as illustrated in Figure 5.6, so that the corresponding subtraction terms at each stage has to be included in an additive manner. This situation is very similar to the one in the

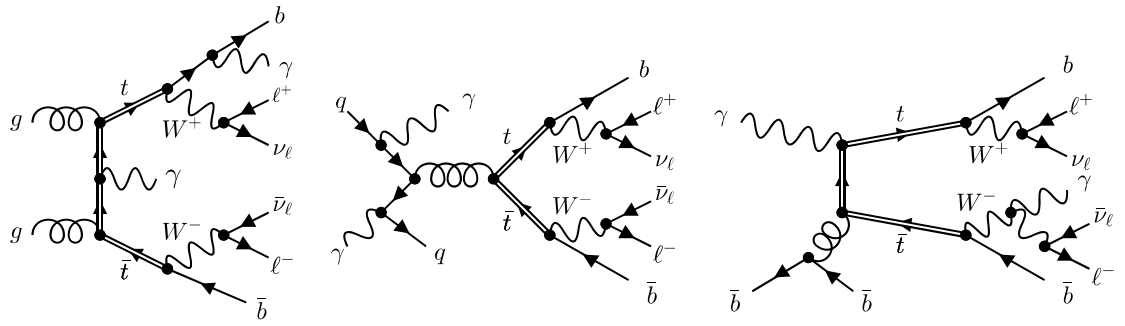

Figure 5.6: *Example Feynman diagrams for* $pp \to t\bar{t}\gamma$ *contributing to* NLO_2.

calculation of NLO QCD corrections to the $pp \to t\bar{t}j(j)$ process in the NWA [165, 173], where unresolved jets can appear simultaneously in the production and decay of the top-quark pair in the *Mixed* contribution. Finally, photon induced partonic subprocesses give rise to the last set of subprocesses in NLO_2, given by

$$
\begin{aligned}
& g\gamma/\gamma g \to \ell^+\nu_\ell\,\ell^-\bar{\nu}_\ell\,b\bar{b}\,\gamma(\gamma)\,g\,, \\
\gamma q/q\gamma \;&\to\; \ell^+\nu_\ell\,\ell^-\bar{\nu}_\ell\,b\bar{b}\,\gamma(\gamma)\,q\,, \qquad & \gamma\bar{q}/\bar{q}\gamma \;&\to\; \ell^+\nu_\ell\,\ell^-\bar{\nu}_\ell\,b\bar{b}\,\gamma(\gamma)\,\bar{q}\,, \\
\gamma b/b\gamma \;&\to\; \ell^+\nu_\ell\,\ell^-\bar{\nu}_\ell\,b\bar{b}\,\gamma(\gamma)\,b\,, \qquad & \gamma\bar{b}/\bar{b}\gamma \;&\to\; \ell^+\nu_\ell\,\ell^-\bar{\nu}_\ell\,b\bar{b}\,\gamma(\gamma)\,\bar{b}\,,
\end{aligned}
\tag{5.9}
$$

which are obtained from gluon radiation in the $g\gamma$ channel in LO_2 and from the crossing of initial- and final-state particles of the subprocesses in Eq. (5.8). The $g\gamma$ channel can be uniquely identified as a part of the NLO QCD corrections to LO_2, while the other subprocesses contain at the same time initial-state collinear singularities of QCD and QED origin due to the $\gamma \to q\bar{q}$ and $q \to gq$ splittings, which is exemplified in Figure 5.6. Thus, also for the real corrections it is not possible to completely separate the corrections into parts of pure QCD and EW origin.

Also for the NLO_3 contribution at $\mathcal{O}(\alpha_s^1\alpha^{6+n_\gamma})$ a clear distinction between QCD and EW corrections is not fully possible. In particular, we encounter in the calculation of the virtual corrections the interference of one-loop diagrams at $\mathcal{O}(g^{8+n_\gamma})$ with the tree-level ones at $\mathcal{O}(g_s^2 g^{4+n_\gamma})$, which can be uniquely identified as a part of the NLO EW corrections to LO_2. Since EW corrections do not alter the color structure, this contribution vanishes again in the $q\bar{q}$ channel. The interference of one-loop amplitudes at $\mathcal{O}(g_s^2 g^{6+n_\gamma})$ with tree-level ones at $\mathcal{O}(g^{6+n_\gamma})$ can be seen as either the NLO EW corrections to LO_2 or the NLO QCD corrections to LO_3, where the one-loop contribution at $\mathcal{O}(g_s^2 g^{6+n_\gamma})$ includes QCD one-loop corrections to the Born amplitudes at $\mathcal{O}(g^{6+n_\gamma})$ and EW one-loop corrections to the Born amplitudes at $\mathcal{O}(g_s^2 g^{4+n_\gamma})$. In the $\gamma\gamma$ channel, this contribution contains only QCD corrections. Finally, the interference of one-loop diagrams at $\mathcal{O}(g_s^1 g^{7+n_\gamma})$ with tree-level ones at $\mathcal{O}(g_s^1 g^{5+n_\gamma})$ in $g\gamma$ have to be included, in which only EW corrections are present. NLO_3 contains a comparable large number of partonic subprocesses with respect to NLO_2 in the calculation of real corrections. In particular, the first set of subprocesses can be obtained by gluon radiation from the Born subprocesses in LO_3 resulting in

$$
\begin{aligned}
& \gamma\gamma \to \ell^+\nu_\ell\,\ell^-\bar{\nu}_\ell\,b\bar{b}\,\gamma(\gamma)g\,, \\
q\bar{q}/\bar{q}q \;&\to\; \ell^+\nu_\ell\,\ell^-\bar{\nu}_\ell\,b\bar{b}\,\gamma(\gamma)g\,, \qquad & b\bar{b}/\bar{b}b \;&\to\; \ell^+\nu_\ell\,\ell^-\bar{\nu}_\ell\,b\bar{b}\,\gamma(\gamma)\,g\,,
\end{aligned}
\tag{5.10}
$$

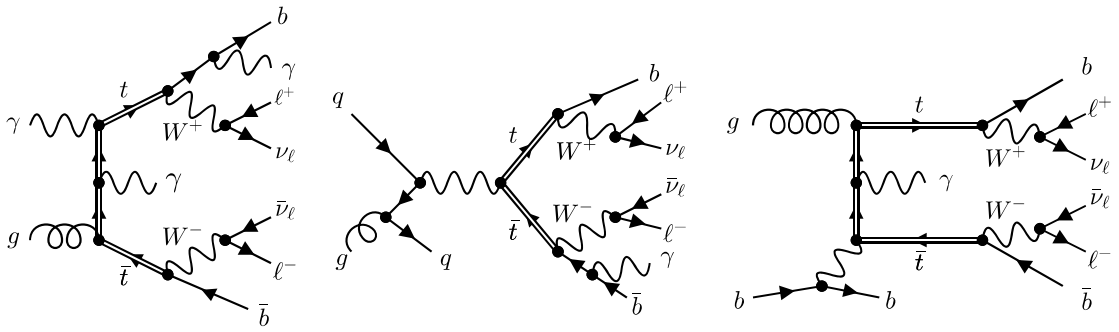

Figure 5.7: *Example Feynman diagrams for* $pp \to t\bar{t}\gamma$ *contributing to* NLO_3.

which contain only QCD singularities. The crossing of initial and finial-state particles leads to new partonic subprocesses that are given by

$$\begin{aligned} gq/qg &\to \ell^+\nu_\ell\,\ell^-\bar{\nu}_\ell\,b\bar{b}\,\gamma(\gamma)\,q\,, & g\bar{q}/\bar{q}g &\to \ell^+\nu_\ell\,\ell^-\bar{\nu}_\ell\,b\bar{b}\,\gamma(\gamma)\,\bar{q}\,, \\ gb/bg &\to \ell^+\nu_\ell\,\ell^-\bar{\nu}_\ell\,b\bar{b}\,\gamma(\gamma)\,b\,, & g\bar{b}/\bar{b}g &\to \ell^+\nu_\ell\,\ell^-\bar{\nu}_\ell\,b\bar{b}\,\gamma(\gamma)\,\bar{b}\,. \end{aligned} \tag{5.11}$$

Similar to the γq channel in NLO_2, these subprocesses simultaneously contain QCD and QED collinear initial-state singularities, as shown in Figure 5.7. Finally, additional subprocesses are present due to photon radiation from the two channels $g\gamma$ and $b\bar{b}$, as illustrated in Figure 5.7. These two channels with all possible crossings of particles in the initial and final state can be summarized as

$$\begin{aligned} g\gamma/\gamma g &\to \ell^+\nu_\ell\,\ell^-\bar{\nu}_\ell\,b\bar{b}\,\gamma\gamma(\gamma) & b\bar{b}/\bar{b}b &\to \ell^+\nu_\ell\,\ell^-\bar{\nu}_\ell\,b\bar{b}\,\gamma\gamma(\gamma)\,, \\ \gamma b/b\gamma &\to \ell^+\nu_\ell\,\ell^-\bar{\nu}_\ell\,b\bar{b}\,\gamma(\gamma)\,b & \gamma\bar{b}/\bar{b}\gamma &\to \ell^+\nu_\ell\,\ell^-\bar{\nu}_\ell\,b\bar{b}\,\gamma(\gamma)\,\bar{b}\,. \end{aligned} \tag{5.12}$$

The corresponding channels with q instead of b vanish again due to color algebra, since these partonic subprocesses originate from LO_2 with additional photon radiation, which does not modify the color structure.

The last subleading NLO contribution, denoted as NLO_4, corresponds to the EW corrections to the EW production of a top-quark pair in LO_3. Therefore, this contribution is expected to be the smallest contribution, but it is still consistently included in our calculation. The subprocesses can be obtained, in full analogy to the case of NLO_1, by photon radiation from the partonic subprocesses in LO_3 and crossing of initial- and final-state particles. Thus, the whole set of partonic subprocesses is given by

$$\begin{aligned} &\gamma\gamma \to \ell^+\nu_\ell\,\ell^-\bar{\nu}_\ell\,b\bar{b}\,\gamma\gamma(\gamma)\,, \\ q\bar{q}/\bar{q}q &\to \ell^+\nu_\ell\,\ell^-\bar{\nu}_\ell\,b\bar{b}\,\gamma\gamma(\gamma)\,, & b\bar{b}/\bar{b}b &\to \ell^+\nu_\ell\,\ell^-\bar{\nu}_\ell\,b\bar{b}\,\gamma\gamma(\gamma)\,, \\ \gamma q/q\gamma &\to \ell^+\nu_\ell\,\ell^-\bar{\nu}_\ell\,b\bar{b}\,\gamma(\gamma)\,q\,, & \gamma\bar{q}/\bar{q}\gamma &\to \ell^+\nu_\ell\,\ell^-\bar{\nu}_\ell\,b\bar{b}\,\gamma(\gamma)\,\bar{q}\,, \\ \gamma b/b\gamma &\to \ell^+\nu_\ell\,\ell^-\bar{\nu}_\ell\,b\bar{b}\,\gamma(\gamma)\,b\,, & \gamma\bar{b}/\bar{b}\gamma &\to \ell^+\nu_\ell\,\ell^-\bar{\nu}_\ell\,b\bar{b}\,\gamma(\gamma)\,\bar{b}\,, \end{aligned} \tag{5.13}$$

and example Feynman diagrams are shown in Figure 5.8.

Our complete NLO calculation, including all LO and NLO contributions, is simply denoted by NLO and is given by the sum of all contributions as

$$\mathrm{NLO} = \mathrm{LO}_1 + \mathrm{LO}_2 + \mathrm{LO}_3 + \mathrm{NLO}_1 + \mathrm{NLO}_2 + \mathrm{NLO}_3 + \mathrm{NLO}_4. \tag{5.14}$$

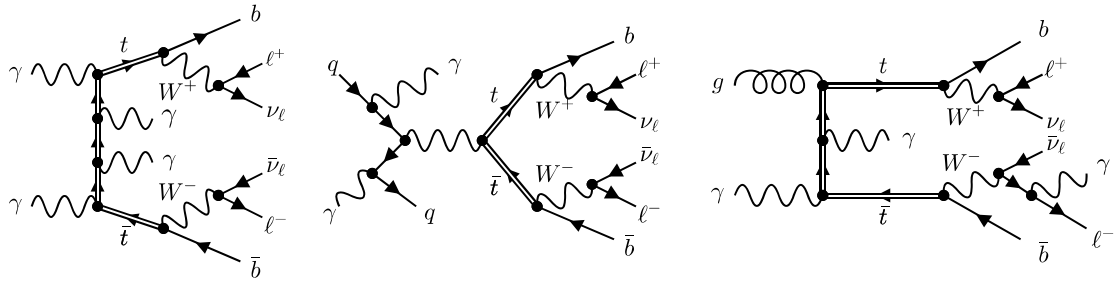

Figure 5.8: *Example Feynman diagrams for $pp \to t\bar{t}\gamma$ contributing to* NLO_2.

In contrast to the previous chapter, where we have divided the full NLO QCD calculation into the different resonant structures *Prod.*, *Mixed* and *Decay* to study the prompt photon distribution, we follow a different strategy in this calculation. From the last chapter we know that photon radiation from top-quark and W-boson decays is essential for a realistic description of $pp \to t\bar{t}\gamma(\gamma)$ and therefore the leading NLO QCD corrections should always be included in all resonant contribution. Moreover, additional photon radiation in the subleading NLO corrections leads to further complications in the decomposition of the full calculation into the different resonant structures due to their mixing at NLO, which was already discussed in detail in the context of NLO QCD corrections to the $pp \to t\bar{t}jj$ process in Ref. [173]. The mixing of the different resonant contributions basically follows from the fact that the *Mixed* contribution at NLO is obtained from the *Mixed* contribution at LO, but also from the *Prod.* contribution at LO with NLO corrections (photon radiation) in the decays and from the *Decay* contribution at LO with NLO corrections in the production of $t\bar{t}$. Instead of trying to divide the full calculation, we perform an alternative calculation, labeled as $\mathrm{NLO}_{\mathrm{prd}}$, where we fully include all LO contributions (LO_{1-3}) and NLO_1, but the subleading NLO corrections are included only in the *Prod.* contribution, restricting these higher-order corrections (and additional radiation) to the production stage of the top-quark pair, in the case where all photons are also radiated in the production process. This can schematically be written as

$$\mathrm{NLO}_{\mathrm{prd}} = \mathrm{LO}_1 + \mathrm{LO}_2 + \mathrm{LO}_3 + \mathrm{NLO}_1 + \mathrm{NLO}_{2,\mathrm{prd}} + \mathrm{NLO}_{3,\mathrm{prd}} + \mathrm{NLO}_{4,\mathrm{prd}}, \tag{5.15}$$

where the subscript *prd* indicates that in these cases the higher-order corrections are only included in the production of $t\bar{t}\gamma(\gamma)$ in the *Prod.* contribution. In other words, the higher-order corrections are neglected in the *Mixed* and *Decay* contributions and in the decays in the *Prod.* contribution. By comparing the full NLO calculation with $\mathrm{NLO}_{\mathrm{prd}}$, we investigate whether this approximation is sufficient to recover the full calculation and to quantify the effects of subleading NLO corrections in top-quark and W-boson decays. This approximation is motivated by the fact that often the largest effects of the subleading corrections come from EW Sudakov logarithms, which can affect the tails of dimensionful distributions. The EW Sudakov logarithms arise from the fact that the initial states in proton-proton collisions are not SU(2) symmetric [489], due to the flavor dependence of the PDFs. In addition, they occur due to the absent cancellation of specific real and virtual corrections. In particular, the contributions of the massive gauge bosons ($W^\pm, Z$) inside loops in virtual corrections are always included in the calculation of EW corrections, while

the corresponding real radiation of these gauge bosons is usually not, because these particles are unstable and therefore lead to different final-state signatures. As we showed for the $pp \to t\bar{t}\gamma\gamma$ process in the last chapter, the high-energy tails are clearly dominated by the *Prod.* contribution with more than 80% of the full calculation, and it is therefore essential to include subleading effects and also the EW Sudakov logarithms at least in the production process. On the other hand, the effects of EW Sudakov logarithms from the *Mixed* and *Decay* contributions can be negligibly small, since both resonant contributions are highly suppressed in the tails, where the EW Sudakov logarithms can become sizeable. In addition, this approximation leads to significant simplifications in the calculation, especially in the case of the real corrections, where the number of different resonant histories is drastically reduced. Furthermore, such an approximation would also simplify the matching to parton showers, since all subleading corrections and all EW corrections are neglected in the decays of unstable particles.

5.2 Input parameters for LHC run II

We perform the calculation of the complete NLO corrections to $pp \to t\bar{t}\gamma(\gamma)$ in the *di-lepton* decay channel at the LHC with $\sqrt{s} = 13$ TeV and use a very similar setup as in the last chapter. In the following, we discuss all modifications with respect to the previous calculation that are required for the consistent inclusion of subleading contributions. In particular, due to the presence of photons in the initial state, we use for this calculation the NNPDF3.1luxQED NLO PDF set [399, 400, 473, 490] with $\alpha_s(m_Z) = 0.118$ in which photons are consistently included in the PDF evolution. Also in this case, the running of the strong coupling constant is performed with two-loop accuracy and the PDF is accessed via the LHAPDF interface [476]. Due to the presence of intermediate Higgs bosons in subleading one-loop corrections, we use the following input parameters for the mass and the width of it

$$m_H = 125 \text{ GeV}\,, \qquad \Gamma_H = 4.07 \cdot 10^{-3} \text{ GeV}\,. \tag{5.16}$$

In regular calculations in the complex-mass scheme, the effects of the non-zero widths of the W and Z bosons would be partially canceled out, as for example in the weak mixing angle $c_w^2 = 1 - s_w^2 = \frac{\mu_W^2}{\mu_Z^2}$. Since we model the decays of the W boson in the NWA, its width is assumed to be zero everywhere except in the resonant Breit-Wigner propagators. Therefore, this cancellation would no longer be present and would introduce artificial higher-order terms. Therefore, we set the Z-boson width to zero to avoid these terms, following the approach in Ref. [113]. Unlike the previous calculation, we use in this case the same top-quark width with NLO QCD and EW corrections in all our LO and NLO contributions. In this scheme, the complete NLO calculation can be obtained in an additive manner as defined in Eq. (5.14). The numerical value of the top-quark width is given by

$$\Gamma_t^{\text{NLO}} = 1.3735727 \text{ GeV}, \tag{5.17}$$

where the NLO QCD top-quark width is the same as in the last chapter and the relative NLO EW corrections were obtained numerically with Helac-Dipoles and Recola as explained in Chapter 3. In this case we obtained $\delta^{\alpha} = 1.349\%$, and the NLO top-quark width is computed in an additive manner with $\Gamma_t^{\text{NLO}} = \Gamma_t^{\text{LO}}(1 + \delta^{\alpha_s} + \delta^{\alpha})$.

The event selection of all Born contributions and additional QCD radiation is identical as before. However, in this calculation we also encounter partonic subprocesses with an additional photon. In contrast to the case of QCD radiation where we encounter collinear singularities between unresolved quarks and photons, in this case no photon isolation is required. Instead we perform a photon recombination with all charged leptons, partons and photons with the *anti-k_T* jet algorithm with $R = 0.4$, where also $\gamma + \gamma \to \gamma$ recombinations are allowed. Similar approaches have been used for the calculation of NLO EW corrections to photon cross sections in the literature, see e.g. Refs. [491, 492]. In addition, we have recomputed these contributions by extending the smooth-cone isolation condition as proposed in Ref. [18] such that photons have to be isolated to partons but also to charged leptons and photons. In this case, the photon recombination is only performed with non-isolated photons. We have found that the differences between both approaches are phenomenologically negligible at the integrated and differential cross-section level. Based on the findings of the previous chapter, we set the factorization and renormalization scales to a common scale $\mu_R = \mu_F = \mu_0$. This common scale is set to $\mu_0 = E_T/4$ where E_T is defined in Eq. (4.17) with $n_\gamma = 1(2)$ for $pp \to t\bar{t}\gamma(\gamma)$. In addition, we present in the case of dimensionful photonic observables also results employing the fixed scale $\mu_0 = m_t$, which have led to a reduction of NLO QCD corrections and scale uncertainties in such observables. Theoretical uncertainties from missing higher-order corrections are again estimated by performing a 7-point scale variation.

5.3 $t\bar{t}\gamma$ in di-lepton channel

5.3.1 Integrated fiducial cross sections

First, we focus on the subleading effects at LO and NLO of the $pp \to t\bar{t}\gamma$ at the integrated level. Therefore, in Table 5.1 we present numerical results at LO, NLO, NLO_{QCD} and NLO_{prd}. In addition, the corresponding theoretical uncertainties from scale variation and the MC integration errors are displayed. The individual LO_i and NLO_i contributions are also shown. Finally, the ratios of all results with respect to LO_1 are given in the last column. The differences between LO and LO_1 amount to less than 1%, and thus the subleading LO contributions are negligible compared to the corresponding scale uncertainties of about 31% and even the NLO scale uncertainties of about 6%. The subleading LO contributions are given by LO_2 and LO_3, which are 0.34% and 0.49% of LO_1. The LO_2 contribution is slightly smaller than LO_3 due to cancellations between the $g\gamma$ and $b\bar{b}$ channels, where the latter contribution is the interference of LO diagrams of the QCD and EW production of $t\bar{t}$ and is negative. To be more precise, the $g\gamma$ channel is actually larger than LO_3 and amounts to 0.56% of LO_1. Finally, the $\gamma\gamma$ channel, which is only present in LO_3, is about 0.0005% of LO_1 and is fully negligible even with respect to the MC integration errors.

The NLO_1 contribution, representing the NLO QCD corrections to the dominant LO configuration LO_1, is the largest NLO contribution with 6.19% of LO_1. We note that in this case we have used the same top-quark width for all LO and NLO contributions. If we had used the LO top-quark width for the LO calculation and the NLO QCD top-quark width for the NLO QCD calculation, as in the calculation of $pp \to t\bar{t}\gamma\gamma$ in the previous chapter, then the NLO_1 contribution would increase to 27% and thus become similar in size as the NLO QCD corrections in $pp \to t\bar{t}\gamma\gamma$ of about 28% in the *di-lepton* decay channel. The

		σ_i [fb]	Ratio to LO_1
LO_1	$\mathcal{O}(\alpha_s^2\alpha^5)$	$55.604(8)^{+31.4\%}_{-22.3\%}$	1.00
LO_2	$\mathcal{O}(\alpha_s^1\alpha^6)$	$0.18775(5)^{+20.1\%}_{-15.4\%}$	+0.34%
LO_3	$\mathcal{O}(\alpha_s^0\alpha^7)$	$0.26970(4)^{+14.3\%}_{-16.9\%}$	+0.49%
NLO_1	$\mathcal{O}(\alpha_s^3\alpha^5)$	+3.44(5)	+6.19%
NLO_2	$\mathcal{O}(\alpha_s^2\alpha^6)$	−0.1553(9)	−0.28%
NLO_3	$\mathcal{O}(\alpha_s^1\alpha^7)$	+0.2339(3)	+0.42%
NLO_4	$\mathcal{O}(\alpha_s^0\alpha^8)$	+0.001595(8)	+0.003%
LO		$56.061(8)^{+31.2\%}_{-22.1\%}$	1.0082
$\mathrm{NLO}_{\mathrm{QCD}}$		$59.05(5)^{+1.6\%}_{-5.9\%}$	1.0620
$\mathrm{NLO}_{\mathrm{prd}}$		$59.08(5)^{+1.5\%}_{-5.9\%}$	1.0626
NLO		$59.59(5)^{+1.6\%}_{-5.9\%}$	1.0717

Table 5.1: *Integrated fiducial cross sections for $pp \to t\bar{t}\gamma$ in the di-lepton decay channel at the LHC with $\sqrt{s} = 13$ TeV. Results are present for* LO, NLO, $\mathrm{NLO}_{\mathrm{QCD}}$ *and* $\mathrm{NLO}_{\mathrm{prd}}$. *The $\mu_0 = E_T/4$ scale setting and the NNPDF3.1luxQED NLO PDF set are used. Scale uncertainties estimated by scale variation and MC integration errors are also displayed.*

subleading NLO corrections turn out to be smaller than the subleading LO contributions with about 0.14% in sum compared to LO_1, where we encounter cancellations between the negative NLO_2 contribution (−0.28%) and the positive NLO_3 contribution (0.42%). The NLO_4 corrections are less than the MC integration errors of the full LO and NLO results and thus are completely irrelevant. Therefore, the differences between $\mathrm{NLO}_{\mathrm{QCD}}$ and NLO of about 1% come mainly from the subleading LO contributions, while the subleading NLO corrections play only a minor role. Taken into account the current size of scale uncertainties of about 6%, the subleading LO and NLO contributions are negligible small at the integrated level. Furthermore, the scale uncertainties are unaffected by these small subleading contributions. The integrated cross sections at $\mathrm{NLO}_{\mathrm{QCD}}$ and $\mathrm{NLO}_{\mathrm{prd}}$ agree within the MC integration errors, where the latter result consists of the $\mathrm{NLO}_{\mathrm{QCD}}$ calculation including subleading LO contributions and subleading NLO corrections to the *Prod.* contribution neglecting those in top-quark decays. In particular, cancellations between the positive subleading LO contributions and the negative subleading NLO corrections to the $t\bar{t}\gamma$ production with about −0.7% lead to the these small differences. Finally, the differences between $\mathrm{NLO}_{\mathrm{prd}}$ and NLO amount to about 1%, which are induced by the missing subleading NLO corrections in the *Mixed* and *Decay* resonant configurations and in the top-quark decays in the *Prod.* contribution.

5.3.2 Differential fiducial cross-section distributions

We continue our discussion of the size of subleading LO and NLO effects at the differential level to find out whether the subleading contributions, which are found to be negligibly

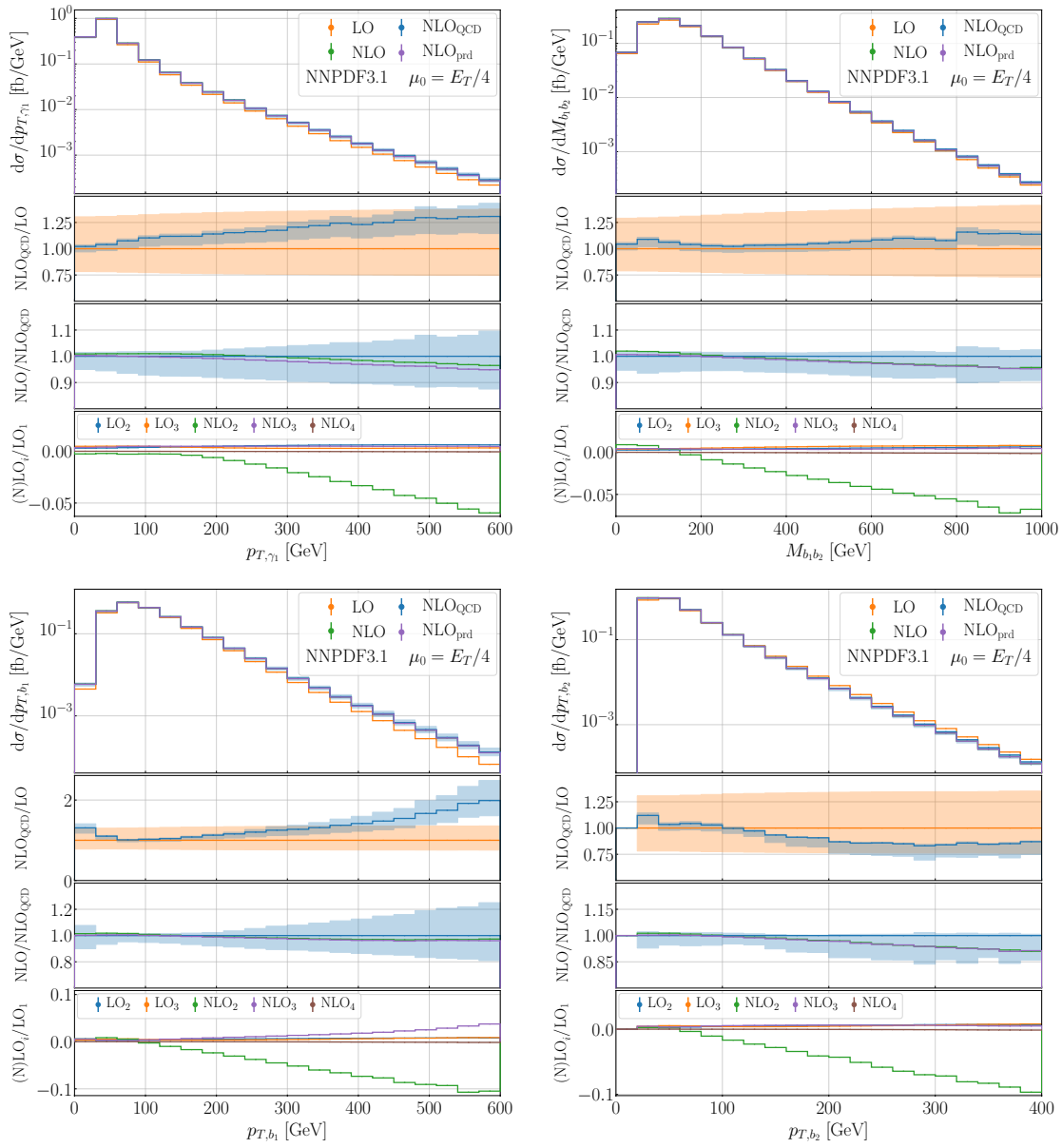

Figure 5.9: *Differential fiducial cross-section distributions for the observables p_{T,γ_1}, $M_{b_1b_2}$, p_{T,b_1} and p_{T,b_2} for $pp \to t\bar{t}\gamma$ in the di-lepton decay channel at the LHC with $\sqrt{s} = 13$ TeV.* LO, NLO, $\mathrm{NLO_{QCD}}$ *and* $\mathrm{NLO_{prd}}$ *results are presented for the $\mu_0 = E_T/4$ scale choice employing the NNPDF3.1luxQED NLO PDF set. The ratios* $\mathrm{NLO_{QCD}/LO}$ *are shown in the second panels, the ratios of all NLO calculations with respect to* $\mathrm{NLO_{QCD}}$ *are shown in the third panels and the ratios of all subleading* LO_i *and* NLO_i *contributions compared to* LO_1 *are presented in the last panels.*

small at the integrated level with only 1% of the $\mathrm{NLO_{QCD}}$ calculation, are enhanced in certain phase-space regions. In Figure 5.9 we present the differential fiducial cross section

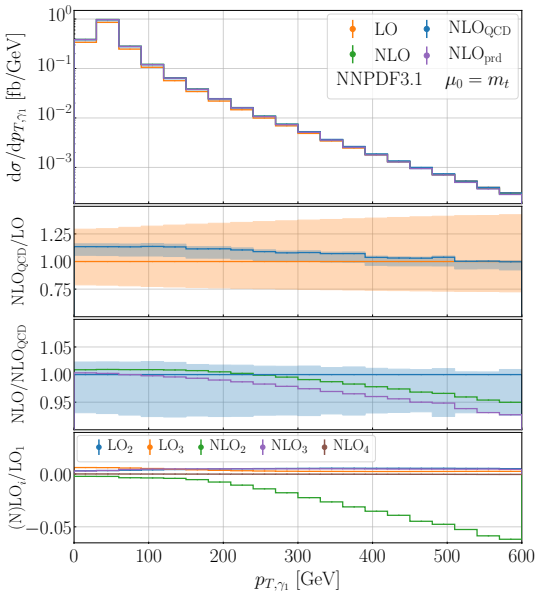

Figure 5.10: *Same as Figure 5.9 but for the observable p_{T,γ_1}. The results are shown for $\mu_0 = m_t$.*

distributions for the observables p_{T,γ_1}, $M_{b_1b_2}$, p_{T,b_1} and p_{T,b_2} using the dynamical scale $\mu_0 = E_T/4$. In particular, results are shown for the LO, NLO, NLO$_{\text{QCD}}$ and NLO$_{\text{prd}}$ calculations in the upper panels. The second panels display the ratio NLO$_{\text{QCD}}$/LO and the third panels show the ratio of the NLO calculations with respect to NLO$_{\text{QCD}}$. The scale uncertainties from the NLO$_{\text{QCD}}$ calculation are shown in all three cases for comparison, and the scale uncertainties of LO are shown in the second panels. The ratios of the subleading LO (LO$_{2-3}$) and NLO contributions (NLO$_{2-4}$) with respect to LO$_1$ are presented in lower panels. We find for the transverse momentum of the hardest photon p_{T,γ_1} that the NLO corrections are dominated by the NLO QCD corrections to LO$_1$ which increase to about 30% in the tail, becoming similar in size as the corresponding LO scale uncertainties of about 38% in this region. The inclusion of subleading LO and NLO contributions leads to a reduction of the NLO$_{\text{QCD}}$ result by up to 4% in the high-energy tail. This reduction originates purely from the EW Sudakov logarithms in NLO$_2$, which are about -6% of LO$_1$, while the sum of the remaining subleading contributions is about 1% of LO$_1$. The NLO scale uncertainties are about twice as large as the subleading effects in this phase-space region and thus the complete NLO calculation is within the uncertainty bands of the NLO$_{\text{QCD}}$ calculation. Furthermore, the NLO$_{\text{prd}}$ calculation, where the subleading NLO effects are only included in the production of $t\bar{t}\gamma$ in the *Prod.* contribution, differs from the full calculation only by up to 2% in the tail. Similar effects of subleading contributions are found the invariant mass of the two b-jet system $M_{b_1b_2}$. In this case, the NLO QCD corrections are rather small with $5\% - 15\%$. These predictions are reduced by the EW Sudakov logarithms in NLO$_2$ by up to 5%. The scale uncertainties of about 8% are comparable in size and the subleading effects are more important in comparison to p_{T,γ_1}. The NLO$_{\text{prd}}$ and NLO calculations fully agree in the tail and only small differences up to 1% are found in the

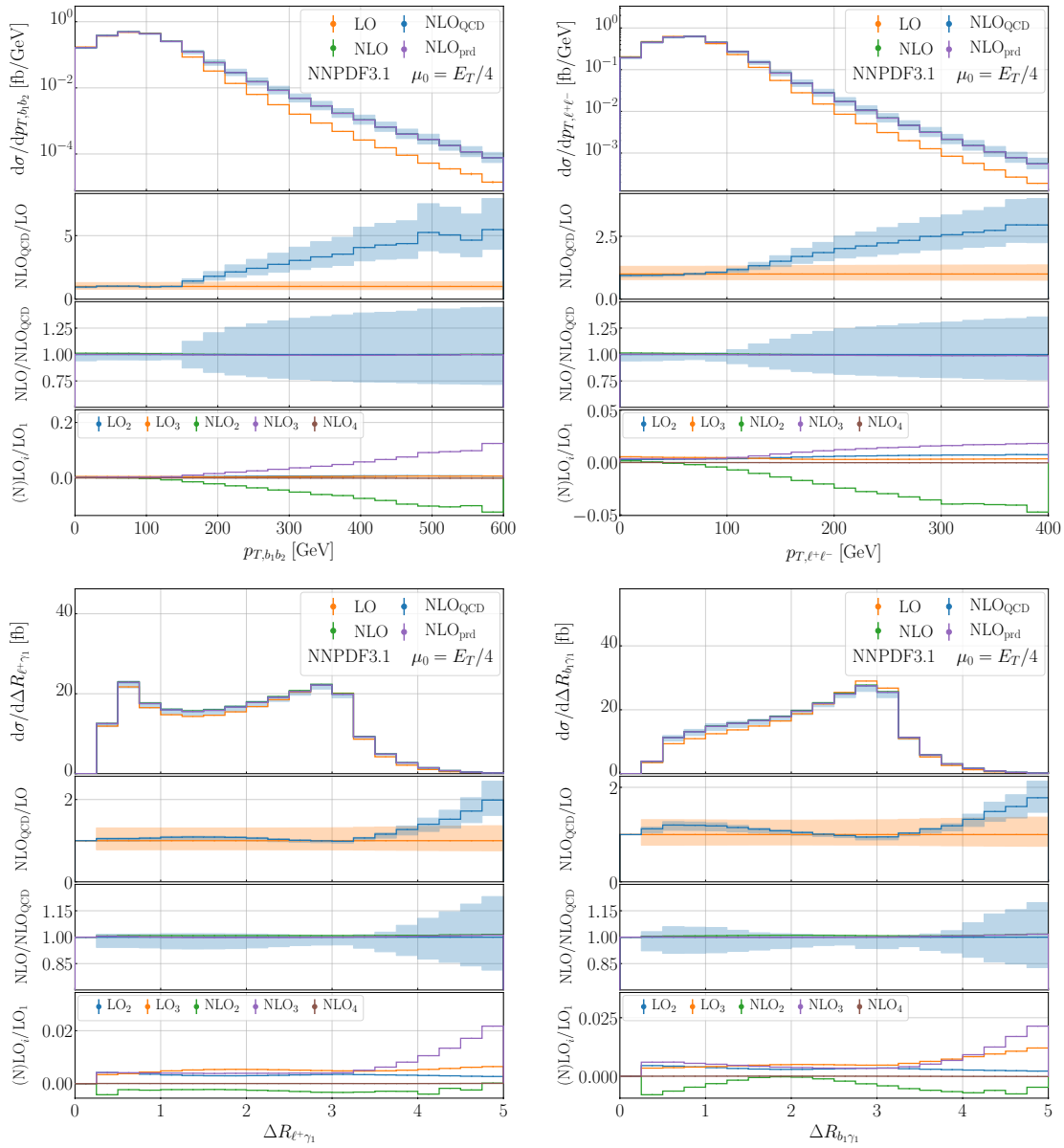

Figure 5.11: *Same as Figure 5.9 but for the observables* p_{T,b_1b_2}, $p_{T,\ell^+\ell^-}$, $\Delta R_{\ell^+\gamma_1}$ *and* $\Delta R_{b_1\gamma_1}$.

bulk of the distribution.

The relative size of NLO_2 with respect to LO_1 is increased for the transverse momentum of the hardest (p_{T,b_1}) and second hardest (p_{T,b_2}) b-jet to 10% in the tails. However, the importance of the subleading effects in the complete NLO calculation is fairly different in both cases. In particular, the $\mathrm{NLO}_{\mathrm{QCD}}$ prediction is decreased by up to 10% for p_{T,b_2} when subleading contributions are included, while the distribution of p_{T,b_1} is decreased by only up to 3%. The different behaviors originate from the enhanced real corrections with

an additional hard jet in the final state in the latter case. This causes that the NLO_3 contribution is enhanced and amounts to $3\% - 4\%$ of LO_1 for p_{T,b_1}. Thus, accidental cancellations are found between NLO_2 and NLO_3, since the origins of both contributions are very different. The latter contribution can be reduced by e.g. applying a jet veto on the additional hard jet as demonstrated in the case of $pp \to t\bar{t}t\bar{t}$ production in Ref. [388]. In contrast, the NLO_2 contribution is rather insensitive to such changes in the event selection, because it is dominated by EW Sudakov logarithms coming from the virtual corrections. In addition, the relative size of the subleading corrections is further suppressed for p_{T,b_1} in the complete calculation, because the same enhancement of the real corrections is also present for NLO_1 due to NLO QCD corrections up to 100%. These large corrections further lead to an increase of the scale uncertainties to about 20% in the tails. All in all, the importance of the subleading corrections is sensitive to the exact event selection, since the size of NLO_1 can also be significantly reduced by a jet veto, which would directly increase the relative size of subleading effects in the full calculation. On the other hand, the NLO corrections of about -10% originating from NLO_2 lead to a reduction of about 10% in the tails of the NLO_{QCD} prediction of p_{T,b_2}, which is comparable in size with the corresponding scale uncertainties of about 15%. In this case, the real corrections are not enhanced and the NLO_1 contribution leads to a reduction of the LO calculation by about 15%. Furthermore, the subleading effects also affect the size of scale uncertainties, which increase to 20% for the complete NLO calculation. Differences of about 1% can be found between the NLO_{prd} and the complete NLO predictions for both observables. This again shows that the NLO_{prd} calculation is fully able to reproduce the results of the complete calculation.

Based on our findings in the last chapter for the $pp \to t\bar{t}\gamma\gamma$ process that the fixed scale $\mu_0 = m_t$ reduces the size of NLO QCD corrections and scale uncertainties in most photonic dimensionful observables, we present for comparison also for this scale choice the corresponding complete NLO calculation. In Figure 5.10 we present the differential distributions of the p_{T,γ_1} observable with $\mu_0 = m_t$ at LO, NLO, NLO_{QCD} and NLO_{prd}. We find that the differences between the NLO_{QCD} and NLO predictions, and therefore the importance of the subleading corrections, slightly increase in the tail to 5% compared to 4% with the dynamical scale choice. This can be attributed to the decrease of the NLO QCD corrections in NLO_1, such that NLO_{QCD} and LO become identical for $\mu_0 = m_t$ in this phase-space region. The relative size of NLO_2 with respect to LO_1 is not affected by the different scale choice, since both contributions are proportional to α_s^2 and thus the dependence on μ_R vanishes completely for $\mu_0 = m_t$ and to a large extent for $\mu_0 = E_T/4$. Finally, the scale uncertainties of $10\% - 11\%$ for $\mu_0 = E_T/4$ are reduced to $7\% - 9\%$ for $\mu_0 = m_t$. Therefore, the size of subleading corrections and scale uncertainties become closer in size and the overall importance of the subleading corrections is slightly increased for the fixed scale setting.

In Figure 5.11 we present the differential distributions for the observables p_{T,b_1b_2} and $p_{T,\ell^+\ell^-}$, which have in common that both distributions are affected by huge NLO QCD corrections in NLO_1 in the tails of up to 450% and 200%, respectively. The origin of these large corrections is additional hard jet recoil against the $t\bar{t}$ system at NLO, as we have discussed in more detail in the last chapter. In particular, we have discussed that the presence of additional photons in the production of $t\bar{t}$ at LO leads to a mild reduction of these corrections, and that the *Prod.* contribution receives smaller QCD corrections than the *Mixed* and *Decay* contributions in the $pp \to t\bar{t}\gamma\gamma$ process. It is therefore evident that

the $pp \to t\bar{t}\gamma$ process is usually affected by larger higher-order corrections in the tails of such observables. Specifically, for the $pp \to t\bar{t}\gamma\gamma$ process the NLO QCD corrections in NLO_1 are reduced to 350% for p_{T,b_1b_2} and to 120% for $p_{T,\ell^+\ell^-}$. We find that NLO_2 is about -10% of LO_1 for p_{T,b_1b_2} and about -5% for $p_{T,\ell^+\ell^-}$. The NLO_3 contribution is also sizeable with about 10% of LO_1 for p_{T,b_1b_2} and 2% for $p_{T,\ell^+\ell^-}$. This enhancement of NLO_3 is of the same origin as the NLO QCD corrections in NLO_1 or the enhancements of NLO_1 and NLO_3 in p_{T,b_1} as discussed above. Thus, NLO_2 and NLO_3 are very similar in size but have different signs, and the subleading corrections cancel each other out to a large extent. Even if NLO_3 was not enhanced for p_{T,b_1b_2}, the subleading contributions would be strongly suppressed due to the large QCD corrections, and only a reduction of the NLO_{QCD} calculation of $2\% - 3\%$ would be found. Thus, the importance of the subleading corrections depends on the exact event selection and can again be enhanced by more exclusive cuts. The NLO_{prd} calculation is able to completely approximate the full calculation, and only tiny differences of about 1% are found at the beginning of both spectra.

Finally, we find that the size of all subleading corrections in regular angular distributions such as the rapidity (y_i), the distance in the azimuthal angle and rapidity plane (ΔR_{ij}) or the (azimuthal) opening angle between two final-state particles ($\cos\theta_{ij}$, $\Delta\phi_{ij}$) are negligibly small. A slight enhancement of NLO_3 is found for the two observables $\Delta R_{\ell^+\gamma_1}$ and $\Delta R_{b_1\gamma_1}$, which are also shown in Figure 5.11. In this case, the size of NLO_3 is increased for large separations in ΔR_{ij} to maximal 2% of LO_1. This region is also affected by large corrections from NLO_1, leading to an increase in scale uncertainties at the level of 20%. Therefore, this enhancement of NLO_3 is still irrelevant. The simultaneous enhancement of NLO_1 and NLO_3 also has a similar origin and stems from the real QCD corrections. Thus, for such observables it is sufficient to include only the dominant QCD corrections contained in NLO_1. The NLO_{prd} calculation can also be used safely in angular distributions, because of these small subleading NLO corrections and only differences up to $1\% - 2\%$ are found for large values of ΔR_{ij} for both angular distributions.

5.4 $t\bar{t}\gamma\gamma$ in di-lepton channel

5.4.1 Integrated fiducial cross sections

We continue the discussion about subleading effects at LO and NLO with the $pp \to t\bar{t}\gamma\gamma$ process in the *di-lepton* decay channel and are interested in any differences with respect to the $pp \to t\bar{t}\gamma$ process. In Table 5.2 the integrated fiducial cross sections at LO, NLO, NLO_{QCD} and NLO_{prd} with the corresponding scale uncertainties are shown. In addition, the individual LO and NLO contributions are presented, and the last column again displays the ratio with respect to the dominant LO contribution LO_1. In comparison to the $pp \to t\bar{t}\gamma$ process, the relative size of the sum of all subleading LO contributions with respect to LO_1 increases slightly from 0.83% to 0.93%, but it still remains below 1% and is therefore negligible compared to the theoretical uncertainties from scale variation. In particular, the relative size of LO_3 is increased from 0.49% to 0.69% due to the $q\bar{q}$ contribution, while LO_2 is decreased from 0.34% to 0.24% solely due to the reduction of the $g\gamma$ channel from 0.56% to 0.46%.

The relative size of the NLO_1 contribution is increased from 6.2% for $pp \to t\bar{t}\gamma$ to 6.9% and is still the largest contribution at NLO. The largest change in the relative size is found

		σ_i [fb]	Ratio to LO_1
LO_1	$\mathcal{O}(\alpha_s^2\alpha^6)$	$0.15928(3)^{+31.3\%}_{-22.1\%}$	1.00
LO_2	$\mathcal{O}(\alpha_s^1\alpha^7)$	$0.0003798(2)^{+25.8\%}_{-19.2\%}$	+0.24%
LO_3	$\mathcal{O}(\alpha_s^0\alpha^8)$	$0.0010991(2)^{+10.6\%}_{-13.1\%}$	+0.69%
NLO_1	$\mathcal{O}(\alpha_s^3\alpha^6)$	+0.0110(2)	+6.89%
NLO_2	$\mathcal{O}(\alpha_s^2\alpha^7)$	−0.00233(2)	−1.46%
NLO_3	$\mathcal{O}(\alpha_s^1\alpha^8)$	+0.000619(1)	+0.39%
NLO_4	$\mathcal{O}(\alpha_s^0\alpha^9)$	−0.0000166(2)	−0.01%
LO		$0.16076(3)^{+30.9\%}_{-21.9\%}$	1.0093
$\mathrm{NLO}_{\mathrm{QCD}}$		$0.1703(2)^{+1.9\%}_{-6.2\%}$	1.0690
$\mathrm{NLO}_{\mathrm{prd}}$		$0.1694(2)^{+1.7\%}_{-5.9\%}$	1.0637
NLO		$0.1700(2)^{+1.8\%}_{-6.0\%}$	1.0674

Table 5.2: *Same as Table 5.1 but for $pp \to t\bar{t}\gamma\gamma$ in the di-lepton decay channel.*

for the NLO_2 contribution, which is enhanced from −0.28% to −1.46%. This enhancement is in agreement with the findings for stable top quarks in Ref. [18]. The NLO_3 corrections are unchanged at the level of 0.4% of LO_1, and NLO_4 is still completely negligible with respect to the scale uncertainties at NLO of about 6% and even the MC integration errors. The enhancement of NLO_2 has the consequence that the cancellations between the different subleading contributions at LO and NLO are increased and the differences between the $\mathrm{NLO}_{\mathrm{QCD}}$ and NLO predictions are reduced from 1% to 0.2%. Similar to the $pp \to t\bar{t}\gamma$ process, the scale uncertainties are barely changed with the inclusion of subleading effects and remain at the level of 6%. The differences of about 0.5% between the $\mathrm{NLO}_{\mathrm{QCD}}$ and $\mathrm{NLO}_{\mathrm{prd}}$ predictions are induced by the cancellations of the subleading LO contributions of about 0.9% with the subleading NLO corrections in the production of $t\bar{t}\gamma\gamma$ in the *Prod.* contribution with about −1.4%, where the latter case is dominated by NLO_2. The further inclusion of subleading corrections in the decays in the *Prod.* contribution and in the *Mixed* and *Decay* contributions leads to an increase of about 0.4%, which was enhanced in the $pp \to t\bar{t}\gamma$ process, where an increase of about 1% was found. Overall, the effects of subleading LO and NLO contributions are slightly reduced for the $pp \to t\bar{t}\gamma\gamma$ due to larger cancellations between the individual contributions, and thus these effects are again negligibly small at the integrated level.

5.4.2 Differential fiducial cross-section distributions

Next, we study the size of the subleading contributions at the differential level for the $pp \to t\bar{t}\gamma\gamma$ process in the *di-lepton* decay channel. Therefore, in Figure 5.12 the differential distributions for the observables $p_{T,\gamma_1\gamma_2}$, $M_{\gamma_1\gamma_2}$, p_{T,γ_1} and p_{T,b_1} are shown. The first two observables, the transverse momentum and the invariant mass of the $\gamma_1\gamma_2$ system, again represent the irreducible background to the $pp \to t\bar{t}H$ process where the Higgs decays into

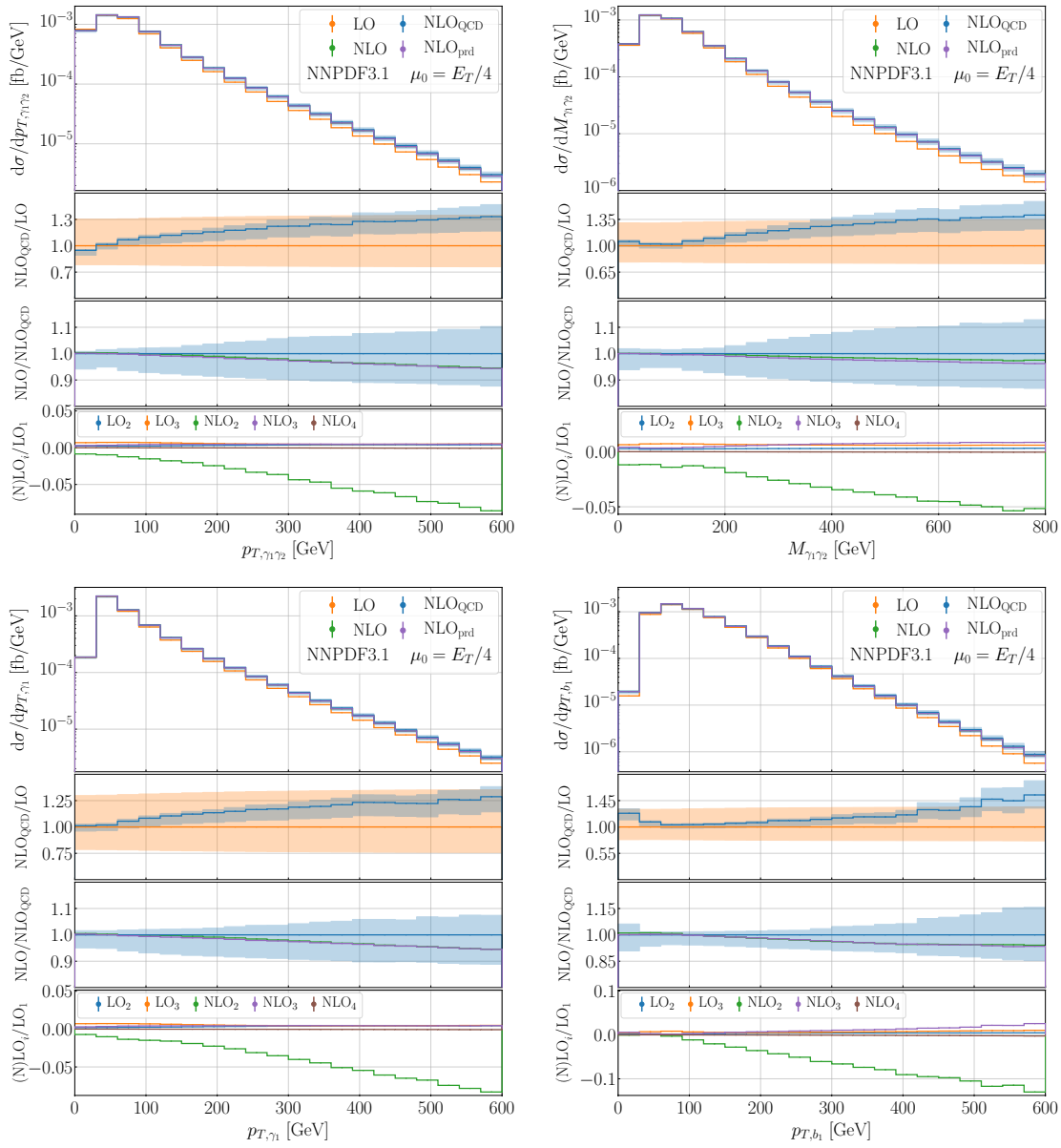

Figure 5.12: *Same as Figure 5.9 but for* $pp \to t\bar{t}\gamma\gamma$ *in the di-lepton decay channel and for the observables* $p_{T,\gamma_1\gamma_2}$, $M_{\gamma_1\gamma_2}$, p_{T,γ_1} *and* p_{T,b_1}.

two photons. In the last chapter we already discussed that large NLO QCD corrections to LO_1 are found for both observables with the dynamical scale choice $\mu_0 = E_T/4$, which exceed the LO scale uncertainties. Due to the different treatment of the top-quark width, that we use in the current calculation the same numerical value at LO and NLO, the NLO_1 corrections are reduced, but are still sizeable and amount to $30\% - 40\%$. The largest subleading contribution is given by NLO_2, where the relative size compared to LO_1 is about -8% for $p_{T,\gamma_1\gamma_2}$ and -5% for $M_{\gamma_1\gamma_2}$. This leads to a reduction of $\mathrm{NLO}_{\mathrm{QCD}}$ by

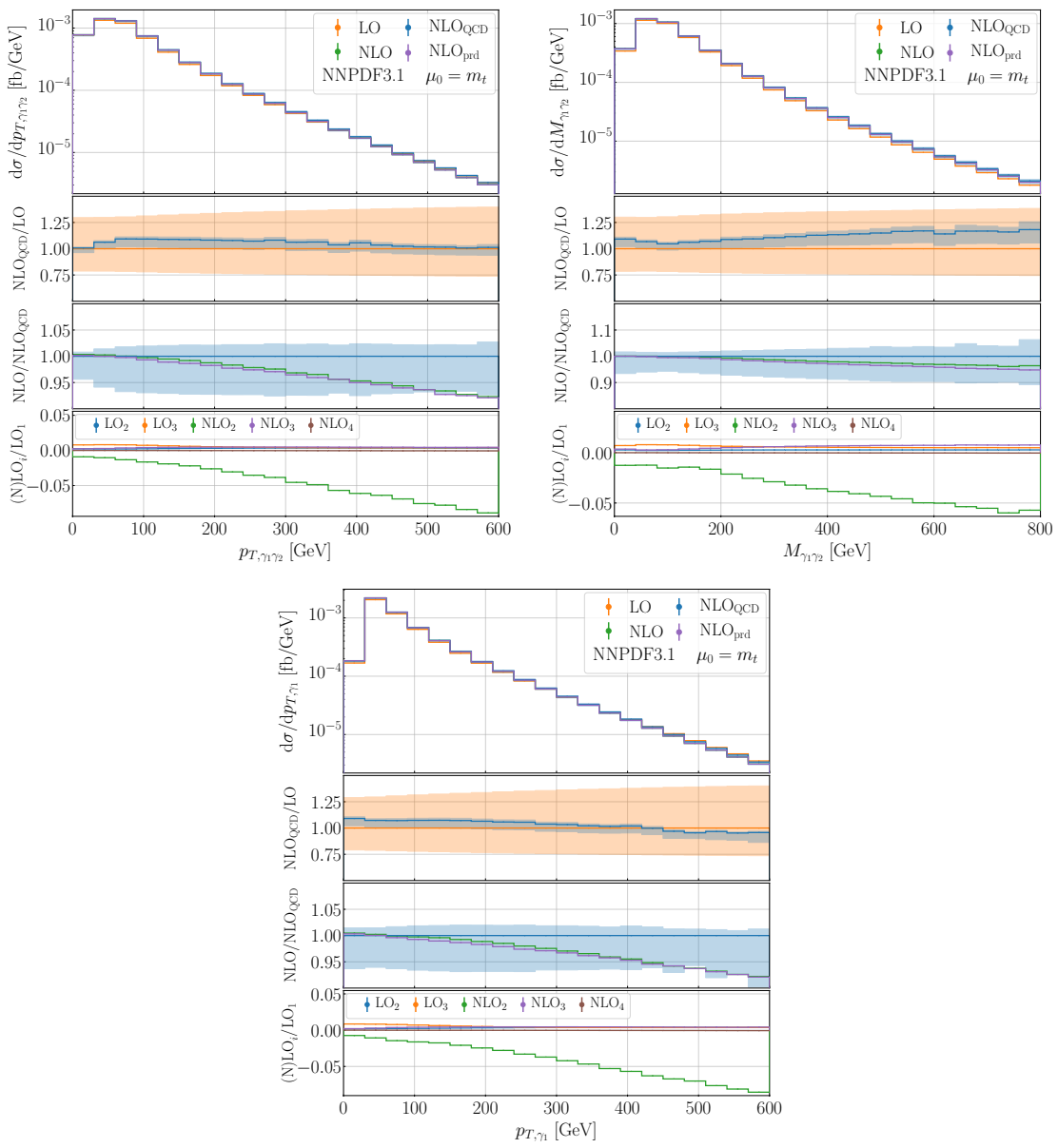

Figure 5.13: *Same as Figure 5.9 but for $pp \to t\bar{t}\gamma\gamma$ in the di-lepton decay channel and for the observables $p_{T,\gamma_1\gamma_2}$, $M_{\gamma_1\gamma_2}$ and p_{T,γ_1}. Results are shown for $\mu_0 = m_t$.*

about 5% and 3%, respectively. The scale uncertainties are still at the level of $11\% - 13\%$ and therefore these corrections play only a secondary role. All other subleading LO and NLO contributions are insignificant. Finally, differences up to 1% are found between NLO and NLO_{prd} for $M_{\gamma_1\gamma_2}$ at high invariant masses, while for $p_{T,\gamma_1\gamma_2}$ the two calculations basically coincide over the entire range. Thus, the NLO_{prd} calculation is completely able to approximate the full calculation at the current precision.

In the case of the two observables p_{T,γ_1} and p_{T,b_1}, the inclusion of subleading corrections

leads to a reduction of the NLO_{QCD} calculation by $5\% - 6\%$ in the tails. In the previous calculation of the $pp \to t\bar{t}\gamma$ process, this reduction was slightly smaller for both observables with about 4%. The scale uncertainties are about twice as large in these phase-space regions with 11% for p_{T,γ_1} and 14% for p_{T,b_1}. The slight enhancement of the subleading corrections is mainly due to the increase of NLO_2 that we have already observed at the integrated level. Furthermore, the size of the real corrections associated with a hard jet are reduced in NLO_1 and NLO_3 for p_{T,b_1}, while both contributions are about the same size for both processes for p_{T,γ_1}. On the one hand, this leads to a reduction of the accidental cancellations between NLO_2 and NLO_3, because of the decrease of NLO_3 from $3\% - 4\%$ to 2%. On the other hand, the NLO QCD corrections in NLO_1 are reduced from 95% to 55%, thus increasing the impact of the subleading corrections on the complete NLO calculation. This reduction is clearly caused by the presence of a second photon already at LO, which can be emitted in the production process and recoil against the $t\bar{t}$ system. Therefore, the importance of subleading corrections in observables that are affected by large real corrections is slightly increased. Similar to the $pp \to t\bar{t}\gamma$ process, the NLO_{prd} predictions can be safely used instead of the complete NLO calculation at the current precision, since differences of less than 1% are found for both observables.

Finally, in Figure 5.13 we present again the photonic differential distributions for the observables $p_{T,\gamma_1\gamma_2}$, $M_{\gamma_1\gamma_2}$ and p_{T,γ_1}, but we use in this case the fixed scale $\mu_0 = m_t$ instead of the dynamical scale setting $\mu_0 = E_T/4$. As already discussed in the last chapter, this scale choice leads to a reduction of QCD corrections in NLO_1 and of the NLO scale uncertainties. In particular, the NLO_1 corrections are reduced from 30% to a few percent in the tail for $p_{T,\gamma_1\gamma_2}$, while QCD corrections of about 10% are found at the beginning of the spectrum. Similarly, the NLO_1 corrections in the tail of $M_{\gamma_1\gamma_2}$ are reduced from $35\% - 40\%$ to $15\% - 20\%$. The NLO QCD scale uncertainties in the tails are reduced from $12\% - 13\%$ to 7% for $p_{T,\gamma_1\gamma_2}$ and to 10% for $M_{\gamma_1\gamma_2}$. Both effects have a direct impact on the importance of the subleading corrections, because on the one hand the reduction of NLO_1 increases the relative size of NLO_2 in the complete NLO calculation, since the relative size of NLO_2 with respect to LO_1 barely depends on the scale setting. This has the effect that the reduction of the NLO_{QCD} calculation due to the inclusion subleading corrections is increased from 5% to 8% for $p_{T,\gamma_1\gamma_2}$ and from 3% to 4% for $M_{\gamma_1\gamma_2}$. On the other hand, the reduction of the NLO scale uncertainties means that the subleading corrections and the scale uncertainties become more similar in size. Especially for the $p_{T,\gamma_1\gamma_2}$ observable, we find that the scale uncertainties and subleading corrections become equal in size in the tail. The same effects can be found again for the p_{T,γ_1} observable, where in this case the NLO_1 corrections are reduced from $20\% - 25\%$ for $\mu_0 = E_T/4$ to -5% for $\mu_0 = m_t$, and the scale uncertainties are reduced from $10\% - 11\%$ to $9\% - 10\%$. The inclusion of subleading contributions then leads to a reduction of the NLO_{QCD} calculation by up to 8% for $\mu_0 = m_t$ compared to the reduction of 5% for $\mu_0 = E_T/4$, where the decrease for the fixed scale is comparable with the corresponding NLO scale uncertainties. Lastly, the predictions with the two scale choices differ at most by 4% for the complete NLO calculation, and are thus well captured by the NLO scale uncertainties.

6. Realistic photon isolation in $t\bar{t}\gamma$

In the final chapter before the conclusions, we discuss the effects of different photon isolation criteria in associated photon production with a top-quark pair, focusing on the $pp \to t\bar{t}\gamma$ process in the *di-lepton* decay channel. The fixed-cone isolation is commonly used in experiments to isolate photons from hadronic activity and to reduce the background of secondary photon production mechanisms. On the theoretical side, only photon isolation criteria based on the smooth-cone isolation were used for theoretical predictions of $pp \to t\bar{t}\gamma$ and $pp \to t\bar{t}\gamma\gamma$, as in the calculations presented in the last two chapters. The use of different isolation criteria in the comparison of theoretical predictions and experimental measurements can generally lead to additional systematic uncertainties of unknown size. The goal of this chapter is to quantify these effects by performing the calculation of $pp \to t\bar{t}\gamma$ in the *di-lepton* decay channel using the fixed-cone isolation and to compare it with alternative predictions using the smooth-cone and hybrid photon isolation criteria. In this comparison, we vary the input parameters of the latter two criteria to find suitable values that lead to theoretical predictions close to those obtained with the fixed-cone isolation, and to assess the dependence of these two photon isolation criteria on the input parameters.

This chapter is structured as follows. First, we summarize in Section 6.1 the differences in the computational setup regarding the process definition and the fiducial phase space. In Section 6.2 we discuss our numerical results with the fixed-cone isolation, and perform a comparison with alternative calculations based on the smooth-cone isolation or the hybrid photon isolation with different input parameters. Finally, we focus on the size of the NLO QCD corrections and the choice of the renormalization/factorization scale in Section 6.3.

6.1 Process definition and LHC setup

The general structure of the calculation is very similar to that of the last chapter. In particular, we consider the $pp \to t\bar{t}\gamma$ in the *di-lepton* decay channel, but work in the full off-shell approach, including all double-, single- and non-resonant diagrams. This means that we do not consider a specific decay chain, but only the following partonic process

$$pp \to e^+\nu_e\,\mu^-\bar{\nu}_\mu\,b\bar{b}\,\gamma. \tag{6.1}$$

The different approach compared to the last chapters, where we used the NWA, is motivated as follows. While the NWA can be used to describe the $pp \to t\bar{t}\gamma$ signal process, its measurement requires the use of various methods such as diagram removal or diagram subtraction to define the $tW\gamma$ background process at NLO QCD to remove the overlap with the $t\bar{t}\gamma$ process, which leads to additional systematic uncertainties. Therefore, we use the full off-shell approach to overcome this issue and to allow for a direct comparison

with experimental measurements, as it was already done for the combined measurement of $t\bar{t}\gamma + tW\gamma$ in the $e\mu$ channel by the ATLAS collaboration [210] compared with the fixed-order predictions using the full off-shell approach based on Ref. [212]. In this study we use only the NLO_{QCD} calculation, consisting of the dominant LO contribution LO_1 and the corresponding NLO QCD corrections NLO_1, and neglect all subleading LO and NLO contributions. This approach is justified because the main dependence on the photon isolation criterion originates from NLO_1, while the subleading contributions were found to be generally small at the integrated level and in most differential distributions. Additionally, the dependence of the subleading NLO corrections on the photon isolation criterion is generally smaller, because the main effects from EW Sudakov logarithms are independent of the photon isolation criterion. Due to the event selection that we use in this calculation, where at least two b-jets of arbitrary charges are required to be resolved, we have to include the following two subprocesses

$$b\bar{b} \;\to\; e^+\nu_e\,\mu^-\bar{\nu}_\mu\,b\bar{b}\,\gamma\,, \qquad\qquad \bar{b}\bar{b} \;\to\; e^+\nu_e\,\mu^-\bar{\nu}_\mu\,\bar{b}\bar{b}\,\gamma\,, \tag{6.2}$$

which contain no double-resonant diagrams and do not exist in the NWA.

Our default setup in the following is the calculation with the fixed-cone isolation, where collinear configurations of photons and partons are allowed. These collinear singularities are subtracted from the real matrix element with a dipole subtraction scheme and absorbed into a redefinition of the quark-to-photon fragmentation function as discussed in Section 2.3. The calculation is performed with the Nagy-Soper subtraction scheme and cross-checked with an alternative calculation using the Catani-Seymour subtraction scheme, where good agreement was found between both calculations. The modifications in both subtraction schemes to include the photonic energy fraction in the dipoles were discussed in Section 3.2.

The calculation of the NLO QCD corrections for the $pp \to e^+\nu_e\,\mu^-\bar{\nu}_\mu\,b\bar{b}\,\gamma$ process is performed for the LHC Run III center-of-mass energy of $\sqrt{s} = 13.6$ TeV. Similar to the previous calculations, we work in the five-flavor scheme, including bottom quarks in the initial state, and keep the CKM matrix diagonal. The contribution of the $b\bar{b}/\bar{b}b$ channel is 0.2% and the $bb/\bar{b}\bar{b}$ channel is 0.02% of the full process at LO, and are therefore negligibly small, but are still consistently included. The NNPDF3.1 NLO PDF set [473] is used for all computations in this chapter, which is interfaced through LHAPDF [476] and where the running of α_s is performed with two-loop accuracy. As in the previous calculations, the presence of photons in the final state requires a mixed scheme for the electromagnetic coupling constant α, where the total power of α is split into $\alpha^n = \alpha_{G_\mu}^{n-n_\gamma}\alpha(0)^{n_\gamma}$ with $n_\gamma = 1$ in this case. The electromagnetic coupling constants in the G_μ scheme (α_{G_μ}) and the on-shell scheme ($\alpha(0)$) are defined in Section 4.2, where we use the following numerical values for the on-shell masses and widths of the gauge bosons

$$\begin{aligned} m_W^{\text{OS}} &= 80.377\ \text{GeV}\,, & \Gamma_W^{\text{OS}} &= 2.085\ \text{GeV}\,, \\ m_Z^{\text{OS}} &= 91.1876\ \text{GeV}\,, & \Gamma_Z^{\text{OS}} &= 2.4955\ \text{GeV}\,, \end{aligned} \tag{6.3}$$

which were taken from Ref. [20]. The on-shell values are converted to the corresponding pole values as described in Ref. [493] by

$$m_V = \frac{m_V^{\text{OS}}}{\sqrt{1 + \left(\Gamma_V^{\text{OS}}/m_V^{\text{OS}}\right)^2}}\,, \qquad\qquad \Gamma_V = \frac{\Gamma_V^{\text{OS}}}{\sqrt{1 + \left(\Gamma_V^{\text{OS}}/m_V^{\text{OS}}\right)^2}}\,, \tag{6.4}$$

which are used as input parameters in the calculation. The numerical values of the mass and width of the Higgs boson as well as the mass of the top quark are unchanged. However, the calculation in the full off-shell approach also requires the calculation of the top-quark width with an off-shell W boson. The corresponding top-quark widths at LO and NLO QCD are given by

$$\Gamma^{\text{LO}}_{t,\text{off-shell}} = 1.4580658 \text{ GeV}\,, \qquad \Gamma^{\text{NLO QCD}}_{t,\text{off-shell}} = 1.3329042 \text{ GeV}\,, \tag{6.5}$$

which is based on the conventions in Ref. [110], the NLO QCD corrections calculated in Ref. [469] and the renormalization scale in the strong coupling constant is set to m_t. The masses and widths of all other fermions are set to zero.

In the calculation with the fixed-cone isolation we use the ALEPH LO quark-to-photon fragmentation function [433] and provide additional results with the BFGII parton-to-photon fragmentation functions for comparison. The latter set includes flavor-dependent quark-to-photon and gluon-to-photon fragmentation functions, where the latter is not required in our case, but is still included. The parametrization of the ALEPH LO quark-to-photon fragmentation function is given in Eq. (2.63), while the parton-to-photon fragmentation functions of the BFGII set are obtained from JETPHOX [494], where we have additionally checked its inclusion in our framework by recovering the results of the fragmentation contribution of the $pp \to \gamma j$ process presented in Table 1 in Ref. [486]. In the case of the ALEPH LO quark-to-photon fragmentation function, the dependence on the fragmentation scale is the same (up to a relative minus sign) for the direct and fragmentation contributions as defined in Eq. (2.54) and Eq. (2.55), respectively. This means that the full NLO_{QCD} calculation is independent of the fragmentation scale. In particular, the direct contribution $\sigma^{\text{NLO QCD}}_{\text{dir}}$ consists of the photon radiation at the matrix element and the counterterm from the factorization of the quark-to-photon fragmentation function, and is thus independent of the parton-to-photon fragmentation functions. The full dependence of the different parametrizations of the fragmentation functions is encoded in the fragmentation contribution $\sigma^{\text{NLO QCD}}_{\text{frag}}$, which is the convolution of the partonic $pp \to e^+\nu_e\,\mu^-\bar{\nu}_\mu\,b\bar{b}\,j$ process with the parton-to-photon fragmentation function, where j is either a gluon or a massless quark.

Our event selection is inspired by the recent measurement of the $pp \to t\bar{t}\gamma$ process by the ATLAS collaboration [13], where two fixed-cone photon isolation criteria are used to restrict the energy deposition in the calorimeter in a cone with the radius $R = 0.4$ around the photon candidate and the sum of the transverse momenta of tracks in a smaller cone with the size $R = 0.2$. The two photon isolation criteria are realized in our calculation by requiring that the transverse hadronic energy $E_{T,\text{had}}$, as defined in Eq. (2.46), inside the cone around the photon candidate with the radius $R = 0.4$ is limited by

$$E_{T,\text{had}} < 0.022 \cdot E_{T,\gamma} + 2.45 \text{ GeV}, \tag{6.6}$$

and within the smaller cone with radius $R = 0.2$ by

$$E_{T,\text{had}} < 0.05 \cdot E_{T,\gamma}. \tag{6.7}$$

The fixed-cone isolation with the smaller cone has only a minor effect and reduces the integrated cross section by less than 0.5%. The calculation with the fixed-cone isolation is

then compared with predictions using the smooth-cone and hybrid photon isolation criteria, where in both cases the input parameters of the (inner) smooth-cone isolation are varied. In this calculation we require at least two b-jets, two oppositely charged leptons and one photon in the final state. In contrast to the calculations in the last two chapters, where we defined a b-jet as a jet with nonzero net bottomness, in this calculation we follow closely the experimental environment, where it is hardly possible to tag the charge of a b-jet. Therefore, the charges of b-jets are neglected in the recombination in the jet algorithm, which can be translated into the following recombination rules

$$bg \to b, \qquad \bar{b}g \to \bar{b}, \qquad b\bar{b} \to g, \qquad bb \to g, \qquad \bar{b}\bar{b} \to g, \tag{6.8}$$

which corresponds to the charge-blind b-jet tagging scheme in Ref. [191]. The *anti-k_T* jet algorithm with $R = 0.4$ is used to cluster partons into jets after the photon isolation criterion is applied. Compared to the event selection in the last two calculations, the fiducial phase-space of the prompt photon is modified to

$$p_{T,\gamma} > 20 \text{ GeV}\,, \qquad\qquad |y_\gamma| < 2.37\,, \tag{6.9}$$

while the cuts on b-jets, charged leptons and all ΔR separations remain unchanged.

We again set the renormalization and factorization scales to the common scale $\mu_0 = E_T/4$ as defined in Eq. (4.17). Since it is not possible to obtain the momenta of the two top quarks directly in the full off-shell calculation, in this case the top-quark momenta are reconstructed by minimizing the following quantity

$$\mathcal{Q} = |M(t) - m_t| + |M(\bar{t}) - m_t|, \tag{6.10}$$

where $M(t)$ and $M(\bar{t})$ are the invariant masses of the reconstructed top and anti-top quarks, respectively. We use the MC truth for the two charged leptons and neutrinos, and allow the photon to be radiated in the production process or in the decay of one of the two top quarks. Furthermore, we neglect the charges of the b-jets and additional radiation of light jets in the reconstruction. Therefore, we encounter 6 different resonant histories at LO, due to the three possibilities from where the photon can be radiated and the facts that the two b-jets in the two top-quark decays can be swapped. At NLO QCD, the number of resonant histories is increased to 18 in the bg channel in the case of three resolved b-jets. Theoretical uncertainties from missing higher orders are again estimated by performing a 7-point scale variation of the renormalization and factorization scales. Any uncertainties due to the different parametrizations of the parton-to-photon fragmentation functions or the choice of the fragmentation scale in the case of the BFGII set are not taken into account in the full calculation due to the small relative size of the fragmentation contribution.

6.2 Comparison of photon isolation criteria

Before discussing the effects of different photon isolation criteria and their dependence on the input parameters, we first focus on the size of the fragmentation contribution. Therefore, in Table 6.1 we present the full NLO QCD calculation, $\sigma^{\text{NLO QCD}}$, of the $pp \to e^+\nu_e\,\mu^-\bar{\nu}_\mu\,b\bar{b}\,\gamma$ process with the ALEPH LO and BFGII parton-to-photon fragmentation functions. In addition, we display the fragmentation contribution, $\sigma^{\text{NLO QCD}}_{\text{frag}}$, for both

	ALEPH LO	BFGII	ALEPH LO / BFGII
$\sigma^{\text{NLO QCD}}$ [fb]	$21.50(2)^{+1.4\%}_{-5.0\%}$	$21.48(2)^{+1.4\%}_{-5.0\%}$	1.001
$\sigma^{\text{NLO QCD}}_{\text{frag}}$ [fb]	0.038724(8)	0.017020(4)	2.275

Table 6.1: *Integrated fiducial cross sections at NLO QCD for the* $pp \to e^+\nu_e\,\mu^-\bar{\nu}_\mu\,b\bar{b}\,\gamma$ *process at the LHC with* $\sqrt{s} = 13.6$ TeV *using the fixed-cone isolation and the ALEPH LO and the BFGII parton-to-photon fragmentation functions. Results are presented for the full NLO QCD calculation as well as for the fragmentation contribution only. Scale uncertainties estimated by scale variation and MC integration errors are also displayed.*

parametrizations. Scale uncertainties are displayed for the full NLO QCD calculations. The last column shows the ratio of the results obtained with the ALPEH LO quark-to-photon fragmentation function to the BFGII parton-to-photon fragmentation functions. For this comparison, we have set the fragmentation scale to $\mu_{\text{Fr}} = R\,p_{T,\gamma}$ with $R = 0.4$ following Ref. [495]. We note again that the sum of the direct and the fragmentation contribution is independent of μ_{Fr} for the ALEPH LO quark-to-photon fragmentation function. This means that the fragmentation scale is only relevant in our discussion to separate the direct and fragmentation contributions. We find that the fragmentation contribution with the ALEPH LO parametrization is about 130% larger than the prediction with the BFGII set. This large difference is partially induced by the inner cone of $R = 0.2$ in the fixed-cone isolation. The enhancement of the prediction with the ALEPH LO quark-to-photon fragmentation function is reduced to 80% without the inner cone. Similar large differences between these parametrization were already found in previous calculations of isolated photon production as in Ref. [496] and originate mainly from the different scale evolution of the quark-to-photon fragmentation function. Therefore, these differences decrease when the fixed-order NLO quark-to-photon fragmentation function, as first determined in Ref. [432, 435], is used instead of the ALEPH LO one. However, the relative size of the fragmentation contribution in the full NLO QCD calculation is less than 0.2% for the ALEPH LO quark-to-photon fragmentation and less than 0.1% for the BFGII set. Thus, the fragmentation contribution and the differences between the two sets of fragmentation functions in the full NLO QCD calculation are negligibly small compared to the scale uncertainties of about 5%. The fragmentation contribution highly depends on the actual event selection and the photon isolation criterion, but its small size is also related to the absence of light jets at LO. Because of that, the fragmentation contribution in the gg and $q\bar{q}$ channels is strongly suppressed, since both b-jets in the final state have to be resolved and are not allowed to fragment into a photon. Thus, only the additional gluon can fragment into a photon, where the corresponding gluon-to-photon fragmentation is only included in the BFGII set and is heavily suppressed. Therefore, the main contribution comes from the qg channel, where the additional light quark in the final state can fragment into a photon. Only in the PDF-suppressed bg channel, where a third bottom quark is present in the final state, one of the (three) bottom quarks can fragment into a photon. Thus, the fragmentation contribution can be enhanced in the *lepton + jet* decay channel, because in this

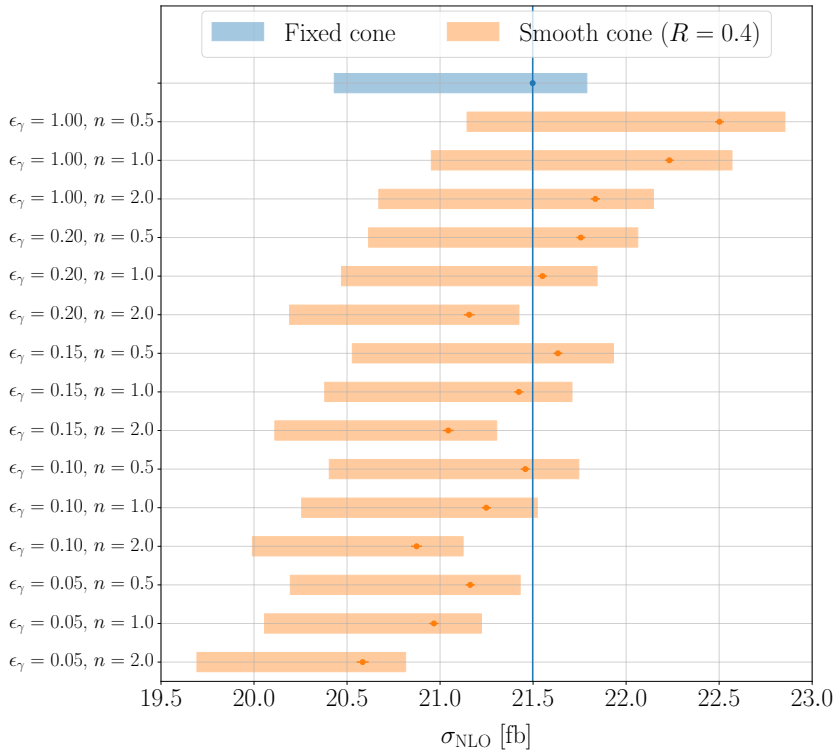

Figure 6.1: *Comparison of integrated fiducial cross sections at NLO QCD for the* $pp \to e^+\nu_e\,\mu^-\bar{\nu}_\mu\,b\bar{b}\,\gamma$ *process at the LHC with* $\sqrt{s} = 13.6$ TeV *of the fixed-cone isolation and the smooth-cone isolation with the parameters* $\epsilon_\gamma \in \{0.05, 0.10, 0.15, 0.20, 1.00\}$, $n \in \{0.5, 1.0, 2.0\}$ *and* $R_{\gamma j} = 0.4$. *Results are obtained with* $\mu_0 = E_T/4$ *and the NNPDF3.1 NLO PDF set. Scale uncertainties and MC integration errors are also displayed.*

case the quarks from the W-boson decay can fragment into a photon. Therefore, the gg and $q\bar{q}$ channels are enhanced and no longer vanish for the ALEPH LO quark-to-photon fragmentation function.

Next, we perform a comparison between the calculation with the fixed-cone isolation and alternative predictions with the smooth-cone isolation that we have used in the previous chapters. In Figure 6.1 we present the NLO QCD calculations with the corresponding scale uncertainties for the fixed-cone isolation (blue) and the smooth-cone isolation (orange), where we set $R_{\gamma j} = 0.4$ and vary the other parameters in the ranges $\epsilon_\gamma \in \{0.05, 0.10, 0.15, 0.20, 1.00\}$ and $n \in \{0.5, 1.0, 2.0\}$. The largest differences between the two isolation criteria are found for $(\epsilon_\gamma, n) = (1.00, 0.5)$ with 4.7% and for $(\epsilon_\gamma, n) = (0.05, 2.0)$ with 4.3%. These differences are of similar size as the NLO QCD scale uncertainties of about 5% and are therefore not negligible. Our standard choice of the input parameters in the smooth-cone isolation in the last two chapters corresponds to $(\epsilon_\gamma, n) = (1.00, 1.0)$, which differs from the prediction with the fixed-cone isolation by about 3.4% and is therefore still relevant compared to the scale uncertainties. These differences in the normalization can be avoided by tuning the input parameters. In this way, these differences are reduced to negligible $0.2\% - 0.4\%$ for $(\epsilon_\gamma, n) = (0.20, 1.0)$, $(\epsilon_\gamma, n) = (0.15, 1.0)$ and $(\epsilon_\gamma, n) = (0.10, 0.5)$. Still, we find that the cross section is very sensitive to the specific input values, and in

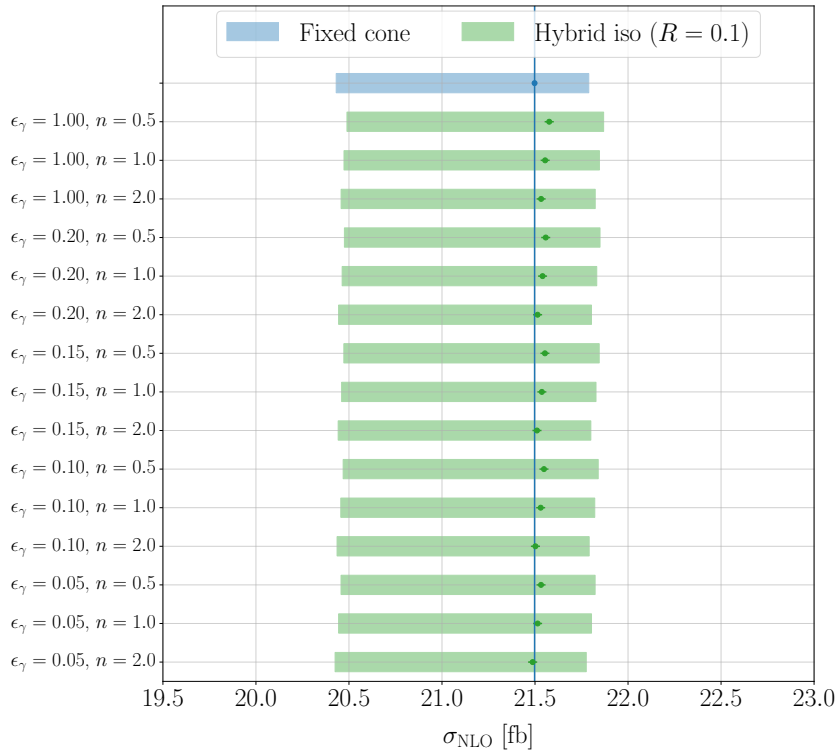

Figure 6.2: *Same as Figure 6.1 but for the hybrid photon isolation with the parameters* $\epsilon_\gamma \in \{0.05, 0.10, 0.15, 0.20, 1.00\}$*,* $n \in \{0.5, 1.0, 2.0\}$ *and* $R_{\gamma j} = 0.1$ *instead of the smooth-cone isolation.*

our case the different parametrizations differ by up to 9%. Thus, it is expected that the tuning of the smooth-cone isolation generally leads to different input parameters for other processes such as $pp \to t\bar{t}\gamma\gamma$ or other decay channels like the *lepton + jet* one, because the sensitivity on the input parameters is increased with more photons and jets in the final state. In Chapter 4 we have already briefly elaborated on the dependence of the input parameters of the smooth-cone isolation for the $pp \to t\bar{t}\gamma\gamma$ process by performing alternative calculations with different input parameters. In particular, we have found that the differences between the predictions obtained with the two input parameter sets $(\epsilon_\gamma, n) = (1.00, 1.0)$ and $(\epsilon_\gamma, n) = (0.50, 1.0)$ are about 5% for the *lepton + jet* and about 3% in the *di-lepton* decay channel. This difference is reduced to about 1.5% in our current case of $pp \to t\bar{t}\gamma$ in the *di-lepton* decay channel, which clearly shows that the dependence is indeed greatly reduced due to less photons and jets in the final state.

Instead of relying completely on the smooth-cone isolation, it is also possible to use a hybrid photon isolation, where a smooth-cone isolation with a smaller radius is applied first, followed by the fixed-cone isolation. Due to the use of the smooth-cone isolation, the fragmentation contribution also vanishes in this case. This approach has the advantage that the dependence on the input parameters of the inner smooth-cone isolation is reduced as presented in Figure 6.2, which again shows the integrated fiducial cross section with the corresponding scale uncertainties obtained with the fixed-cone isolation compared to the case with the hybrid photon isolation. In the latter case, a smooth-cone isolation with

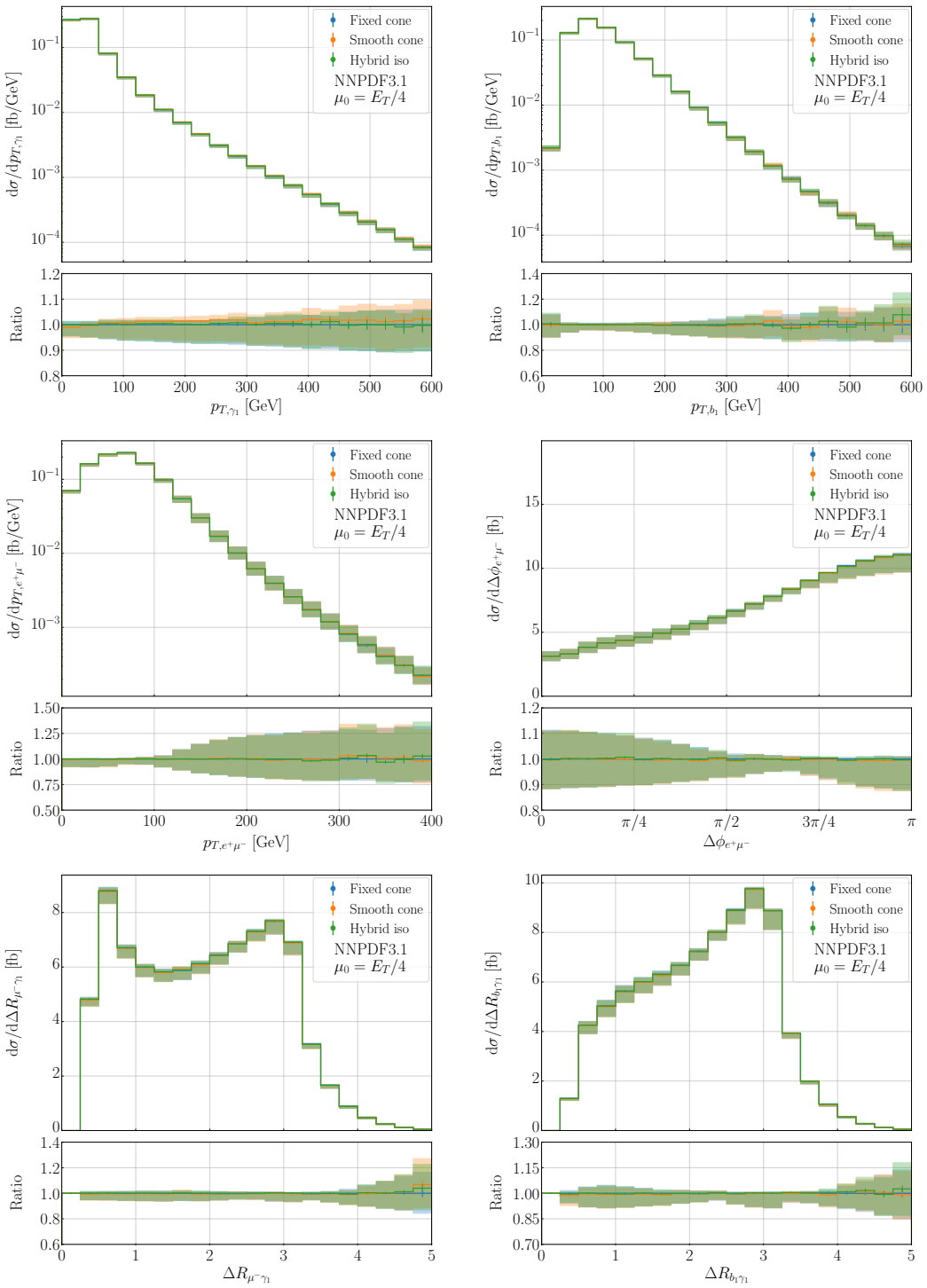

Figure 6.3: *Differential fiducial cross-section distributions for the observables p_{T,γ_1}, p_{T,b_1}, $p_{T,e^+\mu^-}$, $\Delta\phi_{e^+\mu^-}$, $\Delta R_{\mu^-\gamma_1}$ and $\Delta R_{b_1\gamma_1}$ at NLO QCD for the $pp \to e^+\nu_e\,\mu^-\bar{\nu}_\mu\,b\bar{b}\,\gamma$ process at the LHC with $\sqrt{s} = 13.6$ TeV. Results are presented for the fixed-cone isolation, the smooth-cone isolation and the hybrid photon isolation. Lower panels show the ratio compared to the fixed-cone isolation. Scale uncertainties and MC integration errors are also displayed.*

$R_{\gamma j} = 0.1$ is used and the other parameters are set to $\epsilon_\gamma \in \{0.05, 0.10, 0.15, 0.20, 1.00\}$ and $n \in \{0.5, 1.0, 2.0\}$. We find that the dependence of the inner smooth-cone isolation on the input parameters is negligibly small with differences of only 0.4%. Furthermore, all predictions of the hybrid photon isolation agree very well with the fixed-cone isolation, where the largest differences are only 0.4%, which are negligibly small with respect to the scale uncertainties. We have checked that the dependence on the input parameters is slightly larger if we increase the radius of the (inner) smooth-cone isolation. In particular, the spread of the predictions with the hybrid photon isolation with different input parameters is increased from about 0.4% for $R_{\gamma j} = 0.1$ to 0.7% for $R_{\gamma j} = 0.15$ and to 1.0% for $R_{\gamma j} = 0.2$, while the other parameters are again varied in the same ranges as before. Nevertheless, the hybrid isolation can be safely used instead of the fixed-cone isolation, since the largest differences between the two photon isolation criteria are less than 0.4% for $R_{\gamma j} = 0.15$ and less than 0.7% for $R_{\gamma j} = 0.2$. In principle, it is possible to increase the radius even further, but in this case the radius of the smooth-cone isolation would be larger than the radius of the inner cone of the fixed-cone isolation. This means that for certain values of ϵ_γ and n, the fixed-cone isolation at $R = 0.2$ would have no effect. Moreover, the dependence on $R_{\gamma j}$ is increased for decreasing ϵ_γ and increasing n. In particular, we find for the two extreme cases in our study that the hybrid photon isolation with $(\epsilon_\gamma, n) = (1.00, 0.5)$ barely depends on $R_{\gamma j}$ and differences of less than 0.1% are found for the three values $R_{\gamma j} \in \{0.10, 0.15, 0.20\}$, while for the other extreme case of $(\epsilon_\gamma, n) = (0.05, 2.0)$ the calculations for the three values of $R_{\gamma j}$ differ by about 0.6%. For tuned values of the input parameters leading to small differences in the central values compared to the calculation with the fixed-cone isolation, the scale uncertainties are identical with all three photon isolation criteria. All in all, the dependence on the input parameters of the (inner) smooth-cone isolation is greatly reduced in the hybrid photon isolation. Even without a tuning of these input parameters, a good agreement with the calculation using the fixed-cone isolation is found.

Next, we investigate whether additional effects appear at the differential level when different photon isolation criteria are used. Based on the findings at the integrated level, we choose the parameters of the smooth-cone isolation as $(\epsilon_\gamma, n) = (0.10, 0.5)$ with $R_{\gamma j} = 0.4$, which have led to differences of only 0.3% compared to the prediction using the fixed-cone isolation. The parameters of the hybrid photon isolation are inspired by the input parameters used to generate the signal process in a recent measurement of $pp \to t\bar{t}\gamma$ by the ATLAS collaboration [13]. In this case, the input parameters of the inner smooth-cone isolation are set to $(\epsilon_\gamma, n) = (0.10, 2.0)$ with $R_{\gamma j} = 0.1$, for which we find that the central value of the integrated cross section is basically the same as with the fixed-cone isolation. Overall, we find for all observables considered in our study that the predictions for the three different photon isolation criteria agree very well. As an example, the observables p_{T,γ_1}, p_{T,b_1}, $p_{T,e^+\mu^-}$, $\Delta\phi_{e^+\mu^-}$, $\Delta R_{\mu^-\gamma_1}$ and $\Delta R_{b_1\gamma_1}$ at NLO QCD are shown in Figure 6.3 for three isolation criteria, where the differences are indeed very small compared to the scale uncertainties and similar in size as the MC integration errors, which are also both shown. Only for the p_{T,γ_1} observable we find a small tendency that the prediction with the smooth-cone isolation is consistently larger than the predictions with the other two photon isolation criteria over almost the entire range but only by about $1\% - 2\%$, which can still be neglected with respect to the corresponding scale uncertainties of $5\% - 10\%$.

Finally, it is important to note that, in general, the use of a different photon isolation criterion not only modifies the normalization, but can also leads to additional shape dis-

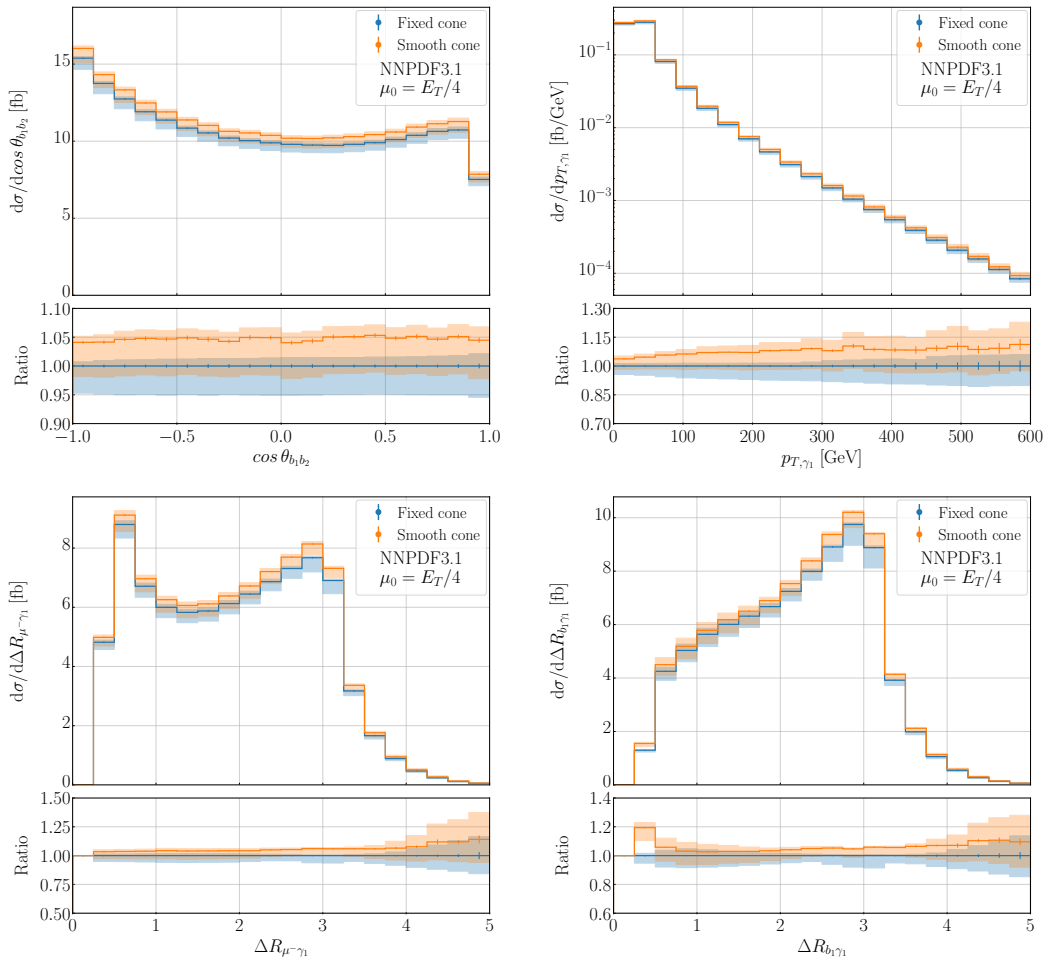

Figure 6.4: *Differential fiducial cross-section distributions for the observables* $cos\theta_{b_1b_2}$, p_{T,γ_1}, $\Delta R_{\mu^-\gamma_1}$ *and* $\Delta R_{b_1\gamma_1}$ *at NLO QCD for the* $pp \to e^+\nu_e\,\mu^-\bar{\nu}_\mu\,b\bar{b}\,\gamma$ *process at the LHC with* $\sqrt{s} = 13.6$ *TeV. Results are presented for the fixed-cone isolation and the smooth-cone isolation with the input parameters* $(\epsilon_\gamma, n) = (1.00, 0.5)$ *with* $R_{\gamma j} = 0.4$. *Lower panels show the ratio compared to the fixed-cone isolation. Scale uncertainties and MC integration errors are also displayed.*

tortions at the differential level. This is especially the case for observables connected with the kinematics of the photon. In Figure 6.4 we present the differential distributions for the observables $cos\theta_{b_1b_2}$, p_{T,γ_1}, $\Delta R_{\mu^-\gamma_1}$ and $\Delta R_{b_1\gamma_1}$ at NLO QCD with the corresponding scale uncertainties using the fixed-cone and the smooth-cone isolation, where in the latter case the input parameters are set to $(\epsilon_\gamma, n) = (1.00, 0.5)$ with $R_{\gamma j} = 0.4$. This set of parameters corresponds to the case that has led to the largest differences of about 4.7% at the integrated level compared to the calculation with the fixed-cone isolation. While the two predictions differ by about $4\% - 5\%$ in most parts due to the normalization as for example in the case of $cos\theta_{b_1b_2}$, larger differences are found in certain phase-space regions. In particular, we find for p_{T,γ_1} that the differences between the two isolation criteria increase towards the tails from $4\% - 5\%$ to about 10%. On the other hand, the differences between

μ_0	$\sigma^{\text{LO QCD}}$ [fb]	$\sigma^{\text{NLO QCD}}$ [fb]	$\mathcal{K} = \sigma^{\text{NLO QCD}}/\sigma^{\text{LO QCD}}$
$E_T/4$	$17.512(8)^{+30.9\%}_{-22.1\%}$	$21.50(2)^{+1.4\%}_{-5.0\%}$	1.23
$H_T/4$	$19.409(9)^{+31.9\%}_{-22.6\%}$	$21.38(2)^{+1.4\%}_{-7.5\%}$	1.10
m_t	$15.877(7)^{+30.1\%}_{-21.6\%}$	$21.13(2)^{+1.4\%}_{-6.4\%}$	1.33

Table 6.2: *Integrated fiducial cross sections at LO and NLO QCD for the* $pp \to e^+\nu_e\,\mu^-\bar{\nu}_\mu\,b\bar{b}\,\gamma$ *process at the LHC with* $\sqrt{s} = 13.6$ TeV *using the fixed-cone isolation and the ALEPH LO quark-to-photon fragmentation function. Results are presented for the three scale choices* $\mu_0 = E_T/4$, $\mu_0 = H_T/4$ *and* $\mu_0 = m_t$. *Scale uncertainties estimated by scale variation and MC integration errors are also displayed.*

the two photon isolation criteria are rather constant of about 5% for the angular separation between charged leptons and the photon, $\Delta R_{\mu^-\gamma_1}$, while for large angular separations above $\Delta R_{\mu^-\gamma_1} > 4$ these differences increase to more than 10%. Finally, for the angular separation between the hardest b-jet and the photon, $\Delta R_{b_1\gamma_1}$, we find similar differences of about 10% for large angular separations, but in addition the region at small angular separations is also affected by differences up to 20%.

6.3 NLO QCD corrections

Next, we briefly study the size of the NLO QCD corrections for the new setup at the center-of-mass energy of $\sqrt{s} = 13.6$ TeV, with the fixed-cone isolation and the full off-shell approach. Since the general behavior is very similar to that already found in the last chapter for the $pp \to t\bar{t}\gamma$ process in the *di-lepton* decay channel using the NWA, we will focus here on the differences with respect to the previous setup and discuss the scale choice for this process. In particular, we consider three different choices consisting of our default scale set to $\mu_0 = E_T/4$, and the two scale settings $\mu_0 = H_T/4$ with

$$H_T = p_{T,b_1} + p_{T,b_2} + p_{T,e^+} + p_{T,\mu^-} + p_{T,miss} + p_{T,\gamma_1} \tag{6.11}$$

and $\mu_0 = m_t$. The latter scale choice is simply motivated by the findings of the last two chapters that it is an adequate alternative scale choice at the integrated level for the $pp \to t\bar{t}\gamma\gamma$ process in the *di-lepton* and *lepton + jet* decay channels and for photonic observables in the $pp \to t\bar{t}\gamma(\gamma)$ process in the *di-lepton* decay channel. The scale $\mu_0 = H_T/4$ was used in previous calculations of the $pp \to t\bar{t}\gamma$ process in the *di-lepton* decay channel using either the full off-shell or the NWA approach [12, 212] and therefore serves as an alternative dynamical scale choice. In addition, this scale does not require the reconstruction of the top-quark pair which can become ambiguous in the full off-shell calculation due to single- and non-resonant contributions where only one or even zero resonant top quarks are present. In Table 6.2 we present the integrated fiducial cross section at LO and NLO QCD with the corresponding scale uncertainties for the $pp \to e^+\nu_e\,\mu^-\bar{\nu}_\mu\,b\bar{b}\,\gamma$ process with the three scale settings $\mu_0 = E_T/4$, $\mu_0 = H_T/4$ and $\mu_0 = m_t$. The last column displays the ratio $\mathcal{K} = \sigma^{\text{NLO QCD}}/\sigma^{\text{LO QCD}}$. The NLO QCD predictions are obtained with the default setup

consisting of the two fixed-cone isolation criteria with the ALEPH LO quark-to-photon fragmentation function. With respect to the previous setup in the last chapter, which we have used for the calculation of the complete NLO corrections for the $pp \to t\bar{t}\gamma$ in the *di-lepton* decay channel using the NWA, the NLO QCD corrections of NLO_1 are reduced from 27% to 23% for $\mu_0 = E_T/4$, where we used the LO and NLO QCD top-quark widths for the LO and NLO QCD predictions, respectively. This reduction is purely due to the different photon isolation criteria used in the two calculations. In particular, the fixed-cone isolation in the current calculation is more restrictive than the smooth-cone isolation with the input parameters $(\epsilon_\gamma, n) = (1.00, 1.0)$ and $R_{\gamma j} = 0.4$, as we have demonstrated in the last section. Indeed, when using the same smooth-cone isolation, the NLO QCD corrections become identical with about 27%, even though the two setups differ slightly in the center-of-mass energy and the fiducial cuts on the isolated photon. We note that in this calculation we used the full off-shell approach instead of the NWA as in the last chapter. However, the different top-quark modeling approaches have barely any impact on the discussion of the NLO QCD corrections at the integrated level, as shown in Ref. [12] that in the ratio of the NLO and LO cross sections the full off-shell effects cancel to a large extent. For the other two scale choices we find NLO QCD corrections of 10% for $\mu_0 = H_T/4$ and of 33% for $\mu_0 = m_t$. The different relative sizes of the NLO QCD corrections originate from large differences of the LO predictions, where the largest are found between $\mu_0 = H_T/4$ and $\mu_0 = m_t$ of about 20%. These differences at LO are covered by the corresponding scale uncertainties of about 30%. At NLO QCD the differences between the three scales are reduced to less than 2% and are covered within the corresponding scale uncertainties of about 5.0% for $\mu_0 = E_T/4$, 7.5% for $\mu_0 = H_T/4$ and 6.4% for $\mu_0 = m_t$.

At last, in Figure 6.5 we present the differential distributions for the observables p_{T,γ_1}, $M_{e^+\mu^-}$, $\Delta\phi_{e^+\mu^-}$ and $\Delta R_{\mu^-\gamma_1}$ at NLO QCD with the corresponding scale uncertainties for the three scale settings $\mu_0 = E_T/4$, $\mu_0 = H_T/4$ and $\mu_0 = m_t$. In the middle panels we show the differential $\mathcal{K}$-factor for all three scales with the LO scale uncertainties in dashed lines for comparison. The last panels display the differential ratios of the NLO QCD calculations with respect to $\mu_0 = E_T/4$. The corresponding scale uncertainties and MC integration errors are also shown in all panels. For the transverse momentum of the hardest photon, p_{T,γ_1}, we find that the behavior of the QCD corrections is fairly different for the three scale choices. In particular, the NLO QCD corrections decrease from 34% in the bulk of the distribution to 15% in the tail for $\mu_0 = m_t$. On the other hand, the NLO QCD corrections consistently increase towards the tails to about 55% for the two dynamical scale settings exceeding the LO uncertainty bands. However, the size of the higher-order corrections are different at the beginning of the spectrum, where they are about 10% for $\mu_0 = H_T/4$ and 20% for $\mu_0 = E_T/4$. The central values of the differential cross section differ by less than 2%, which is negligible compared to the corresponding scale uncertainties which are about 10% in the tail and are reduced to 5% for $\mu_0 = E_T/4$, 8% for $\mu_0 = H_T/4$ and 6% for $\mu_0 = m_t$ at the beginning of the spectrum, closely resembling the behavior of the different scales at the integrated level. In the case of $M_{b_1 b_2}$ the general behavior is similar for all three scale settings, where we find that the NLO QCD corrections decrease towards the tails. In particular, we find that the higher-order QCD corrections are 35% for $\mu_0 = E_T/4$, 23% for $\mu_0 = H_T/4$, and 52% for $\mu_0 = m_t$ at the beginning of the spectrum compared to 7%, -4% and -18% in the tail. Thus, the largest shape distortions are found for $\mu_0 = m_t$, where in addition the largest scale uncertainties of about 40% are found in

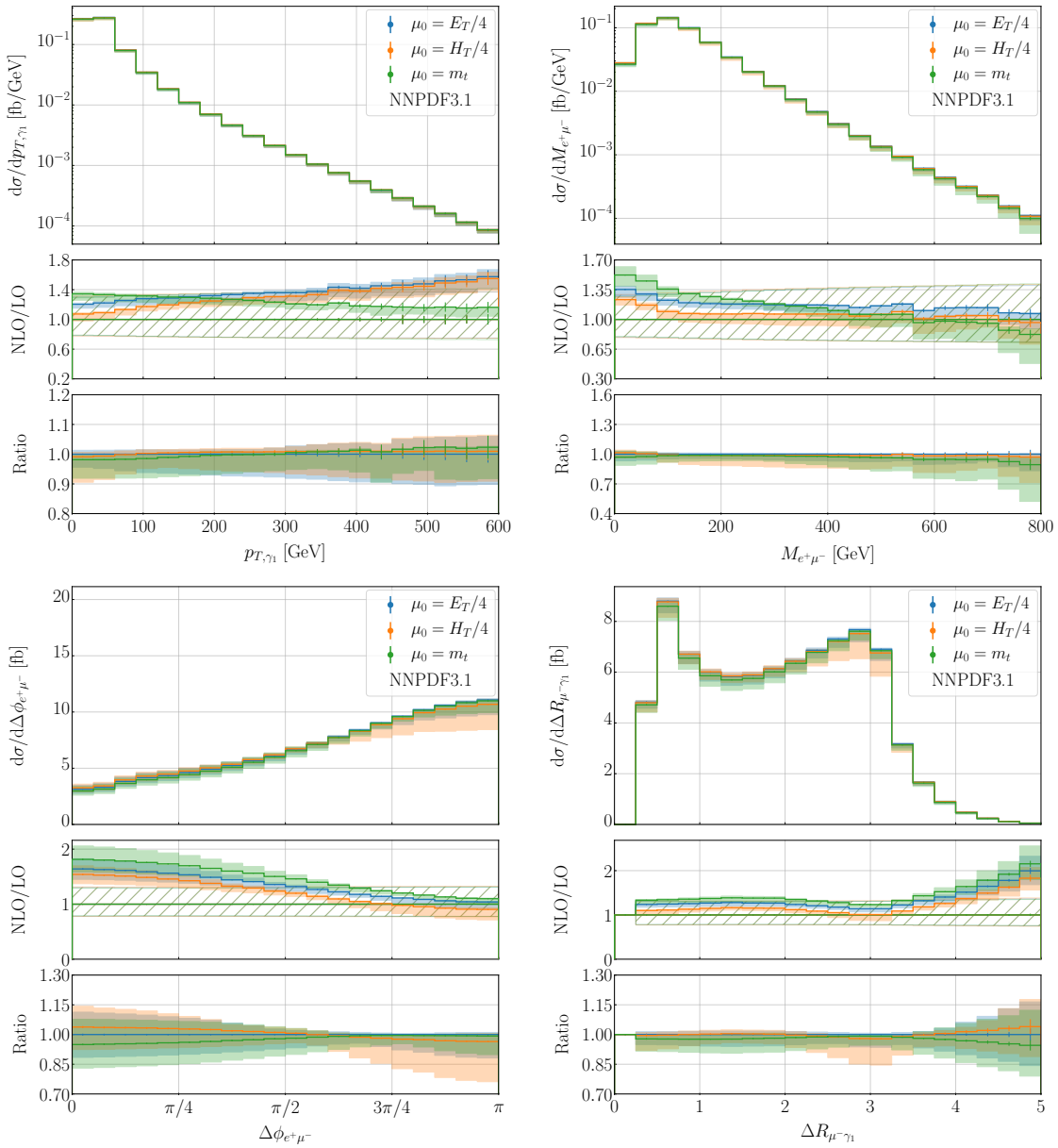

Figure 6.5: *Differential fiducial cross-section distributions for the observables* p_{T,γ_1}, $M_{e^+\mu^-}$, $\Delta\phi_{e^+\mu^-}$ *and* $\Delta R_{\mu^-\gamma_1}$ *at NLO QCD for the* $pp \to e^+\nu_e\,\mu^-\bar{\nu}_\mu\,b\bar{b}\,\gamma$ *process at the LHC with* $\sqrt{s} = 13.6$ *TeV. Results are presented for the three scale settings* $\mu_0 = E_T/4$, $\mu_0 = H_T/4$ *and* $\mu_0 = m_t$. *Middle panels show the differential* $\mathcal{K}$*-factor with the corresponding LO scale uncertainties in dashed lines for comparison and the lower panels the ratio of the NLO QCD results with respect to* $\mu_0 = E_T/4$. *Scale uncertainties and MC integration errors are also displayed.*

the tail, which are as large as the LO ones. These uncertainties are reduced to $10\% - 15\%$ for $\mu_0 = E_T/4$ and $20\% - 25\%$ for $\mu_0 = H_T/4$ at NLO QCD. For $\mu_0 = H_T/4$ we find that the scale uncertainties are enhanced to 12% in the range 200 GeV $< M_{b_1 b_2} <$ 400 GeV, while the corresponding scale uncertainties in the case of $\mu_0 = E_T/4$ are about half as small. The differences in the central value between the two dynamical scale are less than 3% and increase to 10% in the case of the fixed scale.

For angular distributions such as $\Delta\phi_{e^+\mu^-}$ and $\Delta R_{\mu^-\gamma_1}$ we find that the general behavior of the NLO QCD corrections is the same for all three scales and is very similar to that found in Chapter 4 for $\Delta R_{\ell^+\gamma_1}$ and $\Delta\Phi_{\ell^+\ell^-}$ and will therefore not be repeated again. The differences in the relative size of the NLO QCD corrections between the different scale settings arise from the different $\mathcal{K}$-factors at the integrated level. Thus, the largest higher-order QCD corrections are again found for $\mu_0 = m_t$. The scale $\mu_0 = H_T/4$ leads to differences up to 4% compared to our default scale $\mu_0 = E_T/4$, while the scale $\mu_0 = m_t$ leads to differences up to 6%. The NLO scale uncertainties are very similar for the $\mu_0 = E_T/4$ and $\mu_0 = m_t$ scale settings and are about $5\% - 13\%$ for $\Delta\phi_{e^+\mu^-}$ and $\Delta R_{\mu^-\gamma_1}$, while in the latter case the scale uncertainties are further enhanced to $15\% - 20\%$ for large angular separations due to large QCD corrections. For $\mu_0 = H_T/4$, the scale uncertainties are enhanced in certain phase-space regions, such as large angular separations in $\Delta\phi_{e^+\mu^-}$, where the scale uncertainties increase from 10% to 20%, and in the back-to-back region in $\Delta R_{\mu^-\gamma_1}$ at $\Delta R_{\mu^-\gamma_1} \approx 3$, where the scale uncertainties increase from $5\% - 6\%$ to $10\% - 13\%$.

From this discussion we conclude that our default scale choice $\mu_0 = E_T/4$ is preferable to the other two, because on the one hand a dynamical scale is generally necessary for accurate predictions in high-energy tails, and on the other hand the alternative dynamical scale $\mu_0 = H_T/4$ leads to larger scale uncertainties that can be twice as large as those from our default scale or the fixed scale $\mu_0 = m_t$. In high-energy tails, the predictions of the two dynamical scales become very similar, and the fixed scale can be used as an alternative scale for angular observables.

7. Summary

The main focus of this thesis was the improvement in the modeling of top-quark pair production with one and two isolated photons. For this purpose, we have extended the functionalities of the HELAC-NLO framework in several aspects and especially in the calculation of real corrections with HELAC-DIPOLES. In particular, we have discussed the extension of the original formulation of the Nagy-Soper subtraction scheme for calculations involving internal on-shell resonances, such as top quarks or W bosons, by generalizing the Nagy-Soper subtraction for decay processes. This generalization required various modifications in the code and the calculation of a new integrated dipole corresponding to the case of a massless/massive final-state emitter with a massive initial-state spectator for decay processes such as $t \to W^+bg$. Furthermore, we have extended the implementation of the Catani-Seymour and Nagy-Soper subtraction schemes for calculations involving QED-like IR singularities, where the previous implementation was designed only for QCD singularities. With these modifications, the current implementation of the Nagy-Soper subtraction scheme in HELAC-DIPOLES is able to perform the calculation of real correction with massless/massive charged/colored final-state particles in nested decay chains in processes such as $pp \to t\bar{t}\gamma(\gamma)$ in the NWA. On the other hand, the current implementation of the Catani-Seymour subtraction scheme supports only massless emitters in decay processes and was therefore only used for partial cross-checks. The use of realistic photon isolation criteria, such as the fixed-cone isolation, requires that the dipoles are differential in the photonic momentum fraction z_γ. This was achieved in the Catani-Seymour and the Nagy-Soper subtraction schemes in two different ways, where in the first case the integrated dipoles are calculated analytically and in the latter case a semi-numerical approach similar to the calculation of the regular integrated dipoles is used. In addition, we have incorporated the possibility to deal with multiple matrix elements at different orders in α_s and α and to construct the corresponding dipoles, where in general one has to take into account QED and QCD ones at the same time. This allows the simultaneous and efficient calculation of several (N)LO contributions at different orders in α_s and α in a single run.

For the calculation of tree-level and one-loop matrix elements we have implemented a new interface between HELAC-DIPOLES and RECOLA, which allows an efficient evaluation of matrix elements with contributions at different orders in α_s and α and with QCD and EW one-loop corrections, where the one-loop tensor and scalar integrals are calculated with COLLIER. It can also be used directly to generate matrix elements with a specific resonance structure for calculations in the NWA. In addition, we have implemented the random polarization method in RECOLA to improve the efficiency of the phase-space generation, and an alternative reduction method based on the OPP reduction technique implemented in CUTTOOLS in combination with ONELOOP. In this case, the reduction to scalar integrals

and the calculation of one-loop integrals are performed with quadruple precision, which is used for phase-space points that are marked by COLLIER to contain possibly unstable tensor integrals. Finally, a second fully automated method for the calculation of matrix elements in the NWA was implemented, which is based on the corresponding on-shell matrix elements of the individual subprocesses in the decay chain which are obtained from RECOLA. These subamplitudes are then combined accordingly in helicity and color space to obtain the matrix element for the full process in the NWA. On the one hand, this allows for additional cross-checks with the calculation of matrix elements directly with RECOLA, and on the other hand, it is possible to select or neglect one-loop corrections in specific subprocesses of the decay chain within this approach. The latter functionality is essential to quantify the relevance of higher-order corrections in decay processes of unstable particles.

One of the main results of the thesis is the calculation of NLO QCD corrections to the $pp \to t\bar{t}\gamma\gamma$ process in the *di-lepton* and *lepton + jet* decay channels at the LHC with $\sqrt{s} =$ 13 TeV. In this case, top-quark and W-boson decays are modeled in the NWA preserving spin correlations. NLO QCD corrections and photon bremsstrahlung in the production of the top-quark pair and its decays are consistently included. Previous calculations have neglected fixed-order NLO QCD corrections and photon radiation in top-quark decays, where the latter effect can lead to a significant underestimation of the cross section. In particular, we have found at the integrated level that the *Prod.* contribution, where both photons are emitted in the production process of the $t\bar{t}$ pair, amounts to about 40% for the *di-lepton* and 48% for the *lepton + jet* decay channel of the full process. Thus, the inclusion of photon radiation in the decays of unstable particles leads to an increase of more than a factor of two. In addition, large shape differences in differential observables as for example in $R_{\ell^+\gamma_1}$ can be found when neglecting photon radiation in the decay processes. In this case, a complete peak in the angular spectrum due to collinear photon emission off W bosons in top-quark decays and photon emission in the decay of the W boson would be absent. The relative size of the *Prod.* contribution increases towards the tails of dimensionful observables and clearly dominates the full calculation. Still, the *Mixed* contribution can lead to sizeable effects of up to $20\% - 25\%$ for observables such as $p_{T,\gamma_1\gamma_2}$ or $M_{b_1b_2}$ in these regions. Thus, only a complete calculation with photon radiation from all stages in the decay chain leads to accurate predictions.

The NLO QCD corrections at the integrated level are about 30% and the scale uncertainties are reduced from about 30% to 6% at NLO for the *di-lepton* decay channel. The internal PDF uncertainties obtained for the NNPDF3.1, CT18 and MSHT20 PDF sets are about $1\% - 2\%$, which are similar in size to the differences in the central value of the cross section. The behavior of the NLO QCD correction varies drastically between the *di-lepton* and *lepton + jet* decay channels. In the latter case, large NLO QCD corrections up to 140% are found, due to an enhancement of the real corrections because of kinematic configurations where an additional hard jet is produced in the $t\bar{t}$ production process. In contrast to the two quarks produced in the decay of the W boson, this additional jet is free from any kinematic restrictions due to the finite mass of the W boson or the top quark. Thus, the hardest jet is usually produced in the production process, while one jet from the W boson may be unresolved, or the two jets may be combined into a single jet by the jet algorithm. Such events with only one resolved jet from the W-boson decay are not included in the LO definition of the process, which are therefore responsible for the large higher-order corrections. In order to enhance the contribution in which the two jets

from the W-boson decay are resolved and to reduce the size of the NLO QCD corrections, additional cuts on the invariant of at least one light jet pair are applied. By requiring $|m_W - M_{jj}| < 15$ GeV, the size of the NLO QCD corrections becomes similar to those in the *di-lepton* decay channel with 23%, and the scale uncertainties are again reduced to about $5\% - 6\%$.

At the differential level we encounter additional shape distortions, e.g. in the tails of dimensionful observables or even in angular distributions such as $\Delta\Phi_{\ell^+\ell^-}$, where NLO QCD corrections of up to 80% are found. Therefore, it is not possible to approximate the QCD corrections at the differential level with a global scaling factor, but they have to be consistently included. In addition, we have considered two different scale settings, $\mu_0 = E_T/4$ and $\mu_0 = m_t$, which resulted in similar results at the integrated level, and have found that in general the dynamical scale is essential to accurately describe the tails of dimensionful observables, while the fixed scale can lead to perturbative instabilities. On the other hand, the use of the fixed scale leads to a reduction of higher-order QCD corrections and NLO scale uncertainties for almost all purely photonic dimensionful observables such as p_{T,γ_1} or $p_{T,\gamma_1\gamma_2}$. In the case of the *lepton + jet* decay channel, the NLO QCD corrections are further enhanced in hadronic observables and especially in those connected with the kinematics of the two hardest non-b flavored jets due to additional (hard) radiation in the production process.

Next, we have studied the effects of subleading LO and NLO contributions for the $pp \to t\bar{t}\gamma$ and $pp \to t\bar{t}\gamma\gamma$ processes in the *di-lepton* decay channel at the LHC with $\sqrt{s} =$ 13 TeV by performing the complete NLO calculation. The findings are essentially the same for both processes and can be summarized as follows. At the integrated level and generally in angular distributions, the subleading LO and NLO contributions are negligibly small compared to the corresponding scale uncertainties at NLO. In particular, the sum of all subleading effects at the integrated level is less than 1% for $pp \to t\bar{t}\gamma$ and less than 0.5% for $pp \to t\bar{t}\gamma\gamma$ of the NLO_{QCD} calculation, where in the latter case the cancellations between the different contributions are slightly larger. The scale uncertainties of about 6% are significantly larger than the subleading effects in both cases. Only in the tails of dimensionful distributions, the subleading effects can be as large as the NLO scale uncertainties and are dominated by the EW Sudakov logarithms in NLO_2. In general, the size is highly dependent on the exact event selection, because accidental cancellations are found between NLO_2 and NLO_3 for a few observables, where the latter contribution is dominated by real QCD corrections. Thus, a more exclusive event selection with a possible jet veto can decrease the size of NLO_3, while the size of the EW Sudakov logarithms in NLO_2 is rather unaffected. In addition, such a jet veto would reduce the dominant NLO QCD corrections in NLO_1, which would further increase the relative size of the subleading effects in the complete NLO calculation. The reduction of NLO_1 is also found in most dimensionful photonic observables when the fixed scale is used instead of the dynamical scale. This leads to an increase in the relative size of the subleading contributions, which become closer in size with the NLO scale uncertainties, that are also slightly reduced for $\mu_0 = m_t$. Finally, the NLO_{prd} approximation, where all LO contributions and NLO_1 are fully included, while the subleading NLO corrections are only included in the $t\bar{t}$ production in the *Prod.* contribution, is almost able to fully reproduce the full calculation and only small differences up to $1\% - 2\%$ are found, which are still negligible compared to the corresponding scale uncertainties.

At last we have investigated the issue of realistic photon isolation in the calculation of NLO QCD corrections to the full off-shell $pp \to t\bar{t}\gamma$ process in the $pp \to e^+\nu_e\,\mu^-\bar{\nu}_\mu\,b\bar{b}\,\gamma$ final state at the LHC with $\sqrt{s} = 13.6$ TeV. In particular, we have considered the fixed-cone isolation that is used in experimental measurements, where a certain amount of hadronic energy is allowed within a cone of a given radius. In contrast to the smooth-cone isolation used in the other two calculations in this thesis, the fixed-cone isolation leads to additional collinear singularities from photon radiation off unresolved quarks, which are absorbed into a redefinition of the non-perturbative parton-to-photon fragmentation functions. The considered realistic photon isolation is based on a recent measurement by the ATLAS collaboration [13], consisting of two fixed-cone isolation criteria with the radii $R = 0.2$ and $R = 0.4$. In this case, we found that the fragmentation contribution is only 0.2% of the full calculation, and is thus negligibly small compared to the scale uncertainties of about 5%. In addition, we have also performed alternative calculations with the smooth-cone isolation with $R_{\gamma j} = 0.4$ and varying the other input parameters in the ranges $\epsilon_\gamma \in \{0.05, 0.10, 0.15, 0.20, 1.00\}$ and $n \in \{0.5, 1.0, 2.0\}$. The different parametrizations lead to differences up to 8%−9%, which shows that a tuning of these input parameters is mandatory for accurate theoretical predictions in comparisons with experimental measurements when the smooth-cone isolation has to be used instead of the fixed-cone isolation. For our default values of the smooth-cone isolation of $(\epsilon_\gamma, n) = (1.00, 1.0)$ with $R_{\gamma j} = 0.4$, the prediction differs by about 3.4% from the one with the fixed-cone isolation. The dependence on these input parameters can be reduced with the hybrid photon isolation, where a smooth-cone isolation, usually with a smaller radius, is used first to remove the fragmentation contribution followed by the fixed-cone isolation. In this way, by using an inner smooth-cone isolation with $R_{\gamma j} = 0.1$ and varying the other two input parameters ϵ_γ and n in the same ranges as before, the differences between the various parametrizations are reduced to 0.4% and differences of at most 0.4% with the fixed-cone isolation are found. Even when increasing the radius of the inner smooth-cone isolation to $R_{\gamma j} = 0.15$ or $R_{\gamma j} = 0.2$ the dependence is still small, and the largest differences from the fixed-cone isolation are 0.4% and 0.7%, respectively. Thus, in the hybrid photon isolation the tuning of the input parameters in the inner smooth-cone isolation plays only a secondary role and all considered input parameters lead to negligible differences with respect to the fixed-cone isolation compared to the scale uncertainties of about 5%. Finally, we find no significant additional differences at the differential level between the tuned smooth-cone and hybrid photon isolation criteria compared to the fixed-cone isolation.

In conclusion, in this work we have addressed several aspects for more accurate predictions of $pp \to t\bar{t}\gamma(\gamma)$, where we have concentrated on the inclusion of photon radiation in the production of $t\bar{t}$ and all decay processes, the calculation of subleading LO and NLO contributions, and lastly the application of a realistic photon isolation criterion in the $pp \to e^+\nu_e\,\mu^-\bar{\nu}_\mu\,b\bar{b}\,\gamma$ process. Since the dependence on the photon isolation criterion is generally process dependent, it would be valuable to extend this study of realistic photon isolation criteria to the $pp \to t\bar{t}\gamma\gamma$ process and/or to the *lepton + jet* decay channel. In this way, the dependence of the smooth-cone and hybrid photon isolation criteria can be quantified and these parameters can be tuned to reproduce the results when using the fixed-cone isolation. Such studies can be performed directly within our framework and no further modifications are required.

Acknowledgments

First, I would like to thank Prof. Malgorzata Worek for her supervision, advice and the opportunity to write this thesis at the Institute for Theoretical Particle Physics and Cosmology at the RWTH Aachen university. I also thank my second reviewer of this thesis, Prof. Robert Harlander. I am grateful to my collaborators Dr. Giuseppe Bevilacqua, Dr. Jonathan Hermann and Dr. Michele Lupattelli for their collaborations on previous projects. Finally, I would like to thank my family for their support.

A. PDF summation in KP operator

A standard trick in the calculation of cross sections is the usage of symmetries of the matrix elements for the different quark flavors. For example, the matrix element is invariant under the simultaneous transformations $u \leftrightarrow c$ and $d \leftrightarrow s$ as long as all four quarks are massless and a diagonal CKM matrix is used. Therefore, this can be used to reduce the number of independent subprocesses in the generation and to simply sum over the PDFs for subprocesses with the same matrix element. For example in the case of top-quark pair production, this can be used to simplify the generation of subprocess initiated by up-type quarks as follows

$$\left(f_u f_{\bar{u}} \mathcal{A}_{u\bar{u}\to t\bar{t}} + f_c f_{\bar{c}} \mathcal{A}_{c\bar{c}\to t\bar{t}}\right) = \left(f_u f_{\bar{u}} + f_c f_{\bar{c}}\right) \mathcal{A}_{u\bar{u}\to t\bar{t}}, \tag{A.1}$$

where the arguments of the PDFs and the matrix element are suppressed. The same can be done for the down-type quarks, and in pure QCD it is possible to use the fact that the matrix elements are the same for up-type and down-type quarks to combine even these partonic subprocesses. These tricks were already implemented in all parts of HELAC-NLO except in the **KP** operator, in which non-diagonal terms in the flavor space are present. The calculation of the **KP** operator in HELAC-DIPOLES is organized by selecting a specific partonic subprocess and all partons that should be considered in the hadron. For example, when selecting the partonic subprocess $u\bar{u} \to t\bar{t}$ and considering all partons in the proton, then we get in the calculation terms that are proportional to the PDFs of the $u\bar{u}$, $g\bar{u}$ and ug initial states. To explain the PDF summation in the **KP** operator we first describe how the weights of the **KP** operator are split in HELAC-DIPOLES, which is also used to store the information in the modified LHEFs based on Ref. [451]. In the case of QCD dipoles, the weight of the **KP** operator is written as

$$\begin{aligned}
w(\mu_F) \;=\; & \left(L0_{A1_g} + L1_{A1_g} \log\mu_F^2\right) F_{A1_g} \;+\; \left(L0_{A2_g} + L1_{A2_g} \log\mu_F^2\right) F_{A2_g} \\
+\; & \left(L0_{B1_g} + L1_{B1_g} \log\mu_F^2\right) F_{B1_g} \;+\; \left(L0_{B2_g} + L1_{B2_g} \log\mu_F^2\right) F_{B2_g} \\
+\; & \left(L0_{A1_q} + L1_{A1_q} \log\mu_F^2\right) F_{A1_q} \;+\; \left(L0_{A2_q} + L1_{A2_q} \log\mu_F^2\right) F_{A2_q} \\
+\; & \left(L0_{B1_q} + L1_{B1_q} \log\mu_F^2\right) F_{B1_q} \;+\; \left(L0_{B2_q} + L1_{B2_q} \log\mu_F^2\right) F_{B2_q},
\end{aligned} \tag{A.2}$$

where the PDFs are only present in the coefficients outside the brackets, which are defined as

$$\begin{aligned} F_{A1_g} &= f_g(x_a/x'_a,\mu_F)/x'_a\, f_b(x_b,\mu_F), \\ F_{B1_g} &= f_g(x_a,\mu_F)\, f_b(x_b,\mu_F), \\ F_{A1_q} &= \sum_{a'} f_{a'}(x_a/x'_a,\mu_F)/x'_a\, f_b(x_b,\mu_F), \\ F_{B1_q} &= \sum_{a'} f_{a'}(x_a,\mu_F)\, f_b(x_b,\mu_F), \end{aligned} \tag{A.3}$$

where a and b are the initial-state particles of the partonic subprocess and the sum over a' runs over all quarks considered in the first hadron. The coefficients F_{A2_g}, F_{B2_g}, F_{A2_q} and F_{B2_q} are obtained from the Eq. (A.3) with the replacements $a \leftrightarrow b$ and $a' \leftrightarrow b'$. Since the PDFs only occur in these coefficients, it is sufficient to perform the PDF summation for partonic subprocesses with the same matrix element at level of these coefficients. In particular, this is achieved by replacing the PDF depending coefficients in Eq. (A.2), abbreviated in the following as $F_{...}$, by $\bar{F}_{...}$, which are defined as

$$\bar{F}_{...} = \sum_{(a,b)\in \text{ipdf}} F_{...}(a,b), \tag{A.4}$$

where in ipdf all different initial-state pairs of the PDF summation are included, and in addition the dependence on a and b of the coefficients $F_{...}$ are indicated explicitly. Considering again the example above of top-quark pair production, the two partonic subprocesses $u\bar{u} \to t\bar{t}$ and $c\bar{c} \to t\bar{t}$ can then be combined using the PDF summation by defining ipdf $= \{(u,\bar{u}),(c,\bar{c})\}$. The PDF summation is implemented for both subtraction schemes, while in the case of the Catani-Seymour subtraction scheme we have modified the implementation to directly calculate the corresponding coefficients. This new implementation of the PDF summation in the **KP** operator was first used in the calculation of the NLO QCD corrections to $pp \to t\bar{t}jj$ in the *di-lepton* decay channel using the NWA [173], where the number of partonic subprocesses in the **KP** operator is reduced from 117 to 18 in the case where both jets are produced in the $t\bar{t}$ production.

In the case of QED-like dipoles, we have to take into account the quark charge in the definition of the coefficients $F_{...}$, since they are different for up-type and down-type quarks. Thus, in this case the weight of the **KP** operator is then again given by Eq. (A.2) with the substitution $g \to \gamma$ and the coefficients $F_{...}$ are given by

$$\begin{aligned} F_{A1_\gamma} &= Q_a^2\, f_\gamma(x_a/x'_a,\mu_F)/x'_a\, f_b(x_b,\mu_F), \\ F_{B1_\gamma} &= Q_a^2\, f_\gamma(x_a,\mu_F)\, f_b(x_b,\mu_F), \\ F_{A1_q} &= \sum_{a'} Q_{a'}^2\, f_{a'}(x_a/x'_a,\mu_F)/x'_a\, f_b(x_b,\mu_F), \\ F_{B1_q} &= \sum_{a'} Q_{a'}^2\, f_{a'}(x_a,\mu_F)\, f_b(x_b,\mu_F). \end{aligned} \tag{A.5}$$

Bibliography

[1] CDF collaboration, *Observation of top quark production in $\bar{p}p$ collisions*, *Phys. Rev. Lett.* **74** (1995) 2626 [hep-ex/9503002].

[2] D0 collaboration, *Observation of the top quark*, *Phys. Rev. Lett.* **74** (1995) 2632 [hep-ex/9503003].

[3] J. H. Christenson, J. W. Cronin, V. L. Fitch and R. Turlay, *Evidence for the 2π Decay of the K_2^0 Meson*, *Phys. Rev. Lett.* **13** (1964) 138.

[4] E288 collaboration, *Observation of a Dimuon Resonance at 9.5-GeV in 400-GeV Proton-Nucleus Collisions*, *Phys. Rev. Lett.* **39** (1977) 252.

[5] B. Pietrzyk, *LEP asymmetries and fits of the standard model*, in *29th Rencontres de Moriond: Electroweak Interactions and Unified Theories*, pp. 137–144, 1994, hep-ex/9406001.

[6] C. Quigg, *Top-ology*, *Phys. Today* **50N5** (1997) 20 [hep-ph/9704332].

[7] LEP Electroweak Working Group, SLD Heavy Flavor Group collaboration, *A Combination of preliminary electroweak measurements and constraints on the standard model*, *CERN-PPE-96-183, SLAC-REPRINT-1996-037*.

[8] D0, CDF collaboration, *Top quark mass measurements from the Tevatron*, in *32nd Rencontres de Moriond: Electroweak Interactions and Unified Theories*, pp. 77–86, 1997, hep-ex/9706011.

[9] G. Degrassi, S. Di Vita, J. Elias-Miro, J. R. Espinosa, G. F. Giudice, G. Isidori et al., *Higgs mass and vacuum stability in the Standard Model at NNLO*, *JHEP* **08** (2012) 098 [1205.6497].

[10] ATLAS collaboration, *Observation of top-quark pair production in association with a photon and measurement of the $t\bar{t}\gamma$ production cross section in pp collisions at $\sqrt{s} = 7$ TeV using the ATLAS detector*, *Phys. Rev. D* **91** (2015) 072007 [1502.00586].

[11] K. Melnikov, M. Schulze and A. Scharf, *QCD corrections to top quark pair production in association with a photon at hadron colliders*, *Phys. Rev. D* **83** (2011) 074013 [1102.1967].

[12] G. Bevilacqua, H. B. Hartanto, M. Kraus, T. Weber and M. Worek, *Off-shell vs on-shell modelling of top quarks in photon associated production*, *JHEP* **03** (2020) 154 [1912.09999].

[13] ATLAS collaboration, *Measurements of inclusive and differential cross-sections of $t\bar{t}\gamma$ production in pp collisions at $\sqrt{s} = 13$ TeV with the ATLAS detector*, 2403.09452.

[14] CMS collaboration, *Measurement of the inclusive and differential $\mathrm{t\bar{t}}\gamma$ cross sections in the dilepton channel and effective field theory interpretation in proton-proton collisions at $\sqrt{s}$ =13 TeV*, *JHEP* **05** (2022) 091 [2201.07301].

[15] S. Frixione, *Isolated photons in perturbative QCD*, *Phys. Lett. B* **429** (1998) 369 [hep-ph/9801442].

[16] ATLAS collaboration, *CP Properties of Higgs Boson Interactions with Top Quarks in the $t\bar{t}H$ and tH Processes Using $H \to \gamma\gamma$ with the ATLAS Detector*, *Phys. Rev. Lett.* **125** (2020) 061802 [2004.04545].

[17] CMS collaboration, *Measurements of $t\bar{t}H$ Production and the CP Structure of the Yukawa Interaction between the Higgs Boson and Top Quark in the Diphoton Decay Channel*, *Phys. Rev. Lett.* **125** (2020) 061801 [2003.10866].

[18] D. Pagani, H.-S. Shao, I. Tsinikos and M. Zaro, *Automated EW corrections with isolated photons: $t\bar{t}\gamma$, $t\bar{t}\gamma\gamma$ and $t\gamma j$ as case studies*, *JHEP* **09** (2021) 155 [2106.02059].

[19] A. H. Hoang, *What is the Top Quark Mass?*, *Ann. Rev. Nucl. Part. Sci.* **70** (2020) 225 [2004.12915].

[20] Particle Data Group collaboration, *Review of Particle Physics*, *PTEP* **2022** (2022) 083C01.

[21] K. Agashe et al., *Report of the Topical Group on Top quark physics and heavy flavor production for Snowmass 2021*, 2209.11267.

[22] I. I. Y. Bigi, M. A. Shifman, N. G. Uraltsev and A. I. Vainshtein, *The Pole mass of the heavy quark. Perturbation theory and beyond*, *Phys. Rev. D* **50** (1994) 2234 [hep-ph/9402360].

[23] M. Beneke and V. M. Braun, *Heavy quark effective theory beyond perturbation theory: Renormalons, the pole mass and the residual mass term*, *Nucl. Phys. B* **426** (1994) 301 [hep-ph/9402364].

[24] M. Beneke, *Renormalons*, *Phys. Rept.* **317** (1999) 1 [hep-ph/9807443].

[25] M. Beneke, P. Marquard, P. Nason and M. Steinhauser, *On the ultimate uncertainty of the top quark pole mass*, *Phys. Lett. B* **775** (2017) 63 [1605.03609].

[26] A. H. Hoang, C. Lepenik and M. Preisser, *On the Light Massive Flavor Dependence of the Large Order Asymptotic Behavior and the Ambiguity of the Pole Mass*, *JHEP* **09** (2017) 099 [1706.08526].

[27] LHC Top Working Group collaboration, https://twiki.cern.ch/twiki/bin/view/LHCPhysics/LHCTopWGSummaryPlots (visited on 17.02.2024), copyright terms of the CC BY 4.0 license apply.

[28] CMS collaboration, *Combination of measurements of the top quark mass from data collected by the ATLAS and CMS experiments at $\sqrt{s} = 7$ and 8 TeV*, 2402.08713.

[29] S. Alioli, P. Fernandez, J. Fuster, A. Irles, S.-O. Moch, P. Uwer et al., *A new observable to measure the top-quark mass at hadron colliders*, *Eur. Phys. J. C* **73** (2013) 2438 [1303.6415].

[30] I. I. Y. Bigi, Y. L. Dokshitzer, V. A. Khoze, J. H. Kuhn and P. M. Zerwas, *Production and Decay Properties of Ultraheavy Quarks*, *Phys. Lett. B* **181** (1986) 157.

[31] CMS collaboration, *Measurement of the top quark polarization and $\mathrm{t\bar{t}}$ spin correlations using dilepton final states in proton-proton collisions at $\sqrt{s} = 13$ TeV*, *Phys. Rev. D* **100** (2019) 072002 [1907.03729].

[32] ATLAS collaboration, *Measurements of top-quark pair spin correlations in the $e\mu$ channel at $\sqrt{s} = 13$ TeV using pp collisions in the ATLAS detector*, *Eur. Phys. J. C* **80** (2020) 754 [1903.07570].

[33] ATLAS collaboration, *Observation of quantum entanglement in top-quark pairs using the ATLAS detector*, 2311.07288.

[34] S. L. Glashow, J. Iliopoulos and L. Maiani, *Weak Interactions with Lepton-Hadron Symmetry*, *Phys. Rev. D* **2** (1970) 1285.

[35] Top Quark Working Group collaboration, *Working Group Report: Top Quark*, in *Snowmass 2013: Snowmass on the Mississippi*, 11, 2013, 1311.2028.

[36] CMS collaboration, *Measurement of the ratio $\mathcal{B}(t \to Wb)/\mathcal{B}(t \to Wq)$ in pp collisions at $\sqrt{s} = 8$ TeV*, *Phys. Lett. B* **736** (2014) 33 [1404.2292].

[37] CMS collaboration, *Measurement of the Single-Top-Quark t-Channel Cross Section in pp Collisions at $\sqrt{s} = 7$ TeV*, *JHEP* **12** (2012) 035 [1209.4533].

[38] L. Chen, X. Chen, X. Guan and Y.-Q. Ma, *Top-Quark Decay at Next-to-Next-to-Next-to-Leading Order in QCD*, 2309.01937.

[39] ATLAS collaboration, *Measurement of the top-quark decay width in top-quark pair events in the dilepton channel at $\sqrt{s} = 13$ TeV with the ATLAS detector*, *ATLAS-CONF-2019-038, ATLAS-CONF-2019-038.*

[40] D. Chang, W.-F. Chang and E. Ma, *Alternative interpretation of the Tevatron top events*, *Phys. Rev. D* **59** (1999) 091503 [hep-ph/9810531].

[41] D. Chang, W.-F. Chang and E. Ma, *Fitting precision electroweak data with exotic heavy quarks*, *Phys. Rev. D* **61** (2000) 037301 [hep-ph/9909537].

[42] CDF collaboration, *Exclusion of Exotic Top-Like Quarks with -4/3 Electric Charge using Jet-Charge Tagging in Single-Lepton $t\bar{t}$ Events at CDF*, *Phys. Rev. D* **88** (2013) 032003 [1304.4141].

[43] D0 collaboration, *Measurement of the Electric Charge of the Top Quark in $t\bar{t}$ Events*, *Phys. Rev. D* **90** (2014) 051101 [1407.4837].

[44] CMS collaboration, *Constraints on the Top-Quark Charge from Top-Pair Events*, *CMS-PAS-TOP-11-031*.

[45] ATLAS collaboration, *Measurement of the top quark charge in pp collisions at $\sqrt{s}$ = 7 TeV with the ATLAS detector*, *JHEP* **11** (2013) 031 [1307.4568].

[46] J. H. Kühn, A. Scharf and P. Uwer, *Weak Interactions in Top-Quark Pair Production at Hadron Colliders: An Update*, *Phys. Rev. D* **91** (2015) 014020 [1305.5773].

[47] CMS collaboration, *Measurement of the top quark Yukawa coupling from $\mathrm{t\bar{t}}$ kinematic distributions in the lepton+jets final state in proton-proton collisions at $\sqrt{s}$ = 13 TeV*, *Phys. Rev. D* **100** (2019) 072007 [1907.01590].

[48] CMS collaboration, *Measurement of the top quark Yukawa coupling from $\mathrm{t\bar{t}}$ kinematic distributions in the dilepton final state in proton-proton collisions at $\sqrt{s}$ = 13 TeV*, *Phys. Rev. D* **102** (2020) 092013 [2009.07123].

[49] M. Czakon, P. Fiedler and A. Mitov, *Total Top-Quark Pair-Production Cross Section at Hadron Colliders Through $O(\alpha_S^4)$*, *Phys. Rev. Lett.* **110** (2013) 252004 [1303.6254].

[50] CDF, D0 collaboration, *Combination of Measurements of the Top-Quark Pair Production Cross Section from the Tevatron Collider*, *Phys. Rev. D* **89** (2014) 072001 [1309.7570].

[51] ATLAS collaboration, *Measurement of the $t\bar{t}$ production cross-section in pp collisions at $\sqrt{s}$ = 5.02 TeV with the ATLAS detector*, *JHEP* **06** (2023) 138 [2207.01354].

[52] CMS collaboration, *Measurement of the inclusive $\mathrm{t\bar{t}}$ production cross section in proton-proton collisions at $\sqrt{s}$ = 5.02 TeV*, *JHEP* **04** (2022) 144 [2112.09114].

[53] ATLAS, CMS collaboration, *Combination of inclusive top-quark pair production cross-section measurements using ATLAS and CMS data at $\sqrt{s}$ = 7 and 8 TeV*, *JHEP* **07** (2023) 213 [2205.13830].

[54] ATLAS collaboration, *Inclusive and differential cross-sections for dilepton $t\bar{t}$ production measured in $\sqrt{s}$ = 13 TeV pp collisions with the ATLAS detector*, *JHEP* **07** (2023) 141 [2303.15340].

[55] CMS collaboration, *Measurement of the $\mathrm{t\bar{t}}$ production cross section, the top quark mass, and the strong coupling constant using dilepton events in pp collisions at $\sqrt{s}$ = 13 TeV*, *Eur. Phys. J. C* **79** (2019) 368 [1812.10505].

[56] ATLAS collaboration, *Measurement of the $t\bar{t}$ production cross-section in the lepton+jets channel at $\sqrt{s} = 13$ TeV with the ATLAS experiment*, *Phys. Lett. B* **810** (2020) 135797 [2006.13076].

[57] CMS collaboration, *Measurement of differential $t\bar{t}$ production cross sections in the full kinematic range using lepton+jets events from proton-proton collisions at $\sqrt{s} =$ 13 TeV*, *Phys. Rev. D* **104** (2021) 092013 [2108.02803].

[58] ATLAS collaboration, *Measurement of the $t\bar{t}$ cross section and its ratio to the Z production cross section using pp collisions at $\sqrt{s} = 13.6$ TeV with the ATLAS detector*, *Phys. Lett. B* **848** (2024) 138376 [2308.09529].

[59] CMS collaboration, *First measurement of the top quark pair production cross section in proton-proton collisions at $\sqrt{s} =$ 13.6 TeV*, *JHEP* **08** (2023) 204 [2303.10680].

[60] P. Nason, S. Dawson and R. K. Ellis, *The Total Cross-Section for the Production of Heavy Quarks in Hadronic Collisions*, *Nucl. Phys. B* **303** (1988) 607.

[61] P. Nason, S. Dawson and R. K. Ellis, *The One Particle Inclusive Differential Cross-Section for Heavy Quark Production in Hadronic Collisions*, *Nucl. Phys. B* **327** (1989) 49.

[62] W. Beenakker, H. Kuijf, W. L. van Neerven and J. Smith, *QCD Corrections to Heavy Quark Production in p anti-p Collisions*, *Phys. Rev. D* **40** (1989) 54.

[63] W. Beenakker, W. L. van Neerven, R. Meng, G. A. Schuler and J. Smith, *QCD corrections to heavy quark production in hadron hadron collisions*, *Nucl. Phys. B* **351** (1991) 507.

[64] W. Beenakker, A. Denner, W. Hollik, R. Mertig, T. Sack and D. Wackeroth, *Electroweak one loop contributions to top pair production in hadron colliders*, *Nucl. Phys. B* **411** (1994) 343.

[65] J. H. Kuhn, A. Scharf and P. Uwer, *Electroweak corrections to top-quark pair production in quark-antiquark annihilation*, *Eur. Phys. J. C* **45** (2006) 139 [hep-ph/0508092].

[66] W. Bernreuther, M. Fuecker and Z.-G. Si, *Weak interaction corrections to hadronic top quark pair production*, *Phys. Rev. D* **74** (2006) 113005 [hep-ph/0610334].

[67] J. H. Kuhn, A. Scharf and P. Uwer, *Electroweak effects in top-quark pair production at hadron colliders*, *Eur. Phys. J. C* **51** (2007) 37 [hep-ph/0610335].

[68] W. Hollik and M. Kollar, *NLO QED contributions to top-pair production at hadron collider*, *Phys. Rev. D* **77** (2008) 014008 [0708.1697].

[69] P. Bärnreuther, M. Czakon and A. Mitov, *Percent Level Precision Physics at the Tevatron: First Genuine NNLO QCD Corrections to $q\bar{q} \to t\bar{t} + X$*, *Phys. Rev. Lett.* **109** (2012) 132001 [1204.5201].

[70] M. Czakon and A. Mitov, *NNLO corrections to top-pair production at hadron colliders: the all-fermionic scattering channels*, *JHEP* **12** (2012) 054 [1207.0236].

[71] M. Czakon and A. Mitov, *NNLO corrections to top pair production at hadron colliders: the quark-gluon reaction*, *JHEP* **01** (2013) 080 [1210.6832].

[72] M. Czakon, P. Fiedler, D. Heymes and A. Mitov, *NNLO QCD predictions for fully-differential top-quark pair production at the Tevatron*, *JHEP* **05** (2016) 034 [1601.05375].

[73] M. Czakon, D. Heymes and A. Mitov, *Dynamical scales for multi-TeV top-pair production at the LHC*, *JHEP* **04** (2017) 071 [1606.03350].

[74] S. Catani, S. Devoto, M. Grazzini, S. Kallweit and J. Mazzitelli, *Top-quark pair production at the LHC: Fully differential QCD predictions at NNLO*, *JHEP* **07** (2019) 100 [1906.06535].

[75] M. Czakon, D. Heymes, A. Mitov, D. Pagani, I. Tsinikos and M. Zaro, *Top-pair production at the LHC through NNLO QCD and NLO EW*, *JHEP* **10** (2017) 186 [1705.04105].

[76] S. Catani, S. Devoto, M. Grazzini, S. Kallweit and J. Mazzitelli, *Top-quark pair hadroproduction at NNLO: differential predictions with the $\overline{MS}$ mass*, *JHEP* **08** (2020) 027 [2005.00557].

[77] N. Kidonakis and G. F. Sterman, *Subleading logarithms in QCD hard scattering*, *Phys. Lett. B* **387** (1996) 867.

[78] N. Kidonakis and G. F. Sterman, *Resummation for QCD hard scattering*, *Nucl. Phys. B* **505** (1997) 321 [hep-ph/9705234].

[79] N. Kidonakis, *Two-loop soft anomalous dimensions and NNLL resummation for heavy quark production*, *Phys. Rev. Lett.* **102** (2009) 232003 [0903.2561].

[80] A. Ferroglia, M. Neubert, B. D. Pecjak and L. L. Yang, *Two-loop divergences of scattering amplitudes with massive partons*, *Phys. Rev. Lett.* **103** (2009) 201601 [0907.4791].

[81] A. Ferroglia, M. Neubert, B. D. Pecjak and L. L. Yang, *Two-loop divergences of massive scattering amplitudes in non-abelian gauge theories*, *JHEP* **11** (2009) 062 [0908.3676].

[82] N. Kidonakis, *Next-to-next-to-leading soft-gluon corrections for the top quark cross section and transverse momentum distribution*, *Phys. Rev. D* **82** (2010) 114030 [1009.4935].

[83] M. Czakon, A. Mitov and G. F. Sterman, *Threshold Resummation for Top-Pair Hadroproduction to Next-to-Next-to-Leading Log*, *Phys. Rev. D* **80** (2009) 074017 [0907.1790].

[84] V. Ahrens, A. Ferroglia, M. Neubert, B. D. Pecjak and L.-L. Yang, *RG-improved single-particle inclusive cross sections and forward-backward asymmetry in $t\bar{t}$ production at hadron colliders*, *JHEP* **09** (2011) 070 [1103.0550].

[85] N. Kidonakis, *The top quark rapidity distribution and forward-backward asymmetry*, *Phys. Rev. D* **84** (2011) 011504 [1105.5167].

[86] M. Beneke, P. Falgari, S. Klein and C. Schwinn, *Hadronic top-quark pair production with NNLL threshold resummation*, *Nucl. Phys. B* **855** (2012) 695 [1109.1536].

[87] N. Kidonakis, *NNNLO soft-gluon corrections for the top-antitop pair production cross section*, *Phys. Rev. D* **90** (2014) 014006 [1405.7046].

[88] N. Kidonakis, *NNNLO soft-gluon corrections for the top-quark p_T and rapidity distributions*, *Phys. Rev. D* **91** (2015) 031501 [1411.2633].

[89] N. Kidonakis, *The top quark forward-backward asymmetry at approximate N^3LO*, *Phys. Rev. D* **91** (2015) 071502 [1501.01581].

[90] N. Kidonakis, *Top-quark double-differential distributions at approximate N^3LO*, *Phys. Rev. D* **101** (2020) 074006 [1912.10362].

[91] S. Frixione and B. R. Webber, *Matching NLO QCD computations and parton shower simulations*, *JHEP* **06** (2002) 029 [hep-ph/0204244].

[92] S. Frixione, P. Nason and B. R. Webber, *Matching NLO QCD and parton showers in heavy flavor production*, *JHEP* **08** (2003) 007 [hep-ph/0305252].

[93] P. Nason, *A New method for combining NLO QCD with shower Monte Carlo algorithms*, *JHEP* **11** (2004) 040 [hep-ph/0409146].

[94] S. Frixione, P. Nason and C. Oleari, *Matching NLO QCD computations with Parton Shower simulations: the POWHEG method*, *JHEP* **11** (2007) 070 [0709.2092].

[95] J. M. Campbell, R. K. Ellis, P. Nason and E. Re, *Top-Pair Production and Decay at NLO Matched with Parton Showers*, *JHEP* **04** (2015) 114 [1412.1828].

[96] J. Mazzitelli, P. F. Monni, P. Nason, E. Re, M. Wiesemann and G. Zanderighi, *Next-to-Next-to-Leading Order Event Generation for Top-Quark Pair Production*, *Phys. Rev. Lett.* **127** (2021) 062001 [2012.14267].

[97] J. Mazzitelli, P. F. Monni, P. Nason, E. Re, M. Wiesemann and G. Zanderighi, *Top-pair production at the LHC with MINNLO$_{PS}$*, *JHEP* **04** (2022) 079 [2112.12135].

[98] P. F. Monni, P. Nason, E. Re, M. Wiesemann and G. Zanderighi, *MiNNLO$_{PS}$: a new method to match NNLO QCD to parton showers*, *JHEP* **05** (2020) 143 [1908.06987].

[99] P. F. Monni, E. Re and M. Wiesemann, *MiNNLO$_{PS}$: optimizing $2 \to 1$ hadronic processes*, *Eur. Phys. J. C* **80** (2020) 1075 [2006.04133].

[100] W. Bernreuther, A. Brandenburg, Z. G. Si and P. Uwer, *Top quark pair production and decay at hadron colliders*, *Nucl. Phys. B* **690** (2004) 81 [hep-ph/0403035].

[101] K. Melnikov and M. Schulze, *NLO QCD corrections to top quark pair production and decay at hadron colliders*, *JHEP* **08** (2009) 049 [0907.3090].

[102] S. Biswas, K. Melnikov and M. Schulze, *Next-to-leading order QCD effects and the top quark mass measurements at the LHC*, *JHEP* **08** (2010) 048 [1006.0910].

[103] J. M. Campbell and R. K. Ellis, *Top-Quark Processes at NLO in Production and Decay*, *J. Phys. G* **42** (2015) 015005 [1204.1513].

[104] W. Bernreuther and Z.-G. Si, *Distributions and correlations for top quark pair production and decay at the Tevatron and LHC.*, *Nucl. Phys. B* **837** (2010) 90 [1003.3926].

[105] J. Gao and A. S. Papanastasiou, *Top-quark pair-production and decay at high precision*, *Phys. Rev. D* **96** (2017) 051501 [1705.08903].

[106] A. Behring, M. Czakon, A. Mitov, A. S. Papanastasiou and R. Poncelet, *Higher order corrections to spin correlations in top quark pair production at the LHC*, *Phys. Rev. Lett.* **123** (2019) 082001 [1901.05407].

[107] M. Czakon, A. Mitov and R. Poncelet, *NNLO QCD corrections to leptonic observables in top-quark pair production and decay*, *JHEP* **05** (2021) 212 [2008.11133].

[108] A. Denner, S. Dittmaier, S. Kallweit and S. Pozzorini, *NLO QCD corrections to WWbb production at hadron colliders*, *Phys. Rev. Lett.* **106** (2011) 052001 [1012.3975].

[109] G. Bevilacqua, M. Czakon, A. van Hameren, C. G. Papadopoulos and M. Worek, *Complete off-shell effects in top quark pair hadroproduction with leptonic decay at next-to-leading order*, *JHEP* **02** (2011) 083 [1012.4230].

[110] A. Denner, S. Dittmaier, S. Kallweit and S. Pozzorini, *NLO QCD corrections to off-shell top-antitop production with leptonic decays at hadron colliders*, *JHEP* **10** (2012) 110 [1207.5018].

[111] R. Frederix, *Top Quark Induced Backgrounds to Higgs Production in the $WW^{(*)} \to ll\nu\nu$ Decay Channel at Next-to-Leading-Order in QCD*, *Phys. Rev. Lett.* **112** (2014) 082002 [1311.4893].

[112] F. Cascioli, S. Kallweit, P. Maierhöfer and S. Pozzorini, *A unified NLO description of top-pair and associated Wt production*, *Eur. Phys. J. C* **74** (2014) 2783 [1312.0546].

[113] A. Denner and M. Pellen, *NLO electroweak corrections to off-shell top-antitop production with leptonic decays at the LHC*, *JHEP* **08** (2016) 155 [1607.05571].

[114] A. Denner and M. Pellen, *Off-shell production of top-antitop pairs in the lepton+jets channel at NLO QCD*, *JHEP* **02** (2018) 013 [1711.10359].

[115] T. Ježo, J. M. Lindert, P. Nason, C. Oleari and S. Pozzorini, *An NLO+PS generator for $t\bar{t}$ and Wt production and decay including non-resonant and interference effects*, *Eur. Phys. J. C* **76** (2016) 691 [1607.04538].

[116] T. Ježo, J. M. Lindert and S. Pozzorini, *Resonance-aware NLOPS matching for off-shell $t\bar{t}$ + tW production with semileptonic decays*, *JHEP* **10** (2023) 008 [2307.15653].

[117] S. Alioli, P. Nason, C. Oleari and E. Re, *A general framework for implementing NLO calculations in shower Monte Carlo programs: the POWHEG BOX*, *JHEP* **06** (2010) 043 [1002.2581].

[118] S. Frixione, P. Nason and G. Ridolfi, *A Positive-weight next-to-leading-order Monte Carlo for heavy flavour hadroproduction*, *JHEP* **09** (2007) 126 [0707.3088].

[119] J. Alwall, R. Frederix, S. Frixione, V. Hirschi, F. Maltoni, O. Mattelaer et al., *The automated computation of tree-level and next-to-leading order differential cross sections, and their matching to parton shower simulations*, *JHEP* **07** (2014) 079 [1405.0301].

[120] R. Frederix and S. Frixione, *Merging meets matching in MC@NLO*, *JHEP* **12** (2012) 061 [1209.6215].

[121] CMS collaboration, *First measurement of the cross section for top quark pair production with additional charm jets using dileptonic final states in pp collisions at $\sqrt{s} = 13\ TeV$*, *Phys. Lett. B* **820** (2021) 136565 [2012.09225].

[122] M. L. Mangano, *Standard Model backgrounds to supersymmetry searches*, *Eur. Phys. J. C* **59** (2009) 373 [0809.1567].

[123] C. Englert, B. Jager, M. Worek and D. Zeppenfeld, *Observing Strongly Interacting Vector Boson Systems at the CERN Large Hadron Collider*, *Phys. Rev. D* **80** (2009) 035027 [0810.4861].

[124] C. Englert, B. Jager and D. Zeppenfeld, *QCD Corrections to Vector-Boson Fusion Processes in Warped Higgsless Models*, *JHEP* **03** (2009) 060 [0812.2564].

[125] F. Campanario, M. Kubocz and D. Zeppenfeld, *Gluon-fusion contributions to Phi + 2 Jet production*, *Phys. Rev. D* **84** (2011) 095025 [1011.3819].

[126] M. I. Gresham, I.-W. Kim and K. M. Zurek, *Searching for Top Flavor Violating Resonances*, *Phys. Rev. D* **84** (2011) 034025 [1102.0018].

[127] ATLAS collaboration, *Search for resonant top plus jet production in $t\bar{t}$ + jets events with the ATLAS detector in pp collisions at $\sqrt{s} = 7\ TeV$*, *Phys. Rev. D* **86** (2012) 091103 [1209.6593].

[128] D. L. Rainwater and D. Zeppenfeld, *Observing $H \to W^*W^* \to e^\pm\mu^\mp \not{p}_T$ in weak boson fusion with dual forward jet tagging at the CERN LHC*, *Phys. Rev. D* **60** (1999) 113004 [hep-ph/9906218].

[129] N. Kauer, T. Plehn, D. L. Rainwater and D. Zeppenfeld, *$H \to W^+W^-$ as the discovery mode for a light Higgs boson*, *Phys. Lett. B* **503** (2001) 113 [hep-ph/0012351].

[130] CMS collaboration, *Search for standard model production of four top quarks in proton-proton collisions at $\sqrt{s}$ = 13 TeV*, *Phys. Lett. B* **772** (2017) 336 [1702.06164].

[131] ATLAS collaboration, *Search for four-top-quark production in the single-lepton and opposite-sign dilepton final states in pp collisions at $\sqrt{s}$ = 13 TeV with the ATLAS detector*, *Phys. Rev. D* **99** (2019) 052009 [1811.02305].

[132] W. Buchmuller and D. Wyler, *Effective Lagrangian Analysis of New Interactions and Flavor Conservation*, *Nucl. Phys. B* **268** (1986) 621.

[133] J. A. Aguilar-Saavedra, *A Minimal set of top anomalous couplings*, *Nucl. Phys. B* **812** (2009) 181 [0811.3842].

[134] J. A. Aguilar-Saavedra, B. Fuks and M. L. Mangano, *Pinning down top dipole moments with ultra-boosted tops*, *Phys. Rev. D* **91** (2015) 094021 [1412.6654].

[135] CMS collaboration, *Search for Anomalous Top Chromomagnetic Dipole Moments from angular distributions in $t\bar{t}$ Dileptonic events at $\sqrt{s} = 7$ TeV with the CMS detector.*, *CMS-PAS-TOP-14-005*.

[136] CMS collaboration, *Measurements of t t-bar spin correlations and top quark polarization using dilepton final states in pp collisions at sqrt(s) = 8 TeV*, *Phys. Rev. D* **93** (2016) 052007 [1601.01107].

[137] O. Antunano, J. H. Kuhn and G. Rodrigo, *Top quarks, axigluons and charge asymmetries at hadron colliders*, *Phys. Rev. D* **77** (2008) 014003 [0709.1652].

[138] S. Berge and S. Westhoff, *Top-Quark Charge Asymmetry Goes Forward: Two New Observables for Hadron Colliders*, *JHEP* **07** (2013) 179 [1305.3272].

[139] S. Berge and S. Westhoff, *Observing the Top Energy Asymmetry at the LHC*, *Phys. Rev. D* **95** (2017) 014035 [1608.00574].

[140] S. Berge and S. Westhoff, *Top-Quark Charge Asymmetry with a Jet Handle*, *Phys. Rev. D* **86** (2012) 094036 [1208.4104].

[141] S. Alte, S. Berge and H. Spiesberger, *Top quark charge asymmetry: searching for light axigluons in $t\bar{t}$ + jet production at the LHC*, *JHEP* **09** (2014) 084 [1406.0501].

[142] A. Basan, P. Berta, L. Masetti, E. Vryonidou and S. Westhoff, *Measuring the top energy asymmetry at the LHC: QCD and SMEFT interpretations*, *JHEP* **03** (2020) 184 [2001.07225].

[143] CMS collaboration, *Inclusive and differential cross section measurements of* $\mathrm{t\bar{t}b\bar{b}}$ *production in the lepton+jets channel at* $\sqrt{s}$ *= 13 TeV*, 2309.14442.

[144] ATLAS collaboration, *Measurement of* $t\bar{t}$ *production with a veto on additional central jet activity in pp collisions at sqrt(s) = 7 TeV using the ATLAS detector*, *Eur. Phys. J. C* **72** (2012) 2043 [1203.5015].

[145] ATLAS collaboration, *Measurement of the* $t\bar{t}$ *production cross-section as a function of jet multiplicity and jet transverse momentum in 7 TeV proton-proton collisions with the ATLAS detector*, *JHEP* **01** (2015) 020 [1407.0891].

[146] ATLAS collaboration, *Measurements of fiducial cross-sections for* $t\bar{t}$ *production with one or two additional b-jets in pp collisions at* $\sqrt{s}$ *=8 TeV using the ATLAS detector*, *Eur. Phys. J. C* **76** (2016) 11 [1508.06868].

[147] ATLAS collaboration, *Measurement of jet activity in top quark events using the* $e\mu$ *final state with two b-tagged jets in pp collisions at* $\sqrt{s} = 8$ *TeV with the ATLAS detector*, *JHEP* **09** (2016) 074 [1606.09490].

[148] CMS collaboration, *Measurement of jet multiplicity distributions in* $\mathrm{t\bar{t}}$ *production in pp collisions at* $\sqrt{s} = 7$ *TeV*, *Eur. Phys. J. C* **74** (2015) 3014 [1404.3171].

[149] CMS collaboration, *Measurement of* $\mathrm{t\bar{t}}$ *production with additional jet activity, including* b *quark jets, in the dilepton decay channel using pp collisions at* $\sqrt{s} = 8$ *TeV*, *Eur. Phys. J. C* **76** (2016) 379 [1510.03072].

[150] CMS collaboration, *Measurement of the differential production cross section for top-quark pairs as a function of jet multiplicity in the lepton+jets final state at* $\sqrt{s} = 8$ *TeV with the CMS detector*, *CMS-PAS-TOP-15-006*.

[151] ATLAS collaboration, *Determination of the top-quark pole mass using* $t\bar{t}$ *+ 1-jet events collected with the ATLAS experiment in 7 TeV pp collisions*, *JHEP* **10** (2015) 121 [1507.01769].

[152] CMS collaboration, *Determination of the normalised invariant mass distribution of* $\mathrm{t\bar{t}}$*+jet and extraction of the top quark mass*, *CMS-PAS-TOP-13-006*.

[153] ATLAS collaboration, *Measurement of the top-quark mass in* $t\bar{t} + 1$*-jet events collected with the ATLAS detector in pp collisions at* $\sqrt{s} = 8$ *TeV*, *JHEP* **11** (2019) 150 [1905.02302].

[154] ATLAS collaboration, *Measurement of jets produced in top quark events using the di-lepton final state with 2 b-tagged jets in pp collisions at* $\sqrt{s} = 13$ *TeV with the ATLAS detector*, *ATLAS-CONF-2015-065*.

[155] ATLAS collaboration, *Measurement of jet activity produced in top-quark events with an electron, a muon and two b-tagged jets in the final state in pp collisions at* $\sqrt{s} = 13$ *TeV with the ATLAS detector*, *Eur. Phys. J. C* **77** (2017) 220 [1610.09978].

[156] ATLAS collaboration, *Measurements of differential cross sections of top quark pair production in association with jets in pp collisions at $\sqrt{s} = 13$ TeV using the ATLAS detector*, *JHEP* **10** (2018) 159 [1802.06572].

[157] CMS collaboration, *Differential cross section measurements for the production of top quark pairs and of additional jets using dilepton events from pp collisions at $\sqrt{s}$ = 13 TeV*, 2402.08486.

[158] CMS collaboration, *Measurement of the top quark pole mass using $t\bar{t}$+jet events in the dilepton final state in proton-proton collisions at $\sqrt{s}$ = 13 TeV*, *JHEP* **07** (2023) 077 [2207.02270].

[159] ATLAS collaboration, *Measurements of inclusive and differential fiducial cross-sections of $t\bar{t}$ production with additional heavy-flavour jets in proton-proton collisions at $\sqrt{s}$ = 13 TeV with the ATLAS detector*, *JHEP* **04** (2019) 046 [1811.12113].

[160] CMS collaboration, *Measurements of $t\bar{t}$ cross sections in association with b jets and inclusive jets and their ratio using dilepton final states in pp collisions at $\sqrt{s}$ = 13 TeV*, *Phys. Lett. B* **776** (2018) 355 [1705.10141].

[161] CMS collaboration, *Measurement of the cross section for $t\bar{t}$ production with additional jets and b jets in pp collisions at $\sqrt{s}$ = 13 TeV*, *JHEP* **07** (2020) 125 [2003.06467].

[162] S. Dittmaier, P. Uwer and S. Weinzierl, *NLO QCD corrections to t anti-t + jet production at hadron colliders*, *Phys. Rev. Lett.* **98** (2007) 262002 [hep-ph/0703120].

[163] S. Dittmaier, P. Uwer and S. Weinzierl, *Hadronic top-quark pair production in association with a hard jet at next-to-leading order QCD: Phenomenological studies for the Tevatron and the LHC*, *Eur. Phys. J. C* **59** (2009) 625 [0810.0452].

[164] K. Melnikov and M. Schulze, *NLO QCD corrections to top quark pair production in association with one hard jet at hadron colliders*, *Nucl. Phys. B* **840** (2010) 129 [1004.3284].

[165] K. Melnikov, A. Scharf and M. Schulze, *Top quark pair production in association with a jet: QCD corrections and jet radiation in top quark decays*, *Phys. Rev. D* **85** (2012) 054002 [1111.4991].

[166] A. Kardos, C. Papadopoulos and Z. Trocsanyi, *Top quark pair production in association with a jet with NLO parton showering*, *Phys. Lett. B* **705** (2011) 76 [1101.2672].

[167] M. Czakon, H. B. Hartanto, M. Kraus and M. Worek, *Matching the Nagy-Soper parton shower at next-to-leading order*, *JHEP* **06** (2015) 033 [1502.00925].

[168] S. Alioli, S.-O. Moch and P. Uwer, *Hadronic top-quark pair-production with one jet and parton showering*, *JHEP* **01** (2012) 137 [1110.5251].

[169] G. Bevilacqua, H. B. Hartanto, M. Kraus and M. Worek, *Top Quark Pair Production in Association with a Jet with Next-to-Leading-Order QCD Off-Shell Effects at the Large Hadron Collider*, *Phys. Rev. Lett.* **116** (2016) 052003 [1509.09242].

[170] G. Bevilacqua, H. B. Hartanto, M. Kraus and M. Worek, *Off-shell Top Quarks with One Jet at the LHC: A comprehensive analysis at NLO QCD*, *JHEP* **11** (2016) 098 [1609.01659].

[171] G. Bevilacqua, M. Czakon, C. G. Papadopoulos and M. Worek, *Dominant QCD Backgrounds in Higgs Boson Analyses at the LHC: A Study of pp -> t anti-t + 2 jets at Next-To-Leading Order*, *Phys. Rev. Lett.* **104** (2010) 162002 [1002.4009].

[172] G. Bevilacqua, M. Czakon, C. G. Papadopoulos and M. Worek, *Hadronic top-quark pair production in association with two jets at Next-to-Leading Order QCD*, *Phys. Rev. D* **84** (2011) 114017 [1108.2851].

[173] G. Bevilacqua, M. Lupattelli, D. Stremmer and M. Worek, *Study of additional jet activity in top quark pair production and decay at the LHC*, *Phys. Rev. D* **107** (2023) 114027 [2212.04722].

[174] S. Höche, P. Maierhöfer, N. Moretti, S. Pozzorini and F. Siegert, *Next-to-leading order QCD predictions for top-quark pair production with up to three jets*, *Eur. Phys. J. C* **77** (2017) 145 [1607.06934].

[175] K. Hamilton, P. Nason and G. Zanderighi, *MINLO: Multi-Scale Improved NLO*, *JHEP* **10** (2012) 155 [1206.3572].

[176] C. Gütschow, J. M. Lindert and M. Schönherr, *Multi-jet merged top-pair production including electroweak corrections*, *Eur. Phys. J. C* **78** (2018) 317 [1803.00950].

[177] S. Hoeche, F. Krauss, P. Maierhoefer, S. Pozzorini, M. Schonherr and F. Siegert, *Next-to-leading order QCD predictions for top-quark pair production with up to two jets merged with a parton shower*, *Phys. Lett. B* **748** (2015) 74 [1402.6293].

[178] A. Bredenstein, A. Denner, S. Dittmaier and S. Pozzorini, *NLO QCD corrections to t anti-t b anti-b production at the LHC: 1. Quark-antiquark annihilation*, *JHEP* **08** (2008) 108 [0807.1248].

[179] A. Bredenstein, A. Denner, S. Dittmaier and S. Pozzorini, *NLO QCD corrections to pp —> t anti-t b anti-b + X at the LHC*, *Phys. Rev. Lett.* **103** (2009) 012002 [0905.0110].

[180] G. Bevilacqua, M. Czakon, C. G. Papadopoulos, R. Pittau and M. Worek, *Assault on the NLO Wishlist: pp —> t anti-t b anti-b*, *JHEP* **09** (2009) 109 [0907.4723].

[181] A. Bredenstein, A. Denner, S. Dittmaier and S. Pozzorini, *NLO QCD Corrections to Top Anti-Top Bottom Anti-Bottom Production at the LHC: 2. full hadronic results*, *JHEP* **03** (2010) 021 [1001.4006].

[182] M. Worek, *On the next-to-leading order QCD K-factor for top $t\bar{t}b\bar{b}$ production at the TeVatron*, *JHEP* **02** (2012) 043 [1112.4325].

[183] G. Bevilacqua and M. Worek, *On the ratio of $t\bar{t}b\bar{b}$ and $t\bar{t}jj$ cross sections at the CERN Large Hadron Collider*, *JHEP* **07** (2014) 135 [1403.2046].

[184] A. Kardos and Z. Trócsányi, *Hadroproduction of t anti-t pair with a b anti-b pair using PowHel*, *J. Phys. G* **41** (2014) 075005 [1303.6291].

[185] M. V. Garzelli, A. Kardos and Z. Trócsányi, *Hadroproduction of $t\bar{t}b\bar{b}$ final states at LHC: predictions at NLO accuracy matched with Parton Shower*, *JHEP* **03** (2015) 083 [1408.0266].

[186] F. Cascioli, P. Maierhöfer, N. Moretti, S. Pozzorini and F. Siegert, *NLO matching for $t\bar{t}b\bar{b}$ production with massive b-quarks*, *Phys. Lett. B* **734** (2014) 210 [1309.5912].

[187] G. Bevilacqua, M. V. Garzelli and A. Kardos, *$t\bar{t}b\bar{b}$ hadroproduction with massive bottom quarks with PowHel*, 1709.06915.

[188] T. Ježo, J. M. Lindert, N. Moretti and S. Pozzorini, *New NLOPS predictions for $t\bar{t}$ + b -jet production at the LHC*, *Eur. Phys. J. C* **78** (2018) 502 [1802.00426].

[189] F. Buccioni, S. Kallweit, S. Pozzorini and M. F. Zoller, *NLO QCD predictions for $t\bar{t}b\bar{b}$ production in association with a light jet at the LHC*, *JHEP* **12** (2019) 015 [1907.13624].

[190] A. Denner, J.-N. Lang and M. Pellen, *Full NLO QCD corrections to off-shell $t\bar{t}b\bar{b}$ production*, *Phys. Rev. D* **104** (2021) 056018 [2008.00918].

[191] G. Bevilacqua, H.-Y. Bi, H. B. Hartanto, M. Kraus, M. Lupattelli and M. Worek, *$t\bar{t}b\bar{b}$ at the LHC: on the size of corrections and b-jet definitions*, *JHEP* **08** (2021) 008 [2105.08404].

[192] G. Bevilacqua, H.-Y. Bi, H. B. Hartanto, M. Kraus, M. Lupattelli and M. Worek, *$t\bar{t}b\bar{b}$ at the LHC: On the size of off-shell effects and prompt b-jet identification*, *Phys. Rev. D* **107** (2023) 014028 [2202.11186].

[193] F. Maltoni, D. Pagani and I. Tsinikos, *Associated production of a top-quark pair with vector bosons at NLO in QCD: impact on $t\bar{t}H$ searches at the LHC*, *JHEP* **02** (2016) 113 [1507.05640].

[194] U. Baur, M. Buice and L. H. Orr, *Direct measurement of the top quark charge at hadron colliders*, *Phys. Rev. D* **64** (2001) 094019 [hep-ph/0106341].

[195] O. Bessidskaia Bylund, F. Maltoni, I. Tsinikos, E. Vryonidou and C. Zhang, *Probing top quark neutral couplings in the Standard Model Effective Field Theory at NLO in QCD*, *JHEP* **05** (2016) 052 [1601.08193].

[196] A. O. Bouzas and F. Larios, *Electromagnetic dipole moments of the Top quark*, *Phys. Rev. D* **87** (2013) 074015 [1212.6575].

[197] M. Fael and T. Gehrmann, *Probing top quark electromagnetic dipole moments in single-top-plus-photon production*, *Phys. Rev. D* **88** (2013) 033003 [1307.1349].

[198] J. A. Aguilar-Saavedra, E. Álvarez, A. Juste and F. Rubbo, *Shedding light on the $t\bar{t}$ asymmetry: the photon handle*, *JHEP* **04** (2014) 188 [1402.3598].

[199] M. Schulze and Y. Soreq, *Pinning down electroweak dipole operators of the top quark*, *Eur. Phys. J. C* **76** (2016) 466 [1603.08911].

[200] S. M. Etesami, S. Khatibi and M. Mohammadi Najafabadi, *Measuring anomalous $WW\gamma$ and $t\,\bar{t}\gamma$ couplings using top+ γ production at the LHC*, *Eur. Phys. J. C* **76** (2016) 533 [1606.02178].

[201] U. Baur, A. Juste, L. H. Orr and D. Rainwater, *Probing electroweak top quark couplings at hadron colliders*, *Phys. Rev. D* **71** (2005) 054013 [hep-ph/0412021].

[202] T. Ibrahim and P. Nath, *The Top quark electric dipole moment in an MSSM extension with vector like multiplets*, *Phys. Rev. D* **82** (2010) 055001 [1007.0432].

[203] T. Ibrahim and P. Nath, *The Chromoelectric Dipole Moment of the Top Quark in Models with Vector Like Multiplets*, *Phys. Rev. D* **84** (2011) 015003 [1104.3851].

[204] J. A. Aguilar-Saavedra, *Single lepton charge asymmetries in $t\bar{t}$ and $t\bar{t}\gamma$ production at the LHC*, *Eur. Phys. J. C* **78** (2018) 434 [1802.05721].

[205] J. Bergner and M. Schulze, *The top quark charge asymmetry in $t\bar{t}\gamma$ production at the LHC*, *Eur. Phys. J. C* **79** (2019) 189 [1812.10535].

[206] CDF collaboration, *Evidence for $t\bar{t}\gamma$ Production and Measurement of $\sigma_{t\bar{t}\gamma}/\sigma_{t\bar{t}}$*, *Phys. Rev. D* **84** (2011) 031104 [1106.3970].

[207] ATLAS collaboration, *Measurement of the $t\bar{t}\gamma$ production cross section in proton-proton collisions at $\sqrt{s} = 8$ TeV with the ATLAS detector*, *JHEP* **11** (2017) 086 [1706.03046].

[208] CMS collaboration, *Measurement of the semileptonic* $\mathrm{t\bar{t}}$ *+ γ production cross section in pp collisions at $\sqrt{s} = 8$ TeV*, *JHEP* **10** (2017) 006 [1706.08128].

[209] ATLAS collaboration, *Measurements of inclusive and differential fiducial cross-sections of $t\bar{t}\gamma$ production in leptonic final states at $\sqrt{s} = 13$ TeV in ATLAS*, *Eur. Phys. J. C* **79** (2019) 382 [1812.01697].

[210] ATLAS collaboration, *Measurements of inclusive and differential cross-sections of combined $t\bar{t}\gamma$ and $tW\gamma$ production in the $e\mu$ channel at 13 TeV with the ATLAS detector*, *JHEP* **09** (2020) 049 [2007.06946].

[211] CMS collaboration, *Measurement of the inclusive and differential $t\bar{t}\gamma$ cross sections in the single-lepton channel and EFT interpretation at $\sqrt{s} = 13$ TeV*, *JHEP* **12** (2021) 180 [2107.01508].

[212] G. Bevilacqua, H. B. Hartanto, M. Kraus, T. Weber and M. Worek, *Hard Photons in Hadroproduction of Top Quarks with Realistic Final States*, *JHEP* **10** (2018) 158 [1803.09916].

[213] G. Bevilacqua, H. B. Hartanto, M. Kraus, T. Weber and M. Worek, *Precise predictions for $t\bar{t}\gamma/t\bar{t}$ cross section ratios at the LHC*, *JHEP* **01** (2019) 188 [1809.08562].

[214] ATLAS collaboration, *Measurement of the charge asymmetry in top-quark pair production in association with a photon with the ATLAS experiment*, *Phys. Lett. B* **843** (2023) 137848 [2212.10552].

[215] P.-F. Duan, W.-G. Ma, R.-Y. Zhang, L. Han, L. Guo and S.-M. Wang, *QCD corrections to associated production of $t\bar{t}\gamma$ at hadron colliders*, *Phys. Rev. D* **80** (2009) 014022 [0907.1324].

[216] P.-F. Duan, R.-Y. Zhang, W.-G. Ma, L. Han, L. Guo and S.-M. Wang, *Next-to-leading order QCD corrections to $t\bar{t}\gamma$ production at the 7 TeV LHC*, *Chin. Phys. Lett.* **28** (2011) 111401 [1110.2315].

[217] P.-F. Duan, Y. Zhang, Y. Wang, M. Song and G. Li, *Electroweak corrections to top quark pair production in association with a hard photon at hadron colliders*, *Phys. Lett. B* **766** (2017) 102 [1612.00248].

[218] N. Kidonakis and A. Tonero, *Higher-order corrections in $t\bar{t}\gamma$ cross sections*, *Phys. Rev. D* **107** (2023) 034013 [2212.00096].

[219] A. Kardos and Z. Trócsányi, *Hadroproduction of t anti-t pair in association with an isolated photon at NLO accuracy matched with parton shower*, *JHEP* **05** (2015) 090 [1406.2324].

[220] A. Kardos and Z. Trócsányi, *Hadroproduction of $t\bar{t}$ pair with two isolated photons with PowHel*, *Nucl. Phys. B* **897** (2015) 717 [1408.0278].

[221] H. van Deurzen, R. Frederix, V. Hirschi, G. Luisoni, P. Mastrolia and G. Ossola, *Spin Polarisation of $t\bar{t}\gamma\gamma$ production at NLO+PS with GoSam interfaced to MadGraph5_aMC@NLO*, *Eur. Phys. J. C* **76** (2016) 221 [1509.02077].

[222] ATLAS collaboration, *Observation of a new particle in the search for the Standard Model Higgs boson with the ATLAS detector at the LHC*, *Phys. Lett. B* **716** (2012) 1 [1207.7214].

[223] CMS collaboration, *Observation of a New Boson at a Mass of 125 GeV with the CMS Experiment at the LHC*, *Phys. Lett. B* **716** (2012) 30 [1207.7235].

[224] LHC Higgs Cross Section Working Group collaboration, *Handbook of LHC Higgs Cross Sections: 4. Deciphering the Nature of the Higgs Sector*, 1610.07922.

[225] ATLAS collaboration, *Observation of Higgs boson production in association with a top quark pair at the LHC with the ATLAS detector*, *Phys. Lett. B* **784** (2018) 173 [1806.00425].

[226] CMS collaboration, *Observation of $t\bar{t}H$ production*, *Phys. Rev. Lett.* **120** (2018) 231801 [1804.02610].

[227] ATLAS collaboration, *Search for $H \to \gamma\gamma$ produced in association with top quarks and constraints on the Yukawa coupling between the top quark and the Higgs boson using data taken at 7 TeV and 8 TeV with the ATLAS detector*, *Phys. Lett. B* **740** (2015) 222 [1409.3122].

[228] ATLAS collaboration, *Search for the Standard Model Higgs boson produced in association with top quarks and decaying into $b\bar{b}$ in pp collisions at $\sqrt{s}$ = 8 TeV with the ATLAS detector*, *Eur. Phys. J. C* **75** (2015) 349 [1503.05066].

[229] ATLAS collaboration, *Search for the Standard Model Higgs boson decaying into $b\bar{b}$ produced in association with top quarks decaying hadronically in pp collisions at $\sqrt{s} = 8$ TeV with the ATLAS detector*, *JHEP* **05** (2016) 160 [1604.03812].

[230] CMS collaboration, *Search for the Standard Model Higgs Boson Produced in Association with a Top-Quark Pair in pp Collisions at the LHC*, *JHEP* **05** (2013) 145 [1303.0763].

[231] CMS collaboration, *Search for a Standard Model Higgs Boson Produced in Association with a Top-Quark Pair and Decaying to Bottom Quarks Using a Matrix Element Method*, *Eur. Phys. J. C* **75** (2015) 251 [1502.02485].

[232] ATLAS collaboration, *Search for the associated production of the Higgs boson with a top quark pair in multilepton final states with the ATLAS detector*, *Phys. Lett. B* **749** (2015) 519 [1506.05988].

[233] CMS collaboration, *Search for the associated production of the Higgs boson with a top-quark pair*, *JHEP* **09** (2014) 087 [1408.1682].

[234] CMS collaboration, *Search for CP violation in ttH and tH production in multilepton channels in proton-proton collisions at $\sqrt{s}$ = 13 TeV*, *JHEP* **07** (2023) 092 [2208.02686].

[235] ATLAS collaboration, *Evidence for the associated production of the Higgs boson and a top quark pair with the ATLAS detector*, *Phys. Rev. D* **97** (2018) 072003 [1712.08891].

[236] CMS collaboration, *Evidence for associated production of a Higgs boson with a top quark pair in final states with electrons, muons, and hadronically decaying τ leptons at $\sqrt{s}$ = 13 TeV*, *JHEP* **08** (2018) 066 [1803.05485].

[237] CMS collaboration, *Measurement of the Higgs boson production rate in association with top quarks in final states with electrons, muons, and hadronically decaying tau leptons at $\sqrt{s}$ = 13 TeV*, *Eur. Phys. J. C* **81** (2021) 378 [2011.03652].

[238] ATLAS collaboration, *Search for the standard model Higgs boson produced in association with top quarks and decaying into a $b\bar{b}$ pair in pp collisions at $\sqrt{s}$ = 13 TeV with the ATLAS detector*, *Phys. Rev. D* **97** (2018) 072016 [1712.08895].

[239] CMS collaboration, *Search for* $\mathrm{t\bar{t}H}$ *production in the* $\mathrm{H} \to \mathrm{b\bar{b}}$ *decay channel with leptonic* $\mathrm{t\bar{t}}$ *decays in proton-proton collisions at* $\sqrt{s} = 13$ *TeV*, *JHEP* **03** (2019) 026 [1804.03682].

[240] ATLAS collaboration, *Measurement of Higgs boson decay into b-quarks in associated production with a top-quark pair in pp collisions at* $\sqrt{s} = 13$ *TeV with the ATLAS detector*, *JHEP* **06** (2022) 097 [2111.06712].

[241] CMS collaboration, *A search for decays of the Higgs boson to invisible particles in events with a top-antitop quark pair or a vector boson in proton-proton collisions at* $\sqrt{s} = 13$ *TeV*, *Eur. Phys. J. C* **83** (2023) 933 [2303.01214].

[242] W. Beenakker, S. Dittmaier, M. Kramer, B. Plumper, M. Spira and P. M. Zerwas, *Higgs radiation off top quarks at the Tevatron and the LHC*, *Phys. Rev. Lett.* **87** (2001) 201805 [hep-ph/0107081].

[243] L. Reina and S. Dawson, *Next-to-leading order results for t anti-t h production at the Tevatron*, *Phys. Rev. Lett.* **87** (2001) 201804 [hep-ph/0107101].

[244] W. Beenakker, S. Dittmaier, M. Kramer, B. Plumper, M. Spira and P. M. Zerwas, *NLO QCD corrections to t anti-t H production in hadron collisions*, *Nucl. Phys. B* **653** (2003) 151 [hep-ph/0211352].

[245] S. Dawson, L. H. Orr, L. Reina and D. Wackeroth, *Associated top quark Higgs boson production at the LHC*, *Phys. Rev. D* **67** (2003) 071503 [hep-ph/0211438].

[246] S. Dawson, C. Jackson, L. H. Orr, L. Reina and D. Wackeroth, *Associated Higgs production with top quarks at the large hadron collider: NLO QCD corrections*, *Phys. Rev. D* **68** (2003) 034022 [hep-ph/0305087].

[247] S. Frixione, V. Hirschi, D. Pagani, H. S. Shao and M. Zaro, *Weak corrections to Higgs hadroproduction in association with a top-quark pair*, *JHEP* **09** (2014) 065 [1407.0823].

[248] Y. Zhang, W.-G. Ma, R.-Y. Zhang, C. Chen and L. Guo, *QCD NLO and EW NLO corrections to* $t\bar{t}H$ *production with top quark decays at hadron collider*, *Phys. Lett. B* **738** (2014) 1 [1407.1110].

[249] S. Frixione, V. Hirschi, D. Pagani, H. S. Shao and M. Zaro, *Electroweak and QCD corrections to top-pair hadroproduction in association with heavy bosons*, *JHEP* **06** (2015) 184 [1504.03446].

[250] A. Kulesza, L. Motyka, T. Stebel and V. Theeuwes, *Soft gluon resummation for associated* $t\bar{t}H$ *production at the LHC*, *JHEP* **03** (2016) 065 [1509.02780].

[251] A. Broggio, A. Ferroglia, B. D. Pecjak, A. Signer and L. L. Yang, *Associated production of a top pair and a Higgs boson beyond NLO*, *JHEP* **03** (2016) 124 [1510.01914].

[252] A. Broggio, A. Ferroglia, B. D. Pecjak and L. L. Yang, *NNLL resummation for the associated production of a top pair and a Higgs boson at the LHC*, *JHEP* **02** (2017) 126 [1611.00049].

[253] A. Kulesza, L. Motyka, T. Stebel and V. Theeuwes, *Associated $t\bar{t}H$ production at the LHC: Theoretical predictions at NLO+NNLL accuracy*, *Phys. Rev. D* **97** (2018) 114007 [1704.03363].

[254] M. van Beekveld and W. Beenakker, *The role of the threshold variable in soft-gluon resummation of the $t\bar{t}h$ production process*, *JHEP* **05** (2021) 196 [2012.09170].

[255] W.-L. Ju and L. L. Yang, *Resummation of soft and Coulomb corrections for $t\bar{t}h$ production at the LHC*, *JHEP* **06** (2019) 050 [1904.08744].

[256] R. Frederix, S. Frixione, V. Hirschi, F. Maltoni, R. Pittau and P. Torrielli, *Scalar and pseudoscalar Higgs production in association with a top–antitop pair*, *Phys. Lett. B* **701** (2011) 427 [1104.5613].

[257] M. V. Garzelli, A. Kardos, C. G. Papadopoulos and Z. Trocsanyi, *Standard Model Higgs boson production in association with a top anti-top pair at NLO with parton showering*, *EPL* **96** (2011) 11001 [1108.0387].

[258] H. B. Hartanto, B. Jager, L. Reina and D. Wackeroth, *Higgs boson production in association with top quarks in the POWHEG BOX*, *Phys. Rev. D* **91** (2015) 094003 [1501.04498].

[259] D. Pagani, T. Vitos and M. Zaro, *Improving NLO QCD event generators with high-energy EW corrections*, 2309.00452.

[260] A. Denner and R. Feger, *NLO QCD corrections to off-shell top-antitop production with leptonic decays in association with a Higgs boson at the LHC*, *JHEP* **11** (2015) 209 [1506.07448].

[261] A. Denner, J.-N. Lang, M. Pellen and S. Uccirati, *Higgs production in association with off-shell top-antitop pairs at NLO EW and QCD at the LHC*, *JHEP* **02** (2017) 053 [1612.07138].

[262] D. Stremmer and M. Worek, *Production and decay of the Higgs boson in association with top quarks*, *JHEP* **02** (2022) 196 [2111.01427].

[263] S. Catani, I. Fabre, M. Grazzini and S. Kallweit, *$t\bar{t}H$ production at NNLO: the flavour off-diagonal channels*, *Eur. Phys. J. C* **81** (2021) 491 [2102.03256].

[264] J. Chen, C. Ma, G. Wang, L. L. Yang and X. Ye, *Two-loop infrared singularities in the production of a Higgs boson associated with a top-quark pair*, *JHEP* **04** (2022) 025 [2202.02913].

[265] F. Buccioni, P. A. Kreer, X. Liu and L. Tancredi, *One loop QCD corrections to $gg \to t\bar{t}H$ at $\mathcal{O}(\epsilon^2)$*, 2312.10015.

[266] F. Febres Cordero, G. Figueiredo, M. Kraus, B. Page and L. Reina, *Two-Loop Master Integrals for Leading-Color $pp \to t\bar{t}H$ Amplitudes with a Light-Quark Loop*, 2312.08131.

[267] G. Wang, T. Xia, L. L. Yang and X. Ye, *Two-loop QCD amplitudes for $t\bar{t}H$ production from boosted limit*, 2402.00431.

[268] S. Catani, S. Devoto, M. Grazzini, S. Kallweit, J. Mazzitelli and C. Savoini, *Higgs Boson Production in Association with a Top-Antitop Quark Pair in Next-to-Next-to-Leading Order QCD*, *Phys. Rev. Lett.* **130** (2023) 111902 [2210.07846].

[269] R. Frederix, D. Pagani and M. Zaro, *Large NLO corrections in $t\bar{t}W^{\pm}$ and $t\bar{t}t\bar{t}$ hadroproduction from supposedly subleading EW contributions*, *JHEP* **02** (2018) 031 [1711.02116].

[270] F. Maltoni, M. L. Mangano, I. Tsinikos and M. Zaro, *Top-quark charge asymmetry and polarization in $t\bar{t}W^{\pm}$ production at the LHC*, *Phys. Lett. B* **736** (2014) 252 [1406.3262].

[271] G. Bevilacqua, H.-Y. Bi, H. B. Hartanto, M. Kraus, J. Nasufi and M. Worek, *NLO QCD corrections to off-shell $t\bar{t}W^{\pm}$ production at the LHC: correlations and asymmetries*, *Eur. Phys. J. C* **81** (2021) 675 [2012.01363].

[272] CMS collaboration, *Search for production of four top quarks in final states with same-sign or multiple leptons in proton-proton collisions at $\sqrt{s} = 13$ TeV*, *Eur. Phys. J. C* **80** (2020) 75 [1908.06463].

[273] ATLAS collaboration, *Evidence for $t\bar{t}t\bar{t}$ production in the multilepton final state in proton–proton collisions at $\sqrt{s} = 13$ TeV with the ATLAS detector*, *Eur. Phys. J. C* **80** (2020) 1085 [2007.14858].

[274] ATLAS collaboration, *Observation of four-top-quark production in the multilepton final state with the ATLAS detector*, *Eur. Phys. J. C* **83** (2023) 496 [2303.15061].

[275] CMS collaboration, *Observation of four top quark production in proton-proton collisions at $\sqrt{s} = 13$ TeV*, *Phys. Lett. B* **847** (2023) 138290 [2305.13439].

[276] R. M. Barnett, J. F. Gunion and H. E. Haber, *Discovering supersymmetry with like sign dileptons*, *Phys. Lett. B* **315** (1993) 349 [hep-ph/9306204].

[277] M. Guchait and D. P. Roy, *Like sign dilepton signature for gluino production at CERN LHC including top quark and Higgs boson effects*, *Phys. Rev. D* **52** (1995) 133 [hep-ph/9412329].

[278] H. Baer, C.-h. Chen, F. Paige and X. Tata, *Signals for minimal supergravity at the CERN large hadron collider. 2: Multi - lepton channels*, *Phys. Rev. D* **53** (1996) 6241 [hep-ph/9512383].

[279] J. Maalampi and N. Romanenko, *Single production of doubly charged Higgs bosons at hadron colliders*, *Phys. Lett. B* **532** (2002) 202 [hep-ph/0201196].

[280] H.-C. Cheng, K. T. Matchev and M. Schmaltz, *Bosonic supersymmetry? Getting fooled at the CERN LHC*, *Phys. Rev. D* **66** (2002) 056006 [hep-ph/0205314].

[281] S. von Buddenbrock, N. Chakrabarty, A. S. Cornell, D. Kar, M. Kumar, T. Mandal et al., *Phenomenological signatures of additional scalar bosons at the LHC*, *Eur. Phys. J. C* **76** (2016) 580 [1606.01674].

[282] S. von Buddenbrock, A. S. Cornell, A. Fadol, M. Kumar, B. Mellado and X. Ruan, *Multi-lepton signatures of additional scalar bosons beyond the Standard Model at the LHC*, *J. Phys. G* **45** (2018) 115003 [1711.07874].

[283] S. von Buddenbrock, A. S. Cornell, E. D. R. Iarilala, M. Kumar, B. Mellado, X. Ruan et al., *Constraints on a 2HDM with a singlet scalar and implications in the search for heavy bosons at the LHC*, *J. Phys. G* **46** (2019) 115001 [1809.06344].

[284] S. Buddenbrock, A. S. Cornell, Y. Fang, A. Fadol Mohammed, M. Kumar, B. Mellado et al., *The emergence of multi-lepton anomalies at the LHC and their compatibility with new physics at the EW scale*, *JHEP* **10** (2019) 157 [1901.05300].

[285] F. del Aguila, J. A. Aguilar-Saavedra and R. Miquel, *Constraints on top couplings in models with exotic quarks*, *Phys. Rev. Lett.* **82** (1999) 1628 [hep-ph/9808400].

[286] F. del Aguila, M. Perez-Victoria and J. Santiago, *Effective description of quark mixing*, *Phys. Lett. B* **492** (2000) 98 [hep-ph/0007160].

[287] F. del Aguila, M. Perez-Victoria and J. Santiago, *Observable contributions of new exotic quarks to quark mixing*, *JHEP* **09** (2000) 011 [hep-ph/0007316].

[288] J. A. Aguilar-Saavedra, *Mixing with vector-like quarks: constraints and expectations*, *EPJ Web Conf.* **60** (2013) 16012 [1306.4432].

[289] R. Contino and G. Servant, *Discovering the top partners at the LHC using same-sign dilepton final states*, *JHEP* **06** (2008) 026 [0801.1679].

[290] A. De Simone, O. Matsedonskyi, R. Rattazzi and A. Wulzer, *A First Top Partner Hunter's Guide*, *JHEP* **04** (2013) 004 [1211.5663].

[291] F. M. L. Almeida, Jr., Y. do Amaral Coutinho, J. A. Martins Simoes, P. P. Queiroz Filho and C. M. Porto, *Same sign dileptons as a signature for heavy Majorana neutrinos in hadron hadron collisions*, *Phys. Lett. B* **400** (1997) 331 [hep-ph/9703441].

[292] Y. Bai and Z. Han, *Top-antitop and Top-top Resonances in the Dilepton Channel at the CERN LHC*, *JHEP* **04** (2009) 056 [0809.4487].

[293] E. L. Berger, Q.-H. Cao, C.-R. Chen, C. S. Li and H. Zhang, *Top Quark Forward-Backward Asymmetry and Same-Sign Top Quark Pairs*, *Phys. Rev. Lett.* **106** (2011) 201801 [1101.5625].

[294] A. Belloni et al., *Report of the Topical Group on Electroweak Precision Physics and Constraining New Physics for Snowmass 2021*, 2209.08078.

[295] I. Brivio, S. Bruggisser, F. Maltoni, R. Moutafis, T. Plehn, E. Vryonidou et al., *O new physics, where art thou? A global search in the top sector*, *JHEP* **02** (2020) 131 [1910.03606].

[296] J. de Blas, Y. Du, C. Grojean, J. Gu, V. Miralles, M. E. Peskin et al., *Global SMEFT Fits at Future Colliders*, in *Snowmass 2021*, 6, 2022, 2206.08326.

[297] ATLAS collaboration, *Measurement of the total and differential cross-sections of $t\bar{t}W$ production in pp collisions at 13 TeV with the ATLAS detector*, *ATLAS-CONF-2023-019*.

[298] CMS collaboration, *Measurement of the cross section of top quark-antiquark pair production in association with a W boson in proton-proton collisions at $\sqrt{s}$ = 13 TeV*, *JHEP* **07** (2023) 219 [2208.06485].

[299] ATLAS collaboration, *Inclusive and differential cross section measurements of $t\bar{t}Z$ production in pp collisions at $\sqrt{s} = 13$ TeV with the ATLAS detector, including EFT and spin correlations interpretations*, *ATLAS-CONF-2023-065*.

[300] CMS collaboration, *Measurement of top quark pair production in association with a Z boson in proton-proton collisions at $\sqrt{s}$ = 13 TeV*, *JHEP* **03** (2020) 056 [1907.11270].

[301] L. Buonocore, S. Devoto, M. Grazzini, S. Kallweit, J. Mazzitelli, L. Rottoli et al., *Precise Predictions for the Associated Production of a W Boson with a Top-Antitop Quark Pair at the LHC*, *Phys. Rev. Lett.* **131** (2023) 231901 [2306.16311].

[302] A. Kulesza, L. Motyka, D. Schwartländer, T. Stebel and V. Theeuwes, *Associated top quark pair production with a heavy boson: differential cross sections at NLO+NNLL accuracy*, *Eur. Phys. J. C* **80** (2020) 428 [2001.03031].

[303] ATLAS collaboration, *Measurement of the $t\bar{t}W$ and $t\bar{t}Z$ production cross sections in pp collisions at $\sqrt{s} = 8$ TeV with the ATLAS detector*, *JHEP* **11** (2015) 172 [1509.05276].

[304] CMS collaboration, *Observation of top quark pairs produced in association with a vector boson in pp collisions at $\sqrt{s} = 8$ TeV*, *JHEP* **01** (2016) 096 [1510.01131].

[305] ATLAS collaboration, *Measurement of the $t\bar{t}Z$ and $t\bar{t}W$ production cross sections in multilepton final states using 3.2 fb^{-1} of pp collisions at $\sqrt{s}$ = 13 TeV with the ATLAS detector*, *Eur. Phys. J. C* **77** (2017) 40 [1609.01599].

[306] ATLAS collaboration, *Measurement of the $t\bar{t}Z$ and $t\bar{t}W$ cross sections in proton-proton collisions at $\sqrt{s} = 13$ TeV with the ATLAS detector*, *Phys. Rev. D* **99** (2019) 072009 [1901.03584].

[307] ATLAS collaboration, *Measurement of the total and differential cross-sections of $t\bar{t}W$ production in pp collisions at $\sqrt{s} = 13$ TeV with the ATLAS detector*, 2401.05299.

[308] CMS collaboration, *Measurement of the cross section for top quark pair production in association with a W or Z boson in proton-proton collisions at $\sqrt{s} = 13$ TeV*, *JHEP* **08** (2018) 011 [1711.02547].

[309] S. Badger, J. M. Campbell and R. K. Ellis, *QCD Corrections to the Hadronic Production of a Heavy Quark Pair and a W-Boson Including Decay Correlations*, *JHEP* **03** (2011) 027 [1011.6647].

[310] R. Frederix, S. Frixione, V. Hirschi, D. Pagani, H. S. Shao and M. Zaro, *The automation of next-to-leading order electroweak calculations*, *JHEP* **07** (2018) 185 [1804.10017].

[311] P. Bärnreuther, M. Czakon and P. Fiedler, *Virtual amplitudes and threshold behaviour of hadronic top-quark pair-production cross sections*, *JHEP* **02** (2014) 078 [1312.6279].

[312] M. K. Mandal, P. Mastrolia, J. Ronca and W. J. Bobadilla Torres, *Two-loop scattering amplitude for heavy-quark pair production through light-quark annihilation in QCD*, *JHEP* **09** (2022) 129 [2204.03466].

[313] A. A. Penin, *Two-loop photonic corrections to massive Bhabha scattering*, *Nucl. Phys. B* **734** (2006) 185 [hep-ph/0508127].

[314] A. Mitov and S. Moch, *The Singular behavior of massive QCD amplitudes*, *JHEP* **05** (2007) 001 [hep-ph/0612149].

[315] T. Becher and K. Melnikov, *Two-loop QED corrections to Bhabha scattering*, *JHEP* **06** (2007) 084 [0704.3582].

[316] S. Badger, H. B. Hartanto and S. Zoia, *Two-Loop QCD Corrections to $Wb\bar{b}$ Production at Hadron Colliders*, *Phys. Rev. Lett.* **127** (2021) 012001 [2102.02516].

[317] S. Abreu, F. Febres Cordero, H. Ita, M. Klinkert, B. Page and V. Sotnikov, *Leading-color two-loop amplitudes for four partons and a W boson in QCD*, *JHEP* **04** (2022) 042 [2110.07541].

[318] N. Kidonakis and C. Foster, *Soft-gluon corrections in $t\bar{t}W$ production*, 2312.00861.

[319] H. T. Li, C. S. Li and S. A. Li, *Renormalization group improved predictions for $t\bar{t}W^{\pm}$ production at hadron colliders*, *Phys. Rev. D* **90** (2014) 094009 [1409.1460].

[320] A. Broggio, A. Ferroglia, G. Ossola and B. D. Pecjak, *Associated production of a top pair and a W boson at next-to-next-to-leading logarithmic accuracy*, *JHEP* **09** (2016) 089 [1607.05303].

[321] A. Kulesza, L. Motyka, D. Schwartländer, T. Stebel and V. Theeuwes, *Associated production of a top quark pair with a heavy electroweak gauge boson at NLO+NNLL accuracy*, *Eur. Phys. J. C* **79** (2019) 249 [1812.08622].

[322] A. Broggio, A. Ferroglia, R. Frederix, D. Pagani, B. D. Pecjak and I. Tsinikos, *Top-quark pair hadroproduction in association with a heavy boson at NLO+NNLL including EW corrections*, *JHEP* **08** (2019) 039 [1907.04343].

[323] M. V. Garzelli, A. Kardos, C. G. Papadopoulos and Z. Trocsanyi, *$t\bar{t}W^{\pm}$ and $t\bar{t}Z$ Hadroproduction at NLO accuracy in QCD with Parton Shower and Hadronization effects*, *JHEP* **11** (2012) 056 [1208.2665].

[324] F. Febres Cordero, M. Kraus and L. Reina, *Top-quark pair production in association with a $W^{\pm}$ gauge boson in the POWHEG-BOX*, *Phys. Rev. D* **103** (2021) 094014 [2101.11808].

[325] G. Bevilacqua, H.-Y. Bi, H. B. Hartanto, M. Kraus and M. Worek, *The simplest of them all: $t\bar{t}W^{\pm}$ at NLO accuracy in QCD*, *JHEP* **08** (2020) 043 [2005.09427].

[326] A. Denner and G. Pelliccioli, *NLO QCD corrections to off-shell $t\bar{t}W^{+}$ production at the LHC*, *JHEP* **11** (2020) 069 [2007.12089].

[327] A. Denner and G. Pelliccioli, *Combined NLO EW and QCD corrections to off-shell $t\bar{t}W$ production at the LHC*, *Eur. Phys. J. C* **81** (2021) 354 [2102.03246].

[328] G. Bevilacqua, H. Y. Bi, F. Febres Cordero, H. B. Hartanto, M. Kraus, J. Nasufi et al., *Modeling uncertainties of $t\bar{t}W^{\pm}$ multilepton signatures*, *Phys. Rev. D* **105** (2022) 014018 [2109.15181].

[329] S. von Buddenbrock, R. Ruiz and B. Mellado, *Anatomy of inclusive $t\bar{t}W$ production at hadron colliders*, *Phys. Lett. B* **811** (2020) 135964 [2009.00032].

[330] R. Frederix and I. Tsinikos, *On improving NLO merging for* $\mathrm{t\bar{t}W}$ *production*, *JHEP* **11** (2021) 029 [2108.07826].

[331] H.-Y. Bi, M. Kraus, M. Reinartz and M. Worek, *NLO QCD predictions for off-shell $t\bar{t}W$ production in association with a light jet at the LHC*, *JHEP* **09** (2023) 026 [2305.03802].

[332] N. Greiner, K. Kong, J.-C. Park, S. C. Park and J.-C. Winter, *Model-Independent Production of a Top-Philic Resonance at the LHC*, *JHEP* **04** (2015) 029 [1410.6099].

[333] P. Cox, A. D. Medina, T. S. Ray and A. Spray, *Novel collider and dark matter phenomenology of a top-philic Z'*, *JHEP* **06** (2016) 110 [1512.00471].

[334] N. Kumar and S. P. Martin, *Vectorlike Leptons at the Large Hadron Collider*, *Phys. Rev. D* **92** (2015) 115018 [1510.03456].

[335] J. H. Kim, K. Kong, S. J. Lee and G. Mohlabeng, *Probing TeV scale Top-Philic Resonances with Boosted Top-Tagging at the High Luminosity LHC*, *Phys. Rev. D* **94** (2016) 035023 [1604.07421].

[336] P. J. Fox, I. Low and Y. Zhang, *Top-philic Z' forces at the LHC*, *JHEP* **03** (2018) 074 [1801.03505].

[337] E. Alvarez, A. Juste, M. Szewc and T. Vazquez Schroeder, *Topping-up multilepton plus b-jets anomalies at the LHC with a Z' boson*, *JHEP* **05** (2021) 125 [2011.06514].

[338] S. Bißmann, G. Hiller, C. Hormigos-Feliu and D. F. Litim, *Multi-lepton signatures of vector-like leptons with flavor*, *Eur. Phys. J. C* **81** (2021) 101 [2011.12964].

[339] U. Baur, A. Juste, D. Rainwater and L. H. Orr, *Improved measurement of ttZ couplings at the CERN LHC*, *Phys. Rev. D* **73** (2006) 034016 [hep-ph/0512262].

[340] E. L. Berger, Q.-H. Cao and I. Low, *Model Independent Constraints Among the Wtb, Zb anti-b, and Zt anti-t Couplings*, *Phys. Rev. D* **80** (2009) 074020 [0907.2191].

[341] R. Röntsch and M. Schulze, *Constraining couplings of top quarks to the Z boson in $t\bar{t}$ + Z production at the LHC*, *JHEP* **07** (2014) 091 [1404.1005].

[342] R. Röntsch and M. Schulze, *Probing top-Z dipole moments at the LHC and ILC*, *JHEP* **08** (2015) 044 [1501.05939].

[343] A. Buckley, C. Englert, J. Ferrando, D. J. Miller, L. Moore, M. Russell et al., *Constraining top quark effective theory in the LHC Run II era*, *JHEP* **04** (2016) 015 [1512.03360].

[344] N. P. Hartland, F. Maltoni, E. R. Nocera, J. Rojo, E. Slade, E. Vryonidou et al., *A Monte Carlo global analysis of the Standard Model Effective Field Theory: the top quark sector*, *JHEP* **04** (2019) 100 [1901.05965].

[345] F. Maltoni, L. Mantani and K. Mimasu, *Top-quark electroweak interactions at high energy*, *JHEP* **10** (2019) 004 [1904.05637].

[346] G. Durieux, A. Irles, V. Miralles, A. Peñuelas, R. Pöschl, M. Perelló et al., *The electro-weak couplings of the top and bottom quarks — Global fit and future prospects*, *JHEP* **12** (2019) 98 [1907.10619].

[347] Y. Afik, S. Bar-Shalom, K. Pal, A. Soni and J. Wudka, *Multi-lepton probes of new physics and lepton-universality in top-quark interactions*, *Nucl. Phys. B* **980** (2022) 115849 [2111.13711].

[348] U. Haisch, P. Pani and G. Polesello, *Determining the CP nature of spin-0 mediators in associated production of dark matter and $t\bar{t}$ pairs*, *JHEP* **02** (2017) 131 [1611.09841].

[349] G. Bevilacqua, H. B. Hartanto, M. Kraus, T. Weber and M. Worek, *Towards constraining Dark Matter at the LHC: Higher order QCD predictions for $t\bar{t} + Z(Z \to \nu_\ell \bar{\nu}_\ell)$*, *JHEP* **11** (2019) 001 [1907.09359].

[350] J. Hermann and M. Worek, *The impact of top-quark modelling on the exclusion limits in $t\bar{t} + DM$ searches at the LHC*, *Eur. Phys. J. C* **81** (2021) 1029 [2108.01089].

[351] ATLAS collaboration, *Measurements of the inclusive and differential production cross sections of a top-quark–antiquark pair in association with a Z boson at $\sqrt{s} = 13$ TeV with the ATLAS detector*, *Eur. Phys. J. C* **81** (2021) 737 [2103.12603].

[352] ATLAS collaboration, *Inclusive and differential cross-section measurements of $t\bar{t}Z$ production in pp collisions at $\sqrt{s} = 13$ TeV with the ATLAS detector, including EFT and spin-correlation interpretations*, 2312.04450.

[353] CMS collaboration, *Search for physics beyond the standard model in top quark production with additional leptons in the context of effective field theory*, *JHEP* **12** (2023) 068 [2307.15761].

[354] A. Lazopoulos, T. McElmurry, K. Melnikov and F. Petriello, *Next-to-leading order QCD corrections to $t\bar{t}Z$ production at the LHC*, *Phys. Lett. B* **666** (2008) 62 [0804.2220].

[355] A. Kardos, Z. Trocsanyi and C. Papadopoulos, *Top quark pair production in association with a Z-boson at NLO accuracy*, *Phys. Rev. D* **85** (2012) 054015 [1111.0610].

[356] A. Broggio, A. Ferroglia, G. Ossola, B. D. Pecjak and R. D. Sameshima, *Associated production of a top pair and a Z boson at the LHC to NNLL accuracy*, *JHEP* **04** (2017) 105 [1702.00800].

[357] M. V. Garzelli, A. Kardos, C. G. Papadopoulos and Z. Trocsanyi, *Z0 - boson production in association with a top anti-top pair at NLO accuracy with parton shower effects*, *Phys. Rev. D* **85** (2012) 074022 [1111.1444].

[358] M. Ghezzi, B. Jäger, S. L. P. Chavez, L. Reina and D. Wackeroth, *Hadronic production of top-quark pairs in association with a pair of leptons in the powheg box framework*, *Phys. Rev. D* **106** (2022) 014001 [2112.08892].

[359] G. Bevilacqua, H. B. Hartanto, M. Kraus, J. Nasufi and M. Worek, *NLO QCD corrections to full off-shell production of $t\bar{t}Z$ including leptonic decays*, *JHEP* **08** (2022) 060 [2203.15688].

[360] A. Denner, D. Lombardi and G. Pelliccioli, *Complete NLO corrections to off-shell $t\bar{t}Z$ production at the LHC*, 2306.13535.

[361] B. Lillie, J. Shu and T. M. P. Tait, *Top Compositeness at the Tevatron and LHC*, *JHEP* **04** (2008) 087 [0712.3057].

[362] A. Pomarol and J. Serra, *Top Quark Compositeness: Feasibility and Implications*, *Phys. Rev. D* **78** (2008) 074026 [0806.3247].

[363] K. Kumar, T. M. P. Tait and R. Vega-Morales, *Manifestations of Top Compositeness at Colliders*, *JHEP* **05** (2009) 022 [0901.3808].

[364] G. Cacciapaglia, R. Chierici, A. Deandrea, L. Panizzi, S. Perries and S. Tosi, *Four tops on the real projective plane at LHC*, *JHEP* **10** (2011) 042 [1107.4616].

[365] M. Perelstein and A. Spray, *Four boosted tops from a Regge gluon*, *JHEP* **09** (2011) 008 [1106.2171].

[366] M. Toharia and J. D. Wells, *Gluino decays with heavier scalar superpartners*, *JHEP* **02** (2006) 015 [hep-ph/0503175].

[367] T. Plehn and T. M. P. Tait, *Seeking Sgluons*, *J. Phys. G* **36** (2009) 075001 [0810.3919].

[368] S. Calvet, B. Fuks, P. Gris and L. Valery, *Searching for sgluons in multitop events at a center-of-mass energy of 8 TeV*, *JHEP* **04** (2013) 043 [1212.3360].

[369] L. Beck, F. Blekman, D. Dobur, B. Fuks, J. Keaveney and K. Mawatari, *Probing top-philic sgluons with LHC Run I data*, *Phys. Lett. B* **746** (2015) 48 [1501.07580].

[370] L. Darmé, B. Fuks and F. Maltoni, *Top-philic heavy resonances in four-top final states and their EFT interpretation*, *JHEP* **09** (2021) 143 [2104.09512].

[371] E. Alvarez, D. A. Faroughy, J. F. Kamenik, R. Morales and A. Szynkman, *Four tops for LHC*, *Nucl. Phys. B* **915** (2017) 19 [1611.05032].

[372] E. Alvarez, A. Juste and R. M. S. Seoane, *Four-top as probe of light top-philic New Physics*, *JHEP* **12** (2019) 080 [1910.09581].

[373] D. Dicus, A. Stange and S. Willenbrock, *Higgs decay to top quarks at hadron colliders*, *Phys. Lett. B* **333** (1994) 126 [hep-ph/9404359].

[374] N. Craig, F. D'Eramo, P. Draper, S. Thomas and H. Zhang, *The Hunt for the Rest of the Higgs Bosons*, *JHEP* **06** (2015) 137 [1504.04630].

[375] N. Craig, J. Hajer, Y.-Y. Li, T. Liu and H. Zhang, *Heavy Higgs bosons at low* $\tan\beta$*: from the LHC to 100 TeV*, *JHEP* **01** (2017) 018 [1605.08744].

[376] G. Banelli, E. Salvioni, J. Serra, T. Theil and A. Weiler, *The Present and Future of Four Top Operators*, *JHEP* **02** (2021) 043 [2010.05915].

[377] C. Zhang, *Constraining qqtt operators from four-top production: a case for enhanced EFT sensitivity*, *Chin. Phys. C* **42** (2018) 023104 [1708.05928].

[378] D. Barducci et al., *Interpreting top-quark LHC measurements in the standard-model effective field theory*, 1802.07237.

[379] ATLAS collaboration, *Measurement of the* $t\bar{t}t\bar{t}$ *production cross section in pp collisions at* $\sqrt{s}$ *= 13 TeV with the ATLAS detector*, *JHEP* **11** (2021) 118 [2106.11683].

[380] CMS collaboration, *Evidence for four-top quark production in proton-proton collisions at* $\sqrt{s} = 13\ TeV$, *Phys. Lett. B* **844** (2023) 138076 [2303.03864].

[381] M. van Beekveld, A. Kulesza and L. M. Valero, *Threshold Resummation for the Production of Four Top Quarks at the LHC*, *Phys. Rev. Lett.* **131** (2023) 211901 [2212.03259].

[382] CMS collaboration, *Search for physics beyond the standard model in events with two leptons of same sign, missing transverse momentum, and jets in proton–proton collisions at* $\sqrt{s} = 13$ *TeV*, *Eur. Phys. J. C* **77** (2017) 578 [1704.07323].

[383] CMS collaboration, *Search for standard model production of four top quarks with same-sign and multilepton final states in proton–proton collisions at* $\sqrt{s} = 13$ *TeV*, *Eur. Phys. J. C* **78** (2018) 140 [1710.10614].

[384] ATLAS collaboration, *Search for new phenomena in events with same-charge leptons and b-jets in pp collisions at* $\sqrt{s} = 13$ *TeV with the ATLAS detector*, *JHEP* **12** (2018) 039 [1807.11883].

[385] CMS collaboration, *Search for the production of four top quarks in the single-lepton and opposite-sign dilepton final states in proton-proton collisions at* $\sqrt{s} = 13$ *TeV*, *JHEP* **11** (2019) 082 [1906.02805].

[386] G. Bevilacqua and M. Worek, *Constraining BSM Physics at the LHC: Four top final states with NLO accuracy in perturbative QCD*, *JHEP* **07** (2012) 111 [1206.3064].

[387] T. Ježo and M. Kraus, *Hadroproduction of four top quarks in the powheg box*, *Phys. Rev. D* **105** (2022) 114024 [2110.15159].

[388] N. Dimitrakopoulos and M. Worek, *Four top final states with NLO accuracy in perturbative QCD: 4 lepton channel*, 2401.10678.

[389] J. Campbell, J. Huston and F. Krauss, *The Black Book of Quantum Chromodynamics : a Primer for the LHC Era*. Oxford University Press, 2018, 10.1093/oso/9780199652747.001.0001.

[390] S. Höche, *Introduction to parton-shower event generators*, in *Theoretical Advanced Study Institute in Elementary Particle Physics: Journeys Through the Precision Frontier: Amplitudes for Colliders*, pp. 235–295, 2015, DOI [1411.4085].

[391] J. M. Campbell et al., *Event Generators for High-Energy Physics Experiments*, in *Snowmass 2021*, 3, 2022, 2203.11110.

[392] G. Altarelli and G. Parisi, *Asymptotic Freedom in Parton Language*, *Nucl. Phys. B* **126** (1977) 298.

[393] J. C. Collins, D. E. Soper and G. F. Sterman, *Transverse Momentum Distribution in Drell-Yan Pair and W and Z Boson Production*, *Nucl. Phys. B* **250** (1985) 199.

[394] J. C. Collins, D. E. Soper and G. F. Sterman, *Factorization for Short Distance Hadron - Hadron Scattering*, *Nucl. Phys. B* **261** (1985) 104.

[395] V. N. Gribov and L. N. Lipatov, *Deep inelastic e p scattering in perturbation theory*, *Sov. J. Nucl. Phys.* **15** (1972) 438.

[396] L. N. Lipatov, *The parton model and perturbation theory*, *Yad. Fiz.* **20** (1974) 181.

[397] Y. L. Dokshitzer, *Calculation of the Structure Functions for Deep Inelastic Scattering and e+ e- Annihilation by Perturbation Theory in Quantum Chromodynamics.*, *Sov. Phys. JETP* **46** (1977) 641.

[398] L. Buonocore, P. Nason, F. Tramontano and G. Zanderighi, *Leptons in the proton*, *JHEP* **08** (2020) 019 [2005.06477].

[399] A. Manohar, P. Nason, G. P. Salam and G. Zanderighi, *How bright is the proton? A precise determination of the photon parton distribution function*, *Phys. Rev. Lett.* **117** (2016) 242002 [1607.04266].

[400] A. V. Manohar, P. Nason, G. P. Salam and G. Zanderighi, *The Photon Content of the Proton*, *JHEP* **12** (2017) 046 [1708.01256].

[401] E. Byckling and K. Kajantie, *Particle Kinematics: (Chapters I-VI, X)*. University of Jyvaskyla, Jyvaskyla, Finland, 1971.

[402] R. Kleiss and R. Pittau, *Weight optimization in multichannel Monte Carlo*, *Comput. Phys. Commun.* **83** (1994) 141 [hep-ph/9405257].

[403] A. Denner, S. Dittmaier, M. Roth and D. Wackeroth, *Predictions for all processes $e^+e^- \to 4$ fermions + γ*, *Nucl. Phys. B* **560** (1999) 33 [hep-ph/9904472].

[404] S. Catani and M. H. Seymour, *A General algorithm for calculating jet cross-sections in NLO QCD*, *Nucl. Phys. B* **485** (1997) 291 [hep-ph/9605323].

[405] S. Catani, S. Dittmaier, M. H. Seymour and Z. Trocsanyi, *The Dipole formalism for next-to-leading order QCD calculations with massive partons*, *Nucl. Phys. B* **627** (2002) 189 [hep-ph/0201036].

[406] G. Bevilacqua, M. Czakon, M. Kubocz and M. Worek, *Complete Nagy-Soper subtraction for next-to-leading order calculations in QCD*, *JHEP* **10** (2013) 204 [1308.5605].

[407] M. Czakon, C. G. Papadopoulos and M. Worek, *Polarizing the Dipoles*, *JHEP* **08** (2009) 085 [0905.0883].

[408] P. Draggiotis, R. H. P. Kleiss and C. G. Papadopoulos, *On the computation of multigluon amplitudes*, *Phys. Lett. B* **439** (1998) 157 [hep-ph/9807207].

[409] P. D. Draggiotis, R. H. P. Kleiss and C. G. Papadopoulos, *Multijet production in hadron collisions*, *Eur. Phys. J. C* **24** (2002) 447 [hep-ph/0202201].

[410] D. Goetz, C. Schwan and S. Weinzierl, *Random Polarisations of the Dipoles*, *Phys. Rev. D* **85** (2012) 116011 [1205.4109].

[411] J. Bellm et al., *Herwig 7.0/Herwig++ 3.0 release note*, *Eur. Phys. J. C* **76** (2016) 196 [1512.01178].

[412] T. Sjöstrand, S. Ask, J. R. Christiansen, R. Corke, N. Desai, P. Ilten et al., *An introduction to PYTHIA 8.2*, *Comput. Phys. Commun.* **191** (2015) 159 [1410.3012].

[413] Sherpa collaboration, *Event Generation with Sherpa 2.2*, *SciPost Phys.* **7** (2019) 034 [1905.09127].

[414] S. Hoeche, F. Krauss, M. Schonherr and F. Siegert, *QCD matrix elements + parton showers: The NLO case*, *JHEP* **04** (2013) 027 [1207.5030].

[415] T. Gehrmann, S. Hoche, F. Krauss, M. Schonherr and F. Siegert, *NLO QCD matrix elements + parton showers in e^+e^- —> hadrons*, *JHEP* **01** (2013) 144 [1207.5031].

[416] B. Andersson, G. Gustafson, G. Ingelman and T. Sjostrand, *Parton Fragmentation and String Dynamics*, *Phys. Rept.* **97** (1983) 31.

[417] B. Andersson, *The Lund Model*, vol. 7 of *Cambridge Monographs on Particle Physics, Nuclear Physics and Cosmology*. Cambridge University Press, 7, 2023, 10.1017/9781009401296.

[418] D. Amati and G. Veneziano, *Preconfinement as a Property of Perturbative QCD*, *Phys. Lett. B* **83** (1979) 87.

[419] R. V. Harlander, S. Y. Klein and M. Lipp, *FeynGame*, *Comput. Phys. Commun.* **256** (2020) 107465 [2003.00896].

[420] S. Frixione, E. Laenen, P. Motylinski, B. R. Webber and C. D. White, *Single-top hadroproduction in association with a W boson*, *JHEP* **07** (2008) 029 [0805.3067].

[421] W. Hollik, J. M. Lindert and D. Pagani, *NLO corrections to squark-squark production and decay at the LHC*, *JHEP* **03** (2013) 139 [1207.1071].

[422] ATLAS collaboration, *Studies on top-quark Monte Carlo modelling for Top2016*, *ATL-PHYS-PUB-2016-020*.

[423] ATLAS collaboration, *Probing the quantum interference between singly and doubly resonant top-quark production in pp collisions at $\sqrt{s} = 13$ TeV with the ATLAS detector*, *Phys. Rev. Lett.* **121** (2018) 152002 [1806.04667].

[424] T. Ježo and P. Nason, *On the Treatment of Resonances in Next-to-Leading Order Calculations Matched to a Parton Shower*, *JHEP* **12** (2015) 065 [1509.09071].

[425] A. Denner, S. Dittmaier, M. Roth and L. H. Wieders, *Electroweak corrections to charged-current e+ e- —> 4 fermion processes: Technical details and further results*, *Nucl. Phys. B* **724** (2005) 247 [hep-ph/0505042].

[426] A. Denner and S. Dittmaier, *The Complex-mass scheme for perturbative calculations with unstable particles*, *Nucl. Phys. B Proc. Suppl.* **160** (2006) 22 [hep-ph/0605312].

[427] A. Denner and S. Dittmaier, *Electroweak Radiative Corrections for Collider Physics*, *Phys. Rept.* **864** (2020) 1 [1912.06823].

[428] A. Denner, *Techniques for calculation of electroweak radiative corrections at the one loop level and results for W physics at LEP-200*, *Fortsch. Phys.* **41** (1993) 307 [0709.1075].

[429] A. Denner and J.-N. Lang, *The Complex-Mass Scheme and Unitarity in perturbative Quantum Field Theory*, *Eur. Phys. J. C* **75** (2015) 377 [1406.6280].

[430] F. Siegert, *A practical guide to event generation for prompt photon production with Sherpa*, *J. Phys. G* **44** (2017) 044007 [1611.07226].

[431] E. W. N. Glover and A. G. Morgan, *Measuring the photon fragmentation function at LEP*, *Z. Phys. C* **62** (1994) 311.

[432] A. Gehrmann-De Ridder and E. W. N. Glover, *A Complete $\mathcal{O}(\alpha\alpha_s)$ calculation of the photon + 1 jet rate in e^+e^- annihilation*, *Nucl. Phys. B* **517** (1998) 269 [hep-ph/9707224].

[433] ALEPH collaboration, *First measurement of the quark to photon fragmentation function*, *Z. Phys. C* **69** (1996) 365.

[434] T. Gehrmann and R. Schürmann, *Photon fragmentation in the antenna subtraction formalism*, *JHEP* **04** (2022) 031 [2201.06982].

[435] A. Gehrmann-De Ridder, T. Gehrmann and E. W. N. Glover, *Radiative corrections to the photon + 1 jet rate at LEP*, *Phys. Lett. B* **414** (1997) 354 [hep-ph/9705305].

[436] A. Gehrmann-De Ridder and E. W. N. Glover, *Final state photon production at LEP*, *Eur. Phys. J. C* **7** (1999) 29 [hep-ph/9806316].

[437] L. Bourhis, M. Fontannaz and J. P. Guillet, *Quarks and gluon fragmentation functions into photons*, *Eur. Phys. J. C* **2** (1998) 529 [hep-ph/9704447].

[438] S. Actis, A. Denner, L. Hofer, A. Scharf and S. Uccirati, *Recursive generation of one-loop amplitudes in the Standard Model*, *JHEP* **04** (2013) 037 [1211.6316].

[439] S. Actis, A. Denner, L. Hofer, J.-N. Lang, A. Scharf and S. Uccirati, *RECOLA: REcursive Computation of One-Loop Amplitudes*, *Comput. Phys. Commun.* **214** (2017) 140 [1605.01090].

[440] F. J. Dyson, *The S matrix in quantum electrodynamics*, *Phys. Rev.* **75** (1949) 1736.

[441] J. S. Schwinger, *On the Green's functions of quantized fields. 1.*, *Proc. Nat. Acad. Sci.* **37** (1951) 452.

[442] J. S. Schwinger, *On the Green's functions of quantized fields. 2.*, *Proc. Nat. Acad. Sci.* **37** (1951) 455.

[443] A. Kanaki and C. G. Papadopoulos, *HELAC: A Package to compute electroweak helicity amplitudes*, *Comput. Phys. Commun.* **132** (2000) 306 [hep-ph/0002082].

[444] C. G. Papadopoulos and M. Worek, *Multi-parton cross sections at hadron colliders*, *Eur. Phys. J. C* **50** (2007) 843 [hep-ph/0512150].

[445] A. Cafarella, C. G. Papadopoulos and M. Worek, *Helac-Phegas: A Generator for all parton level processes*, *Comput. Phys. Commun.* **180** (2009) 1941 [0710.2427].

[446] A. Denner, S. Dittmaier and L. Hofer, *Collier: a fortran-based Complex One-Loop LIbrary in Extended Regularizations*, *Comput. Phys. Commun.* **212** (2017) 220 [1604.06792].

[447] F. Maltoni, K. Paul, T. Stelzer and S. Willenbrock, *Color Flow Decomposition of QCD Amplitudes*, *Phys. Rev. D* **67** (2003) 014026 [hep-ph/0209271].

[448] A. van Hameren, *Kaleu: A General-Purpose Parton-Level Phase Space Generator*, 1003.4953.

[449] A. van Hameren, *PARNI for importance sampling and density estimation*, *Acta Phys. Polon. B* **40** (2009) 259 [0710.2448].

[450] J. Alwall et al., *A Standard format for Les Houches event files*, *Comput. Phys. Commun.* **176** (2007) 300 [hep-ph/0609017].

[451] Z. Bern, L. J. Dixon, F. Febres Cordero, S. Höche, H. Ita, D. A. Kosower et al., *Ntuples for NLO Events at Hadron Colliders*, *Comput. Phys. Commun.* **185** (2014) 1443 [1310.7439].

[452] Z. Nagy and D. E. Soper, *Parton showers with quantum interference*, *JHEP* **09** (2007) 114 [0706.0017].

[453] Z. Nagy and D. E. Soper, *Parton showers with quantum interference: Leading color, with spin*, *JHEP* **07** (2008) 025 [0805.0216].

[454] Z. Nagy and D. E. Soper, *Parton showers with quantum interference: Leading color, spin averaged*, *JHEP* **03** (2008) 030 [0801.1917].

[455] Z. Nagy and Z. Trocsanyi, *Next-to-leading order calculation of four jet observables in electron positron annihilation*, *Phys. Rev. D* **59** (1999) 014020 [hep-ph/9806317].

[456] Z. Nagy, *Next-to-leading order calculation of three jet observables in hadron hadron collision*, *Phys. Rev. D* **68** (2003) 094002 [hep-ph/0307268].

[457] Z. Nagy and D. E. Soper, *Ordering variable for parton showers*, *JHEP* **06** (2014) 178 [1401.6366].

[458] A. Denner, L. Hofer, A. Scharf and S. Uccirati, *Electroweak corrections to lepton pair production in association with two hard jets at the LHC*, *JHEP* **01** (2015) 094 [1411.0916].

[459] A. van Hameren, C. G. Papadopoulos and R. Pittau, *Automated one-loop calculations: A Proof of concept*, *JHEP* **09** (2009) 106 [0903.4665].

[460] G. Ossola, C. G. Papadopoulos and R. Pittau, *Reducing full one-loop amplitudes to scalar integrals at the integrand level*, *Nucl. Phys. B* **763** (2007) 147 [hep-ph/0609007].

[461] G. Ossola, C. G. Papadopoulos and R. Pittau, *CutTools: A Program implementing the OPP reduction method to compute one-loop amplitudes*, *JHEP* **03** (2008) 042 [0711.3596].

[462] A. van Hameren, *OneLOop: For the evaluation of one-loop scalar functions*, *Comput. Phys. Commun.* **182** (2011) 2427 [1007.4716].

[463] F. Buccioni, S. Pozzorini and M. Zoller, *On-the-fly reduction of open loops*, *Eur. Phys. J. C* **78** (2018) 70 [1710.11452].

[464] A. Sirlin, *Radiative Corrections in the SU(2)-L x U(1) Theory: A Simple Renormalization Framework*, *Phys. Rev. D* **22** (1980) 971.

[465] W. F. L. Hollik, *Radiative Corrections in the Standard Model and their Role for Precision Tests of the Electroweak Theory*, *Fortsch. Phys.* **38** (1990) 165.

[466] W. J. Marciano and A. Sirlin, *Radiative Corrections to Neutrino Induced Neutral Current Phenomena in the SU(2)-L x U(1) Theory*, *Phys. Rev. D* **22** (1980) 2695.

[467] M. Lupattelli, *Precise predictions for top-quark pair production with additional jets at the LHC*, Ph.D. thesis, RWTH Aachen University, 2023.

[468] J. M. Campbell, R. K. Ellis and F. Tramontano, *Single top production and decay at next-to-leading order*, *Phys. Rev. D* **70** (2004) 094012 [hep-ph/0408158].

[469] M. Jezabek and J. H. Kuhn, *QCD Corrections to Semileptonic Decays of Heavy Quarks*, *Nucl. Phys. B* **314** (1989) 1.

[470] A. Czarnecki, *QCD corrections to the decay t —> W b in dimensional regularization*, *Phys. Lett. B* **252** (1990) 467.

[471] L. Basso, S. Dittmaier, A. Huss and L. Oggero, *Techniques for the treatment of IR divergences in decay processes at NLO and application to the top-quark decay*, *Eur. Phys. J. C* **76** (2016) 56 [1507.04676].

[472] D. Stremmer and M. Worek, *Associated production of a top-quark pair with two isolated photons at the LHC through NLO in QCD*, *JHEP* **08** (2023) 179 [2306.16968].

[473] NNPDF collaboration, *Parton distributions from high-precision collider data*, *Eur. Phys. J. C* **77** (2017) 663 [1706.00428].

[474] S. Bailey, T. Cridge, L. A. Harland-Lang, A. D. Martin and R. S. Thorne, *Parton distributions from LHC, HERA, Tevatron and fixed target data: MSHT20 PDFs*, *Eur. Phys. J. C* **81** (2021) 341 [2012.04684].

[475] T.-J. Hou et al., *New CTEQ global analysis of quantum chromodynamics with high-precision data from the LHC*, 1912.10053.

[476] A. Buckley, J. Ferrando, S. Lloyd, K. Nordström, B. Page, M. Rüfenacht et al., *LHAPDF6: parton density access in the LHC precision era*, *Eur. Phys. J. C* **75** (2015) 132 [1412.7420].

[477] Particle Data Group collaboration, *Review of Particle Physics*, *PTEP* **2022** (2022) 083C01.

[478] M. Cacciari, G. P. Salam and G. Soyez, *The anti-k_t jet clustering algorithm*, *JHEP* **04** (2008) 063 [0802.1189].

[479] Z. Bern, G. Diana, L. J. Dixon, F. Febres Cordero, S. Hoche, H. Ita et al., *Driving Missing Data at Next-to-Leading Order*, *Phys. Rev. D* **84** (2011) 114002 [1106.1423].

[480] J. M. Campbell, R. K. Ellis and C. Williams, *Driving missing data at the LHC: NNLO predictions for the ratio of $\gamma + j$ and $Z + j$*, *Phys. Rev. D* **96** (2017) 014037 [1703.10109].

[481] X. Chen, T. Gehrmann, N. Glover, M. Höfer and A. Huss, *Isolated photon and photon+jet production at NNLO QCD accuracy*, *JHEP* **04** (2020) 166 [1904.01044].

[482] H. A. Chawdhry, M. Czakon, A. Mitov and R. Poncelet, *NNLO QCD corrections to three-photon production at the LHC*, *JHEP* **02** (2020) 057 [1911.00479].

[483] T. Gehrmann, N. Glover, A. Huss and J. Whitehead, *Scale and isolation sensitivity of diphoton distributions at the LHC*, *JHEP* **01** (2021) 108 [2009.11310].

[484] H. A. Chawdhry, M. Czakon, A. Mitov and R. Poncelet, *NNLO QCD corrections to diphoton production with an additional jet at the LHC*, *JHEP* **09** (2021) 093 [2105.06940].

[485] S. Badger, T. Gehrmann, M. Marcoli and R. Moodie, *Next-to-leading order QCD corrections to diphoton-plus-jet production through gluon fusion at the LHC*, *Phys. Lett. B* **824** (2022) 136802 [2109.12003].

[486] X. Chen, T. Gehrmann, E. W. N. Glover, M. Höfer, A. Huss and R. Schürmann, *Single photon production at hadron colliders at NNLO QCD with realistic photon isolation*, *JHEP* **08** (2022) 094 [2205.01516].

[487] S. Badger, M. Czakon, H. B. Hartanto, R. Moodie, T. Peraro, R. Poncelet et al., *Isolated photon production in association with a jet pair through next-to-next-to-leading order in QCD*, 2304.06682.

[488] D. Stremmer and M. Worek, *Complete NLO corrections to top-quark pair production with isolated photons*, *JHEP* **07** (2024) 091 [2403.03796].

[489] M. Ciafaloni, P. Ciafaloni and D. Comelli, *Bloch-Nordsieck violating electroweak corrections to inclusive TeV scale hard processes*, *Phys. Rev. Lett.* **84** (2000) 4810 [hep-ph/0001142].

[490] NNPDF collaboration, *Illuminating the photon content of the proton within a global PDF analysis*, *SciPost Phys.* **5** (2018) 008 [1712.07053].

[491] A. Denner, S. Dittmaier, M. Hecht and C. Pasold, *NLO QCD and electroweak corrections to $W + \gamma$ production with leptonic W-boson decays*, *JHEP* **04** (2015) 018 [1412.7421].

[492] A. Denner, S. Dittmaier, M. Hecht and C. Pasold, *NLO QCD and electroweak corrections to $Z + \gamma$ production with leptonic Z-boson decays*, *JHEP* **02** (2016) 057 [1510.08742].

[493] D. Y. Bardin, A. Leike, T. Riemann and M. Sachwitz, *Energy Dependent Width Effects in e+ e- Annihilation Near the Z Boson Pole*, *Phys. Lett. B* **206** (1988) 539.

[494] S. Catani, M. Fontannaz, J. P. Guillet and E. Pilon, *Cross-section of isolated prompt photons in hadron hadron collisions*, *JHEP* **05** (2002) 028 [hep-ph/0204023].

[495] S. Catani, M. Fontannaz, J. P. Guillet and E. Pilon, *Isolating Prompt Photons with Narrow Cones*, *JHEP* **09** (2013) 007 [1306.6498].

[496] R. Schuermann, X. Chen, T. Gehrmann, E. W. N. Glover, M. Höfer and A. Huss, *NNLO Photon Production with Realistic Photon Isolation*, *PoS* **LL2022** (2022) 034 [2208.02669].